Ordering Phenomena in FeCo-Films and Fe/Cr-Multilayers: An X-ray and Neutron Scattering Study

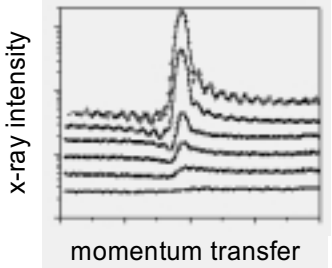

Bert Nickel
Stuttgart, März 2001

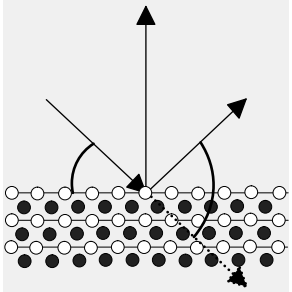

Max-Planck-Institut
für Metallforschung
in Stuttgart

Institut für Theoretische
und Angewandte Physik
der Universität Stuttgart

Ordering Phenomena in FeCo-Films and Fe/Cr-Multilayers: An X-ray and Neutron Scattering Study

Von der Fakultät für Physik der Universität Stuttgart
zur Erlangung der Würde eines Doktors der
Naturwissenschaften (Dr.rer.nat.) genehmigte Abhandlung

Vorgelegt von Bert Nickel aus Frankfurt am Main

Hauptberichter: Prof. Dr. H. Dosch
Mitberichter: Prof. Dr. M. Mehring

Eingereicht am 21. März 2001
Tag der mündlichen Prüfung: 29. Mai 2001

Institut für Theoretische und Angewandte Physik der Universität Stuttgart

2001

Chapter 1

Zusammenfassung

1.1 Motivation

Maßgeschneiderte Materialien wie magnetische Vielfachschichten oder dünne, superharte Filme erfahren im Moment eine hohe Aufmerksamkeit wegen der zu erwartenden und realisierten Anwendungen, z.B. als magnetische Sensoren mit außergewöhnlichen Eigenschaften. Diese resultieren unter anderem aus der Dominanz der Grenz- und Oberflächen. An ihnen zeigt sich ein breites Spektrum neuartiger Phänomene, die man unter dem Begriff Oberflächenphysik zusammenfasst. Beispiele sind die katalysatorische Wirkung von Oberflächen oder die Bildung neuartiger Strukturen an der Grenzfläche (Rekonstruktion), sowie eine Zu- oder Abnahme der magnetischen Momente an der Grenzfläche, oder auch die bevorzugte Anreicherung einer Komponente an der Grenzfläche (Segregation). Diese Oberflächenphänomene sind im Allgemeinem stark von der Realstruktur der Grenzfläche (Rauigkeit σ , atomare Stufen, epitaktische Spannung...) beeinflusst. Oftmals sind sie auf wenige atomare Lagen beschränkt; es gibt aber auch viele Fälle, in denen die Grenzfläche nachhaltig auf den angeschlossenen Festkörper einwirkt. Dies sind meist Systeme, deren thermodynamische Ei-

genschaften auf mikroskopischen, kollektiven Phänomenen beruhen, die sich auf einer charakteristischen Längenskala ξ abspielen. Dazu gehören z.B. ferromagentische Festkörper oder binäre Legierungen. Der von der Oberfläche favorisierte Zustand ist dann in einem oberflächennahen Bereich zu beobachten, der gerade der charakteristischen Längenskala ξ entspricht.

Ein weiterer grundlegender Aspekt ergibt sich aus der endlichen Dicke D solcher Systeme, welche im Nanometerbereich liegt. Gelingt es, die Schichtdicke D in die Größenordnung der systemimanenten Längenskala ξ zu bringen, kann sich das Verhalten eines solchen Festkörpers qualitativ ändern. Das magnetische Kopplungsverhalten von Vielfachschichten ändert sich z.B. drastisch, wenn man die Schichtdicke um nur eine Monolage ändert.

Dieser Aspekt tritt in ähnlicher Form auch ganz allgemein bei Phasenübergängen in dünnen Filmen auf. Ein kritischer Phasenübergang wird von Fluktuationen der lokalen Ordnung getrieben. Die charakteristische Größe (ξ) dieser Fluktuationen wächst bei Annäherung an die Phasenübergangstemperatur ($T \rightarrow T_c$) an. In einem dünnen Film ist dies aber durch die endlichen Schichtdicke D beschränkt. Deshalb erwartet man in diesem Fall in unmittelbarer Nähe des Phasenübergangs ein Ordnungsverhalten, dass den zweidimensionalen Charakter eines dünnen Films wiederspiegelt.

Für den experimentellen Nachweis wird ein Verfahren benötigt, welches es ermöglicht, kontrolliert Schichten einiger atomarer Monolagen herzustellen. Im weiteren wird deshalb die Methode der Molekularstrahl-Epitaxie (MBE) vorgestellt, die in dieser Arbeit zur Probenherstellung eingesetzt wurde. Weiterhin benötigt man tiefenauflösende (profilgebende) experimentelle Methoden mit atomarer Auflösung. Zu diesem Zweck wurden Röntgen- und Neutronen-Streuexperimente konzipiert und durchgeführt. Zwei Systeme werden in dieser Arbeit untersucht, zum einen dünne epitaktische FeCo-Filme auf MgO und zum anderen Fe/Cr Vielfachschichten.

1.1.1 Phasenübergänge in dünnen FeCo-Filmen

FeCo ist eine binäre Legierung, deren Volumen-Phasendiagramm einen Ordnungs-Unordnungs-Phasenübergang ($B2 \rightarrow A2$) aufweist, der experimentell alle wesentlichen Eigenschaften eines kritischen *3d*-Ising-Phasenüberganges zeigt. Dazu gehört auch die Divergenz der Korrelationslänge $\xi = \xi_0 \cdot |t|^{-\nu}$ mit $t = (T_c - T)/\, T_c$ bei Annäherung an T_c, d.h. für $t \rightarrow 0$. Eine endlichen Filmdicke D (realisiert: 50 Å $< D <$ 350 Å) sollte auf Grund einfacher Skalenargumente dazu führen, dass der Ordnungsparameter nahe T_c, d.h. für $t < (D/\, \xi_0)^{-1/\nu}$ *2d*-Verhalten zeigt und dass somit der kritische Exponent β ($\Psi \sim t^{\beta}$, $T < T_c$) seinen Wert von $\beta(3d) \simeq 0.31$ nach $\beta(2d) = 0.125$ ändert. Weiterhin sollte die Divergenz von ξ bei $\xi \approx D/\, 3$ aufgehalten werden[1]. Diese fundamentalen Vorhersagen bezeichnet man auch als *finite-size scaling*. Ihre experimentelle Überprüfung an einfachen Modellsystemen wie FeCo ist Grundlage für das Verständnis der komplexen Schichtsysteme, die heutzutage in Anwendungen realisiert sind und deren Miniaturisierung ständig vorangetrieben wird.

Ein weiterer Aspekt, der in einem dünnen Film eine wichtige Rolle spielt, ist die Frage nach dem Einfluss der Grenzflächen. Bereits eine geringfügige Präferenz der Grenzfläche für eine Komponente (Fe oder Co) induziert auch für $T > T_c$ einen Ordnungsparameter $\Psi(z = 0) > 0$ an der Oberfläche. Auf Grund der kurzreichweitigen Wechselwirkungen sollte dies ein Adsorptionsprofil $\Psi(z) = \Psi_0 \cdot \exp(-z/\, \xi)$ hervorrufen. Da die Zerfallslänge dieses Profils gerade mit der Korrelationslänge ξ identifiziert werden kann, spricht man in diesem Falle auch von *kritischer Adsorption*[2]. Das Ziel der FeCo-Experimente an dünnen Filmen ist deshalb die temperatur- und tiefenaufgelöste Bestimmung der Ordnungsparameterprofile $\Psi(z)$, um diese mit den oben angeführten detaillierten Voraussagen bezüglich *finite-size scaling* und

[1] H. Nakanishi and M. E. Fisher, J. Chem. Phys., **78** (1983) 3279

[2] S. Dietrich, Coll. de France C,**7** (1989) 233

kritischer Adsorption zu vergleichen.

1.1.2 Magnetisches Ordnungsverhalten in Fe/Cr-Mehrfachschichten

Fe/Cr ist das wohl bestuntersuchte magnetische Vielfachschichtsystem, welches einen Riesen-Magnetwiderstand-Effekt bei geeigneter Cr-Dicke zeigt, also eine starke Abnahme des Ohmschen Widerstandes beim Anlegen von äußeren Magnetfeldern H. Dies resultiert aus der Umorientierung der magnetischen Momente benachbarter Eisenschichten, die durch Anlegen eines Feldes parallel (ferromagnetisch) ausgerichtet werden, während im Grundzustand ($H = 0$) eine antiferromagnetische Konfiguration benachbarter Eisenschichten vorliegen kann. Auf Grund umfangreicher experimenteller und theoretischer Aktivitäten in den 80er und 90er Jahren ist das Kopplungsverhalten mittlerweile mit Hilfe der RKKY-Wechselwirkungstheorie verstanden. Es hat sich allerdings auch herausgestellt, dass Realstruktureffekte, wie Grenzflächenrauigkeiten oder Interdiffusion, das Kopplungsverhalten dramatisch ändern können. Die auffälligste Beobachtung ist, dass durch Rauigkeit auch nicht-kolineare Kopplung benachbarter Fe-Schichten stattfinden kann, man spricht dann auch von biquadratischer Kopplung. Ein tieferes Verständnis dieses Phänomens erfordert die Kenntnis der magnetischen Konfiguration an den Grenzflächen, man spricht hierbei auch von der magnetischen Rauigkeit. Die Untersuchung der magnetischen Rauigkeit in Fe/Cr-Vielfachschichten ist deshalb ein zentrales Thema dieser Arbeit.

1.2 Probenherstellung

Die Proben werden mittels Molekularstrahl-Epitaxie(MBE) hergestellt. Hierbei verdampft man das aufzutragende hochreine Material im Ultrahochva-

kuum (UHV) entweder durch Strahlungsheizung (Knudsenzelle) oder mittels eines Elektronenstrahlverdampfers. Typische Wachstumsraten liegen bei bis zu einer Atomlage pro Sekunde. Aufgedampft wurde auf mittels UHV-Standardverfahren[3] präparierten Substraten mit atomar glatter und sauberer Oberfläche. Für beide Systeme (FeCo und Fe/Cr) wird sich die epitaktische Beziehung zwischen Substrat und Film als besonders wichtig zur Interpretation der erzielten Ergebnisse herausstellen. Während die FeCo-Proben in der Stuttgarter[4] Metall-MBE hergestellt wurden, wurde die Fe/Cr Vielfachschicht in der Bochumer[5] MBE-Anlage hergestellt und von Herrn A. Schreyer zur Verfügung gestellt.

1.2.1 FeCo - Wachstum

Die FeCo-Filme wurden auf MgO(001) Substrate aufgedampft. Die epitaktische Beziehung zwischen Film und Substrat ergibt sich dann zu FeCo(001)‖MgO(001) und FeCo(100)‖MgO(110). Man spricht in diesem Falle auch von einer 45°-Epitaxie. Da MgO ein oxidischer Isolator ist, benetzt FeCo das Substrat nur schlecht. Aus diesem Grunde muß bei moderater Substrattemperatur (T_g <300°C) verdampft werden, um Entnetzung während des Wachstums zu verhindern, da man sonst keinen geschlossenen Film erhält. Durch anschließendes Aufheizen der Proben im UHV bei 800°C erhält man glatte Filme (σ <5 Å) mit geringer Mosaizität (0.3°) bei D = 350 Å. Bei geringeren Schichtdicken trat hierbei allerdings Entnetzung auf; der nach dem Wachstum geschlossene FeCo-Film separiert in FeCo-Inseln und blankes Substrat. Um dies zu unterdrücken, wurden die FeCo-Filme nach dem Wachstum zunächst mit einer Deckschicht aus MgO

[3]Sputtern, AES, LEED, RHEED

[4]Max-Planck Institut für Metallforschung, Gruppe Prof. H. Dosch

[5]Ruhr-Universität Bochum, Fakultät für Physik und Astronomie, Gruppe Prof. H. Zabel

bedampft. Dadurch konnte die Entnetzung vollständig unterdrückt werden, was für die erfolgreiche Durchführung der Röntgenmessungen nahe bei $T_c = 720°C$ Voraussetzung ist. Die Unterdrückung des Entnetzens könnte auch für andere technische Anwendung von dünnen Schichten bei erhöhten Temperaturen von Bedeutung sein.

1.2.2 Fe/Cr - Wachstum

Die Fe/Cr Vielfachschicht (200 Doppellagen mit je 19 ÅFe und 42 ÅCr) wurde auf eine Nb(001) Schicht aufgedampft, welche wiederum auf ein *R-plane* Saphirsubstrat aufgedampft wurde ($Al_2O_3(1\bar{1}02)$). Das System Nb-Saphir ist insofern bemerkenswert, als dass *3d*-Epitaxie vorliegt: Niob wächst auf jeder Saphiroberfläche epitaktisch. Da sowohl Niob als auch Saphir hochschmelzend sind, eignet sich das System in idealer Weise als Plattform für Metallepitaxie. Allerdings treten bei einigen Oberflächenorientierungen Anpassungsfehler auf; die Nb(001) Orientierung gehört dazu. Auf Grund eines Versetzungsnetzwerks an der Nb/Saphir Grenzfläche entstehen etwa 30 Å breite Terrassen entlang der Nb[110] Richtung. Diese Terrassenstruktur wird nun beim Wachstum der Fe/Cr Vielfachschicht vererbt, da bei moderater Temperatur ($T_g = 280°C$) aufgedampft wird, um Fe-Cr Interdiffusion zu verhindern. Die so gewachsenen Schichten zeigen erfahrungsgemäß eine besonders ausgeprägte biquadratische Kopplung und Ziel dieser Arbeit ist es, die magnetische Rauigkeit, die durch die Terrassenstruktur verursacht ist, zu charakterisieren.

1.3 Ergebnisse und Diskussion

1.3.1 Röntgen-Streuexperimente an FeCo-Filmen

Die FeCo-Experimente wurden an der europäischen Synchrotronquelle ESRF in Grenoble und am Hamburger Synchrotronstrahlungslabor HASYLAB durchgeführt. Dabei wurden Meßkammern eingesetzt, die es ermöglichten die Experimente unter UHV Bedingungen durchzuführen. Die Probe verlässt dabei das UHV zu keinem Zeitpunkt. Die Probentemperatur wurde mittels eines Pyrometers mit Digitalausgang bestimmt, da sich dies als die zuverlässigste Methode herausstellte. Geheizt wurden die Proben von einem meanderförmigen Tantaldraht. Die Temperaturstabilität war dabei besser als 0.1°C bei 700°C.

Zum Nachweis der Ordnungsparameter-Profile $\Psi(z)$ wurde die Methode der Braggstab-Streuung eingesetzt (engl. crystal truncation rod scattering). $\Psi(z)$ konnte dabei vollständig aus der Intensitätsverteilung um den FeCo(001)-Überstruktur-Reflex rekonstruiert werden. Dies war nur möglich, da die gestreute Intensität in dieser Region auf Grund der Epitaxie aus zwei miteinander interferierenden Beiträgen gleicher Größenordnung besteht, nämlich der Streuamplitude vom Substrat A(MgO) und der vom FeCo-Film A(FeCo). Dadurch übernimmt das Substrat die Rolle einer Phasenreferenz. Umfangreiche Modellrechnungen im Rahmen der kinematischen Streutheorie wurden durchgeführt, um die in den Streuexperimenten beobachteten Intensitätsverteilungen $I(q_z)$ sowohl qualitativ als auch quantitativ zu reproduzieren. Die Auswertung liefert folgende Ergebnisse[6]

- Alle FeCo-Filme sind über die gesamte Dicke einkristallin. Der FeCo-Film wächst in der ungeordneten Phase (B2, $\Psi(z) = 0$) auf. Wird der Film über T_c aufgeheizt und auf Raumtemperatur abgekühlt, liegt

[6]B.Nickel, W.Donner, H.Dosch *et al.*, Phys. Rev. Lett. **85** (2000) 134

eine homogen geordnete Phase ($\Psi(z) = const$) vor, deren Dicke der Schichtdicke entspricht.

- Die Interferenz von Substrat- und Film-Streuamplitude bewirkt eine asymmetrische Verteilung von $I(q_z)$ um den Überstruktur-Bragg-Reflex FeCo(001). Diese Asymmetrie enthält als Information den Abstand d zwischen der ersten aufgedampften Lage und der Substratoberfläche und die Atomspezies des FeCo-Films, die an der Grenzfläche zum Substrat dominiert. Für den 350 Å FeCo-Film ergibt sich $d = 2.30$ Å und eine Cobalt-Anreicherung an der Substrat/Film Grenzfläche.

- Eine gute Beschreibung von $I(q_z)$ ist über den gesamten Temperaturbereich möglich, wenn man $\Psi(z)$ als Summe eines homogenen Ordnungsparameter-Profils Ψ_{hom} und eines exponentiell abfallenden Ordnungsparameter-Profils $\Delta\Psi(z) = \Delta\Psi \cdot exp(-z/\,\xi)$ parametrisiert. Das gesamte Profil ergibt sich dann zu $\Psi(z) = \Psi_{hom} + \Delta\Psi(z)$. Über einen Vergleich der beobachteten und simulierten Intensitätsverteilung $I(q_z)$ sind somit der homogene Ordungsparameter Ψ_{hom}, die Zerfallslänge ξ und die Amplitude $\Delta\Psi$ zugänglich.

- Bei maximaler Temperatur ($T \gg T_c$) wird nur der exponentiell zerfallende Beitrag $\Delta\Psi(z)$ beobachtet. Kühlt man dann die Probe schrittweise ab, beobachtet man ein Anwachsen der Zerfallslänge ξ und einen leichten Anstieg der Amplitude $\Delta\Psi$. Unterhalb einer Temperatur T, die wir mit $T = T_c$ identifizieren, tritt auch der homogene Beitrag Ψ_{hom} auf und dominiert das Profil.

- Die Zerfallslänge ξ wächst bei Annäherung an T_c zunächst mit dem erwarteten Potenzgesetz $\xi(t) = \xi_0 \cdot |t|^{-\nu}$, mit $\xi_0 = 0.43 \pm 0.15$, $\nu = 0.65 \pm 0.02$ und $t = (T - T_c)/\,T_c$, in guter Übereinstimmung mit

den erwarteten *3d*-Ising Verhalten $\xi_0 = 0.448$ und $\nu = 0.643$. Weiterhin beobachtet man für $\Delta\Psi$ ein Temperaturverhalten, welches sich durch ein schwaches Oberflächenfeld h_1 erklären lässt, mit $h_1 \approx 0.1$. Dies bedeutet, dass die Wechselwirkung des Ordungsparameters an der Grenzfläche mit dem Substrat im Vergleich zur Nächsten-Nachbar-Wechselwirkung eher schwach ist. Somit kann das Ordnungsparameter-Profil oberhalb von T_c auf Grund der detailierten Analyse des Temperaturverhaltens der Parameter $\Delta\Psi$ und ξ als *schwache kritische Adsorption* gedeutet werden.

- Auf Grund der Phasensensitivität des Streuexperimentes kann die Lage des Adsorptions-Profils klar der MgO/FeCo Grenzfläche zugeordnet werden. Auch das Aufdampfen einer MgO-Deckschicht induziert kein Profil an der FeCo-Filmoberseite, symmetrische Randbedingungen werden nicht erreicht. Dies deutet darauf hin, dass die treibende Kraft, die das Adsorptionsprofil induziert (h_1-Feld) aus der epitaktischen Beziehung von FeCo und MgO resultiert. Auf Grund ihrer geringeren Kristallinität induziert die MgO-Deckschicht offenbar keine erhöhte Ordnung.

- Auch das Anwachsen von Ψ_{hom} unterhalb von T_c folgt einem Potenzgesetz $\Psi_{hom} = \Psi_0 \, |t|^\beta$ mit $\beta = 0.347 \pm 0.016$ und $\Psi_0 = 1.79 \pm 0.1$. β ist in guter Übereinstimmung mit dem theoretischen Wert für ein *3d*-Ising System $\beta = 0.314 \pm 0.004$. Die Amplitude Ψ_0 weicht von dem theoretischen Ising-Wert $\Psi_0 = 1.49$ für ein *3d*-Ising System leicht ab. Dies ist nicht unerwartet, da die Amplitude Ψ_0 im Gegensatz zu den kritischen Exponenten nicht universell ist, sondern auch von der Reichweite der atomaren Wechselwirkungen abhängt. Eine Berücksichtigung der Wechselwirkungsparameter von FeCo könnte die Übereinstimmung verbessern.

- In einem engen Bereich um T_c ($|t| < 4 \cdot 10^{-4}$) beobachtet man Abweichungen von ξ und Ψ_{hom} von dem oben beschriebenen Potenzverhalten. Für ξ deutet sich eine Sättigung bei $\xi \approx D/\ 3$ an, in Übereinstimmung mit den *finite-size scaling*-Vorhersagen. In dem gleichen engen Temperaturfenster um T_c weicht Ψ_{hom} von dem beobachteten *3d*-Ising Verhalten ab und eine doppelt-logarithmische Auftragung liefert $\beta = 0.125$, also gerade den *2d*-Ising Exponenten. Die vorläufige Auswertung eines dünneren (100 Å)-Films bestätigt den $2d - 3d-crossover$ in einem weitaus größeren Temperaturfenster.

1.3.2 Entwicklung neuartiger Neutronenstreumethoden

Die Fe/Cr Experimente wurden im Rahmen eines zweieinhalbjährigen Aufenthaltes am Hochflußreaktor Institut-Laue-Langevin (ILL) durchgeführt, bei dem die Entwicklung neuartiger Neutronen-Streumethoden am Oberflächen-Neutronen-Diffraktometer EVA im Mittelpunkt stand. Während dieses Aufenthaltes wurde das Instrument mit einem fokussierenden Monochromator versehen, der es erlaubt, den auf die Probe einfallenden Strahl anzustellen. Dadurch besteht nun die Option, die Reflektivität und diffuse Streuung von flüssigen, freien Oberflächen zu messen. Weiterhin wurden Fe/Si-Transmissions-Superspiegel installiert,[7] die als Polarisator und Analysator eingesetzt werden können, so dass z.B. in einem Reflektivitätsexperiment alle vier Neutronen-Wirkungsquerschnitte ($|++\rangle, |+-\rangle, |-+\rangle, |--\rangle$) bestimmt werden können. Diese Spiegel wurden z.B. erfolgreich in einem Experiment in Zusammenarbeit mit G.P. Felcher, Argonne National Laboratory, eingesetzt, bei dem die magnetischen (Vektor-)Profile einer Fe-Schicht gemessen wurden, die an eine CoSm-Schicht

[7] Zur Verfügung gestellt von Herrn T. Krist, Hahn-Meitner Institut, Berlin.

gekoppelt war. Dieses System dient als Modellsystem für einen Federmagneten (engl. spring magnet) und auf Grund der spin-aufgelösten Neutronen-Reflektivitätsmessung war es möglich, die Fächerstruktur der Fe-Momente nachzuweisen.

Für das Fe/Cr Experiment wurde als Analysator - erstmals in einem Reflektivitätsexperiment - ein ^{3}He-Spinfilter eingesetzt. Das ILL ist zur Zeit weltweit Vorreiter in der Herstellung solcher Filter. Dabei handelt es sich um für Neutronen transparente Gefäße (Glas, Silizium), welche mit polarisiertem Heliumgas gefüllt sind und die in einem schwachen, homogenen Magnetfeld plaziert werden. Der Absorbtionsquerschnitt von polarisiertem ^{3}He ist stark abhängig von der Orientierung des einfallenden Neutronenspins und somit ergibt sich die Filterwirkung. Der Einsatz eines solchen Filters ist insofern problematisch, als dass für eine hohe Analysatorstärke eine geringe Transmission in Kauf genommen werden muß. Weiterhin beträgt die Lebensdauer des polarisierten ^{3}He nur ca. 55 Stunden und am Instrument dürfen keine Streufelder vorliegen, was große Sorgfalt bei der Konstruktion des Probenmagneten erfordert[8]. Im vorliegenden Falle war der im Vergleich zu einem Superspiegel wesentlich größere Winkelbereich, der mit einem solchen ^{3}He-Analysator abgedeckt werden konnte, ausschlaggebend. Dadurch war es erstmals möglich, in einem Neutronen-Reflektivitätsexperiment nicht nur die Neutronen-Reflekitivität ($\alpha_i = \alpha_f$) spin-aufgelöst zu messen, sondern auch die nicht spekuläre, diffuse Streuung ($\alpha_i \neq \alpha_f$).

[8]Dr. J. Major, MPI Stuttgart, hat hierzu wertvolle Beiträge geleistet, die für den Erfolg des Experimentes wesentlich waren.

1.3.3 Nachweis der korrelierten magnetischen Rauigkeit in Fe/Cr-Mehrfachschichten

Die neuartige Experimentanordnung erlaubte die spin-aufgelöste Bestimmung der Neutronen-Reflektivität und der diffusen Streuung in einer Messung ($\alpha_i - \alpha_f$-Spektrum)[9]. Auf Grund der Linienform der Streusignale können die verschiedenen Streubeiträge separiert werden. Diese sind 1) Reflektivität 2) Kleinwinkelstreuung von mesoskopischen magnetischen Domänen und 3) diffuse Streuung.

1. Das Reflektivitäts-Signal bestätigt das bereits bekannte Strukturmodell der biquadratischen Kopplung aufeinander folgender Eisenschichten bei moderaten Feldstärken (H_{ext} = 560 G). Die Kohärenzlänge der Mehrfachschicht entspricht 8 Fe/Cr-Doppellagen, das sind 4% der Gesamtdicke.

2. Das Kleinwinkel-Signal weist auf die Existenz von mesoskopischen ($\sim$ 1 μm) magnetischen Domänen entlang der Oberfläche der Mehrfachschicht hin, die durch einmaliges Aufmagnetisieren (H_{ext} >1000 G) ausgerichtet werden können.

3. Der Nachweis der magnetisch-diffusen Streuung (Spinflip-Streuung) ist ein direkter Hinweis für die Existenz magnetischer Rauigkeit.

    - Diese magnetisch-diffuse Streuung ist entlang der Probennormale ($q \parallel q_\perp$) in *Bragg-sheets* stark gebündelt. Dies bedeutet, dass die Rauigkeit in Richtung der Oberflächennormale stark korreliert ist. Ein Vergleich der Halbwertsbreiten von Reflektivität und diffuser Streuung zeigt sogar, dass diese Korrelation maximal ist. Dies

[9] B.Nickel, A.Rühm, W.Donner, J.Major, H.Dosch *et al.*, Rev. Sci. Inst., Jan. 2001

kann nur bedeuten, dass sich die bei Wachstumsbeginn vorhandene Terrassenstruktur der Niob-Schicht voll in die Vielfachschicht vererbt und somit die Rauigkeit strukturiert.

- Die Intensitätsverteilung entlang der *Bragg-sheets* ($q_z = const.$) ist auf Grund der mikroskopischen Terrassenlänge (~ 50 Å) strukturlos. Die qualitativ ähnliche Verteilung der Reflektivitäts- und diffusen Streusignale auf die verschiedenen Spin- und Non-Spinflip-Kanäle bedeutet weiterhin, dass nicht nur die (entlang der Probenoberfläche) gemittelten magnetischen Momente aufeinander folgender Eisenschichten biquadratisch koppeln, sondern auch die lokalen Abweichungen, also einzelne Terrassen.

- Die gewonnenen Daten wurden auch quantitativ ausgewertet. Hierfür wurde ein aus der Neutronen-Reflektivität bekanntes Werkzeug, der Supermatrix-Formalismus[10] eingesetzt. Dieser ermöglicht es, die (komplexe) Neutronen-Wellenfunktion $|\Psi(z)\rangle$ in einer idealisierten magnetischen Vielfachschicht zu berechnen. Die gewonnene Wellenfunktion wird im Rahmen eines DWBA[11]-Ansatz an den (magnetisch) rauen Grenzflächen gestreut[12]. Dr. A. Rühm[13] hat den Formalismus entwickelt und in ein C^{++} Programm übersetzt, welches die experimentell gewonnenen Messdaten numerisch erzeugen kann. Aus dem quantitativen Vergleich von Simulation und Messung folgt, dass die beobachteten Daten reproduziert werden können, wenn man Grenzflächen mit 4 Å Rauigkeit annimmt, die entlang der Probennormale voll korreliert sind und deren Korrelationslänge in der Ebene mikro-

[10] A. Rühm, B.P. Toperverg and H. Dosch, Phys. Rev. B, **60** (1999) 16073

[11] Distorted Wave Born Approximation

[12] S. K. Sinha *et al.*, Phys. Rev. B **38** (1988) 2297

[13] gegenwärtige Adresse: Advanced Photon Source, Argonne National Laboratory, USA

skopisch ist (50 Å). Die magnetische Rauigkeit folgt dabei der strukturellen Rauigkeit.

1.4 Ausblick

1.4.1 FeCo

Nachdem die Ordnungsparameter-Profile in dünnen FeCo-Filmen nun verstanden sind, wäre es wünschenswert auch einen experimentellen Zugang zu den Fluktuationen, oder genauer, zur Korrelationsfunktion zu haben. Der klassische Zugang wäre dabei die Messung der kritisch diffusen Streuung. Diese war bei den durchgeführten Experimenten aber jenseits der Nachweisgrenze. Deshalb sollte evtl. auf ein System ausgewichen werden, bei dem kritisch diffuse Streuung zumindest bei Volumenproben bereits ausführlich studiert wurde, z.B. Fe_3Al. Umfangreiche MBE-Wachstumsstudien wurden für dieses System allerdings noch nicht durchgeführt. Darüber hinaus wären Experimente an Nanostrukturen, also z.B. FeCo-Streifen, sicherlich vielversprechend. Sollte es gelingen, diese Streifen unter UHV-Bedingungen zu erzeugen und anschließend mit einer MgO-Schutzschicht zu bedampfen, hätte man ein ideales Modellsystem für eine Vielzahl interessanter Fragestellungen. Hätten diese Streifen z.B. einen quadratischen Querschnitt der Kantenlänge D, sollte für $\xi \approx D$ ein Übergang von $3d$ nach $1d$ experimentell beobachtbar sein. D sollte dafür in der Größenordnung 100 Å liegen. Die Nutzung moderner Lithographie-Methoden zur Herstellung und der Einsatz eines Mikrofokus-Synchrotronstrahls zur Messung der Bragg-Profile ermöglichen solche Experimente bereits heute. Eine weitere interessante Herausforderung wäre sicherlich auch die Messung der Dynamik kritischer Phänomene in dünnen Filmen, z.B. mittels eines kohärenten Röntgenstrahls. Auch hierbei erwartet man Dünnfilmeffekte, die jedoch bis vor kurzem mit Synchrotron-

Experimenten noch nicht zugänglich waren, da kohärente Röntgenstrahlen nicht in ausreichender Intensität vorlagen.

1.4.2 EVA + Fe/Cr

Die spin-aufgelösten Neutronenstreuexperimente haben eindrucksvoll die ausgezeichnete Stellung von Neutronen zum Nachweis magnetischer Rauigkeit in Vielfachschichten unter Beweis gestellt. Neue feld- und winkelabhängige Messungen wurden bereits durchgeführt[14], um das Potential dieser Methode weiter auszuloten. Hierbei wird sicherlich die Weiterentwicklung des Supermatrix-Formalismus zur Analyse verschiedener Realstruktureffekte wesentlich sein, z.B. die Berücksichtigung von Rauigkeitsgradienten in Wachstumsrichtung (kinetische Aufrauhung). Die Anwendung einer komplementären Messmethode zur Ermittlung der chemischen Rauigkeit (z.B. TEM) ist dabei wünschenswert.

[14]Die Messungen wurden von J.Major und A.Vorobiev am EVA-Reflektometer am ILL in Grenoble durchgeführt.

Contents

Chapter 2

Introduction

Since an appealing and surprisingly high degree of order is discovered at the atomic scale, self-organization and ordering phenomena belong to the building principles of the microscopic world. However, to study the driving forces of these ordering principles in the world of atoms, appropriate experimental techniques must be employed. In this context, diffraction experiments have changed our understanding of what occurs at atomic scale. The famous experiment of Laue [1, 2] [1] proved that atoms are located on regular positions in crystals. Later on, Shull [2] [3, 4] used neutron scattering experiments to study "where the atoms are and what they do", and much of our understanding of cooperative phenomena in solids was induced by his work.

Nowadays, scientists profit from 2nd and 3rd generation x-ray sources such as the European Synchrotron Research Facility (ESRF) or from the high flux neutron reactor Institut-Laue-Langevin (ILL), both situated in Grenoble, France. In the case of x-rays, the high flux combined with the high brilliance and the tunability of the wavelength enables new kinds of experiments. For example biologists use today Laue's technique for the determination of the

[1] Nobel prize 1914
[2] Nobel prize 1994

three-dimensional structure of complex biological systems, such as photosynthetic reaction centers[3].

A theoretical breakthrough in the understanding of ordering phenomena came from a surprisingly simple theoretical model, the Ising model. In this model, atoms are assumed to interact with their nearest and next-nearest neighbor atoms via short-ranged ordering forces. It turns out that many systems may be described with this model, including magnetic and antiferromagnetic ordering in crystals, ordering in binary alloys, and the liquid/vapor phase transition. Moreover, this model permits understanding the nature of phase transitions and especially the importance of critical fluctuations governed by the correlation length ξ in second order phase transitions. The correlation length is typically the order of several Å, but close to a phase transition it may become much larger. Inspired by the good agreement between experimental results and theoretical predictions, the Ising model has been carefully extended. Today even biological systems such as membranes or liquid crystals can be treated with the same concepts such as used for binary alloys.

FeCo

For thin films an obvious question emerges: under which conditions will a thin film, which is a three dimensional object, behave effectively as a two dimensional system? Our system of choice to answer this question experimentally is FeCo, a binary alloy which shows a critical phase transition from the ordered B2 to the disordered bcc phase[5]. In a bulk FeCo-samples, this phase transition is driven by fluctuations of the order parameter on a length scale ξ, which diverges when approaching the phase transition temperature T_c. The prediction is that a thin film will show two-dimensional behavior

[3]Nobel prize 1988

when ξ approaches the order of the film thickness [6].

Further, the presence of the two interfaces in a thin film raises the question of how the regions near the interface will behave. At the interface, the fluctuations are abruptly terminated. Further, the interface may attract one component (Fe or Co) and induce order in subsequent layers, a phenomenon called critical adsorption. Therefore, in order to study the critical phase transition in thin films experimentally, one needs to determine the depth and temperature dependence of the atomic arrangement of the Fe and Co atoms on their respective sublattices, much in the spirit of Laue and Shull. The experimental results obtained mainly at the ID10 beamline (ESRF) and partly at the W1 and CEMO beamlines (HASYLAB) will be given in the first part of this work.

Fe/Cr

There is great interest in the ordering behavior of nanometer-sized systems due to the great potential of these structures as electronic devices. For example, the unusual magneto-transport properties of magnetic sandwiches, the giant magnetoresistance (GMR) discovered in 1988 [7] is today used in hard disks as read/write heads, and soon it will be employed in mechanical devices, such as for automobiles [8].

To understand GMR a detailed picture of the magnetic ordering of ferromagnetic layers, separated by non- or antiferromagnetic layers of some Å thickness is needed. The 180° ordering of Fe layers, separated by a Cr spacer has been discovered in 1986 by means of light scattering [9]. Two years later, it was discovered that the resistance of such a multilayer depends strongly on the external applied field [7] and the resulting orientation of adjacent Fe layers. Soon it was realized that the growth conditions and the resulting sharpness of the interfaces have strong influence on the order-

ing angle, which may change from 180° to 90° [10, 11]; or on the magnetic coupling, which can change from antiferromagnetic to biquadratic. *Ab initio* calculations of real systems are still unsatisfactory, mainly because it is not clear which defects are the most relevant and how they may be included into first principle calculations. Therefore, it is demanding to use experimental methods such as neutron scattering to investigate the nuclear and magnetic real structure of Fe/Cr multilayers. The appealing advantage of neutrons is manifold. First, with polarized neutron reflectivity, one has a tool that can give the depth-resolved magnetization of every layer. This is a clear advantage over the many integrating methods. Second, a careful analysis of the off-specular scattering within the framework of the supermatrix formalism extended to off-specular scattering promises that one can determine not only the depth-resolved mean magnetization, but also the local deviation from the mean structure due to domains and magnetic roughness. In the second part of this work, the experimental results obtained at the EVA instrument (ILL), using a new experimental technique to analyze off-specular neutron scattering with polarized ^{3}He are presented.

Chapter 3

Critical Phenomena in thin films

The aim of this work is to study how critical ordering phenomena occur in a thin film. For this purpose, critical phenomena in bulk systems are reviewed briefly and basic concepts such as the correlation length and the order parameter are introduced. Then, the different scenarios that emerge due to the presence of a surface are considered, with emphasis of a phenomenon called critical adsorption. Finally, the new aspects that arise due to the finite thickness of a film, namely dimensional-crossover and finite size scaling are discussed.

3.1 Introduction

Phase transitions are important for the understanding of the microscopic and macroscopic worlds. The following are some examples of how substantially the properties of condensed matter can change by undergoing phase transitions:

1. Iron: whereas ferromagnetic at low temperatures, above its Curie temperature ($T_c = 1045\ K$), the material is paramagnetic and loses its versatility for data storage applications.

2. H_2O in its different phases, as water, ice or gas. One of our present concerns is that a slight average temperature increase due to the greenhouse warming might result in a melting of large amounts of sea ice, with virtually unpredictable implications for our future climate.

3. ^{4}He: behaving like a normal viscous liquid above $\simeq 2K$, it becomes superfluid at temperatures below this due to Bose condensation, i.e. it contains a component that has no viscosity.

In principle it does not take much to detect a phase transition: a calorimeter is sufficient. Such an experimental apparatus measures the amount of heat $\delta\ Q$ needed to increase the temperature of the sample under investigation for an amount $\delta\ T$. From the result of such a measurement, a phase transition can be either first order or continuous.

If latent heat is observed, the phase transition is called a first order phase transition. This is for example the case for the melting of ice; a certain nonzero amount of heat ($\delta\ Q \simeq 334 J/\ g$) will be needed to transform ice into water, even for an arbitrary small temperature step from below 0^o to above 0^o.

If no latent heat is observed, the phase transition is called continuous. This is the case for Fe near its Curie temperature. If the continuous phase transition is critical, quantities such as the specific heat C and the susceptibility χ will diverge when the phase transition temperature T_c is approached, resulting for example in the well-known "lambda-shape" [12] of the specific heat C, depicted in Fig. 3.1b (solid line). The order parameter $\Psi(T)$ (magnetization, density or fraction of Bose condensed liquid) mirrors the behavior of the specific heat C in a particular way: in a first order phase transition, the

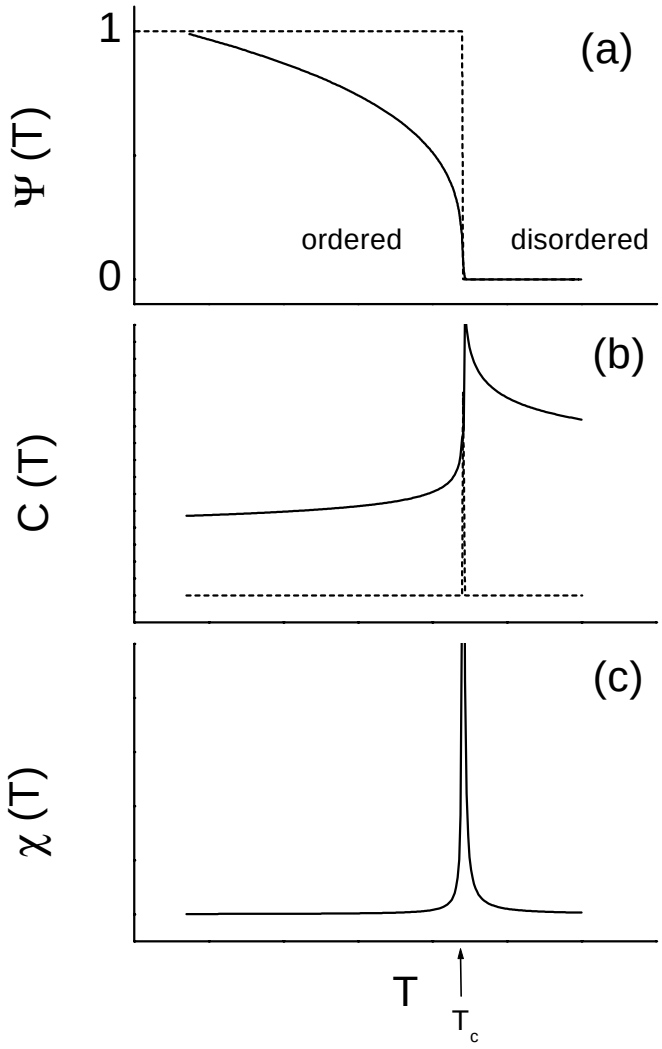

Figure 3.1: Temperature dependence at a critical phase transition (solid lines) and a first order phase transition (dashed lines). (a) The order parameter $\Psi(T)$. (b) The specific heat $C(T)$. For a critical phase transition, $C(T)$ diverges continuously. At a first order phase transition, latent heat occurs, represented here by a delta-function peak at $T = T_c$. (c) Susceptibility $\chi(T)$. The case of a first order phase transition is not shown.

order parameter vanishes abruptly, whereas in a continuous phase transition, the order parameter vanishes continuously, c.f. Fig. 3.1a. The behavior of Ψ, C and χ for a critical phase transition is summarized in Fig. 3.1 using numerical values for a *3d*-Ising model (see below). For comparison, the behavior at a first order phase transition is sketched also. The properties of critical phase transitions shall be discussed now in more detail.

3.2 Bulk critical phenomena

Critical phenomena in bulk systems have been observed experimentally in a variety of systems such as binary alloys (Fe_3Al, β-CuZn, FeCo), antiferromagnets (Cr) and ferromagnets (Fe, Co, Ni), superfluids (^{3}He, ^{4}He), superconductors, binary fluid mixtures and many more, as reviewed e.g. in [13, 14, 15]. The behavior of all these systems close to the phase transition at $T = T_c$ can be described and understood by some fundamental concepts which will be reviewed now.

3.2.1 Power law behavior

The fingerprint of a critical phase transition is the behavior of the vanishing order parameter Ψ and the diverging susceptibility χ_T and specific heat C_Ψ close to T_c. These quantities, defined as

$$\begin{aligned} \Psi &= \frac{\partial F}{\partial H}\Big|_T \\ \chi_T &= \frac{\partial \Psi}{\partial T}\Big|_H \\ C_\Psi &= \frac{\partial S}{\partial T}\Big|_\Psi \end{aligned} \tag{3.1}$$

with the free energy F, the entropy S and the external ordering field H follow power laws close to T_c,

$$\Psi \propto t^\beta, T < T_c \tag{3.2}$$

$$\chi_T \propto t^{-\gamma}$$
$$C_\Psi \propto t^{-\alpha}$$

where $t = |(T_c - T)/\, T_c|$ is defined as the reduced temperature. The exponents $(\alpha, \beta, ...)$ are called *critical exponents* and their determination is the focus of theoretical and experimental efforts. The numerical values of these exponents are determined only by fundamental properties of the system, such as the dimension d, the range of interaction (short range or long range) and the degree of freedom n of the order parameter. One may subdivide the systems into universality classes [13], within each the same set of critical exponents is valid. The most well-known universality class is the Ising spin 1/2 ($n = 1$) class. In this universality class, species are distributed on a regular lattice and each can take one of two states, e.g. "up" or "down", similar to a spin 1/2 particle. The archetypical example for this class is a magnetic structure with atoms carrying a magnetic moment of $J = 1/\,2$. In an Ising model, the species interact via short range forces, i.e. nearest and next-nearest neighbor interactions. It turns out both experimentally and theoretically that many other systems (for example coexistence of binary liquids or the liquid gas phase transition) can be mapped onto this simple universality class [15]. In the following, if n is not given explicitly, $n = 1$ is assumed.

3.2.2 The Ornstein-Zernike (OZ) approach

Every experiment that measures a thermodynamic quantity such as magnetization, density, specific heat or susceptibility is suited for the study of critical phenomena. Indeed all these experimental techniques are applied successfully to determine selected critical exponents. However, scattering experiments using light, electrons, neutrons or x-rays have proven to have outstanding capabilities for the observation of critical phenomena. This is due to the occurrence of critical fluctuations close to T_c, a phenomena ob-

served first 1869. At that time, Andrews observed that carbon dioxide, which phase-separates below $T_c = 31.04^oC$ at $p \cong 0.5$ gm cm^{-3} into a liquid and a lighter gas phase, transforms at T_c into a "mist" of "critical opalescence". The explanation of these "Dichteschwankungen" was a severe theoretical problem, resolved in L. S. Ornstein and F. Zernikes (OZ) famous publication from 1918 [16] in which the concept of correlation length ξ, correlation function $G(r)$ and critical fluctuation was introduced and calculated within a mean field approach.

To interpret the outcome of the OZ approach, it is useful to introduce the microscopic variable $\Psi(r_i) = s_i$, which represents the state of the system at each lattice place. The correlation of the local deviations from the average distribution is then given by the definition of the two point correlation function

$$G(r) \quad = \quad \langle \Psi(0) \cdot \Psi(r) \rangle - \langle \Psi(r) \rangle^2 \tag{3.3}$$

and the order parameter $\Psi(t)$ is defined as

$$\Psi = \langle \Psi(r) \rangle. \tag{3.4}$$

The OZ result for $d = 3$ is

$$G(r) \quad = \quad \frac{\exp\ (-r/\ \xi)}{r}. \tag{3.5}$$

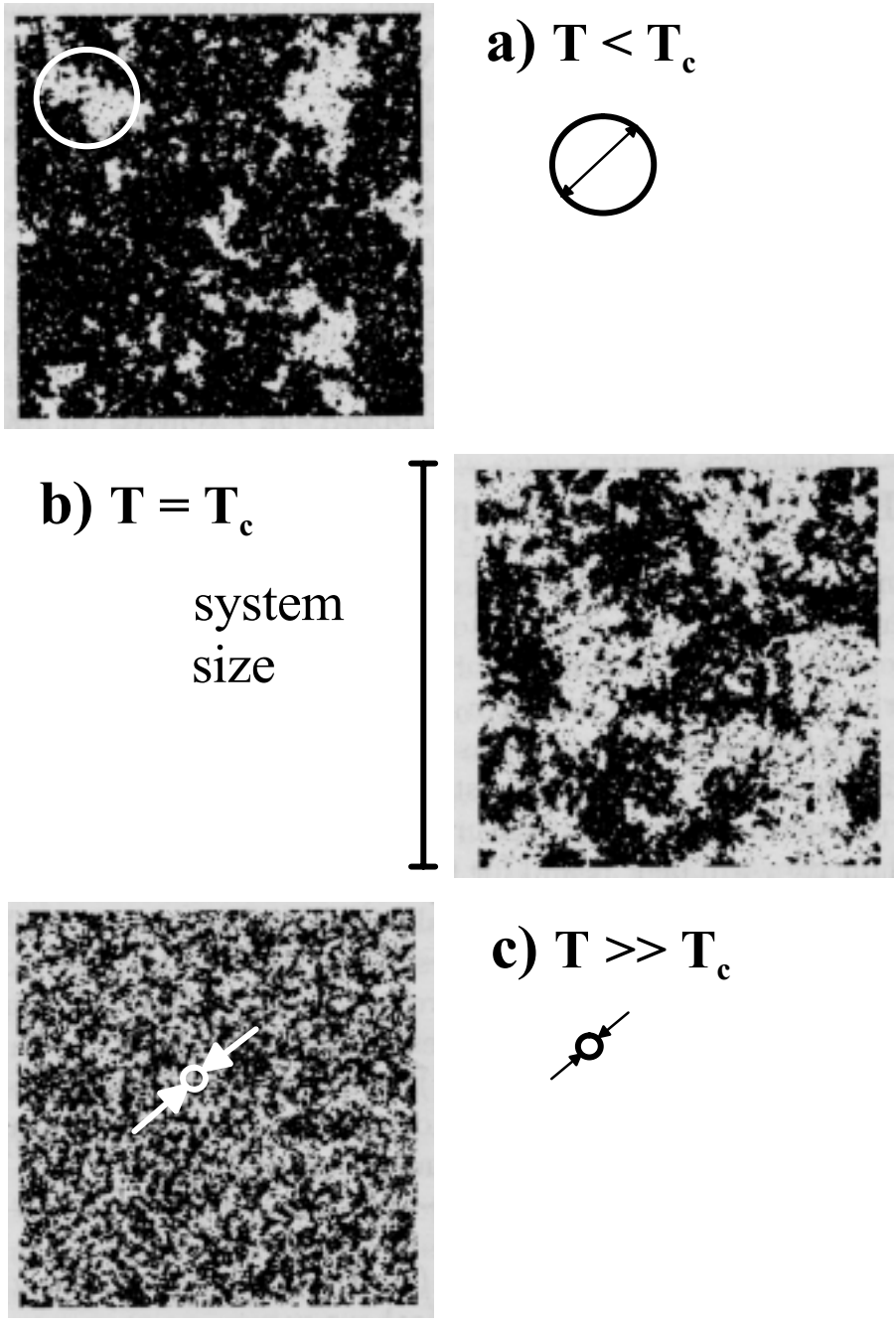

Figure 3.2: Numerical simulation of critical fluctuations in a $2d$-Ising system, from [17]. The correlation length $\xi(T)$ is shown schematically (a) slightly below T_c (b) at T_c (c) above T_c.

Several points of interest should be discussed. First, the OZ form of $G(r)$ is only a function of one variable, a direct result of the translational symmetry of an infinitely extended system. However, one should keep in mind, that the presence of a surface will break this symmetry, and the correlation function close to a surface may be in general a function of two variables. Second, the correlation function defines a new length scale ξ, called the correlation length. OZ realized that ξ acts like an effective particle size of a region with a different density, producing the "critical opalescence". Today, this effective particle is called a fluctuation. It represents a highly correlated region in space of size ξ^3. ξ may be understood as the typical length scale over which local order is preserved in the system (see Fig. 3.2). When T_c is approached, ξ diverges, obeying the power law

$$\xi(t) \;=\; \xi_0 \cdot t^{-\nu} \tag{3.6}$$

with the critical exponent ν . OZ found $\nu = 1/2$. ξ_0 is a microscopic length of the order of the unit cell, which can be estimated theoretically for simple systems [18]. The value of ξ_0 will depend on whether T_c is approached from above or below and this aspect will be discussed in Sec. 3.2.6. OZ were even more exited as they realized that the Boltzmann principle is not applicable within the region of a single fluctuation[1]. Fig. 3.2 visualizes the above scenario using the results of a computer simulation of a $2d$-Ising system, that undergoes a critical phase transition. The used Wolff-algorithm is discussed in [17]. The system can take two states, black and white. Far below T_c, the system state is black (not shown) due to spontaneous symmetry breaking.

[1]OZ close their paper with "*Die Anwendung des Boltzmannschen Prinzips muß beschränkt werden auf Volumenelemente, deren Dimensionen groß gegen ξ sind. Im kritischen Punkt ist dies unmöglich. Es ist also eine völlige Verkennung des Sachverhalts, wenn man den unendlichen Wert der Dichteschwankungen im kritischen Punkt ... dadurch zu verbessern sucht, daß man in der Entwicklung der Entropie höhere Glieder berücksichtigt.*" [16]

Fluctuations arise when the temperature is increased to a value close to but below T_c, as shown in Fig. 3.2a. Their size is characterized by $\xi(T)$. Note that Fig. 3.2a is only a snapshot of the system state; its associated dynamics are their own interesting field of study [13, 19, 20]. At T_c, Fig. 3.2b, the size of the fluctuations is of the order of the system size. To minimize finite size effects, this computer simulation has employed periodic boundary conditions. Later in the text, the periodic boundary conditions are replaced with a real surfaces and this will give rise to new phenomena. The order parameter (Eq. 3.4), is already zero in Fig. 3.2b. Finally, if the temperature is increased above T_c, ξ decreases again, as shown in Fig. 3.2c.

3.2.3 Scaling

Thermodynamics connects the different derivatives of the thermodynamic potentials via the Maxwell relations and furthermore, some inequations, so-called stability criteria, e.g. (Le Chatelier's principle) are valid, as the reader might check e.g. in [21], chapter 7-8. In case of a critical phase transition, these inequalities can become equations, if one assumes the validity of certain scaling properties of the thermodynamic potentials. According to the Widom [22] scaling hypothesis the Helmholtz free energy can be expressed close to T_c by a function Υ

$$F(T, H) = t^{1/y} \cdot \Upsilon(H/\ t^{x/y}). \tag{3.7}$$

This form of the Helmholtz free energy implies that the numerical values of the critical exponents are now related by so-called scaling laws [17]. The first scaling law derived this way reads

$$\alpha + 2\beta + \gamma = 2 \tag{3.8}$$

This expression connects the behavior of specific heat, order parameter and susceptibility close to T_c. For example, from the simultaneous measurement

of the specific heat and the order parameter close to T_c, the behavior of the susceptibility can be predicted. Or, if all three are measured, this measurement can be used to test the scaling hypothesis (Eq. 3.7) experimentally [12]. For the second scaling law, the critical exponent, δ has to be defined first. The field induced order parameter $\Psi(H,t)$ obeys at T_c a power law

$$\Psi(H, t = 0) \propto \Psi_H \cdot H^{1/\delta} \tag{3.9}$$

controlled by the critical exponent δ . The behavior of the field-induced order parameter is connected to the specific heat and the order parameter by the second scaling law

$$\alpha + \beta(\delta + 1) = 2. \tag{3.10}$$

Kadanoff pointed out that two further experimentally-satisfied scaling laws can be deduced, if one assumes that the correlation function $G(r)$ can be written as

$$G(r,t) = \frac{\Upsilon(r \cdot t^{(2-\alpha)/d})}{r^{d-2+\eta}} \tag{3.11}$$

with η as another critical exponent, completing the list of critical exponents for simple Ising systems. Then two further scaling laws follow [17],

$$\nu = (2-\alpha)/\, d \tag{3.12}$$

and

$$\nu = \gamma/\,(2-\eta). \tag{3.13}$$

Eq. 3.12 (Jefferson's law) is interesting since it contains not only exponents, but also the spatial dimension d. It states explicitly that from the knowledge of the critical exponents, one can deduce the dimension d of a system. This is quite interesting since d is not always obvious. For example, a monolayer of

iron ($N = 1$) will surely show two-dimensional behavior ($d = 2$), and indeed, experiments confirm this even for $N = 2$ [23]. But for example, what is expected for 8 atomic layers [24]? This question will be addressed below when systems of finite thickness are considered. $2d$-behavior can also be found for the ordering behavior of nobel gases intercalated in graphite. This implies that the intercalated atoms do not interact with atoms of neighboring planes, resulting in an effective dimension $d = 2$. Electrons in modern complex oxides, build up from sequent layers of different atoms, behave similarly. Depending on the interaction or their bonding character, the charge ordering can be $1d$- (spin- chain or spin-ladder, see e.g. [25, 26]) $2d$- or $3d$-like.

The benefit of the scaling laws is two-fold. First, experimental results for simple, well-understood systems (in terms of d and range of interaction) can be used to test the scaling hypothesis. In a similar way, scaling arguments can be used as a critical test for numerical and perturbative methods, such as Monte-Carlo methods and field theoretical approaches. Second, the scaling laws are motivation for a more fundamental theory that can derive the basic assumptions (Eq. 3.7 and Eq. 3.11) from more general assumptions. This is achieved by renormalization group theory [22, 27].

3.2.4 The correlation function G(r) beyond mean field theory

Comparing Kadanoff's hypothesis (Eq. 3.11, using $d = 3$) to the OZ result (Eq. 3.5), it follows that $\eta = 0$ (OZ). This is, however, wrong. Fisher and Burford calculated 1966 [18] that $\eta = 0.056$ is the correct result for $d = 3$. Furthermore, $\nu = 1/2$ (OZ) should be replaced by $\nu = 0.643$ [18] and for $T = T_c$, the correct form of the correlation function $G(r)$ is given by

$$G_c(r) \propto \frac{1}{r^{d-2+\eta}}, (T = T_c, r \to \infty). \tag{3.14}$$

If one wants to stay with Eq. 3.5, a crossover function $Q(r/\,\xi)$ has to be introduced. Then, $G(r)$ is given by [15]

$$G(r) \quad \propto \quad [1 + Q(r/\,\xi)] \cdot \frac{\exp(-r/\,\xi)}{r^{d-2+\eta}} \tag{3.15}$$

with

$$Q(r/\,\xi) \to 0 \qquad r/\,\xi \to 0 \tag{3.16}$$

$$1 + Q(r/\,\xi)\ (r/\,\xi)^{1/2\cdot(3-d)+\eta} \qquad r/\,\xi \to \infty \tag{3.17}$$

With neutrons and x-rays, it is possible to measure the Fourier-transform (FT) of $G(r)$ [15]. Therefore it is possible to obtain the critical exponents ν and η experimentally from critical diffuse scattering. Experiments of this kind have been done by Als-Nielsen *et al.* on the system CuZn [14] and by Guttman *et al.* on Fe_3Al [28, 29]. Impressive agreement between theory and experiment was found, as can be seen from Table 3.2.

3.2.5 Summary of critical exponents for bulk systems

Table 3.1 summarizes the critical exponents and the way they enter the power-laws and the correlation function, including the conditions that have to be met. Table 3.2 summarizes selected theoretical and experimental results for the exponents β, ν and η for two binary alloy systems. More extensive tables can be found in [14, 30].

3.2.6 Critical amplitudes and critical region

So far, only the critical exponents have been considered. Theory and experiments, however, are often also able to determine amplitudes. For example at the critical point, the amplitude D of the correlation function $G(r) = D \cdot \frac{1}{r^{1+\eta}}$ has been calculated for a $3d$-Ising model to be [18] $D = 0.320(10)$. But it

	power law	condition
order parameter Ψ	$t^{\ \beta}$	$T < T_c \rightarrow T_c, H = 0$
field induced OP $\Psi(H, t = 0)$	$H^{\ 1/\delta}$	$T = T_c, H \rightarrow 0$
susceptibility χ_T	$\lvert t\rvert^{-\gamma}$	$T \rightarrow T_c, H = 0$
specific heat C	$\lvert t\rvert^{-\alpha}$	$T \rightarrow T_c, H = 0$
correlation length ξ	$\lvert t\rvert^{-\nu}$	$T \rightarrow T_c, H = 0$
correlation function $G_c(r)$	$\frac{1}{r^{d-2+\eta}}$	$T = T_c, H = 0, r \rightarrow \infty$
OZ correlation function $G(r)$	$\frac{\exp(-r/\ \xi)}{r^{\frac{1}{2}(d-1)}}$	$T \neq T_c, H = 0, r \rightarrow \infty$

Table 3.1: The critical behavior of bulk systems.

makes a difference whether the underlying lattice is simple cubic (sc), body-centered cubic (bcc) or face centered cubic (fcc), resulting in $D = 0.320$, 0.263 and 0.248, respectively.

Further, if a_0 denotes the lattice constant, $\xi(t)$ is given by [15] p.637

$$\begin{aligned} \xi(t) &= \xi_0 \cdot t^{-\nu} \\ \xi_0 &= \frac{a_0}{F_+}\ ,\ T > T_c \\ \xi_0 &= \frac{a_0}{F_-}\ ,\ T < T_c \end{aligned} \tag{3.18}$$

with $F_+ = 2.0888$ (sc), 2.2435 (bcc), 2.3024 (fcc) and

$$F_- = 2 \cdot F_+. \tag{3.19}$$

The values of F_+ and F_- are important information, since this allows estimating the reduced temperature t^* below which critical behavior is expected. $\xi > a_0$ should be fulfilled, with a_0 as the lattice constant of the system under investigation, e.g. $\xi = N \cdot a_0$ and N of the order of 10. Then t^* is given by

$$t^* \lesssim \Big(\frac{1}{F_+ \cdot N}\Big)^{1/\nu}. \tag{3.20}$$

system	method	β	ν	η	γ
FeCo	neutron scattering [5]	0.303(4)			
CuZn	neutron scattering [14]	0.305(5)	0.65(2)	0.045(15)	1.240(15)
Fe_3Al	x-ray scattering [28, 29]	0.307(3)	0.649(5)	0.080(5)	1.246(10)
Ising	mean field	0.5	0.5	0	1
$3d$-Ising	series approximation [18]	0.314(4)	0.643(3)	0.056(8)	1.250
$2d$-Ising	exact	0.125	1	0.25	1.75

Table 3.2: Selected experimental values for the critical exponents of binary alloy systems, determined by scattering methods. Theoretical results are given for comparison.

$N = 10$ gives $t^* \simeq 8 \cdot 10^{-3}$. Indeed, the experimental results confirm that $t < 10^{-2}$ should be fulfilled in order to observe critical behavior, as reviewed in [31, 32]. This temperature region ($t < t^*$) is called the *critical region*. Outside of the critical region ($t > t^*$) a crossover to mean field behavior occurs.

In a thin film, Eq. 3.20 is also useful since it allows one to estimate the reduced temperature where finite size effects set in. From the most crude assumption, that finite size effects set in for $\xi / a_0 \approx N$, with N the number of unit cells that build up the film, one obtains $t^* \simeq 2 \cdot 10^{-4}$ for $N = 100$. Therefore, to measure finite size effects in thin films ($10 < N < 100$), measurements should be carried out close to T_c, in a reduced temperature region of $t = [10^{-5} \ldots 10^{-2}]$. This is discussed in more detail in Sec. 3.5.

Finally, the amplitude Ψ_0 of the vanishing order parameter $\Psi(t) = \Psi_0 \cdot t^\beta$ is considered. Ψ_0 has been calculated [15] p.671 to $\Psi_0 = 1.57$ (sc), 1.49 (bcc) and 1.488 (fcc) for a $3d$-Ising system.

3.3 Critical behavior near a surface

3.3.1 Introduction

In this section, a critical bulk system in presence of a surface is considered. Two aspects emerge immediately:

1. The presence of the surface represents a massive break of the translational symmetry. Fluctuations are abruptly terminated near the interfaces, see Fig. 3.3.

2. At the surface, the order parameter may be enhanced or lowered, either due to short ranged surface fields h_1 or due to modified interactions between the species at the surface.

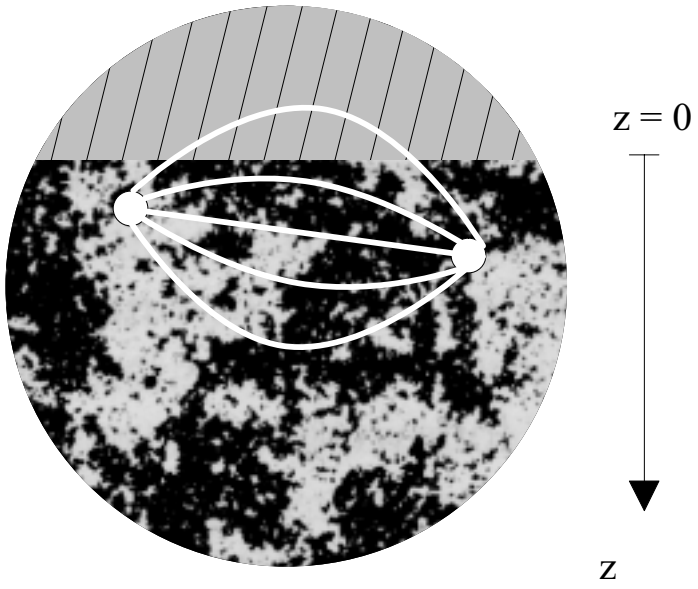

Figure 3.3: Figure of the massive symmetry break caused by the presence of a surface.

Both of these aspects lead to a number of questions. What does the correlation function look like in the surface near region? Will ξ still diverge with a power law, and will ν change? Will the order parameter become depth-dependent?

Surface and excess order

Assuming that an order parameter profile $\Psi(z)$ (see Fig. 3.5) is located at the surface, the question emerges as to whether the order parameter at the surface $\Psi(z=0,t)$ follows a power law

$$\Psi(z=0,t) \propto t^{\beta_1} \tag{3.21}$$

and what determines the value of the surface critical exponent β_1. Furthermore, if the system is semi-infinite, bulk behavior should be recovered ($\Psi(z \to \infty) = \Psi_\infty$) at a distance from the surface larger than the correlation length ($z/\,\xi \gg 1$). Hence, Ψ_∞ should be given by bulk critical exponents and amplitudes ($\Psi_\infty = \Psi_0 \cdot t^\beta$). The experimental and theoretical aim is to determine the order parameter profile $\Psi(z)$ that connects the surface order parameter ($\Psi(z=0)$) with the bulk order parameter (Ψ_∞).

Another valuable quantity is the excess order parameter

$$\Gamma(t) = \int_0^\infty [\Psi(z,t) - \Psi_\infty(t)]\; dz. \tag{3.22}$$

since it takes also into account how far the difference $\Delta\Psi(z) = \Psi(z) - \Psi_\infty$ penetrates into the semi-infinite system and some non-diffraction experimental methods that suffer from limited depth resolution have been used to measure $\Gamma(t)$.

3.3.2 Order parameter profiles from mean field theory

A theoretical treatment of critical phenomena at surfaces requires the solution of the semi-infinite Ising model [33] p.84 with the Hamiltonian

$$\begin{aligned} \mathcal{H} \;=\; -K \sum_{\langle i,j\rangle \,\notin\, \text{surf}} s_i\, s_j \;-\; K_1 \sum_{\langle i,j\rangle \,\in\, \text{surf}} s_i\, s_j \\ -\; h \sum_{\text{all } i} s_i \qquad -\; h_1 \sum_{i \,\in\, \text{surf}} s_i \end{aligned} \tag{3.23}$$

with $h_1 = H_1/\, k_b T$ as the effective surface field, $h = H/\, k_B T$ as the homogenous external field, $K_1 = J_1/\, k_B T$ as the surface coupling constant and $K = J/\, k_B T$ as the bulk coupling constant. The solution turns out to be far from simple. Lubinsky solved the problem in 1975 by means of mean field theory, using a phenomenological form of the free energy. In this approach, the modified surface interaction is represented by a parameter $-c$, the so called negative surface enhancement. In Fig. 3.4, a generic phase diagram is depicted for $h_1 = 0$. The y-axis is temperature T, whereas the x-axis is the negative surface enhancement $-c$. Below T_c, the surface and the bulk show spontaneous order. Above T_c, three scenarios are possible, depending on the surface coupling $(-c)$.

1. If the surface coupling strength is lowered at the surface ($J_1 < J_s$ i.e. $-c < 0$), bulk and surface disorder at the same critical temperature T_c. Below T_c the surface shows less order than the bulk ($\Psi(z = 0) < \Psi_\infty$) as depicted in Fig. 3.5(i). The phase transition between the ordered and the disordered phase is called *ordinary* ("O" in Fig. 3.4).

2. If the surface coupling strength J_1 takes a special value ($J_1 = J_s = 1.52 \cdot J$ i.e. $-c = 0$), the surface order is exactly the same as in the bulk for all temperatures, see Fig. 3.5(ii). The phase transition is then called *special* ("SB" in Fig. 3.4).

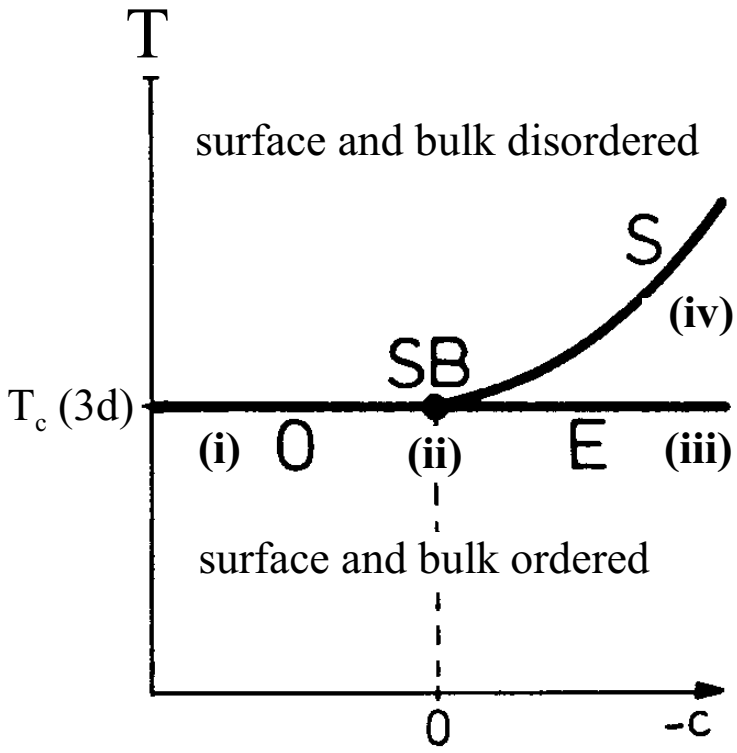

Figure 3.4: Generic surface phase diagram for critical phenomena close to a surface, from [34, 33]. "O", "SB", "E", "S" denotes ordinary, special, extraordinary and surface phase transition. See text for explanation.

3. If the surface coupling strength favors order ($J_1 > J_s$ i.e. $-c > 0$), the order at the surface is enhanced below bulk T_c, see Fig. 3.5(iii). If the temperature is risen above T_c bulk, the surface remains ordered, see Fig. 3.5(iv). This phase transition is called *extraordinary*, denoted "E" in Fig. 3.4. Only a region of magnitude of the bulk correlation length ξ remains ordered above T_c bulk and the details of this profile are discussed in Sec. 3.4 in the context of critical adsorption.

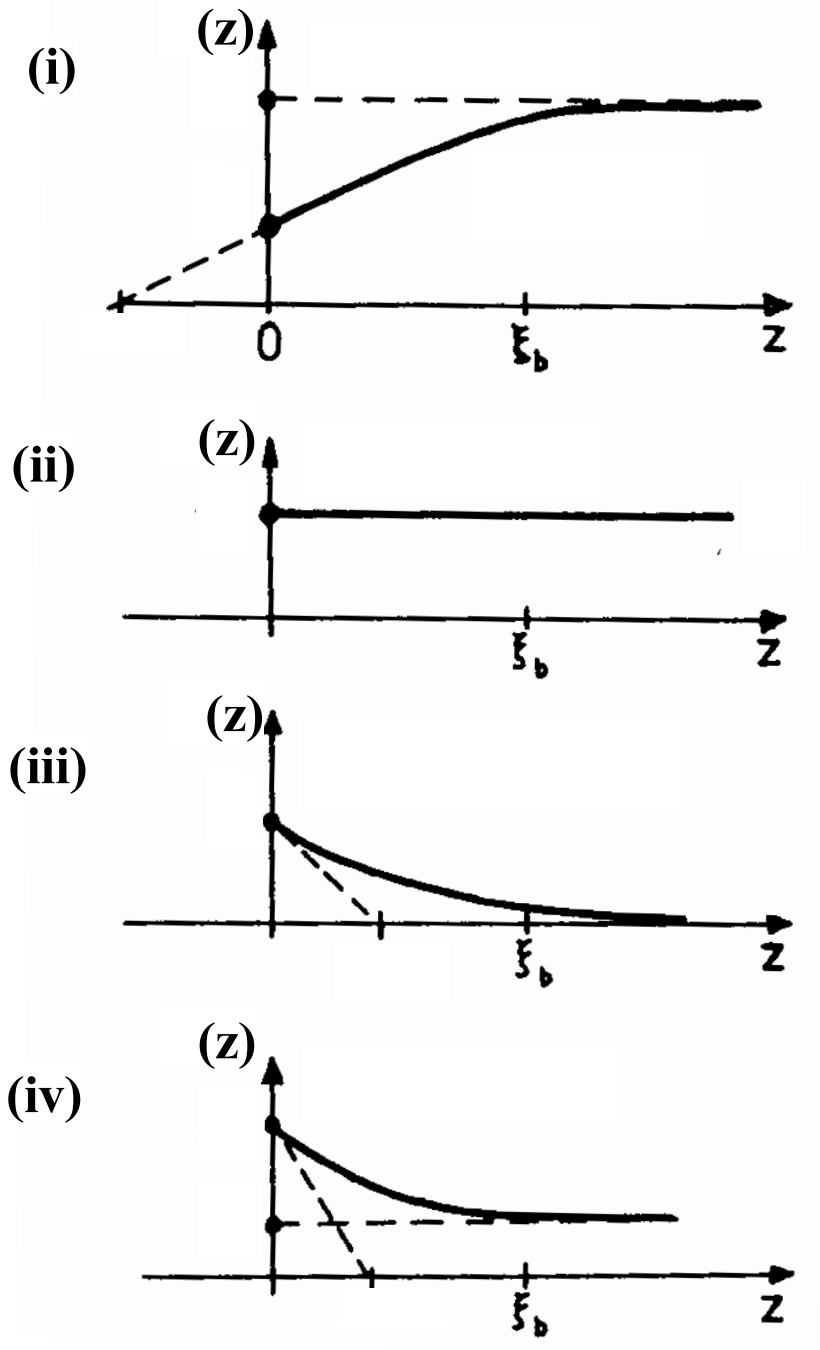

Figure 3.5: Surface order parameter profiles from mean field [35] theory. (i) , (ii), (iii), (iv) as indicated in Fig. 3.4.

At a higher temperature, the surface disorders. This kind of phase transition is called *surface* phase transition, denoted "S" in Fig. 3.4.

Fig. 3.5 confirms that the influence of the surface is restricted to a region proportional to ξ. However, the question arises what will happen at $T = T_c$, when $\xi = \infty$?

3.3.3 The correlation function at T_c: theory and experiments

In a bulk system, symmetry allows one to express the two point correlation function as a function of a single variable r, with $r = |\overrightarrow{x_2} - \overrightarrow{x_1}|$ and without restriction of generality, $\overrightarrow{x_1} = 0$. Close to a surface, only translational symmetry along the surface is possible, therefore the correlation function G becomes a function of

$$G(\overrightarrow{x_1}, \overrightarrow{x_2}) \;=\; G(z_1, z_2, r_{||}) \tag{3.24}$$

with $\overrightarrow{x_1} = (x_1, y_1, z_1)$, $\overrightarrow{x_2} = (x_2, y_2, z_2)$ and $r_{||} = \sqrt{(x_2 - x_1)^2 + (y_2 - y_1)^2}$.

Detailed experiments and calculations have been performed to obtain the functional form of the correlation function close to a surface. At $T = T_c$, one obtains (compare to Eqs. 3.24 and 3.14) [36, 37]

$$\begin{aligned} G(z_1, z_2, r_{||}) &\propto r_{||}^{-(1+\eta_{|})}, \quad (z_1 \text{and } z_2 \text{ fixed, } r_{||} \to \infty) \\ G(z_1, z_2, r_{||}) &\propto z^{-(1+\eta_{\perp})}, \quad (z_1 \text{ fixed, } z = z_2 - z_1 \to \infty) \end{aligned} \tag{3.25}$$

with $\eta_{|}$ and $\eta_{\perp}$ as given in Table 3.3. At T_c, the correlation function at a surface becomes obviously a highly asymmetric object. A critical test of Eq. 3.25 has been done by means of x-ray diffraction on Fe_3Al single crystals with well-prepared surfaces. The predicted signature of a modified critical behavior in a mesoscopic surface near region (Eq. 3.25) was found

[38]. The most peculiar results are the confirmation of the surface critical exponent $\beta_1 = 0.77(2)$ and the cusp-like critical diffuse scattering around a superstructure Bragg reflection, see Fig. 3.6, confirming $\eta_{||} = 1.52$. Due to the observed critical exponents, the surface phase transition in the surface near region of Fe_3Al could be classified as *ordinary*.

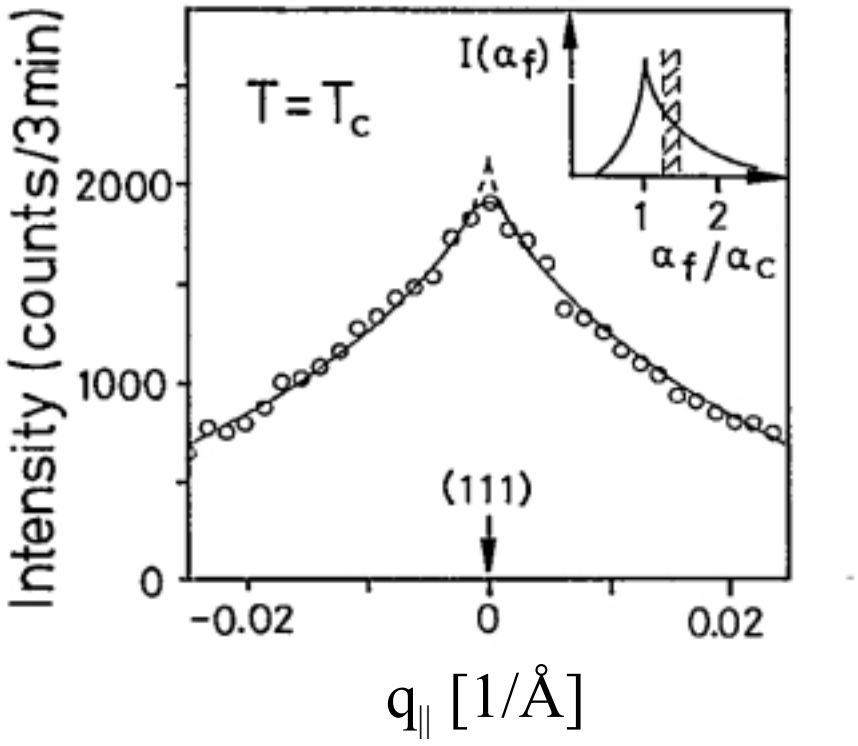

Figure 3.6: Cusp-like critical diffuse scattering from a surface near region, from [38].

Exponent	special (SB)	ordinary (O)	Fe_3Al	FeCo
$\eta_{\parallel}$	-0.165	1.528	1.52(4)	
$\eta_{\perp}$	-0.067	0.801		
β_1	0.263	0.8	0.77(6)	0.79(10)
γ_{11}	0.734	-0.333	-0.34(6)	
γ_1	1.302	0.742		
Δ_1	0.997	0.450		

Table 3.3: Critical surface exponents. Values for "O" and "SB" from massive field theory [39], experimental values for Fe_3Al from [38, 40], for FeCo from [41, 42].

3.3.4 Order above T_c

By controlled variation of the penetration depth Λ of the x-rays between $\Lambda = 30$ Å and 125 Å, the Fe_3Al experiment gave also clear cut evidence that in a microscopic range of the order of 30 Å close to the surface order remained above T_c. This result was discussed controversial [43]. First, no order above T_c is expected for the ordinary phase transition from Fig. 3.4 and 3.5(i). This could change in the presence of a surface field h_1. But h_1-field has so far been only observed in e.g. binary liquids, where one component may be attracted by a chemically tailored wall. Binary alloys were thought to be paradigm examples for systems without (disturbing) h_1 fields. Schmid [44] could show theoretically that an effective h_1-fields can arise for binary alloys when the stoichiometry of the alloy is not ideally and this was just the case for the given example (c(Al) = 29%). From the large number of accumulated surface studies one knows that a truncated solid that looks like a subset of a bulk system is highly unusual, virtually every surface tends to minimize its energy by a rearrangement of atomic positions and segregation-induced order is not unusual [45]. The more serious problem from the theoretical point of

view with the observed order above T_c was that in the limit $h_1 \to \infty$, the phase transitions should become extraordinary. But this was obviously not the case for the present experiments which gave clear cut evidence for an *ordinary* transition. The h_1-field seemed to be so weak that it did not change the universality class of the surface from ordinary to extraordinary, but acted more as a small disturbance. This intuitive picture was confirmed recently [46] and will be discussed in the following sections in a broader context (Sec. 3.4.3).

3.4 Critical adsorption profiles

In a short but seminal paper, Fisher and de Gennes [47] discussed in 1978 scaling aspects of critical adsorption, i.e the evolution of order parameter profiles $\Psi(z)$ in critical systems with surfaces that are exposed to surface fields h_1. The adsorption profile $\Psi(z)$ should scale like

$$\Psi(z) = \Psi_0 \cdot t^{\beta} \cdot Y\left(\frac{z}{\xi},\ \frac{D}{\xi},\ h_1 \cdot t^{-\Delta_1}\right) \tag{3.26}$$

with Δ_1 the critical exponent from $\Psi(z = 0, t = 0, h = 0, h_1) \propto h^{-1/\Delta_1}$ and D the thickness of the system. The scaling function Y is the object to be calculated that makes the crossover from bulk to surface and film behavior. Unfortunately, Y is known only for several limits, which shall be discussed now.

3.4.1 Thick film, strong field ($D/\,\xi \to \infty,\ h_1 \to \infty$)

A thick film with strong, short-ranged surface field ($D/\,\xi \to \infty,\ h_1 \to \infty$) behaves close to the surface like a semi-infinite system. From field theoretical calculations [48, 49, 50] Y is then given by

$T > T_c$

$$\begin{aligned} Y(z) &= c_+ \cdot \left(\frac{z}{\xi}\right)^{-\beta/\nu}, \quad z \ll \xi \\ Y(z) &= P_\infty^+ \cdot \exp(-z/\,\xi), \quad z \gg \xi \end{aligned} \tag{3.27}$$

$T = T_c$

$$\Psi(z, t=0) = \Psi_0 \cdot c_\pm \cdot \left(\frac{z}{\xi_{0\pm}}\right)^{-\beta/\nu} \tag{3.28}$$

$T < T_c$

$$\begin{aligned} Y(z) = & \quad c_- \cdot \left(\frac{z}{\xi}\right)^{-\beta/\nu}, \quad z \ll \xi \\ Y(z) = & \; 1 + P_\infty^-(z/\,\xi) \cdot \exp(-z/\,\xi), \quad z \gg \xi \end{aligned} \tag{3.29}$$

Ψ_0 and $\xi_{0\pm}$ denote the bulk amplitudes (Sec. 3.2.6) and $c_\pm$ are universal constants with

$$\frac{c_+}{c_-} = \left(\frac{\xi_0^-}{\xi_0^+}\right)^{\beta/\nu} \tag{3.30}$$

and $c_+(d=3) = 0.94(5)$ [51], $c_-(d=3) = 1.24(5)$ [51], $P_\infty^+ \approx 1.245$. $P_\infty^-(z/\,\xi)$ is a weakly varying function ($P_\infty^-(0) = 0.208$, $P_\infty^-(3) = 0.237$ using Eq. 45b in [49, 50]). Fig. 3.7 shows by the way of example the two asymptotic parts of $\Psi(z)$ (Eq. 3.26) for $T > T_c$ (Eq. 3.27), with $t = 10^{-3}$, resulting in $\xi \approx 37 \cdot a_0$ and $\Psi_0 \cdot t^\beta \approx 0.14$. The dashed curve shows the algebraic decay, the dashed-dotted curve is the exponential part. Diehl and Smock (DS) [49, 50] have also been able to give an expression for the full function Y (not shown). They emphasize that $\Psi(z)$ is always a monotonic function, indicated here by the solid line that connects the two asymptotic regions. This holds no longer for weak h_1-fields (Fig. 3.40). The solid line is an empirical scaling function (see below Eq. 3.31).

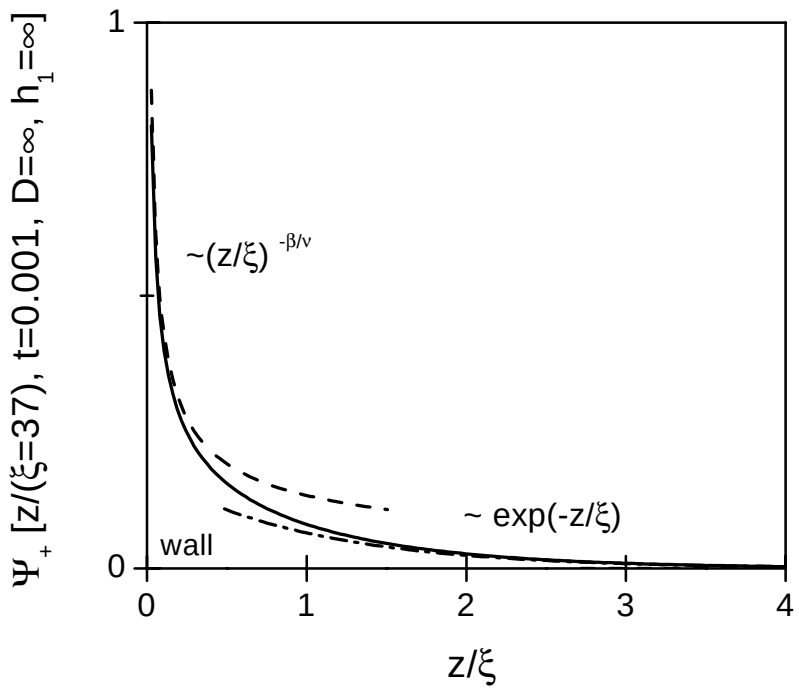

Figure 3.7: Schematic of the two different regimes of $\Psi(z)$, as described in the text.

3.4.2 Related experimental results

Neutron reflectivity experiments on binary liquids

Fig. 3.8 shows experimental data from a neutron reflectivity experiment [52] on a critical binary mixture (2-butoxyethanol+ D_2O) in contact with a silicon surface. The experiment has been done at the BERII reactor (Hahn-Meitner Institut, Berlin, Germany) at the V6 reflectometer. A special rescaling of the axes [53] allows one to test the experimental data directly for β/ν (Eq. 3.28). The straight line indicates $\beta/\nu = 0.53(2)$, in good agreement with the theoretical value $\beta/\nu = 0.516(4)$. Further, the authors find $c_+ = 0.11$, in strong disagreement with the theoretical value. However, to extract c_+ unambiguously, the values of Ψ_0 and ξ_0 need to be known, but the authors had to rely

on values published in the literature.

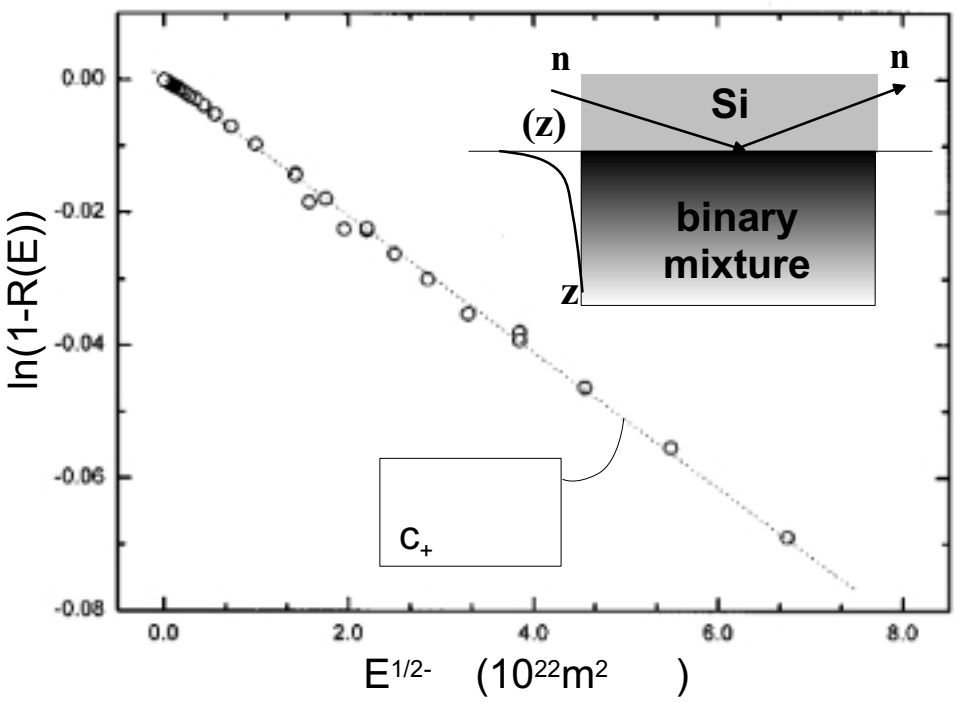

Figure 3.8: Neutron reflectivity study of critical adsorption at $T = T_c$ [52]. With rescaled axes (Dietrich-Schack plot [53]). The straight line suggests $\beta/\nu = 0.52$ and $c_+ = 0.11$, using literature values for ξ_o and Ψ_0. See text.

A similar neutron reflectivity experiment has been done by Zhao et al [54] on a critical methanol + deuterated cyclohexane mixture, using the DESIRE reflectometer at the Orphee reactor in Sarclay, France. They determined $\xi_o = 3.6$ Å and $\Psi_o = 0.71$ independently from a bulk experiment on the same liquid. For their analysis they used a scaling-function proposed initially by Liu and Fisher (LF)[55] (solid line in Fig. 3.7)

$$Y_{LF}(z) = c_+ \cdot \left(\frac{1 + [(P_\infty^+/\, c_+)^{-\beta/\nu}] \cdot z/\, \xi}{z/\, \xi} \right)^{\beta/\nu} \cdot \exp(-z/\, \xi) \quad (3.31)$$

with the limiting forms (see Eq. 3.27)

$$Y_{LF}(z) = \quad c_+ \cdot \left(\frac{z}{\xi}\right)^{-\beta/\nu} \qquad \text{for } z/\,\xi \ll 1, \tag{3.32}$$

$$Y_{LF}(z) = \; P_\infty^+ \cdot \exp\,(-z/\,\xi) \;\text{ for } z/\,\xi \gg 1. \tag{3.33}$$

They obtain $\beta/\,\nu = 0.52$ in good agreement with the theoretical value $\beta/\,\nu = 0.52$. Further, they obtain $c_+ = 0.34$, in contrast to the theoretical value $c_+ = 0.94$ and $P_\infty^+ = 0.104$, whereas DS calculated $P_\infty^+ = 1.245$. The authors emphasize that the data are in agreement with $c_+ = 1.0$ if one restricts the fitting procedure to the data with small q-values and suggest that improved counting statistics and experimental resolution might clarify the origin of the disagreement. However, the small value for c_+ might be also taken as an evidence that the experiment was not in the high-field limit ($h_1 \to \infty$).

X-ray reflectivity and diffraction on liquid crystals

Another important diffraction experiment has been done by Pershan and Als-Nielson (PA) by means of x-ray reflectivity [56, 57, 58] from the free surface of a liquid crystal that undergoes a *nematic* to *smectic-A* critical phase transition. The experiments were carried out at HASYLAB, Hamburg, Germany. The experiments focuses on the exponential contribution ($\exp(-z/\,\xi)$) and the identification of the decay length with the bulk correlation length ξ. The reflectivity scattering geometry is sketched in Fig. 3.9a. In Fig. 3.9b, a reflectivity scan slightly above T_c, in the nematic phase, is shown. One observes a plateau of total reflection at low angles and a bunched intensity at higher angles of incidence. The smectic-A phase is characterized by a layering of the molecules perpendicular to the surface and the bunched intensity is a precursor of the smectic-A phase, or, so to speak, a critical adsorption profile. PA could explain the observed reflectivity with a model (solid lines in Fig. 3.9b+c), taking into account a critical adsorption profile ($\propto \exp(-z/\,\xi)$) and a smearing of the free surface due to (capillary) roughness. Even more

interesting, they could measure the bulk in-plane correlation length ξ independently from diffuse off-specular scattering (not shown here) and found agreement with the decay length. All the other experiments take this as granted.

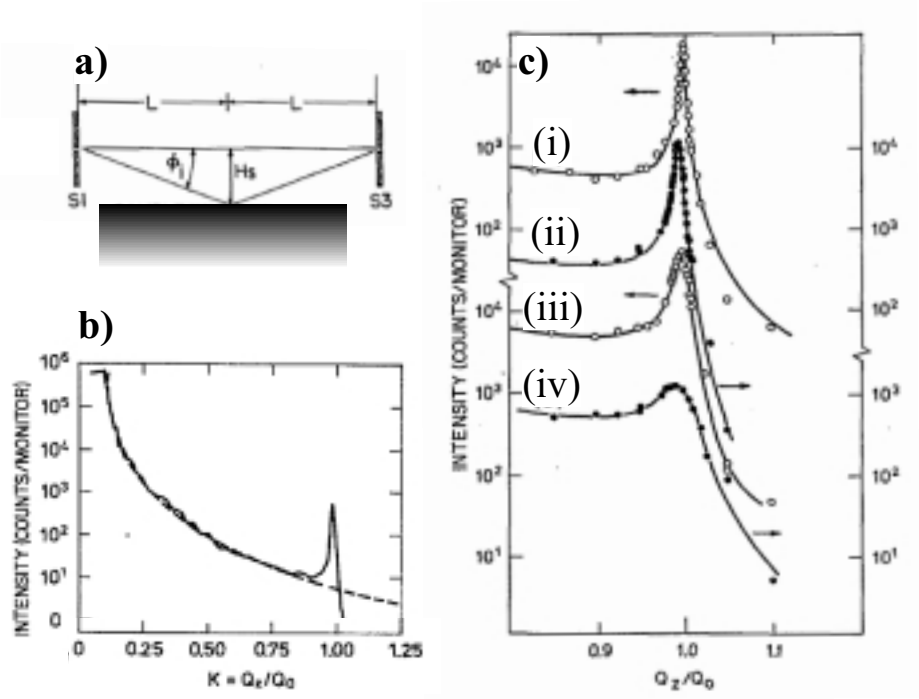

Figure 3.9: x-ray reflectivity study of critical adsorption at a free liquid surface. a) Scattering geometry. b) The reflectivity, including total reflection and a peaked intensity due to a layered adsorption profile. $T = T_c + \Delta T$, $\Delta T = 0.05^o$C. c) Temperature dependence of the peak, (i) $\Delta T = 0.1^o$C (ii) $\Delta T = 0.21^o$C, (iii) $\Delta T = 0.40^o$C, (iv) $\Delta T = 1.80^o$C. From [56].

Light scattering

Whereas the number of diffraction experiments focusing on critical adsorption is still limited, many experiments have been done using light scattering. These experiments are limited by several factors, but the main problem is

the poor ability to resolve features below the probe wavelength. Often, these experiments are performed in an integrating mode, i.e. they probe the excess order parameter $\Gamma(t)$ (Eq. 3.22) or higher moments $\Gamma_n(t)$ of $\Psi(z)$, i.e.

$$\Gamma_n(t) = \int_0^\infty z^n \cdot [\Psi(z,t) - \Psi_\infty(t)]\, dz. \tag{3.34}$$

Fisher and de Gennes initially proposed measuring $\Gamma_0(t)$ [47], since they could show from their general scaling arguments that

$$\Gamma_0(t) \propto t^{\beta-\nu} \tag{3.35}$$

and this power law behavior was actually the reason why the phenomenon is called critical adsorption. Of course, a detailed knowledge of $\Psi(z,t)$ allows one also to calculate the excess (see. e.g. [51]). Experiments with critical binary mixtures in contact with a glass substrate have been done by Schlossmann *et al.* [59] using p-polarized light. These experiments probe the first moment $\Gamma_1(t)$ and from scaling one expects

$$\Gamma_1(t) \propto t^{2\cdot\nu-\beta}. \tag{3.36}$$

Fig. 3.10 shows the experimental results in a logarithmic presentation. The solid line confirms the expected power-law behavior with $2\cdot\nu\ -\beta = 0.88(10)$, the theoretical value is $2\cdot\nu\ -\beta = 0.93$.

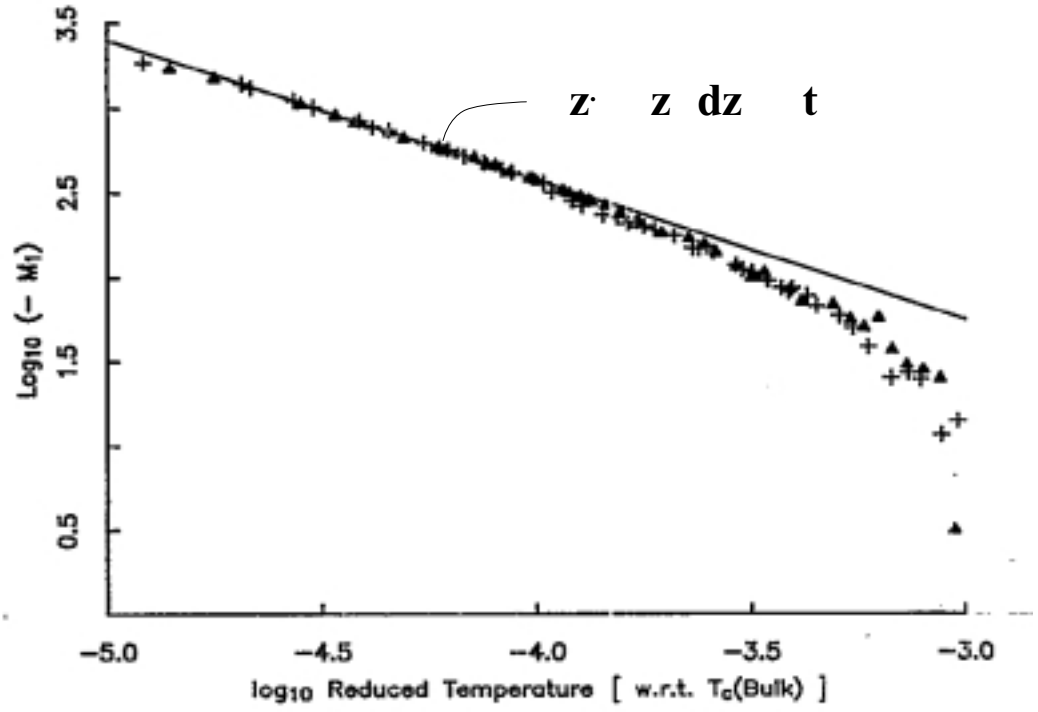

Figure 3.10: $\Gamma_1(t)$ versus the reduced temperature t. Logarithmic representation, the solid line indicates a power-law behavior. See text for details.

Light scattering experiments measuring $\Gamma_0(t)$ have been performed by Bahr *et al.* [60] on a system undergoing a critical *smectic*-A (untilted) to *smectic*-C (tilted) phase transition. They find $\Gamma_0(t) \propto t^{-(\nu-\beta)}$ with $\nu - \beta = 0.5$. Theory predicts $\nu - \beta = 0.32$ for the 3D-XY-universality class, therefore the authors argue that $\nu = 0.67$, the "isotropic" value has to be replaced by $\nu_{\parallel} \approx 0.8$.

Further experiments using light scattering techniques have been done for binary liquid mixtures in contact with their vapor phase [61, 62]. Whereas the critical exponents are usually well-reproduced, the amplitudes are usually not accessible without a large number of assumptions about the details of

the profile [63]. But often the ratio of amplitudes above and below T_c is accessible, e.g. $c_+/\, c_-$ (see Eq. 3.27, Eq. 3.29), as reviewed in [51]. At this point it is worthwhile to note that the surface tension of a liquid is closely related to the critical adsorption profile by the van der Waals relation [64]

$$\sigma \propto \int \left(\frac{d\Psi(z)}{dz}\right)^2 dz \tag{3.37}$$

and therefore some important theoretical and experimental contributions focus on this aspect [65, 66].

Summary

Light, x-ray and neutron scattering experiments have been performed successfully to observe critical adsorption phenomena in semi-infinite ($D/\,\xi \to \infty$) systems. The main predictions from scaling theory have been verified, i.e. the power law behavior of the excess order parameter $\Gamma_1(t)$ and the power law behavior of $\Psi(z, t = 0)$. However, a considerable number of experiments disagree with the theoretical estimates when the amplitudes (P_∞^+, c_+) are compared. One reason for this disagreement may be that these experiments are not described properly by the strong surface field limit ($h_1 \to \infty$). The theoretical estimates for a weak surface field (h_1 <1) which may describe these experiments better is discussed in the next section.

3.4.3 The weak h_1-field, thick film ($D/\,\xi \to \infty,\ h_1 \to 0$) limit

Whereas the surface behavior changes always to extraordinary for a sufficient strong surface field ($h_1 \to \infty$), this is no longer true for a weak h_1-field. Now the influence of the coupling constant at the surface has to be taken into account, that is whether the surface-field free system ($h_1 = 0$) favors order at the surface or not ($-c \lesseqgtr 0$, $J_1 \lesseqgtr 1.52$, see Fig. 3.4 and 3.5). The

experimental observation for FeCo [41, 42] and Fe_3Al [38, 40] is that the surface itself shows *ordinary* behavior while only in a microscopic surface near region of the order of 30 Å order remains above T_c. Therefore this case ($-c \gg 0$ (ordinary), weak h_1-field) has been revisited recently by different authors [46, 67, 68, 69]. As realized earlier, the finite h_1-field gives rise to a second length scale [47, 70]

$$l_1 = A_{l_1} h_1^{-\nu/\Delta_1}, \tag{3.38}$$

with $(-\nu \,/\, \Delta_1) \cong -1.4$ that competes with the bulk correlation length ξ. In a similar way, a finite $-c$ gives rise to a length scale

$$l_c \propto c^{-\nu/\phi}, \tag{3.39}$$

with $\phi = 0.54$ [39] as the shift exponent that determines the critical temperature of the extraordinary transition ($T_c(\text{surface}) = T_c(\text{bulk}) + const. \cdot |c|^{1/\phi}$). In the following $-c \to \infty$ (ordinary) and therefore $l_c \to 0$ is assumed. Then $m(z, h_1)$ is given by [46, 67]

$$m(z/\, l_1, z/\, \xi, h_1) \propto \begin{cases} (z/\, \xi)^{1-\eta_\perp} & \text{for } z/\, l_1 \ll 1, \\ h_1 \cdot (z/\, \xi)^{-\beta/\nu} & \text{for } z/\, l_1 \gg 1, \\ h_1 \cdot \xi^{1-\eta_\perp} \cdot \exp\ (-z/\, \xi) & \text{for } z/\, \xi \ \gg 1, \end{cases} \tag{3.40}$$

with $(1 - \eta_\perp) \cong 0.21$. For $l_1 < \xi$, the region $z/\, \xi < 1$ (Fig. 3.7) will be divided into two regions, depicted in Fig. 3.11 and the profile will no longer be monotonous.

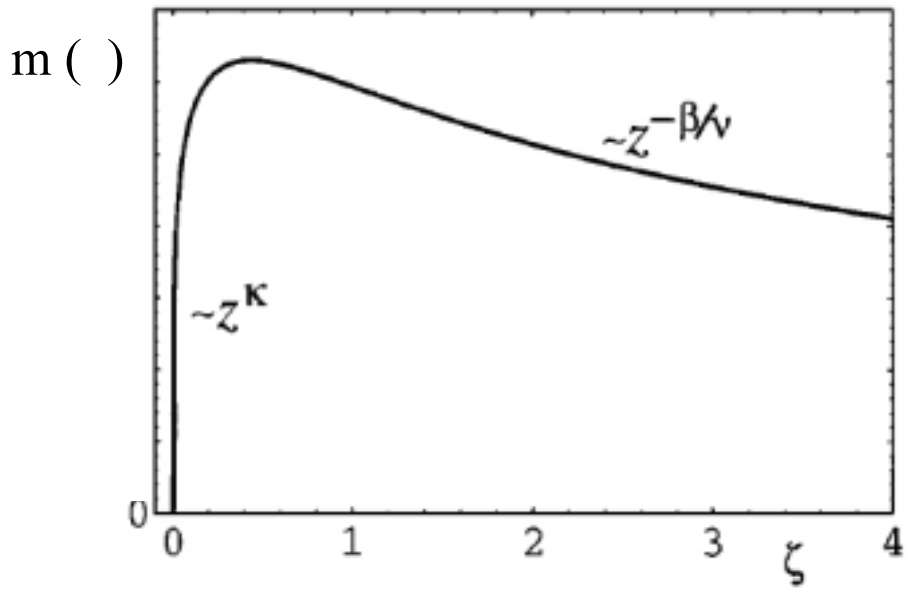

Figure 3.11: Surface order at the ordinary transition, induced by a weak h_1-field [46]. $\zeta = z/\, l_1$, $\kappa = 1 - \eta_\perp$. $T = T_c$ ($\xi \gg l_1$).

The amplitudes in Eq. 3.40 have not been calculated in detail, but from scaling arguments, one expects that they should scale proportionally to h_1 (Eq. 3.40). In this sense, l_1 represents the length scale over which the surface responds paramagnetically to the h_1-field. In the limit of ($h_1 \to \infty$), a crossover to the well-known amplitudes P_0 and P_∞^+ (Sec. 3.4.1) should occur (Eq. 3.27) and the amplitudes should vanish in the limit of ($h_1 \to 0$). One might expect that the apparently small deviation in Fig. 3.11 from the pure $(z/\, \xi)^{-\beta/\nu}$ behavior for ($z \to 0$) might eventually be beyond experimental resolution. However, the amplitudes will be considerable smaller than for ($h_1 \to \infty$) and this should be within experimental resolution if absolute values for $\Psi(z)$ can be obtained. Further, the $(z/\, \xi)^{-\beta/\nu}$ behavior will be

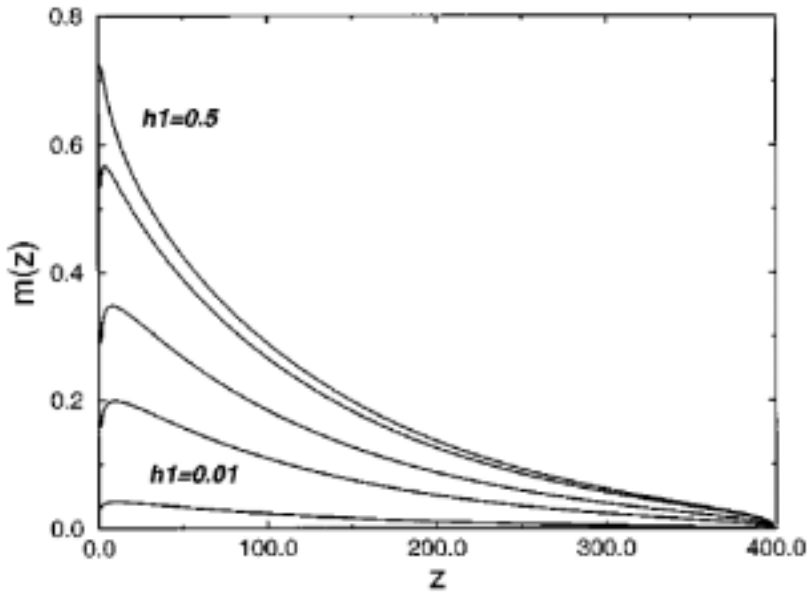

Figure 3.12: Surface order at the ordinary transition, induced by different h_1-fields at $t = 0.004$ ($\xi \approx 125$). $h_1 = 0.5$, 0.25, 0.1, 0.05, 0.01, from top to bottom [68]

missed totally for $l_1 > \xi$. Fig. 3.12 shows a calculation for an actually two dimensional Ising stripe exposed to an h_1-field ranging from 0.5 to 0.01 (in units of $J/\left(k_B T\right)$). For $h_1 = 0.5$ a "normal" adsorption profile is seen (see Fig. 3.7). For $h_1 = 0.25$ a dip occurs for $(z \to 0)$ (see Fig. 3.11). For $h_1 = 0.01$ the divergence of $\Psi(z)$ is strongly suppressed. It is now common practice to use the scaling variable

$$y = \frac{\xi}{l_1}. \tag{3.41}$$

Then three cases are possible [68]:

$$\begin{aligned} \text{case(i)}: \quad & y \to \infty, \\ \text{case(ii)}: \quad & y = \mathcal{O}(1), \\ \text{case(iii)}: \quad & y \to 0. \end{aligned}$$

Case(i) (see Fig. 3.7) is the classical case ($h_1 \to \infty$) nowadays called critical adsorption in the saturated regime, i.e. at the extraordinary fixed point. Case(ii) (see Fig. 3.11) and case (iii) are called critical adsorption in the undersaturated regime, with weak (ii) and very weak (iii) surface fields. $\frac{\xi}{l_1}$ will always tend to zero for ($t \to 0$) and for this reason case(ii) and case(iii) have been mostly neglected in previous studies. However, depending on l_1 this limit may be far beyond the experimental temperature resolution, which is typically of the order of $t \gtrapprox 10^{-5}$ or $\Delta T \approx 1$ mK.

Related experiments (weak h_1 fields)

Since the idea of undersaturated adsorption is relatively new, in principle it has not yet been established as to whether all experiments discussed in Sec. 3.4.2 really belong to case (i), especially the ones which give smaller amplitudes than expected. An experiment by Franck *et al.* [71] provided motivation for the arguments above (Eq. 3.40). In this experiment, a critical binary liquid consisting of carbon disulfide (A) and nitromethane (B) was exposed to a fully-silylated wall that attracts A. Repeated temperature dependent laser light reflectivity measurements of $\Delta R(T)$ from the liquid-solid interface were recorded over several days. From prior experiments it is known that on the time scale of several days, the wall changes gradually from A-attractive to B-attractive, since the silylation is unstable and the clean hydroxylated wall attracts B. Fig. 3.13 shows the temperature dependent reflectivity for successive days. Within several days the signal changes from positive to negative, indicating an exchange of the species attracted by the wall. A careful analysis of the data revealed further that Γ_0 scales, as expected for weak fields [68] like

$$\Gamma_0(t) \propto t^{\beta-\Delta_1} \tag{3.42}$$

in spite of $\Gamma_0(t) \propto t^{\beta-\nu}$ for ($h_1 \to \infty$) (see Eq. 3.35).

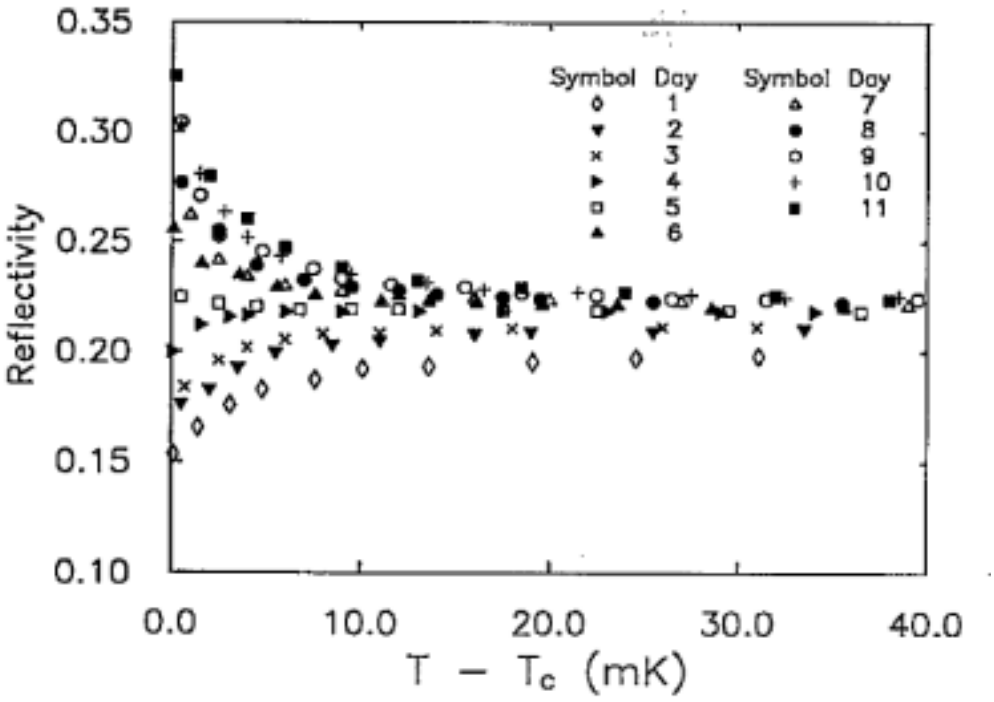

Figure 3.13: Light reflectivity (R) versus temperature ($T - T_c$) for different days (h_1-fields) [71]. See text for details.

3.5 Finite size scaling in thin films

3.5.1 Introduction

To describe the critical behavior of a thin film, one must know the free energy per site [69]

$$f(D, T, h_1) = f_b + f_A/\ D + f_B/\ D + f^*(D)/\ D \tag{3.43}$$

with f_b denoting the bulk free energy F (Eq. 3.7), f_A and f_B the contribution of the two walls and $f^*(D)/\ D$ the contribution from finite size scaling. f^* is closely related to the Casimir (solvation) force

$$f_{\text{solv}} = -(\partial\ f^*/\ \partial\ D)_{H,T} \tag{3.44}$$

i.e. the attraction of the walls at $T = T_c$ due to critical fluctuations. Unfortunately, these contributions are not known exactly for $d = 3$ up to now and the standard methods, mean field theory and ϵ -expansion are not able to treat the dimensional crossover properly [33] p.232. Therefore, one has to rely mostly on heuristic scaling arguments [72, 73] and Monte Carlo [74, 75] methods.

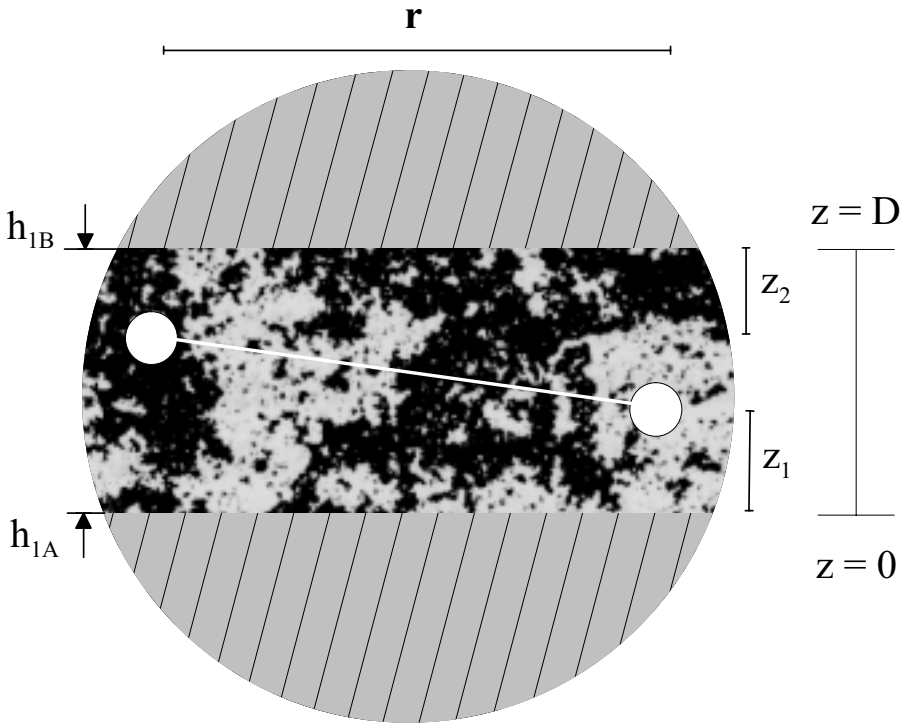

Figure 3.14: Schematic of critical fluctuations in a thin film.

3.5.2 T_c-shifts and dimensional crossover

A qualitatively new aspect arises in a thin film, namely, finite size scaling (f^* in Eq. 3.43). The system size $D = N \cdot a$ is now in competition with l_1 and ξ. This has various implications, the most serious of which is the impaired divergence of ξ normal to the film due to the finite thickness. Fisher argued,

based on qualitaitve arguments [6] that in the limit $\xi \to D$, the system dimension will crossover from 3 to 2:[2]

$$d = 3 \to \dot{d} = 2, \tag{3.45}$$

i.e.

$$\begin{aligned} \beta = 0.314 \ &\to \ \dot{\beta} = 0.125 \\ \nu \ = 0.63 \ &\to \ \dot{\nu} = 1. \end{aligned} \tag{3.46}$$

Simultaneously T_c will shift, depending on D but also on l_1. Since the system is still truly infinite parallel to the surface, these shifts are not generally accompanied by rounding effects which occur for finite systems like e.g. liquids in small pores [76]. The T_c shifts may be estimated from Landau theory [77] to be for small h_1

$$\begin{aligned} \Delta T_c \ &= \ T_c - \dot{T}_c(N) \\ &= \ T_c \cdot N^{-1/\nu} \cdot X_c(h_1 N^{\Delta_1/\nu}) \end{aligned} \tag{3.47}$$

with T_c denoting the bulk critical temperature and $\dot{T}_c(N)$ the critical temperature of the thin film with a thickness of N unit cells. Eq. 3.47 is a very intuitive result, since qualitative scaling arguments predict that ΔT_c will depend on ξ / D and l_1 / D. If t^* is introduced in a way that for $t = t^*$, $\xi / D \approx 1$

$$t^{*-\nu} = N \quad \text{or} \quad t^* = N^{-1/\nu}, \tag{3.48}$$

it becomes apparent that the factor $N^{-1/\nu}$ in Eq. 3.47 indicates, that the T_c-shift is driven by the finite thickness N of the film which impairs the

[2] In the following, the notation used in [6] in adapted, i.e. dotted quantities denote lower dimensional behavior. For example, $t = |T - T_c(\text{bulk})|/T_c(\text{bulk})$, but $\dot{t} = |T - T_c(\text{film})|/T_c(\text{film})$ and so on.

divergence of $\xi_\perp$. The second factor in Eq. 3.47, $X_c(h_1 N^{\Delta_1/\nu})$, is a scaling function close to unity for small h_1. With $h_1 N^{\Delta_1/\nu} = (N/\, l_1)^{\Delta_1/\nu}$ Eq. 3.47 can be recast as

$$\Delta T_c \;=\; T_c \cdot t^* \cdot \tilde{X}_c(N/\, l_1). \tag{3.49}$$

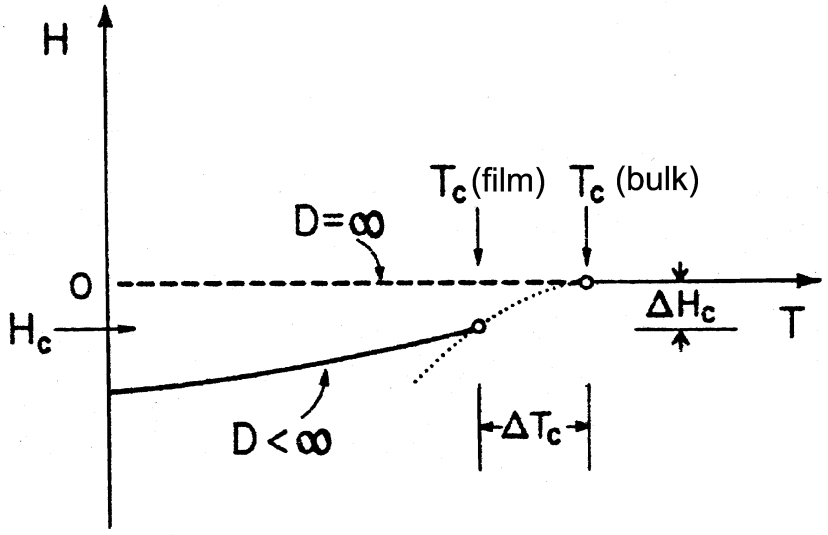

Figure 3.15: The finite thickness and the h_1-field give rise to T_c and H_c shifts.

In Fig. 3.15, the ΔT_c shift is shown schematically. The critical point $(T = T_c, H = 0)$ moves to a lower temperature (Eq. 3.49). If h_1-fields are present, the T_c-shift is accompanied by a H_c-shift, i.e. the critical point moves to a nonzero external field ($H_c \lessgtr 0$ for $h_{1A} = h_{1B} \gtrless 0$). $h_{1A} = h_{1B}$ denotes the symmetric boundary condition. An intuitive explanation of the H_c-shift is, that due to the finite thickness D of the film, one needs a "compensation field" H_c to obtain an effectively "field free" transition. This implicates, that an experiment that is carried out at $H = 0$ will miss the critical point if symmetric surface fields are active. This H_c shift does not arise for $h_{1A} =$

$-h_{1B}$, the asymmetric boundary condition [74]. In Fig. 3.16, the T_c shift is simulated for small ($h_1 \to 0$) and large ($h_1 \to \infty$) *symmetric* surface fields. For $N > 25$ no profound changes are seen, i.e. $T_c \approx \dot{T}_c$ Experimentally relevant effects are anticipated for $N < 25$.

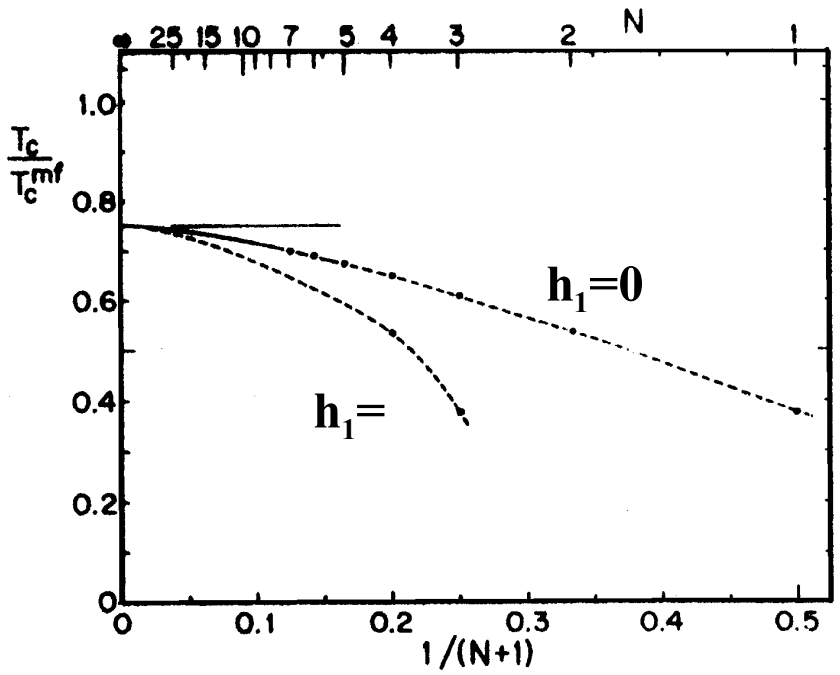

Figure 3.16: The T_c shifts become experimentally relevant at $N < 25$ [77]. See text for explanation.

From Fig. 3.16 one can conclude that the best method to test finite size scaling is to compare the absolute value of $\dot{T}_c$ for films of different thickness. However, another possibility is to test the finite size scaling by Eqs. 3.46 and 3.48 directly. Assuming $h_1 = 0$, the expected temperature dependence of the average order of the film $\overline{\Psi}$, should be as shown in Fig. 3.17.

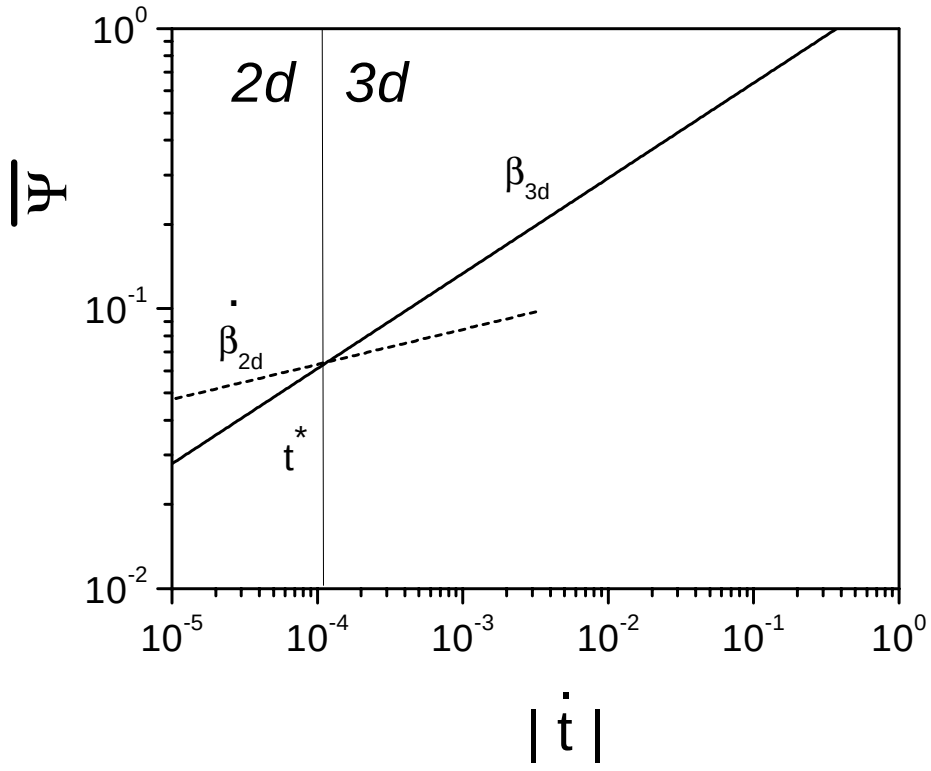

Figure 3.17: The $3d$-$2d$ crossover in thin films.

The solid line indicates the vanishing of the long range order of a $3d$-system. For $\xi \approx D$, a crossover to $2d$-behavior occurs ($\dot{t} = t^*$), as indicated by the dashed line.

3.5.3 Experimental evidence for a $3d$-$2d$ crossover

Optical experiments which exploit the index of refraction have been carried out by Meadows and Scheibner [78, 79, 80] on critical fluid films (2,6-lutidine + water). The fluid films were confined by Ag and SiO_2 coated container walls. These experiments confirm the crossover scenario as drawn in Fig. 3.17.

Furthermore, they confirm the scaling of the T_c-shift according to Eq. 3.47. The experiments were carried out in the presence of h_1-surface fields, originating from the fluid-wall interaction. This interaction was so strong that the value of T_c(bulk) was shifted. The existence of a $3d$-$2d$ crossover in thin nickel films without h_1 surface fields was demonstrated experimentally by Li and Baberschke [81] by means of ferromagnetic resonance (FMR) measurements. In Fig. 3.18, the values for β, obtained in a temperature region of $t \in [10^{-2} \ldots 10^{-1}]$ are depicted for different sample thicknesses. At a film thickness of $N \approx 6$ (shaded area in Fig. 3.18), the critical exponent β crosses from the initial $3d$-value to the $2d$-value ($\dot{\beta} = 0.125$). This suggests that a film has to be extremely thin to behave like a $2d$-system. However, according to Fig. 3.17, this depends crucially on the reduced temperature region that is tested. Indeed, the temperature region $t \in [10^{-2} \ldots 10^{-1}]$ accessible in the experiment may be converted to a (bulk) correlation length of $\xi \approx (5 \cdot 10^{-2})^{-0.64} = 6.8$, in good agreement with the experimentally-observed value for the crossover thickness.

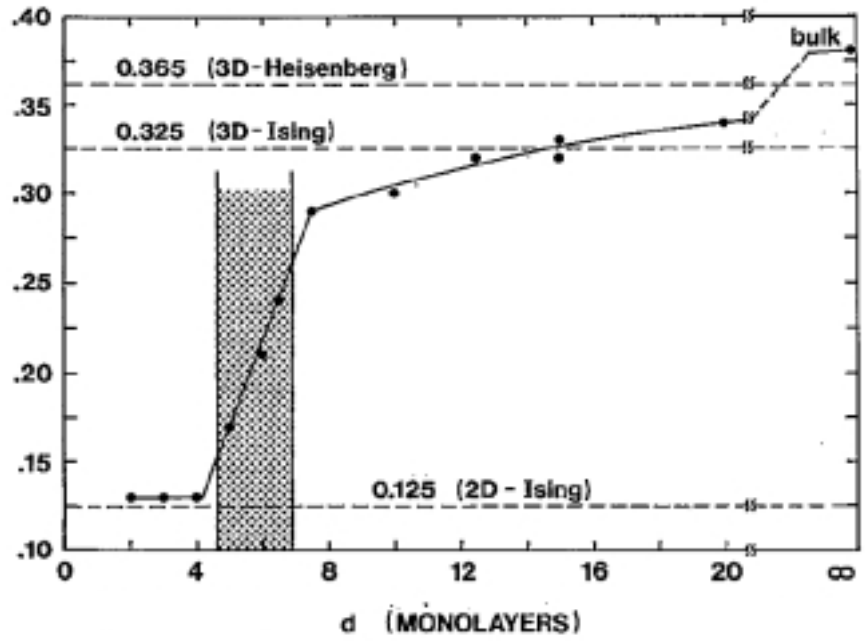

Figure 3.18: The $3d$-$2d$ crossover in thin Ni films.

3.5.4 Dimensional crossover in presence of a weak surface field

What will happen if the surface fields are "switched on" ($h_1 > 0$)? Strictly speaking, for zero bulk field ($H = 0$), the critical point will be missed, (see Fig. 3.15). However, for small enough h_1-fields, i.e. far away from the *extraordinary* transition, one might expect to observe pure $2d$-behavior, analogous to the *ordinary* behavior of a surface in presence of a weak h_1-field and, superimposed, a weak adsorption profile, i.e.

$$\Psi(z, h_{1A}, h_{1B}) = \Psi_{\text{hom}} + \Delta\Psi(z, h_{1A}, h_{1B}). \tag{3.50}$$

Ψ_{hom} represents the part that shows pure $2d$-behavior for $\dot{t} \to 0$ (see Eq. 3.29). $\Delta\Psi(z, h_{1A}, h_{1B})$ represents a weak adsorption profile. The validity for this scenario depends on h_{1A} and h_{1B}, but as h_1 becomes large

($h_1 \to \infty$), even a semi-infinite system shows $2d$-behavior in the surface near region ($\Lambda = \xi$) because the surface decouples from the bulk [33] p.162. Now the question arises as to how the fluctuations in a thin film will react to the finite size. First, the case of no surface field ($h_1 = 0$) is considered. In the vicinity of the (shifted) critical temperature ($\dot{t} \lessdot t^*$), the film will behave like a $2d$-system and the correlation length along the surface ($\dot{\xi}$) will presumably diverge according to the $2d$-power-law ($\dot{\xi} \propto \dot{t}^{-\dot{\nu}}$). But perpendicular to the surface, $\xi_\perp$ stays finite [77] with

$$\xi_\perp \approx N/\,3. \tag{3.51}$$

Unfortunately, the above scenario relies mainly on qualitative arguments [6] and Landau (mean field) theory [77] due to the technical problems in handling the dimensional crossover. A theoretical study of the critical behavior of a thin film at the bulk critical temperature ($t = 0,\ \dot{t} \neq 0$) was presented recently [73, 82] by Parry *et al.*. They used local functional theory to calculate the correlation function $G(\mathbf{r}, z_1, z_2)$ in a thin film. For strong and symmetric surface fields ($h_{1A} = h_{1B} = \infty$) and large in-plane separation ($\mathbf{r} \to \infty$, see Fig. 3.5.1) they find

$$G(\mathbf{r}, z_1, z_2) = C^2 \cdot \Xi_d\Big(\frac{z_1}{D}\Big) \cdot \Xi_d\Big(\frac{z_2}{D}\Big) \cdot \frac{\exp[-|\mathbf{r}|/\,(\xi^0)]}{|\mathbf{r}|^{(d-2)/2}}, \tag{3.52}$$

with $\Xi_d\Big(\frac{z}{D}\Big)$ as a bell-shaped universal function that depends only on $(z/\,D)$. See Fig. 3.19 for a numerical estimate of $\Xi_d\Big(\frac{z}{D}\Big)$ and Fig. 3.14 for the definition of the space coordinates $z_1,\ z_2$ and r. An inspection of Eq. 3.52 confirms that the character of the fluctuations in a thin $3d$-film is two dimensional at the bulk critical temperature ($t = 0$), since Eq. 3.52 is just the OZ-form for the correlation function of a $2d$-Ising system, decorated with a bell-shaped universal function $\widetilde{\Xi}_d$ that determines the z-dependence. To see this directly,

Eq. 3.52 is recast to

$$\begin{aligned} G(\mathbf{r}, z_1, z_2) &= \widetilde{\Xi}_d\Big(\frac{z_1}{D}, \frac{z_2}{D}\Big) \cdot \frac{\exp[-r/\ \dot{\xi}]}{r^{1/2}} \\ &= \widetilde{\Xi}_d\Big(\frac{z_1}{D}, \frac{z_2}{D}\Big) \cdot G_{\dot{d}=2}(r, \dot{\xi}), \end{aligned} \tag{3.53}$$

(see Table 3.1). The quantity of interest free for interpretation is now $\dot{\xi}(t)$. Parry *et al.* find

$$\dot{\xi}(t = 0) = D/\ 7.34. \tag{3.54}$$

In the vicinity of the phase transition, the correlation function is determined by the (in-plane) correlation length $\dot{\xi}$ only. The ultimate experiment (or theory) should therefore determine

$$\dot{\xi}(\dot{t}) = \xi_0 \cdot t^{-\nu} \cdot \dot{g}(\xi/\ D,\ l_{1A}/\ D,\ l_{1B}/\ D) \tag{3.55}$$

and

$$\xi_\perp(\dot{t}) = \xi_0 \cdot t^{-\nu} \cdot g_\perp(\xi/\ D,\ l_{1A}/\ D,\ l_{1B}/\ D) \tag{3.56}$$

separately. Presumably one would find

$$\dot{\xi}(\dot{t} \to 0) = \widetilde{\dot{\xi}_0} \cdot \dot{t}^{-\dot{\nu}} \tag{3.57}$$

and

$$\xi_\perp(\dot{t} \to 0) \approx D/\ 3. \tag{3.58}$$

without disturbing surface fields ($h_{1A} = h_{1B} = 0$). In the presence of surface fields ($h_{1A} \neq 0$ or $h_{1B} \neq 0$), also the $2d$-correlation length $\dot{\xi}$ might not diverge if no "compensation" field H_c (see Fig. 3.15) is present.

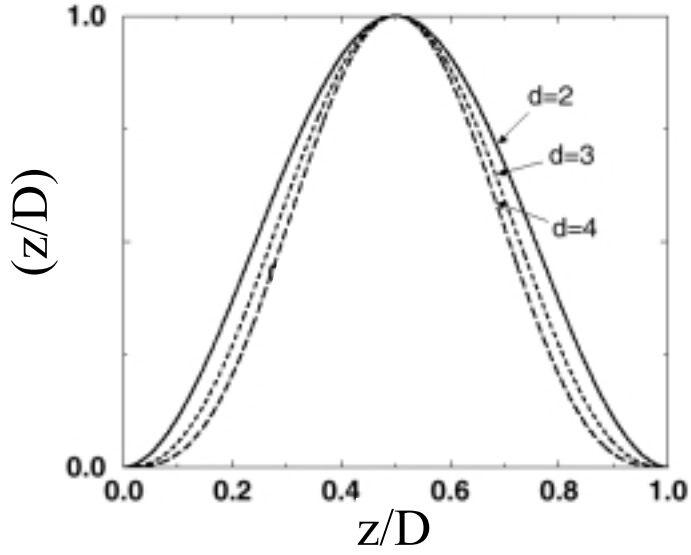

Figure 3.19: The universal function $\Xi_d\left(\frac{z}{D}\right)$ in 2, 3, and 4d-thin films [82], see Eq. 3.52.

3.6 Summary

The critical behavior of a film may be quite complex. The presence of the two interfaces gives rise to critical adsorption if surface fields are active. In a thick film, the surface near region will exhibit the well-known surface critical behavior, e.g. the order decays with the critical exponent $\beta/\ \nu$ and the region far from the interfaces will behave like a 3d-Ising system. In a thin film, the simultaneous presence of the two interfaces will not be negligible and a crossover to the behavior of a two dimensional system can be expected within experimental resolution. This crossover is driven by the impaired divergence of the correlation length. Further, the different length scales (ξ, D, l_1) are in competition and this drives the phase transition.

A straightforward approach to study the phase transition in thin FeCo-

films experimentally is to determine the depth-dependence of the order parameter $\Psi(z)$ from x-ray Bragg scattering (see Chapter 5) and the correlation function $G(\mathbf{r}, z_1, z_2)$ from the diffuse x-ray scattering intensity [83] (see Fig. 3.6). Assuming the validity of Eq. 3.50, one can extract the $3d$-critical exponent β, the $2d$-critical exponent $\dot{\beta}$, and the $3d$-$2d$ crossover temperature t^* from the constant contribution (Ψ_{hom}) to the order parameter profile $\Psi(z)$ (see Fig. 3.17). Furthermore, the surface field h_1 and the correlation length $\xi_\perp$ can be deduced from the adsorption profile $\Delta\Psi(z)$ (Eqs. 3.29/3.40).

Chapter 4

FeCo: an Ising-model system

Due to its high Curie temperature of 950 °C and its high saturation magnetization, FeCo is of technical interest for applications such as turbine engines and recording media. The interplay between the crystalline microstructure and the resulting average magnetic properties has been studied in detail [84, 85] and the bulk phase diagram is well-known. The equilibrium phase diagram is depicted in Fig. 4.1.

4.1 The FeCo phase diagram

The concentration range around Fe(50%)-Co(50%) is considered in the following. At low temperature, the system is in the ordered B2-phase[3] over a broad concentration range [25 at.% - 75 at.%] [87]. In the ordered phase, the Fe and Co atoms occupy different sublattices. When approaching $T_c = 720\ ^\circ C$, the system disorders and finally when T_c is crossed, the long range order is lost and the occupation of the two sublattices is random (A2-phase), this is depicted schematically in Fig. 4.2. At higher temperatures, a structural phase transformation takes place and the lattice becomes fcc. At the same temperature, the ferromagnetism disappears. The structural phase

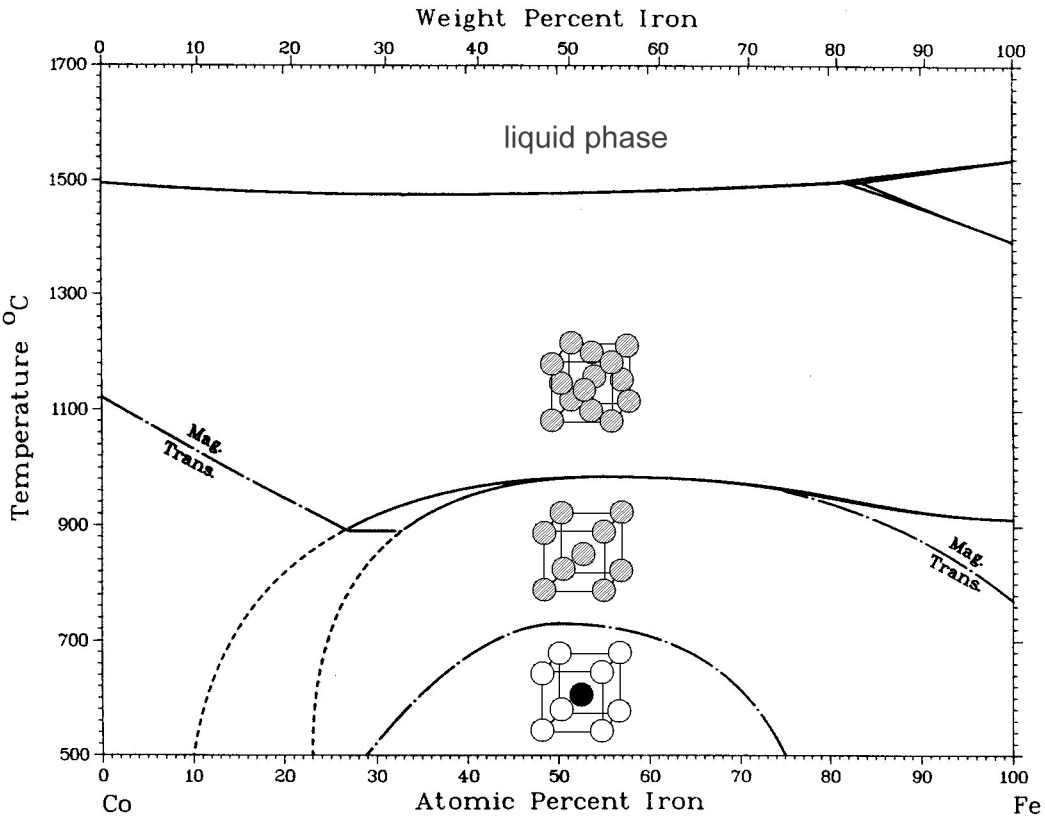

Figure 4.1: The FeCo phase diagram, reproduced from [86].

transition is not reversible in a sense that when cooling the sample down back to low temperature, the crystal breaks up into small single crystalline domains. Therefore, no bulk single crystals are available by classical crystal growth methods and most experiments so far have been done on powders. The thin film growth from the gas phase avoids this structural phase transition, since the films are directly grown in the bcc phase as reported in [41].

Every lattice site can either be occupied by a Fe or a Co atom and these two states can be described efficiently by occupying every lattice site with

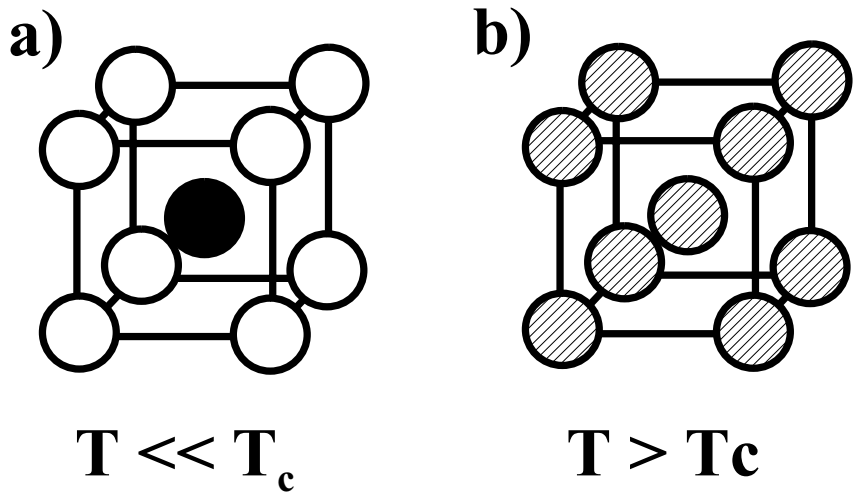

Figure 4.2: a) The B2 unit cell of an ordered FeCo alloy. Black and white balls represent Fe and Co atoms, respectively. b) The bcc unit cell of a disordered FeCo alloy. Striped balls represent a probability of finding an Fe or Co atom on its respective lattice site.

a spin 1/ 2, which has two states (Fe or Co). In this sense, FeCo is indeed a *3d*-Ising system with spin 1/2. To describe the thermodynamic behavior, e.g. by Monte Carlo methods [34], one has to specify the Hamiltonian. For *3d*-Ising, the Hamiltonian reads

$$\mathcal{H} = -\sum_{(i,j)} s_i s_j c_{i,j} - \sum_i s_i H. \tag{4.1}$$

with the interaction parameters c_{ij}. H is a homogeneous external field that couples to the order parameter. Ψ is given by the average spin

$$\Psi = \langle K_i \cdot \Psi(r_i) \rangle \tag{4.2}$$

with the kernel K_i defined as $K_i = 1$ for sublattice A and $K_i = -1$ for sublattice B to take care of the antiferromagnetic character of the order [6].

4.2 The order-disorder phase transition

The order-disorder phase transition of FeCo at 720 °C is of second order [5] and belongs to the *3d*-Ising spin 1/ 2 universality class. The critical exponent β has been determined by neutron experiments $\beta = 0.303(4)$ and is independent of the concentration. Krimmel et. al [41] confirmed this value recently by means of a x-ray experiment using a 1 μm thick FeCo film grown from the gas phase. They found $\beta = 0.307(11)$. The concentration dependence of the critical temperature $T_c(c_{\mathrm{Fe}})$ [5] can be modeled by taking into account the contribution of the magnetism to the next nearest neighbor interaction as reviewed in [88]. These mean field results have been confirmed by first principles calculations based on local spin-density approximations and general perturbation methods [89]. These calculations show that the ordered B2-phase is stabilized by the ferromagnetism.

Fig. 4.3 shows a neutron measurement [5] on a FeCo powder sample. In this experiment, the integrated intensity of a FeCo(001) superstructure Bragg reflection was measured close to the critical phase transition temperature T_c. As it will be explained later in Eq. 5.9, this intensity is directly proportional to Ψ^2 and therefore the fit gives as a result 2β and this can directly be compared with the theoretical value. In the given case, the agreement is excellent ($\beta = 0.303(4)$, $\beta_{3dIsing} = 0.314(3)$).

4.3 Definition of the FeCo order parameter

To mathematically treat the order parameter in FeCo the unit cell is divided into two sublattices, A and B. In the fully ordered state ($\Psi = 1$), sublattice A is occupied by Fe and sublattice B is occupied by Co, see Fig. 4.2a. In the disordered state ($\Psi = 0$). The order parameter Ψ is given by

$$\Psi = 2(r_A - c_{\mathrm{Fe}}) = 2(r_B - c_{\mathrm{Co}}) \tag{4.3}$$

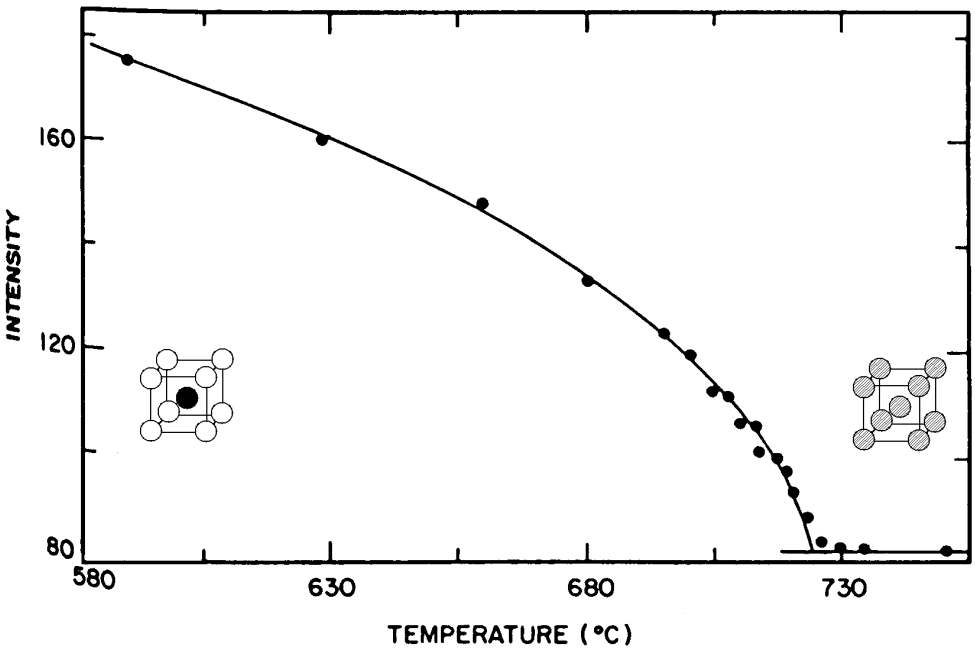

Figure 4.3: Integrated FeCo(001) intensity vs. temperature, reproduced from [5]. The solid line is a fit according to a power law.

with c_{Fe} as the concentration of Fe and c_{Co} as the concentration of Co and $c_{\mathrm{Fe}} + c_{\mathrm{Co}} = 1$. r_A is the percentage of A-places, occupied with Fe atoms and r_B is the percentage of B-places occupied with Co atoms. Eq. 4.3 gives the sublattice occupation in terms of the order-parameter Ψ. If, for example, $r_A = c_{\mathrm{Fe}}$ then Eq. 4.3 gives $\Psi = 0$ in accordance to the fact that in this case, the occupation of sublattice A with Fe atoms is given only by the concentration, so no long ranged order is present. On the other hand, if $r_A = 2 \cdot c_{\mathrm{Fe}}$ then Eq. 4.3 gives $\Psi = 2 \cdot c_{\mathrm{Fe}}$. For $c_{\mathrm{Fe}} = 0.5$ this gives $\Psi = 1$, the maximal possible order in the system.

Chapter 5

Kinematical scattering theory for thin films

5.1 Introduction

In this work, x-ray scattering experiments have been performed to reconstruct the depth- and temperature-dependence of the order parameter $\Psi(z)$ in FeCo films. The thickness of these films ranges from 50 Å to 350 Å. In the following, the appropriate mathematical description of the observed x-ray diffraction patterns is developed using the concepts of kinematical scattering theory. In particular the sensitivity of x-ray diffraction pattern to the peculiar order parameter profiles that can occur is considered.

5.1.1 The lattice sum

The purpose of this section is to introduce the basic notation which will be used to develop new aspects of x-ray scattering from thin films. The notation is adapted to the standard textbooks for x-ray scattering, e.g. [90].

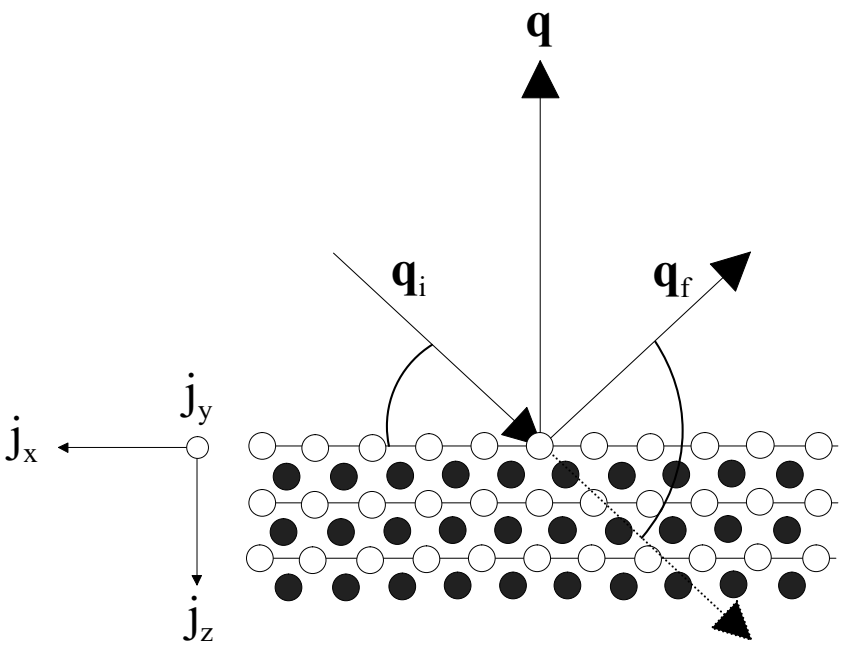

Figure 5.1: The scattering geometry. Here, $\mathbf{q_i}$ and $\mathbf{q_f}$ denote the wave vector of the incoming and scattered x-ray beam. $\mathbf{q}$ is the scattering vector.

Consider a plane monochromatic x-ray wave $A_0 \cdot \exp\ (-i\ \mathbf{q_i} \cdot \mathbf{r})$ that impinges on a single crystal (see Fig. 5.1). Here, $q_i = 2\pi/\ \lambda$ denotes the modulus of the wave vector of the x-ray wave. The amplitude $A(\mathbf{q})$ of the scattered x-ray wave along a direction $\mathbf{q_f}$ is given by the lattice sum [90] p.28

$$\begin{aligned} A(\mathbf{q}) \;=\; & \frac{r_e}{R_0} \cdot A_0 \cdot \sum_{j_x=0}^{N_x-1} \cdot \sum_{j_y=0}^{N_y-1} \cdot \sum_{j_z=0}^{N_z-1} \cdot \sum_{m=1}^{M} f_{\mathrm{m}}(\mathbf{q}) \cdot \\ & \exp\ \Big(i \cdot (q_{\mathrm{x}} j_{\mathrm{x}} a_{\mathrm{x}} + q_{\mathrm{y}} j_{\mathrm{y}} a_{\mathrm{y}} + q_{\mathrm{z}} j_{\mathrm{z}} a_{\mathrm{z}})\Big) \cdot \\ & \exp\ \Big(i \cdot (q_{\mathrm{x}} u_{\mathrm{m,x}} + q_{\mathrm{y}} u_{\mathrm{m,y}} + q_{\mathrm{z}} u_{\mathrm{m,z}})\Big). \end{aligned} \tag{5.1}$$

Here, $(N_{\mathrm{x}}, N_y, N_z)$ denotes the number of unit cells in a direction and $\mathbf{q} =$

$\mathbf{q_f} - \mathbf{q_i} = (\mathbf{q_x}, \mathbf{q_y}, \mathbf{q_z})$ is the scattering vector. $r_e = e^2/\, mc^2 = 3 \cdot 10^{-15}\mathrm{m}$ is the classical electron radius. R_0 is the distance of the scattering center to the detector. $(\mathbf{u}_\mathrm{m})$ is the position of the m-th atom in the unit cell. $f_\mathrm{m}(\mathbf{q})$ is the tabulated atomic scattering factor of the m-th atom in the unit cell, given by the fourier transform of the electron density and resonance terms close to adsorption edges. Assuming spherical symmetry of the atom, the atomic scattering factor is written as

$$f_\mathrm{m}(\mathbf{q}) = \mathbf{f}(\mathbf{q}) + \mathbf{f'}(\mathbf{q}, \mathbf{E}) + \mathbf{i}\ \mathbf{f"}(\mathbf{q}, \mathbf{E}). \tag{5.2}$$

E is the energy of the incident x-ray wave and f' and f" are tabulated for example in [91] and [92].

5.1.2 Scattering amplitude for a film

Now a film of thickness N with a surface normal pointing along $\mathbf{n}$ is considered. The q_z-direction is defined along $\mathbf{n}$

$$q_\mathrm{z} \equiv \mathbf{n} \cdot \mathbf{q}. \tag{5.3}$$

and the scattering vector is restricted to the specular condition

$$q_x = q_y = 0. \tag{5.4}$$

Further, the definition of the unit cell structure factor reads

$$F(\mathbf{q}) \equiv \sum_\mathrm{m} \mathbf{f}_\mathrm{m}(\mathbf{q}) \cdot \exp\ \Big(\mathbf{i} \cdot (\mathbf{q} \cdot \mathbf{u}_\mathrm{m})\Big). \tag{5.5}$$

Then Eq. 5.1 can be rewritten as

$$A(q_\mathrm{z}) = \frac{r_e}{R_0} \cdot A_0 \cdot N_\mathrm{x} \cdot N_\mathrm{y} \cdot F(q_\mathrm{z}) \cdot \sum_{j_\mathrm{z}=0}^{N-1} \exp\ \Big(i \cdot (q_\mathrm{z} \cdot j_\mathrm{z} \cdot a_\mathrm{z})\Big). \tag{5.6}$$

The factor $(N_\mathrm{x} \cdot N_y)$ represents the typical size of a single crystalline domain along the surface. Eq. 5.6 is a geometrical sum and can be transformed to

$$A_{laue}(q_z) = \frac{r_e}{R_0} \cdot A_0 \cdot N_x \cdot N_y \cdot F(q_z) \cdot \frac{1 - \exp\ (i \cdot q_z \cdot N_z \cdot a_z)}{1 - \exp\ (i \cdot q_z \cdot a_z)}. \qquad (5.7)$$

Eq. 5.7 describes the scattering amplitude from a thin film and is often called the Laue function or the N-slit function, since it is also the solution for coherent light scattering from an N-slit apparatus. In this case, a_z is the path between the slit centers and the slit size is included in $F(q_z)$.

Scattering amplitude from a substrate

An also relevant case is the limit of Eq. 5.7 for thick samples ($N_z \longrightarrow \infty$). This limit applies for a substrate with macroscopic thickness and well-defined surface, or, more precisely a thickness much bigger than the coherence length of the x-ray beam. In this sense, a crystal is called semi-infinite. For $q_z \neq n \cdot 2 \cdot \pi / a_z, n = 1, 2, 3, \ldots$ Eq. 5.7 reads [93, 94]

$$A_{rod}(q_z) = \frac{r_e}{R_0} \cdot A_0 \cdot N_x \cdot N_y \cdot F(q_z) \cdot \frac{1}{1 - \exp\ (i \cdot q_z \cdot a_z)}. \qquad (5.8)$$

Eq. 5.7 and 5.8 have to be used with some caution. Special care has to be taken to include the reflectivity from the average electron density properly. This can be taken into account by substituting 5.7 and 5.8 with the Fresnel amplitudes [95] for the 0th Brillouin zone ($q_z < 2\pi / a$), as described in [96]. Furthermore, Eq. 5.8 is not able to describe the scattered amplitude in the vicinity of a bulk Bragg reflection. In this region, a dynamical approach like the Darwin-Prinz theory [97] has to be used. However, these limitations do not apply for the temperature-dependent measurements which will be analyzed later.

5.2 Intensities in a scattering experiment

The experimentally observable quantity is the intensity

$$I_{ideal}(q_z) = P \cdot n \cdot |A(q_z)|^2. \tag{5.9}$$

Here, P is the polarization factor which depends upon the incident x-ray wave polarization with respect to the chosen scattering geometry [90]. It results from the electro-magnetic wave character of x-rays [95]. In case of a horizontally polarized beam and a horizontal scattering geometry it reads

$$P = \cos^2(2\theta) \cdot \cos^2(2\theta_{mono}). \tag{5.10}$$

2θ is the angle between the detector and the incoming x-ray beam. n is the active area F on the sample, normalized to the typical single domain size $N_x \cdot N_y$ [98, 99]. The active area is given by the primary beam size, the sample size and the collimation of the detector. The primary beam will always be smaller than the sample surface for the experiments performed in this study. Then the active sample area is given by the primary beam slits and n reads

$$n = \frac{F}{N_x N_y} = \frac{1}{N_x N_y} \cdot \frac{s_\perp \cdot s_\parallel}{\sin(\theta)}. \tag{5.11}$$

Here $s_\perp$ and $s_\parallel$ denote the respective slit sizes of the primary beam. θ is the angle between the sample surface and the incident wave. q_z and θ are related by Eq. 5.4 to

$$q_z = \frac{4\,\pi}{\lambda}\,\sin(\theta). \tag{5.12}$$

λ is the wavelength of the x-ray beam.

5.2.1 Resolution

In a real experiment, one has to account for the resolution of the diffractometer, given by the divergence defined by the slit system and the energy

resolution of the monochromator. The energy resolution together with the divergence of the beam and the mosaic distribution of the sample lead to an integration of intensity in reciprocal space; this is discussed in appendix A. The integration has two consequences. First, the reciprocal space volume in which this integration is done depends on the scattering angle θ. This is taken into account by the Lorentz factor

$$L(\theta) = \frac{\cos(\theta)}{\sin(\theta)} \tag{5.13}$$

as derived in Eq. A.5. Second, the integration leads to a smearing of the intensity $I_{ideal}(q_z)$ [see e.g. [14]]. This is taken into account by convoluting the intensity with the normalized resolution function. The measured intensity becomes

$$I_{exp} = L(\theta) \cdot \int I(q_z - \Delta_z) \cdot \mathrm{Res}(\Delta_z, \sigma_z) \cdot d\Delta_z. \tag{5.14}$$

Here $\mathrm{Res}(\Delta_z, \sigma_z)$ is the normalized resolution function in q_z direction. In most cases, $\mathrm{Res}(\Delta_z, \sigma_z)$ is given by a Gaussian distribution with σ_z being the half width and

$$\mathrm{Res}(\Delta_z, \sigma_z) = \frac{1}{\sqrt{2\,\pi} \cdot \sigma_z} \cdot \exp\left(-\frac{1}{2} \cdot \left(\frac{\Delta_z}{\sigma_z}\right)^2\right). \tag{5.15}$$

In this case, σ_z is called q_z-resolution. If a reference sample with very sharp delta-function-like Bragg reflections is available then the resolution can be determined from Eq. 5.14 directly.

5.3 FeCo structure factor

Using the definition of the order parameter Ψ introduced in Sec. 4.3, the structure factor of the FeCo unit cell (Eq. 5.5) becomes [90]

$$\begin{aligned} F_{\mathrm{FeCo}}(q_z) \;=\; & [\; f_{\mathrm{Fe}} r_A + f_{\mathrm{Co}}(1 - r_A) \;] \;+ \\ & [\; f_{\mathrm{Co}} r_B + f_{\mathrm{Fe}}(1 - r_B) \;] \cdot \exp\,(i \cdot q_z \cdot a/\,2) \end{aligned} \tag{5.16}$$

or, expressed in terms of Ψ and $c_{\mathrm{Fe}},\ c_{\mathrm{Co}}$,

$$\begin{aligned} F_{\mathrm{FeCo}}(q_z,\Psi) &= [\ \not{f}_{\mathrm{Fe}}\cdot(\frac{\Psi}{2}+c_{\mathrm{Fe}})+\not{f}_{\mathrm{Co}}\cdot(-\frac{\Psi}{2}+c_{\mathrm{Co}})\ ] \\ &\quad +[\ \not{f}_{\mathrm{Co}}\cdot(\frac{\Psi}{2}+c_{\mathrm{Co}})+\not{f}_{\mathrm{Fe}}\cdot(-\frac{\Psi}{2}+c_{\mathrm{Fe}})\ ] \\ &\quad \cdot\exp\ (i\cdot q_z\cdot a/\ 2). \end{aligned} \tag{5.17}$$

For clarity, Eq. 5.17 is divided into the order independent contribution (fundamental, "fund") and the contribution depending on the order parameter Ψ ("order")

$$\begin{aligned} F^{\mathrm{fund}}_{\mathrm{FeCo}}(q_z) &= F_{\mathrm{FeCo}}(q_z,\Psi=0) \\ &= [\ \not{f}_{\mathrm{Fe}}\cdot c_{\mathrm{Fe}}+\not{f}_{\mathrm{Co}}\cdot c_{\mathrm{Co}}\ ]\cdot[\ 1+\exp\ (i\cdot q_z\cdot a/\ 2)\ ], \\ F^{\mathrm{order}}_{\mathrm{FeCo}}(q_z,\Psi) &= F_{\mathrm{FeCo}}(q_z)-F^{\mathrm{fund}}_{\mathrm{FeCo}}(q_z) \\ &= \Psi\cdot\frac{\not{f}_{\mathrm{Fe}}-\not{f}_{\mathrm{Co}}}{2}\cdot[\ 1-\exp\ (i\cdot q_z\cdot a/\ 2)\ ]. \end{aligned} \tag{5.18}$$

Both contributions dominate at different q_z values. At the FeCo(001) reflection $(q_z=2\cdot\pi/\ a)$ one obtains

$$\begin{aligned} F^{\mathrm{fund}}_{\mathrm{FeCo}}(q_z) &= 0 \\ F^{\mathrm{order}}_{\mathrm{FeCo}}(q_z,\Psi) &= \Psi\cdot(\not{f}_{\mathrm{Fe}}-\not{f}_{\mathrm{Co}}). \end{aligned}$$

In contrast, at the FeCo(002) reflection $(q_z=4\cdot\pi/\ a)$ one obtains

$$\begin{aligned} F^{\mathrm{fund}}_{\mathrm{FeCo}}(q_z) &= 2\cdot[\ c_{\mathrm{Fe}}\not{f}_{\mathrm{Fe}}+c_{\mathrm{Co}}\not{f}_{\mathrm{Co}}\ ] \\ F^{\mathrm{order}}_{\mathrm{FeCo}}(q_z,\Psi) &= 0. \end{aligned}$$

Due to Eq. 5.9, the intensity of a bulk sample with delta-shaped (001)-Bragg reflection is proportional to Ψ^2 and indeed many experiments on bulk samples have been performed using Eq. 5.17 for the analysis of the measured intensities. The intensity of the (002)-reflection does not depend on Ψ, but it can be used as a normalization to obtain Ψ on an absolute scale.

5.4 Influence of film thickness

5.4.1 Laue oscillations around the FeCo(002) fundamental reflection

According to Eqs. 5.7 and 5.9, the intensity distribution for a free-standing thin film reads, ignoring n and P,

$$I_{laue}(q_z) \propto \mid F(q_z) \cdot \frac{1 - \exp\ (i \cdot q_z \cdot a_z \cdot N_z)}{1 - \exp\ (i \cdot q_z \cdot a_z)} \mid^2, \tag{5.19}$$

and for a bulk sample with an ideally terminated surface

$$I_{rod}(q_z) \propto \mid F(q_z) \cdot \frac{1}{1 - \exp\ (i \cdot q_z \cdot a_z)} \mid^2 . \tag{5.20}$$

In Fig. 5.2, the intensity distribution around the FeCo(002) reflection is simulated ($q_z(002) = 2\pi L/\ a_z = 4.39$ Å^{-1}).

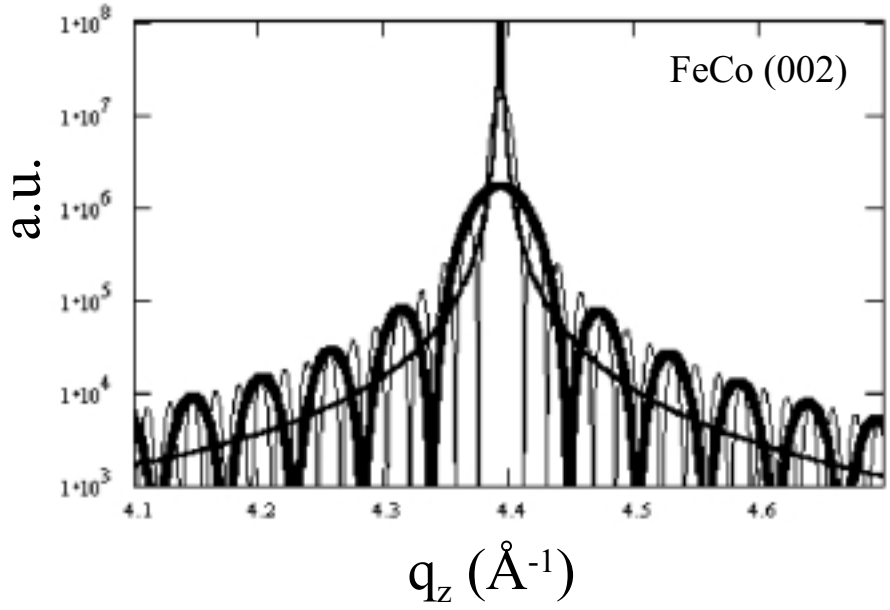

Figure 5.2: Laue oscillations due to finite film thickness. The intensity [a.u.] is plotted vs. q_z(Å^{-1}). The bold line is for $N_z = 40$, the thin line is for $N_z = 120$ and the medium line is for a semi infinite crystal.

For bulk FeCo, a_z is 2.86 Å [100], slightly dependent upon the sample stoichiometry. The wavelength used in the simulation is $\lambda = 0.97$ Å. For suitable thin samples, the finite film thickness gives rise to intensity oscillations, called Laue oscillations (see Fig. 5.2). The intensity in the central maximum is proportional to N_z^2 and the distance $\Lambda(N_z)$ of the relative maxima is

$$\Lambda(N_z) = \frac{2 \cdot \pi}{a_z \cdot N_z} = \frac{2 \cdot \pi}{D} \tag{5.21}$$

with D the film thickness in Å. The FWHM of the central maximum is given by

$$\mathrm{FWHM}(N_z) = \frac{2 \cdot \pi}{D} \cdot \frac{\sqrt{2}}{\pi} \tag{5.22}$$

with an accuracy of better than 1% for $10 < N_z < 1000$. The first minimum is at

$$q_z(I = 0) = \frac{2 \cdot \pi}{D} \tag{5.23}$$

so the FW is just twice $\Lambda(N_z)$. Outside a small q_z range around the FeCo(002) reflection, the intensity distribution of the thin film is of the same order of magnitude as the intensity distribution emerging for a semi infinite crystal (called crystal truncation rod scattering or CTR). This agreement is based on the fact that the intensity of the CTR results mainly from the presence of the surface. This is discussed in more detail in [93, 94].

5.4.2 FeCo Laue oscillations from homogenous order

Now the intensity distribution around the FeCo(001) superstructure reflection resulting from a homogeneous ordered film is considered. The strong dependence of the intensity on Ψ according to Eq. 5.19 is depicted in Fig. 5.3. Since Fe has 26 and Co 27 electrons, the absolute intensity at the FeCo(001)

reflection is some orders of magnitude smaller than at the FeCo(002) reflection due to the weak one electron contrast. A closer inspection reveals a slight asymmetry, resulting from $f'(Co) = 1.67$ and $f'(Fe) = 1.48$ for the chosen wavelength of $\lambda = 0.97$ Å. The sign of Ψ, i.e. the stacking sequence of the film, is not accessible from the intensity distribution. This is called the phase problem and results directly from the fact that the intensity (modulus-squared) and not the amplitude is the observable in these experiments.

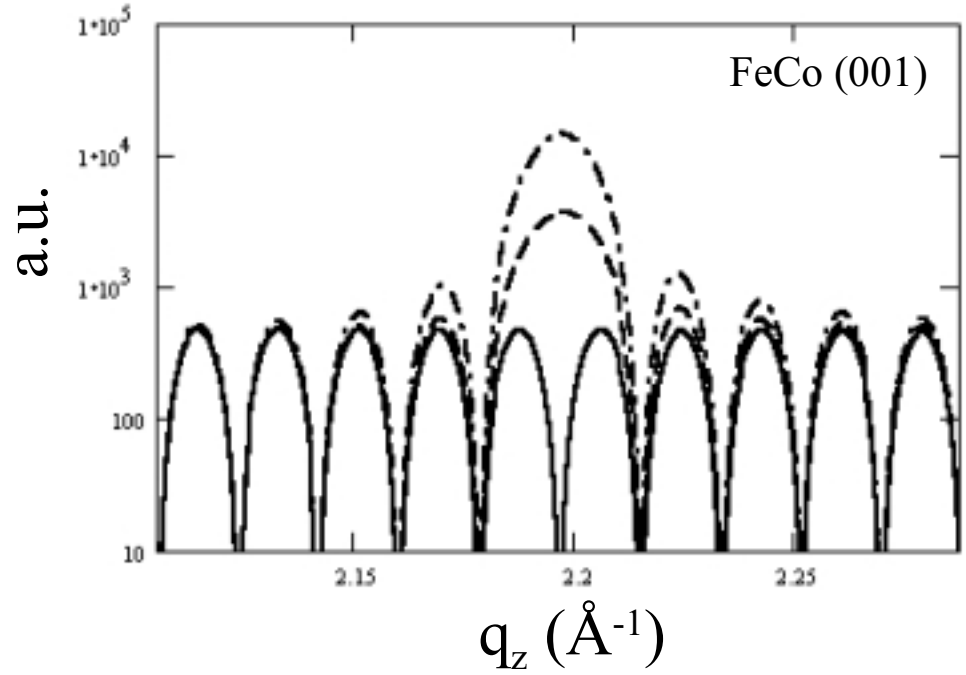

Figure 5.3: Order Laue oscillations. The intensity is plotted vs. $q_z(\text{Å}^{-1})$, the film thickness is $N_z = 120$. Ψ changes from $\Psi = 0$ (solid line) to $\Psi = 0.5$ (dashed line) to $\Psi = 1$ (dashed-dotted line).

5.4.3 Roughness and Laue-oscillations

Since real surfaces have defects, one has to account for missing atoms (holes) or adatoms with respect to the ideally terminated surface or interface. This is usually done by introducing an error-function like occupation distribution $p(j_z, N_z, \sigma)$ of the j_zth layer

$$p(j_z, \sigma) = \sum_{n=-\infty}^{j_z} G(j_z, \sigma) \tag{5.24}$$

$$G(j_z, \sigma) = 2 \cdot \pi / \sqrt{\sigma} \cdot \exp\left(-\frac{1}{2} \cdot \left(\frac{j_z}{\sigma}\right)^2\right) \tag{5.25}$$

This occupation distribution has to be inserted in Eq. 5.1. For a simple Gaussian distribution the sum can be evaluated analytically; however, this can also be done numerically for general distributions. The parameter σ is called roughness. For the MgO-substrate, Eq. 5.8 reads

$$A_{rod}(q_z, \sigma_s) \propto \frac{R(\delta\ q_z, \sigma_s)}{1 - \exp\ (i \cdot q_z \cdot a_z)} \tag{5.26}$$

with

$$R(\delta\ q_z, \sigma_s) = \sum_{\tau} \exp\left(-\frac{1}{2} \cdot \delta\ q_z(\tau)^2 \cdot \sigma_s^2\right). \tag{5.27}$$

σ_s denotes the roughness of the MgO-substrate surface and $\delta\ q_z$ denotes the reduced lattice vector, given by the distance to the MgO Bragg reflections $\delta\ q_z = q_z - q_{00\tau}$ [101].

A thin FeCo-film is described by the interface roughness σ_b and the free surface roughness σ_t. Then Eq. 5.7 reads

$$A_{laue}(q_z) \propto \frac{1 \cdot R(\delta\ q_z, \sigma_b) - \exp\ (i \cdot q_z \cdot N_z \cdot a_z) \cdot R(\delta\ q_z, \sigma_t)}{1 - \exp\ (i \cdot q_z \cdot a_z)}. \tag{5.28}$$

The reduced lattice vector $(\delta\ q_z)$ is calculated with respect to the Bragg reflection (00τ) of the FeCo lattice. The consequence of roughness is quite

subtle since it reveals that the CTR is built up by different overlapping contributions peaked at the Bragg reflections [101]. It is quite instructive to transform Eq. 5.28 to

$$\begin{aligned} A_{laue}(q_z) &\propto \frac{R(\delta\ q_z, \sigma_b) - \exp\ (i \cdot q_z \cdot N_z \cdot a_z) \cdot R(\delta\ q_z, \sigma_t)}{1 - \exp\ (i \cdot q_z \cdot a_z)} \\ &= R(\delta\ q_z, \sigma_b) \cdot \frac{1 - \exp\ (i \cdot q_z \cdot N_z \cdot a_z) \cdot R(\delta\ q_z, \sqrt{\sigma_t^2 - \sigma_b^2}}{1 - \exp\ (i \cdot q_z \cdot a_z)}. \end{aligned}$$

Whereas the prefactor $R(\delta\ q_z, \sigma_b)$ causes the intensity decay of the envelope, the factor $R(\delta\ q_z, \sqrt{\sigma_t^2 - \sigma_b^2}$ damps the oscillations. Therefore, for a film with a flat interface and a rough surface ($\sigma_b \ll \sigma_t$,) the Laue oscillations are damped, as shown in Fig. 5.4 for a FeCo(001) film ($N_z = 40$ unit cells).

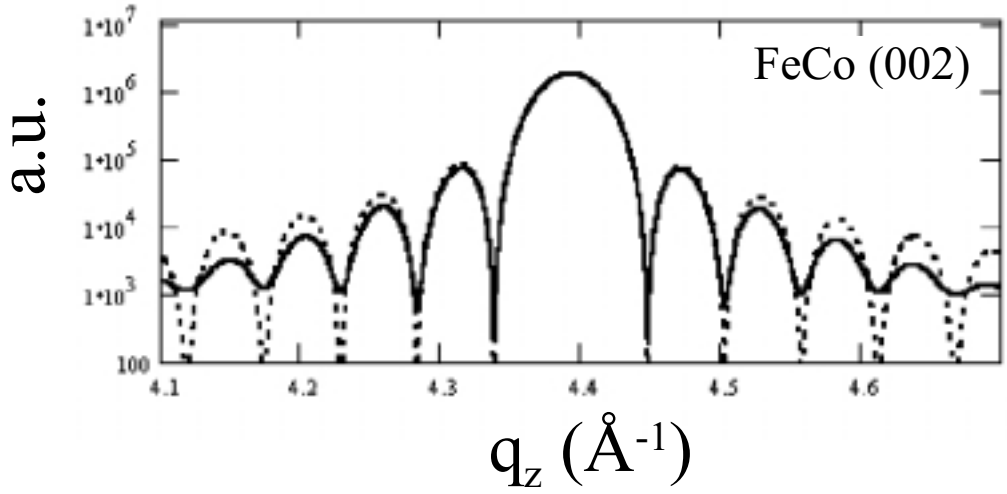

Figure 5.4: Simulation of the influence of roughness on Laue oscillations, using $\sigma_b = \sigma_t = 1$ Å (dashed line) and $\sigma_b = 1$ Å, $\sigma_t = 5$ Å (solid line).

Finally one has to account for small random displacements of the atoms, e.g. due to thermal vibrations. These lead to a Debye-Waller factor

$$DW(q_z, T) = \exp\ \left(-q_z^2 \cdot \left[u(T)^2 + u_0^2\right]\right) \tag{5.29}$$

with $u(T)$ the mean amplitude of the thermal vibrations [90] and u_0 the static displacements. Eq. 5.29 is qualitatively different from Eq. 5.27 since $DW(q_z, T)$ damps the overall intensity and suppresses Bragg reflection with large q_z-components.

5.5 Epitaxial FeCo(001) films on MgO(001)

To simulate the intensity distribution for an epitaxial film, Eq. 5.1 is revisited. For an epitaxial film, a well-defined phase relation exists between the position of the substrate atoms and the film atoms, as depicted in Fig. 5.5. Therefore the lattice sum has to be taken over the whole system. Practically, this boils down into a sum of the scattering amplitudes of the film and the substrate

$$A(q_z) \;=\; A_{\mathrm{film}}(q_z) + A_{\mathrm{sub}}(q_z). \tag{5.30}$$

The observed intensity is given by Eq. 5.9 as

$$\begin{aligned} I(q_z) &\propto |A_{\mathrm{film}}(q_z) + A_{\mathrm{sub}}(q_z)|^2 \\ &\propto |A_{\mathrm{film}}(q_z)|^2 + |A_{\mathrm{sub}}(q_z)|^2 + 2 \cdot \mathrm{Real}\left(\overline{A_{\mathrm{film}}(q_z)} \cdot A_{\mathrm{sub}}(q_z)\right). \end{aligned} \tag{5.31}$$

with the bar denoting the complex conjugate. Whereas the first two terms in 5.31 are familiar, the third term is new. It represents the interference term between the scattering amplitude of the substrate and the film and this term contains qualitatively new information about the ordered state of the film. To evaluate Eq. 5.31, a coordinate system with the zero point ($z = 0$) situated at the last MgO atomic layer is chosen (see Fig. 5.5). The positive $z-$direction points along the FeCo film and the distance between the last MgO layer and the first FeCo layer is called d [Å]. Then Eq. 5.30 reads [102, 103, 38]

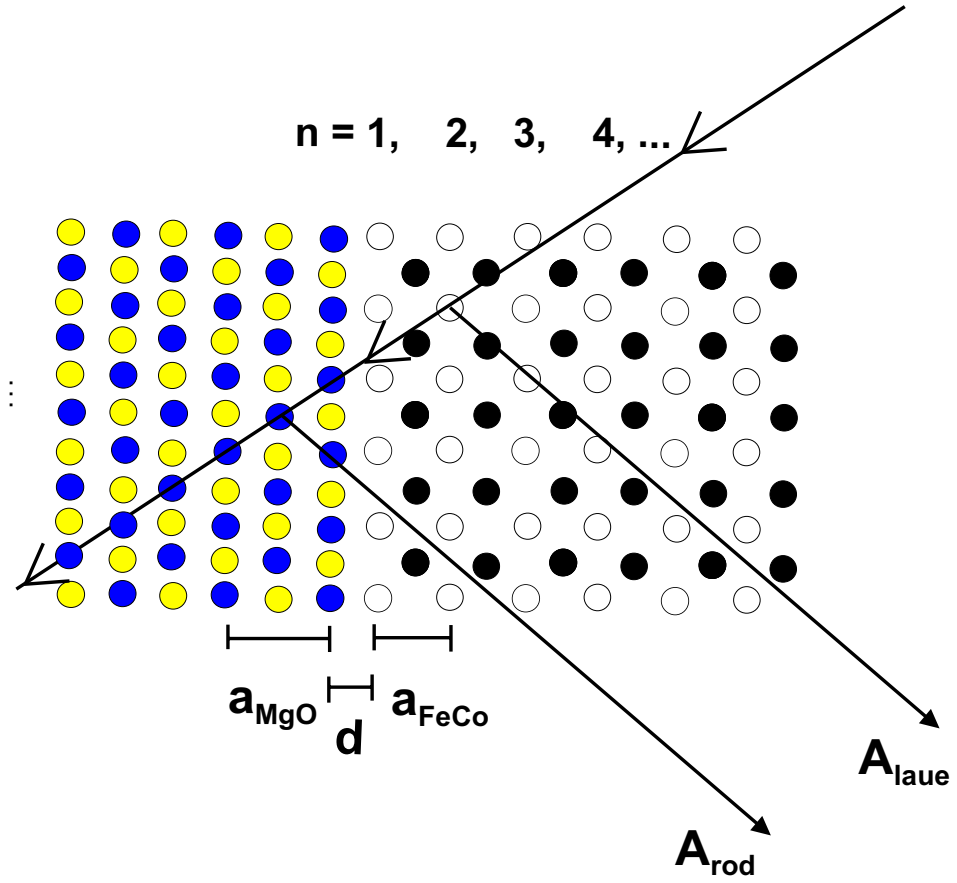

Figure 5.5: Structure model of the epitaxial FeCo film on the MgO substrate with the parameters as introduced in Eq. 5.32. Also shown schematically is the interference of the substrate and the film scattering amplitude.

$$\begin{aligned} A(q_z) &= A_{rod}(q_z) + A_{laue}(q_z) \cdot \exp\ (i \cdot q_z \cdot d) \\ &= F_{\mathrm{MgO}}(q_z) \cdot \frac{1}{1 - \exp\ (-i \cdot q_z \cdot a_{\mathrm{MgO}})} \\ &+ F_{\mathrm{FeCo}}(q_z, \Psi) \cdot \exp\ \Big(i \cdot q_z \cdot d\Big) \cdot \frac{1 - \exp\ (i \cdot q_z \cdot N_{\mathrm{FeCo}} \cdot a_{\mathrm{FeCo}})}{1 - \exp\ (i \cdot q_z \cdot a_{\mathrm{FeCo}})}. \end{aligned} \tag{5.32}$$

The resulting intensity distribution is depicted in Fig. 5.6 for a homogeneously ordered film ($\Psi = 0.88$) with $N_{\mathrm{FeCo}} = 120$ unit cells and FeCo-MgO distance values d based on LEED experiments on iron layers deposited on

MgO(001) [104]. A pronounced asymmetry around the FeCo(001) reflection is observed, which results from the interference term in Eq. 5.31. This asymmetry is continuously shifted with d. In contrast, no strong asymmetry is observed around the FeCo(002) reflection because the intensity is dominated by the quadratic Laue term.

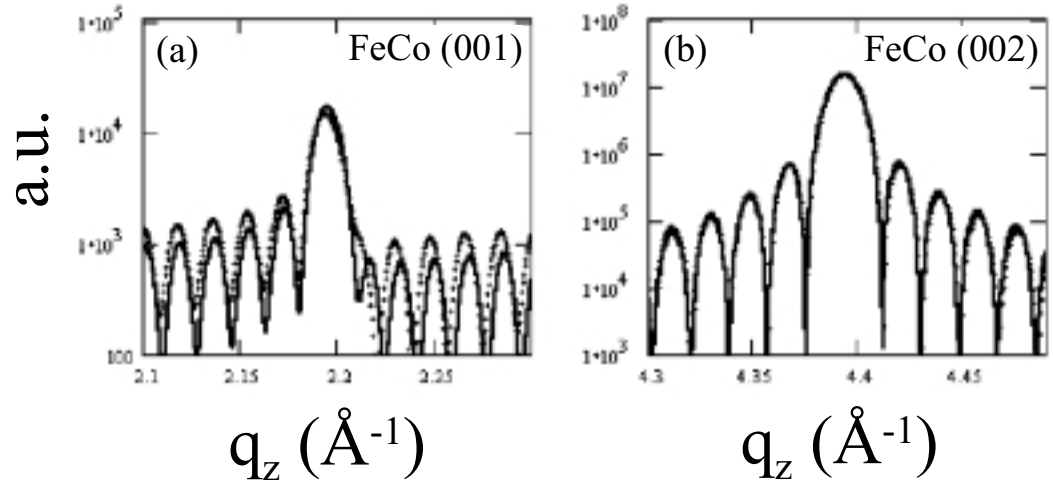

Figure 5.6: Simulated intensity distribution for a homogeneously ordered FeCo film, epitaxially grown on a MgO substrate. The solid line is obtained by $d = 2.0$ Å, the dotted line by $d = 2.3$ Å. a) Intensity distribution around the FeCo(001) reflection, and b) around FeCo(002).

In Fig. 5.6, a positive sign of the order parameter Ψ is assumed and according to Eq. 4.3 this is equivalent to an Fe enriched sublattice A. In this sense, a negative order parameter represents preferred occupation of sublattice A with Co. The intensity distribution for these two cases is depicted in Fig. 5.7, using $N_z = 120$ and $d = 2.3$ Å. For a positive order parameter, the first satellite left to the central maximum is higher than the first satellite right to the central maximum. For $\Psi = -0.88$ the situation is reversed. The interference term makes it possible to extract the sign of the order parameter,

which would not be experimentally accessible for a free standing film. The substrate acts like a phase reference and the phase problem is solved for this special case.

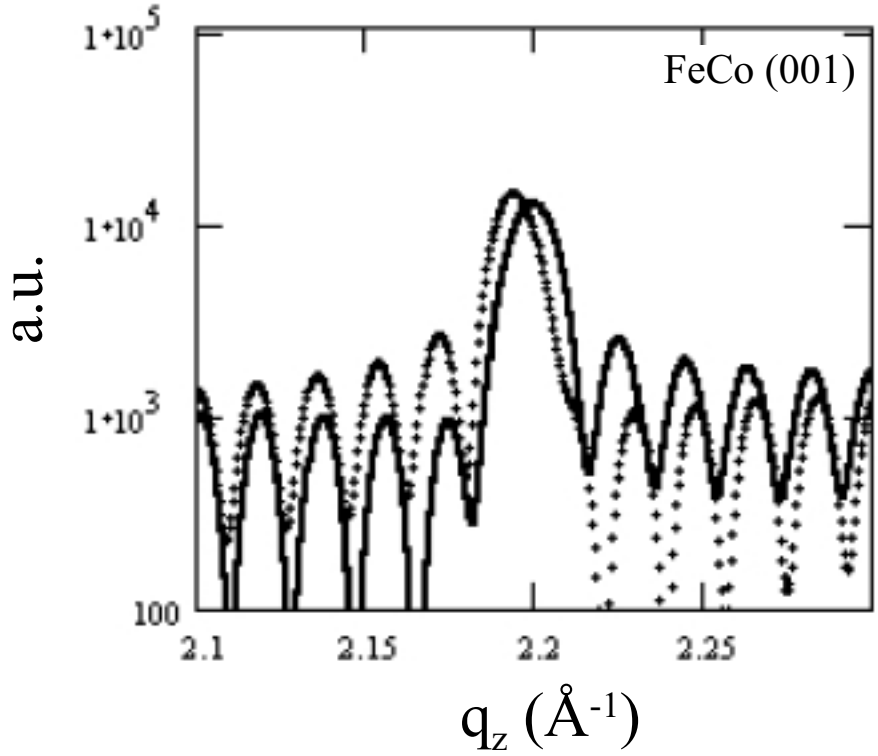

Figure 5.7: Intensity vs. q_z for an ordered FeCo film on a MgO substrate, solid line $\Psi = +0.88$, dotted line $\Psi = -0.88$.

5.6 Exponential decaying order parameter profiles

The dependence of the order parameter $\Psi(z)$ on z may be divided into a depth independent term Ψ_{hom} and a term $\Delta\Psi(z)$ which contains the deviation

$$\Psi(z) = \Psi_{\mathrm{hom}} + \Delta\Psi(z). \tag{5.33}$$

Due to the linearity of Eq. 5.1, the scattering amplitude of the film is given by

$$\begin{aligned} A_{\mathrm{film}}(q_{\mathrm{z}}) &= A^{\mathrm{fund}}_{\mathrm{FeCo}}\Big(q_{\mathrm{z}}, \Psi = 0\Big) + A^{\mathrm{order}}_{\mathrm{FeCo}}\Big(q_{\mathrm{z}}, \Psi = \Psi_{\mathrm{hom}}\Big) \\ &+ A_{\mathrm{profile}}\Big(q_{\mathrm{z}}, \Delta\Psi(z)\Big). \end{aligned} \tag{5.34}$$

This allows one to evaluate expressions for each contribution separately. These terms may be added up finally to obtain the total scattering amplitude. Now the term $A_{\mathrm{profile}}\left(q_{\mathrm{z}}, \Delta\Psi(z)\right)$ that emerges due to the presence of order parameter profiles $\Delta\Psi(z)$ is considered.

5.6.1 Exponentially decaying profile at the interface

First it is assumed that an exponentially-decaying order parameter profile is situated at the substrate film interface. Then $\Delta\Psi(z)$ reads

$$\Delta\Psi(z) = \Delta\Psi_0 \cdot \exp\ \Big(- \frac{z}{N_0 \cdot a_{\mathrm{FeCo}}}\Big) \tag{5.35}$$

with $(N_0 \cdot a_{\mathrm{FeCo}})$ denoting the decay length and $\Delta\Psi_0$ the additional order at the first layer. The contribution from the third term in Eq. 5.34 can be calculated analytically:

$$A_{\text{profile}}\Big(q_{\text{z}}, \Delta\Psi(z)\Big) = \sum_{j_{\text{z}}=0}^{N_{\text{z}}-1} \Big[F\Big(q_{\text{z}}, \Delta\Psi(j_{\text{z}} \cdot a_{\text{FeCo}})\Big) \cdot \exp\ \Big(i \cdot q_{\text{z}} \cdot j_{\text{z}} \cdot a_{\text{FeCo}}\Big)\Big] \tag{5.36}$$

$$= F(q_{\text{z}}, \Delta\Psi_0) \cdot \frac{1 - \exp\ (i \cdot q_{\text{z}} \cdot a_{\text{FeCo}} \cdot N_{\text{z}}) \cdot \exp\ (-N/\, N_0)}{1 - \exp\ (i \cdot q_{\text{z}} \cdot a_{\text{FeCo}}) \cdot \exp\ (-1/\, N_0)}.$$

In case of a large decay length ($N_0 \to \infty$), the well-known Laue function is recovered. The order parameter profile and the associated intensity distribution is depicted in Fig. 5.8.

5.6.2 Exponentially decaying profile at the surface

If, in contrast, an exponentially-decaying order parameter profile is situated at the surface, $\Delta\Psi(z)$ is

$$\Delta\Psi(z) = \Delta\Psi_0 \cdot \exp\ \Big(-\frac{D - z}{N_0 \cdot a_{\text{FeCo}}}\Big) \tag{5.37}$$

and the scattering amplitude of the film reads

$$A_{\text{profile}}(q_{\text{z}}) = \exp\ \Big(i \cdot q_{\text{z}} \cdot a_{\text{FeCo}} \cdot (N-1)\Big) \cdot F(q_{\text{z}}, \Delta\Psi_0) \cdot \frac{1 - \exp\ (-i \cdot q_{\text{z}} \cdot a_{\text{FeCo}} \cdot N_{\text{z}}) \cdot \exp\ (-N/\, N_0)}{1 - \exp\ (-i \cdot q_{\text{z}} \cdot a_{\text{FeCo}}) \cdot \exp\ (-1/\, N_0)} \tag{5.38}$$

which can be inferred either by inserting Eq. 5.37 into 5.34 or from simple symmetry arguments. Eq. 5.38 contains an oscillating term $\exp\ (i \cdot q_{\text{z}} \cdot a_{\text{FeCo}} \cdot (N-1)\ )$, which is the fingerprint of a surface profile.

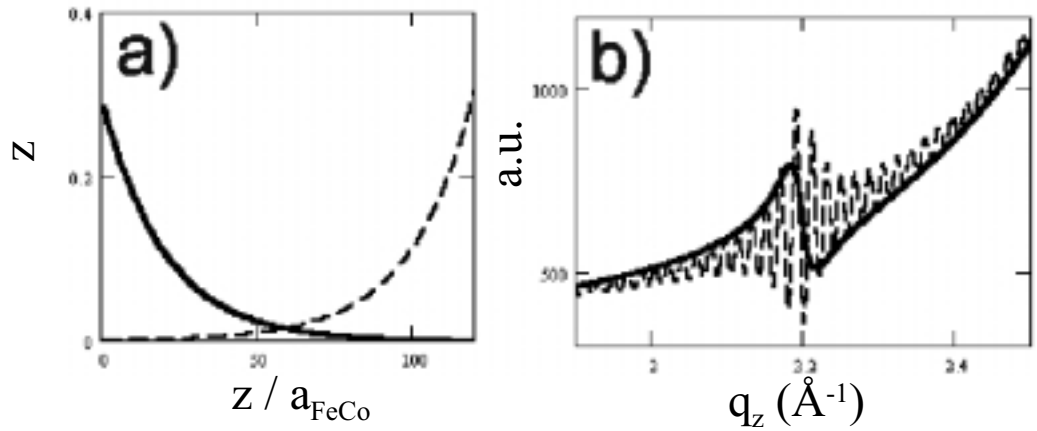

Figure 5.8: a) Order parameter profile $\Psi(z)$ located at the MgO-FeCo interface (solid line) and at the free FeCo-film surface (dashed line). b) The intensity distribution around the FeCo(001) reflection, plotted against q_z (Å^{-1}).

Fig. 5.8 shows the order parameter profiles and the resulting intensity distribution, including the interference with the substrate. The parameters used for the simulation are $N_z = 120$ unit cells for the FeCo-film, a FeCo-MgO distance of $d = 2.3$ Å, a surface order enhancement of $\Delta\Psi_0 = 0.3$ and as decay length $N_0 = 20$ unit cells. The order parameter profile $\Psi(z)$ which is adsorbed at the surface generates intensity oscillations. These oscillations are not Laue oscillations, e.g. the central peak is not wider than the satellites. They could be termed *distance oscillations*, since they result from the distance of the sharp end of the order parameter profile with respect to the surface of the substrate. The order parameter profile at the interface towards the MgO substrate does not generate intensity oscillations.

5.7 Advanced order parameter profiles

5.7.1 The weak adsorption crossover function

To test the experimental data for different adsorption scenarios (weak/strong, see Eq. 3.42) one needs a model function for $\Psi(z)$ that can easily describe these cases by a proper choice of fitting parameters. This is indeed possible by extending the Liu-Fisher function Eq. 3.31 in a way that the $\sim (z/\ l_1)^{\kappa}$ behavior found by Ritschel [46] in the case of weak surface fields (see Eq. 3.40) is reproduced at the interface ($z \to 0$). Then $\Psi(z)$ becomes

$$\Psi(z) = \Psi_{\mathrm{hom}} + A \cdot \Big(\frac{1 + z/\ l_1}{z/\ l_1}\Big)^{-\beta/\nu - \kappa} \cdot \Big(\frac{1 + z/\ \xi}{z/\ \xi}\Big)^{\beta/\nu} \cdot \exp(-z/\ \xi) \quad (5.39)$$

with $-\beta/\ \nu\ - \kappa = -\beta/\ \nu\ - (1 - \eta_{\perp}) \simeq -0.73$. The free fitting parameters are Ψ_{hom}, A, l_1 and ξ. This function will be referred to as the weak adsorption crossover function". The limiting forms are

$$\begin{aligned} \Psi(z) &= \Psi_{\mathrm{hom}} + \quad A \cdot \Big(\frac{\xi}{l_1}\Big)^{\beta/\nu} \cdot \Big(\frac{z}{l_1}\Big)^{\kappa} \quad \text{for } z \to 0 \qquad (5.40) \\ \Psi(z) &= \Psi_{\mathrm{hom}} + \qquad A \cdot \exp(-z/\ \xi) \qquad \text{for } z \to \infty. \end{aligned}$$

$\Psi(z)$ is depicted in Fig. 5.9 for different model functions for $T\ > T_c$, i.e. $\Psi_{\mathrm{hom}} = 0$. The solid line shows an exponentially-decaying profile ($\Psi(z) \sim \exp(-z/\ \xi)$); the dashed line shows the strong adsorption limit ($l_1 = 0$, Eq. 3.31) and the dashed dotted line shows the weak adsorption case, i.e. Eq. 5.39 with $l_1 = \xi$. The inset shows the same profiles as a semi-logarithmic plot. The exponential profile is located between the weak and the strong adsorption profile. To test the influence of l_1, it is now varied from strong ($l_1 \ll \xi$) to weak ($l_1 \ll \xi$) and the resulting profiles are represented in Fig. 5.10 (see Fig. 3.12). Eq. 5.39 is a useful analytical function which can describe the whole range of possible adsorption scenarios. The lattice sum to obtain the respective scattering intensities can be calculated numerically.

However, a certain arbitrariness [105] lies in the proper choice of $(z = 0)$ in $\Psi(z)$, since the calculated order parameter profiles are continuous, while a binary alloy is a discrete system.

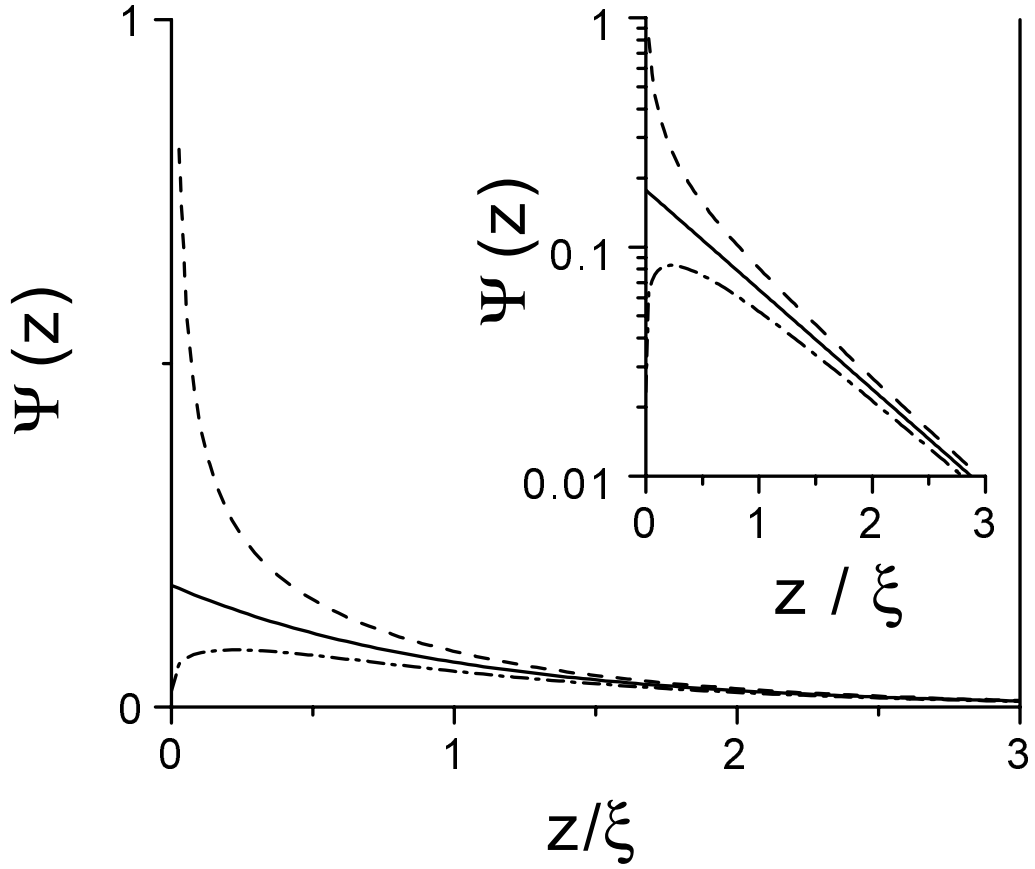

Figure 5.9: Strong $(l_1 = 0)$, weak $(l_1 = \xi)$ and exponential adsorption profiles, drawn as the dashed, dashed dotted, and solid lines, respectively. The inset shows a logarithmic plot.

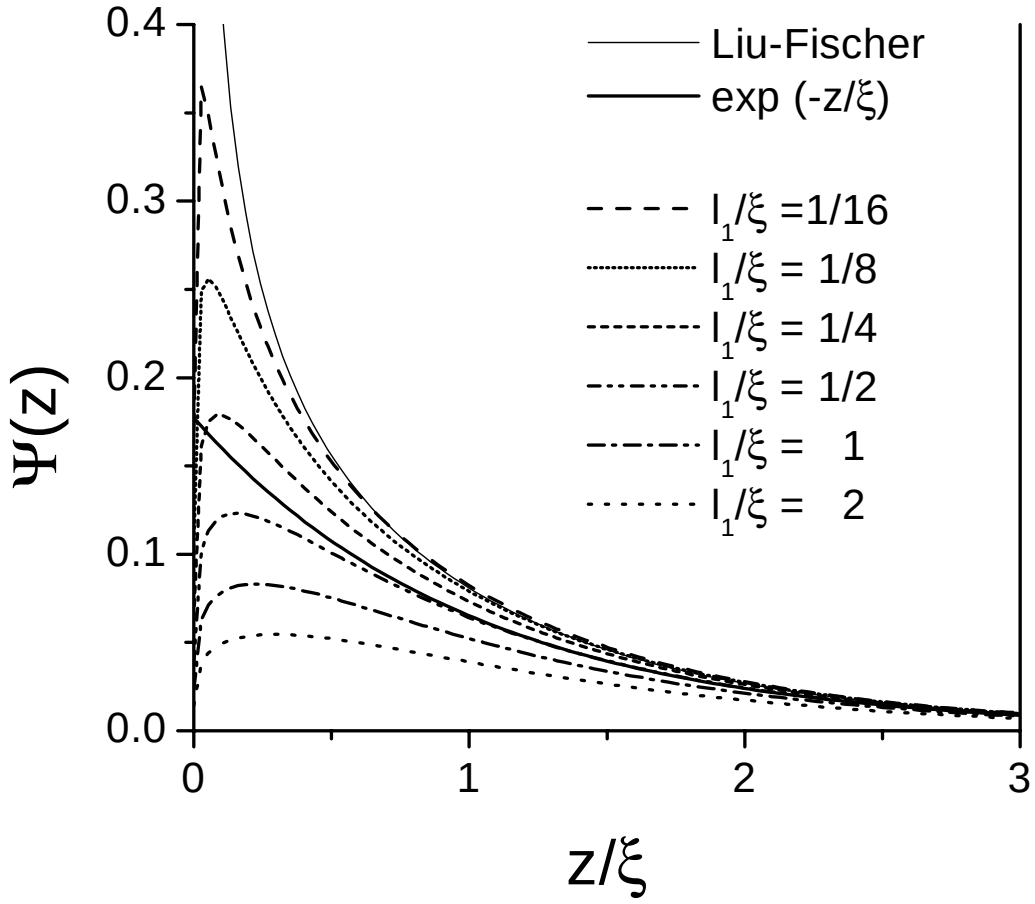

Figure 5.10: Different adsorption models. The thin solid line is the Liu-Fisher model (Eq. 3.31). The thick solid line assumes a pure exponential decay. The broken lines result from the weak adsorption model (Eq. 5.39) with l_1 ranging from strong ($l_1 = \xi/\ 16$) to weak ($l_1 = 2 \cdot \xi$) adsorption.

5.7.2 Roughness and profiles

As introduced in Sec. 5.4.3, roughness is accounted for by an overall occupation density function $p(j_z)$. It is assumed that $p(j_z)$ has an error-function

line shape characterized by σ_t and σ_b

$$p(j_z) = \mathrm{Erf}(j_z, \sigma_b) \cdot \mathrm{Erf}(N - 1 - j_z, \sigma_t), \tag{5.41}$$

as depicted in Fig. 5.11a for a film of $N = 39$ unit cells and $\sigma_b = 1$ unit cells and $\sigma_t = 2$ unit cells. Roughness influences the adsorption-profiles $\Psi(z)$ at the film surface ($z \to D$) and at the interface with the MgO substrate ($z \to 0$). This can be seen in Fig. 5.11b. Depicted is the "effective" adsorption profile $\Psi(z) \cdot p(j_z, \sigma_b, \sigma_t)$ for strong ($l_1 = \xi/\ 16$) and weak ($l_1 = \xi$) adsorption, printed as dots and squares, respectively, to emphasize the discrete nature of the lattice (see Fig. 5.10). The broken line in Fig. 5.11b is a guide to the eye, connecting the points. The solid line is an exponential profile with a reduced amplitude but with the same value for ξ ($\xi = 10$ u.c.). Due to roughness, the exponential profile becomes virtually undistinguishable from the weak adsorption profile with the same ξ. However, the values of the amplitudes (A in Eq. 5.39) differ by 30% ($A = 0.2$ and $A = 0.14$ for the weak and exponential profile, respectively). Qualitatively speaking, σ_b and σ_t represent the lower length scale for $l_{1\mathrm{A}}$ and $l_{1\mathrm{B}}$ that can be resolved experimentally.

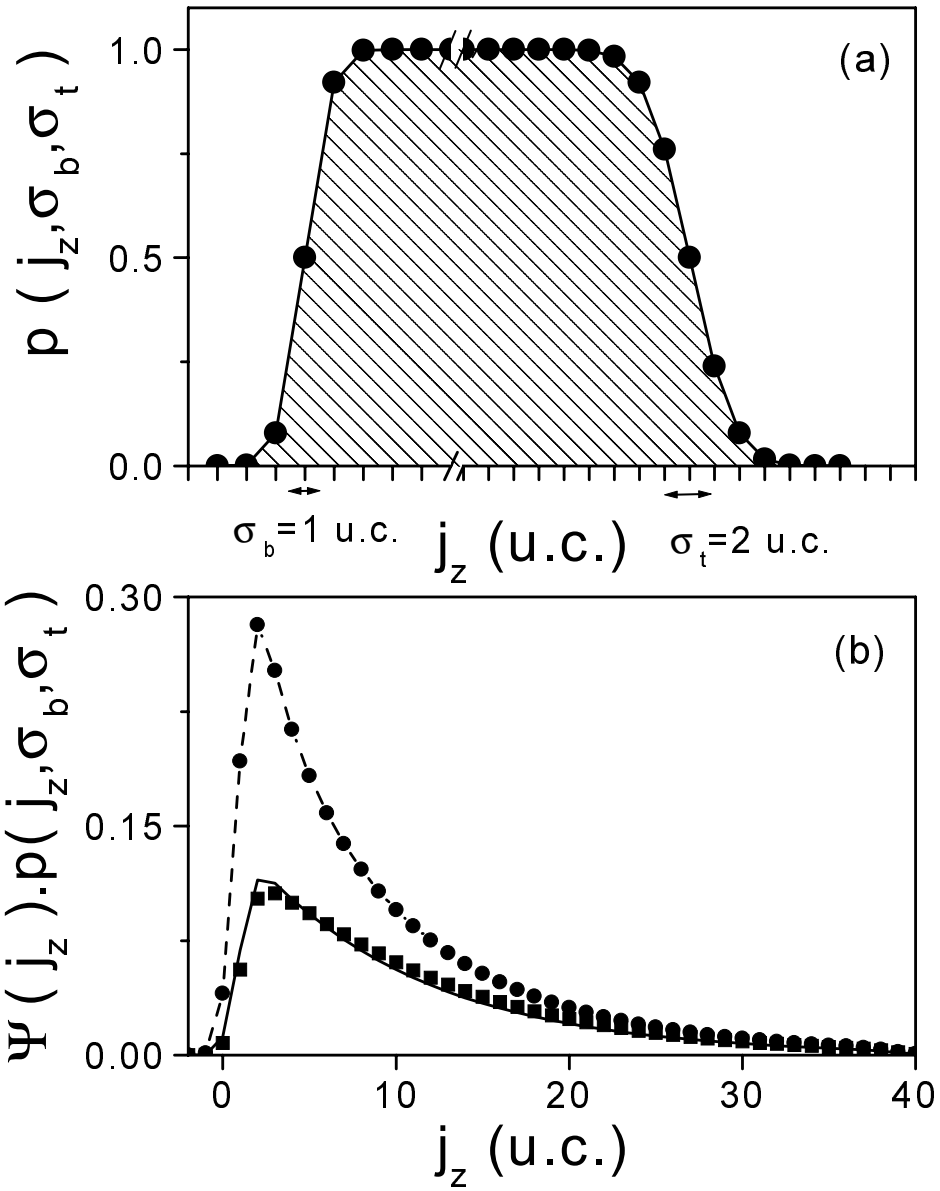

Figure 5.11: Roughness and its influence on $\Psi(z)$ a) Overall occupation probability function $p(j_z, \sigma_b, \sigma_t)$ for $\sigma_b = 1$ u.c. and $\sigma_b = 2$ u.c.. b) "Effective" adsorption profile $\Psi(z) \cdot p(j_z, \sigma_b, \sigma_t)$ for strong ($l_1 = \xi/16$) and weak ($l_1 = \xi$) adsorption, printed as dots and squares, respectively.

Chapter 6

Growth and characterization of single crystal FeCo thin films

6.1 Introduction

A large number of FeCo samples have been prepared during this work using molecular beam epitaxy (MBE) to obtain single crystalline FeCo films. MBE was chosen since it offers detailed control over the basic growth parameters, i.e. the growth-temperature and the growth-rate. Furthermore, a MBE system contains various electron-probe-based instruments (LEED, AES, RHEED, see below) to verify in situ the cleanness and structure of the topmost atomic layers of the sample. However, the technical effort is large since MBE relies on ultrahigh vacuum technique and MBE systems require continuous maintenance. Single-crystal, epitaxially-polished MgO has been chosen as substrate. Previous growth studies [42] indicate that an epitaxial relationship exists between the MgO-substrate and the FeCo-film. For an MgO(001) orientation the deposited FeCo-films are oriented along FeCo(001). A top view of the MgO(001) surface and the FeCo(001) surface is shown in Fig. 6.1. A side view of the FeCo/MgO interface is shown in Fig. 5.5.

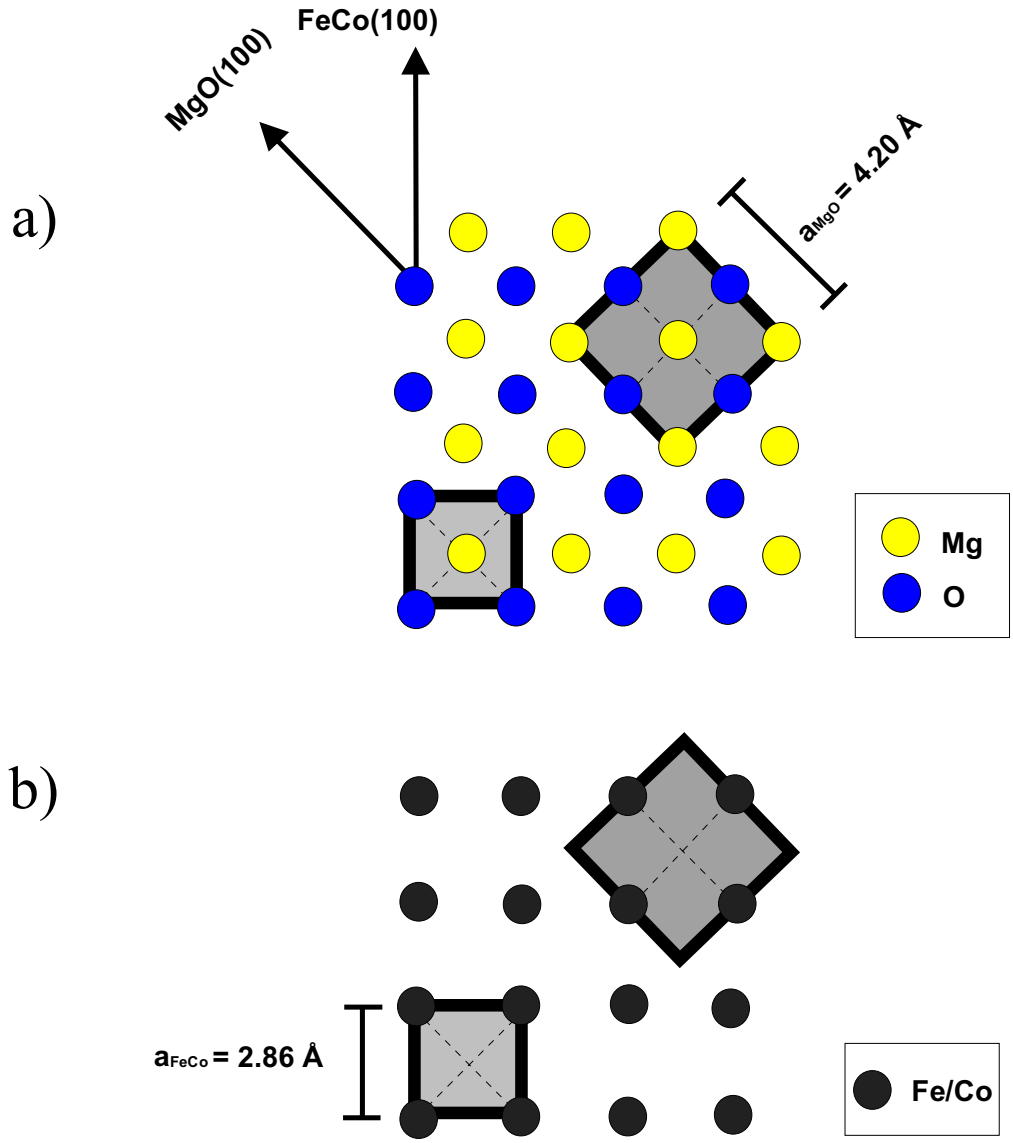

Figure 6.1: a) The MgO surface. Indicated are the FeCo and MgO unit cells and the crystallographic directions along the surface. b) The FeCo surface. The lattice mismatch is between FeCo and MgO is $\sim 4\%$.

One reason why MgO was chosen as substrate is the stability of the MgO/FeCo interface against atomic interdiffusion at elevated temperatures. The interface stability is crucial for the x-ray scattering experiments which are performed at temperatures up to 800 ^{o}C to cover the interesting temperature range needed to explore the order-disorder phase transition. In the course of the research it turned out that the different surface energies of FeCo and MgO promote a dewetting of the FeCo-films from the MgO substrate. To suppress this dewetting transition, capping layers of MgO have been deposited on top of the FeCo films, as reported below.

6.1.1 Thin film growth

Table 6.1 summarizes the prepared samples that are mentioned in the text. The respective instrument and the experimental technique that have been applied are included in the table.

name	D(FeCo)	cap	instrument	method
mbe40			BW6	Laue
mbe47	170 Å		Troïka I	Laue, in plane
mbe61	170 Å		SEM	(Fig. 6.10)
mbe66			light microscope	
mbe67	180 Å		Troïka I	Laue (Fig. 6.8)
mbe73	350 Å		Troïka I	Laue
			W1	Laue resonant
mbe85	7000 Å		Dragon BL	dichroismus
mbe87	50 Å	Pd	Troïka II	reflectivity + diffuse
				(Fig. 6.11)
mbe104	140 Å		Troïka I	Laue (Fig. 6.12)
mbe118	100 Å		SEM	(Fig. 6.9)
mbe139	100 Å	MgO	Troïka I	Laue
			CEMO	Laue resonant
			W1	Laue resonant (Fig. 7.7)
mbe140	50 Å	MgO	Troïka I	Laue resonant
			NSLS	mag. x-ray
mbe155	320 Å	MgO	Troïka I	Laue

Table 6.1: List of FeCo(001) samples grown on MgO(001), including the nominal FeCo film thickness.

The samples were grown using a molecular beam epitaxy (MBE) system manufactured by Riber. The base pressure of the growth chamber is $1 \cdot 10^{-11}$ mbar. During the growth, the base pressure increased up to $2 \cdot 10^{-10}$ mbar. The growth chamber is equipped with two electron beam guns to evaporate iron and cobalt at the same time. The deposition rate is measured with a quartz microbalance. After the precise deposition rate is realized for both components, the partial pressure from the two components is kept constant by using the signal of a mass spectrometer manufactored by Hiden. The stoichiometry was cross checked by growing a 1000 Å film, thick enough to use an x-ray fluorescence microprobe. The agreement was better than 1%. Further, the thickness was cross checked by reflectivity measurements. The thickness deviation from the nominal value was typically less than 10%. For some films a MgO or Pd capping layer was grown with the same evaporator.

The sample is radiation heated from the backside by a tantalum wire. Because MgO itself is transparent, a niobium film of 3000 Å is deposited on the backside of the sample to absorb the radiation. Below 500 °C the temperature is measured with a thermocouple spring loaded against the backside of the sample. Above 500 °C an optical pyrometer ($\Lambda = 900$ nm) manufactured by Maurer is used. Different suppliers have been used for the MgO substrates. The best obtainable quality (HTC) had a maximum misorientation $\leq 0.2^o$ and a root mean square roughness ≤ 4 Å. The substrates were introduced into the system and heated up to 900 °C for 12 h. Afterwards, the surface crystallinity and cleanliness was checked by low energy electron diffraction (LEED) and Auger electron spectroscopy (AES) measurements. These electron-probe-based techniques are very surface sensitive, the measurement signal originates from the topmost layers of about 10 $\mathring{A}$ of the sample. All MgO substrates showed a sharp LEED pattern indicating a single crystalline surface and a strong oxygen peak in the AES spectra. The main contamination observed with AES was sulfur. To improve the sur-

face purity the MgO substrates were heated in an oxygen partial pressure of $1 \cdot 10^{-4}$ mbar or sputtered with Argon at 1kV. However, no significant sulfur reduction was observed. During the growth, the surface morphology and crystallinity was characterized by a reflection of high energy electron diffraction system (RHEED) manufactured by Staib.

6.1.2 In situ analysis (LEED, RHEED, AES)

For Fe growth on MgO it has been observed that different growth modes are possible, depending on the growth temperature[106, 107]. At a low growth temperature, the films are smooth but the crystallinity is low. At higher growth temperatures, the films are no longer closed but islands form. For FeCo on MgO, 280 °C is a reasonable growth temperature. In situ reflection of high energy electron diffraction (RHEED) shows directly after starting the growth process with a total rate of 1 Å/ *sec* well-defined peaks, indicating that the first atomic layer is epitaxial. After several layers, streaks begin to form on the RHEED monitor, indicating a closed film. After growth the film is annealed at temperatures equal or above 500 °C. This produces sharp streaks, indicating a low roughness of few atomic layers and good crystallinity of the surface. The RHEED pattern is shown in Fig. 6.3. Fig. 6.2 shows the RHEED pattern of the substrate. The broadening of the MgO streaks is partly due to charging effects.

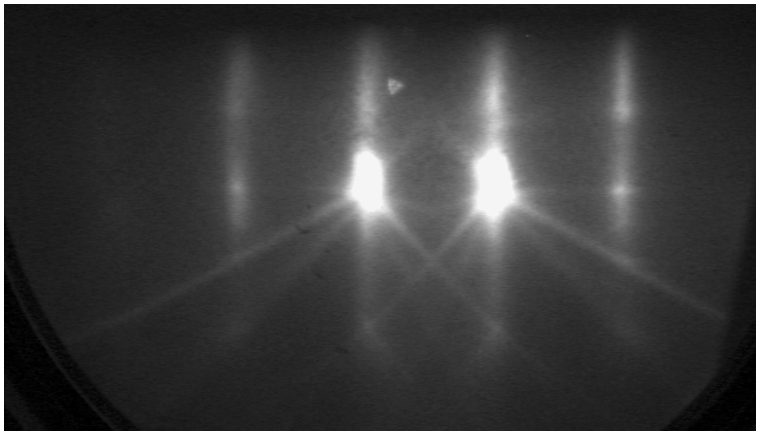

Figure 6.2: RHEED pattern of the MgO substrate before evaporation, oriented in a high symmetry direction. U=20kV.

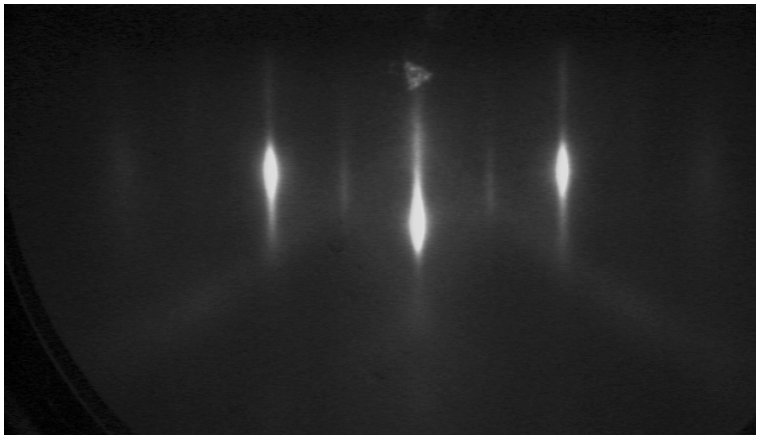

Figure 6.3: The RHEED pattern of a 350 Å FeCo film, after growth and being annealed at 500 °C. Same sample orientation as in Fig. 6.2.

LEED diffraction patterns (see Fig. 6.4) from the FeCo film reflect the

fourfold symmetry of the quadratic bcc unit cell, indicating a well-defined epitaxial relationship resulting in a single crystalline film. AES shows clear spectra of iron and cobalt after growth. No oxygen peak is obverved, demonstrating that the film is closed. A small amount of carbon is also present, probably due to the annealing process. This surface contamination may be removed by moderate argon sputtering at 1 keV for 10 minutes.

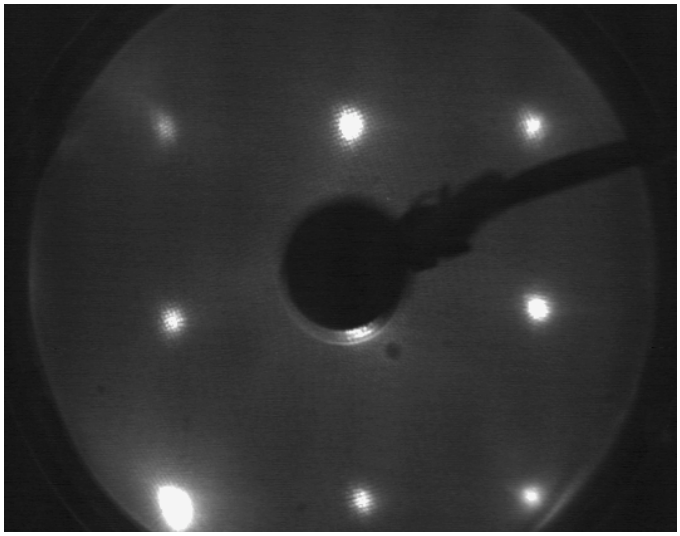

Figure 6.4: The LEED pattern of an 100 Å FeCo film, after growth and being annealed at 750 °C for 30 min. This is the same sample as Fig. 6.2.

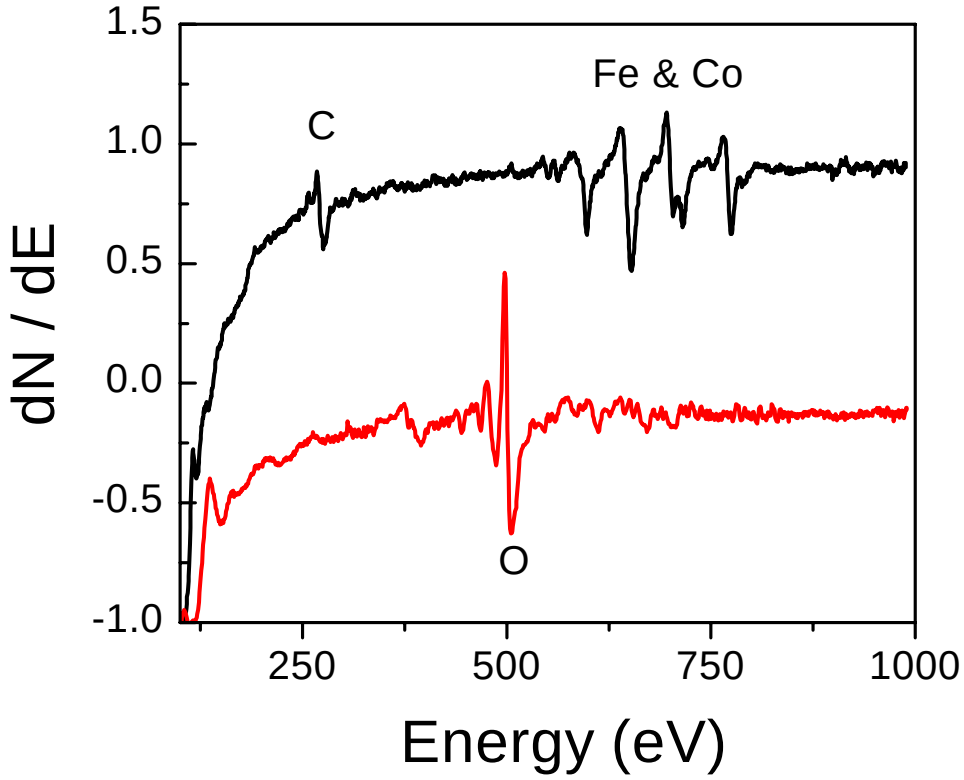

Figure 6.5: Bottom curve: AES spectra of a bare MgO substrate showing strong oxygen peaks at around 500 eV. Top curve (shifted): AES spectra of an 100 Å FeCo film after being annealed at 750 °C during a measurement campaign at HASYLAB.

For some films an MgO capping layer was grown. MgO is evaporated from a powder target with an electron beam evaporator. The rate is 1 Å/ sec and the growth temperature is room temperature, as employed in recent studies of MgO(001) growth on metal surfaces [108]. The LEED pattern of the MgO cap confirms the 45^o epitaxy (see Fig. 6.1). The larger spot diameter with respect to the LEED pattern obtained from the FeCo film surface indicates that the crystallinity is worst than for the FeCo films. From the RHEED pattern recorded during the deposition process, it appears that

after depositing about 100 Å of MgO, the MgO-cap becomes structurally disordered.

6.2 Ex situ analysis

6.2.1 X-ray reflectivity

After growth, the samples have been transferred into a transportable UHV chamber, equipped with two ion getter pumps. The base pressure of these chambers was lower than $1 \cdot 10^{-9}$ mbar. X-ray reflectivity measurements covering a dynamical range of 6 orders of magnitude were performed using a laboratory x-ray source to ensure that the film is closed and the interface roughness is only a few Å and no interdiffusion between the substrate and the film takes place [109]. Figure 6.6 shows by way of example the x-ray reflectivity from a nominally 100 Å FeCo thin film with a nominally 1000 Å cap. The broad intensity oscillations are from the FeCo film, the thin ones are from the MgO capping. The x-ray intensities are analyzed with the Parrat formalism [110]. The fit is shown as a straight line in figure 6.6. For the example shown here a thickness of 103.7 Å for the FeCo film and 1202 Å for the MgO cap was obtained. The FeCo film thickness is reasonably close to the nominal value of 100 Å. The fit gives a roughness of $\sigma = 1.5$ Å for the MgO substrate / FeCo interface and $\sigma = 2.3$ Å for the FeCo surface. The roughness depends crucially on the initial roughness of the substrate.

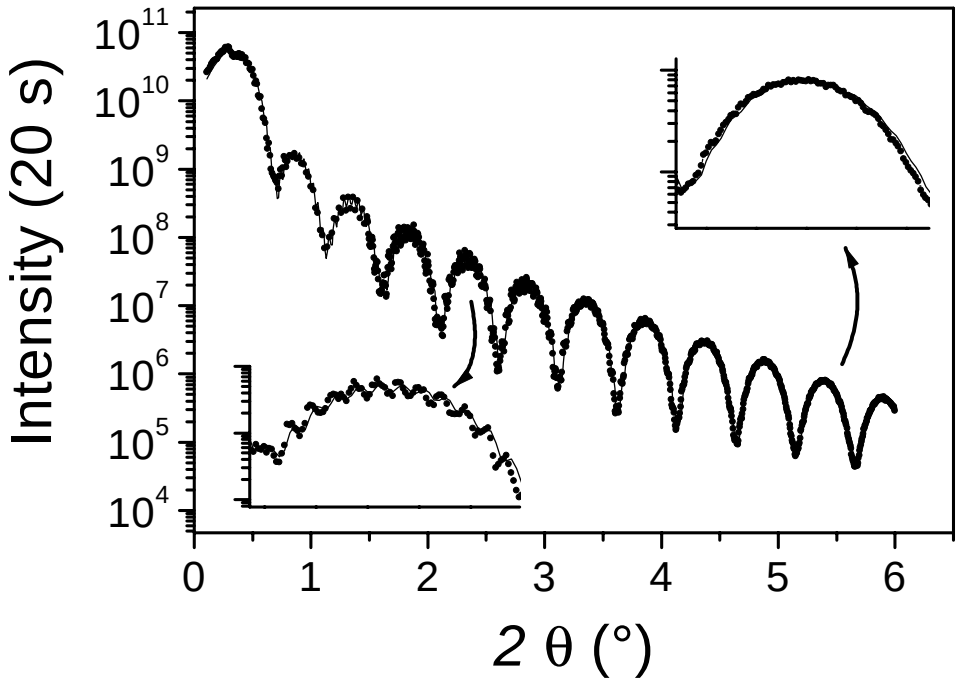

Figure 6.6: X-ray reflectivity curves for a FeCo film with MgO capping layer, measured at room temperature. The solid line shows a simulation (see text).

6.2.2 Laue oscillations

As a next step, the fundamental FeCo(002) reflection is recorded according to the scattering geometry depicted in Fig. 5.1. The data were collected using different instrumental configurations; whereas the thin film was measured near the Co edge (1.67 Å) in combination with an energy dispersive detector (silicon diode) in order to discriminate against fluorescence radiation, the thick film was measured using a wavelength of 0.93 Å with a conventional scintillation counter (NaJ). Thermal diffuse scattering and general background have been determined by rocking scans and subtracted. Fig. 6.7 shows the data set. The fit of the Laue oscillations (solid line in Fig. 6.7) gives a slightly larger thickness than the reflectivity, but the difference is within

the small roughness of 5 Å and therefore not significant. This indicates that the films are crystalline from the bottom to the top. This is a result of the well-chosen growth temperature ($T_g = 280$°C).

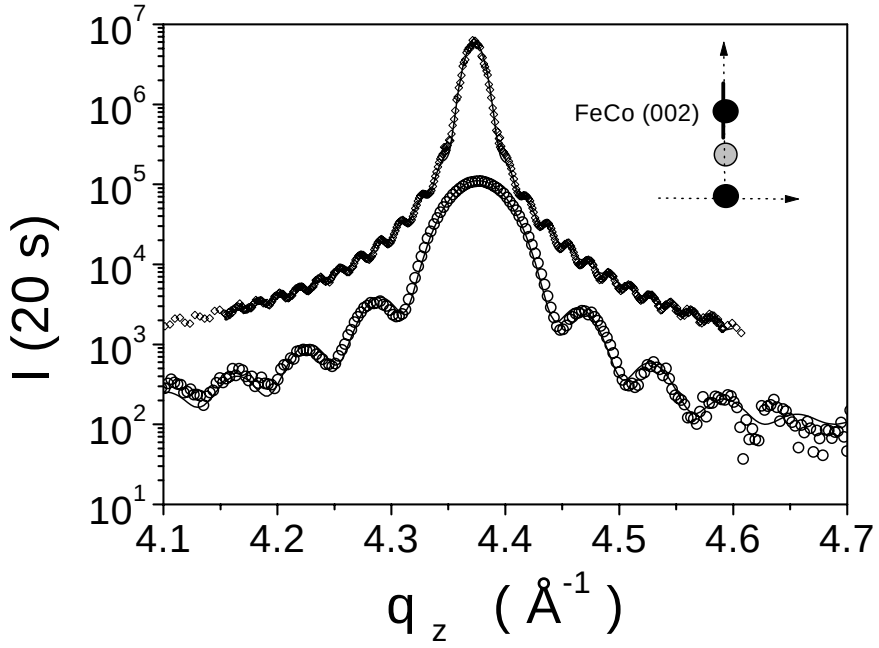

Figure 6.7: FeCo(002) Laue oscillations. open diamonds: 121 unit cells = 348 Å, T = 520 °C. open circles: 37 unit cells = 106.2 Å, T = 500 °C. The solid line shows a simulation.

6.3 Initial ordering after growth

After growth, most of the samples have been annealed at elevated temperatures before they were transferred to the x-ray sources. However, in one case a nominal 180 Å film was grown without annealing. In this film, no order is observed after growth. Fig. 6.8 shows different scans at the FeCo(001) position, For the as grown film, only a monotonous increasing contribution

from the MgO(001) CTR may be detected, indicating that the initial state of the FeCo film exhibits no B2 order. Now the temperature is increased in steps of 50 °C. At 650 °C, first indications of ordering were observed, giving very broad features in the scattering pattern. The first clear peak was seen at 690 °C. At 743 °C, asymmetric Laue oscillation were observed. Whereas the FeCo(002) reflection in Fig.6.7 contains information about the bcc structural order, the line shape of the FeCo(001) reflection is given by the chemical order profile. Therefore the oscillation at the FeCo(001) reflection suggests that a well-defined stacking sequence of the type Co-rich / Iron-rich / Co-rich / ... has formed throughout the FeCo film. Above 743 °C, the order disappears, indicating that T_c has been crossed.

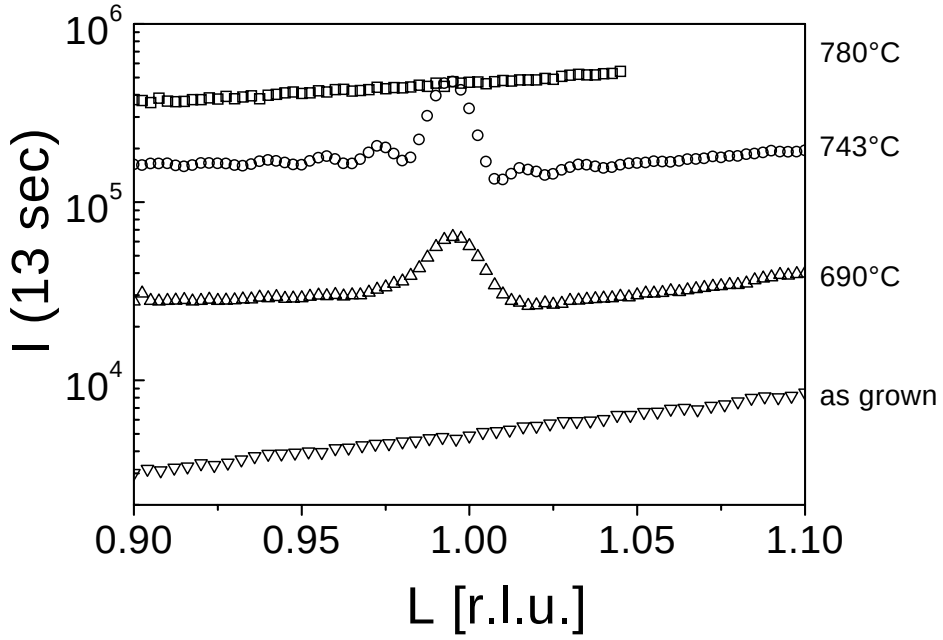

Figure 6.8: Evolution of the B2 order in FeCo in a nominally 180 Å film, grown at 280 °C. To determine the order, L scans at the FeCo (001) positions are performed and the temperature is increased.

6.4 High temperature behavior

6.4.1 Dewetting

When the non-MgO-capped FeCo-films are heated above 800°C for several minutes the entire morphology of the film changes quite dramatically, especially for films with a thickness less than 180 Å. One can detect the transformation by eye inspection, as the film surface is no longer mirror-like. In Fig. 6.9, an electron micrograph from an 100 Å film (MBE118, see Table 6.1) is shown. The film has been heated to 800 °C for several minutes. Afterwards a pronounced finger-like structure is observed.

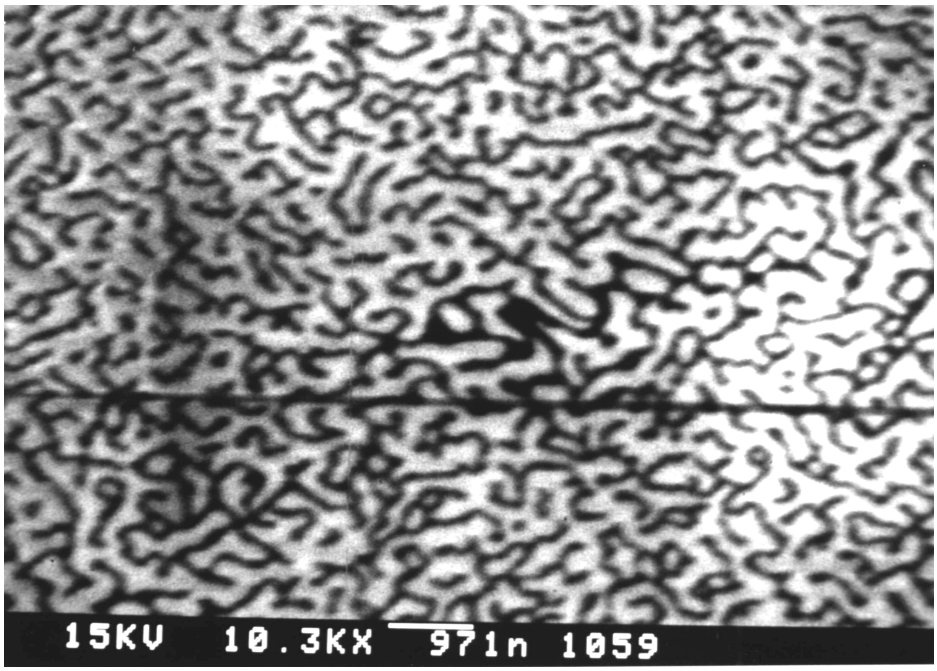

Figure 6.9: Secondary electron micrograph from a nominal 100 Å film after heating to 800 °C for some minutes. The dark areas are electron-rich areas (FeCo). The white bar is 971 nm. The black stripe is from calibrating to adjust the contrast.

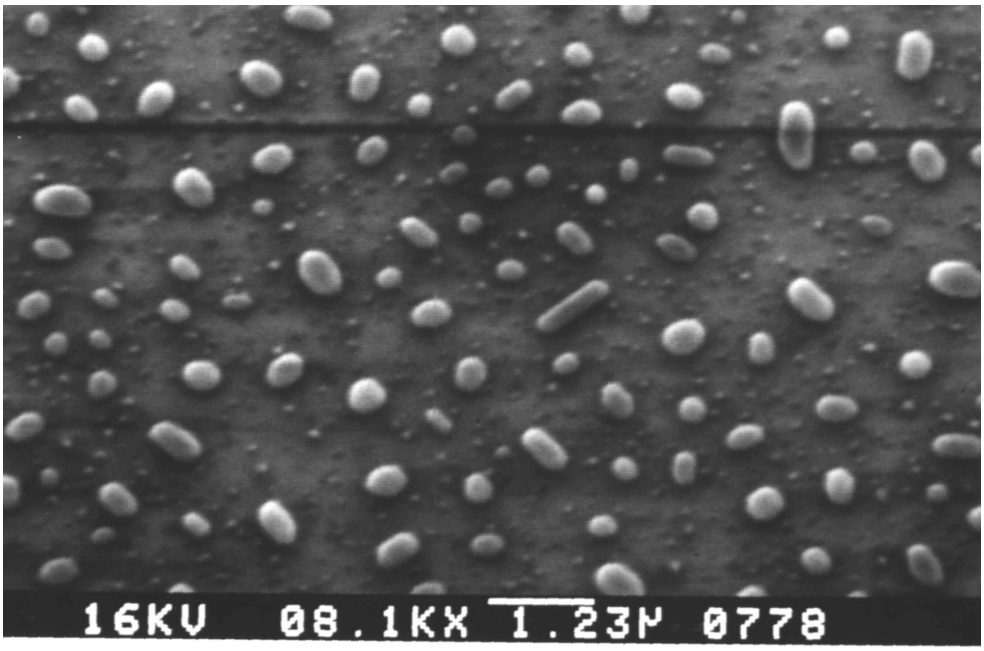

Figure 6.10: Backscattering electron micrograph from a 170 Å film after heating to 1200 °C for several minutes. The bright drops are electron-rich areas (here: FeCo). The white bar is 1230 nm. The average island size is about 4000 Å.

Furthermore, in the AES spectra the Fe and Co signals drop strongly after the heat treatment and the oxygen substrate peak recovers. Since AES is sensitive to a few monolayers, this supports the assumption that a phase separation between the FeCo and the MgO takes place at the interface, yielding FeCo-enriched regions and bare substrate in between. This conclusion is consistent with LEED measurements: after the annealing the substrate reflections reappear.

It is quite instructive to see how the x-ray pattern is influenced by the phase separation. Figure 6.11 shows the reflected intensity from a nominal 50 Å FeCo-film after the annealing at 800 °C for several minutes and capped

with Pd after cooling down to room temperature. Slightly above the angle for total external reflection the reflected intensity reduces down about four orders of magnitude. At larger angles intensity oscillations are observed. But rocking scans reveal that the scattering pattern is dominated by diffuse scattering [111, 112], including a broad component at the position where the specular peak is expected. This indicates a large roughness. The broad component can be modeled with a Gaussian line shape and its width Λ can be converted into a length scale ξ, describing the roughness correlation along the surface. For this sample shown one obtains $\xi = 1.7$ μm, suggesting that the initially continuous film is now structured on a μm-scale (compare Fig. 6.9).

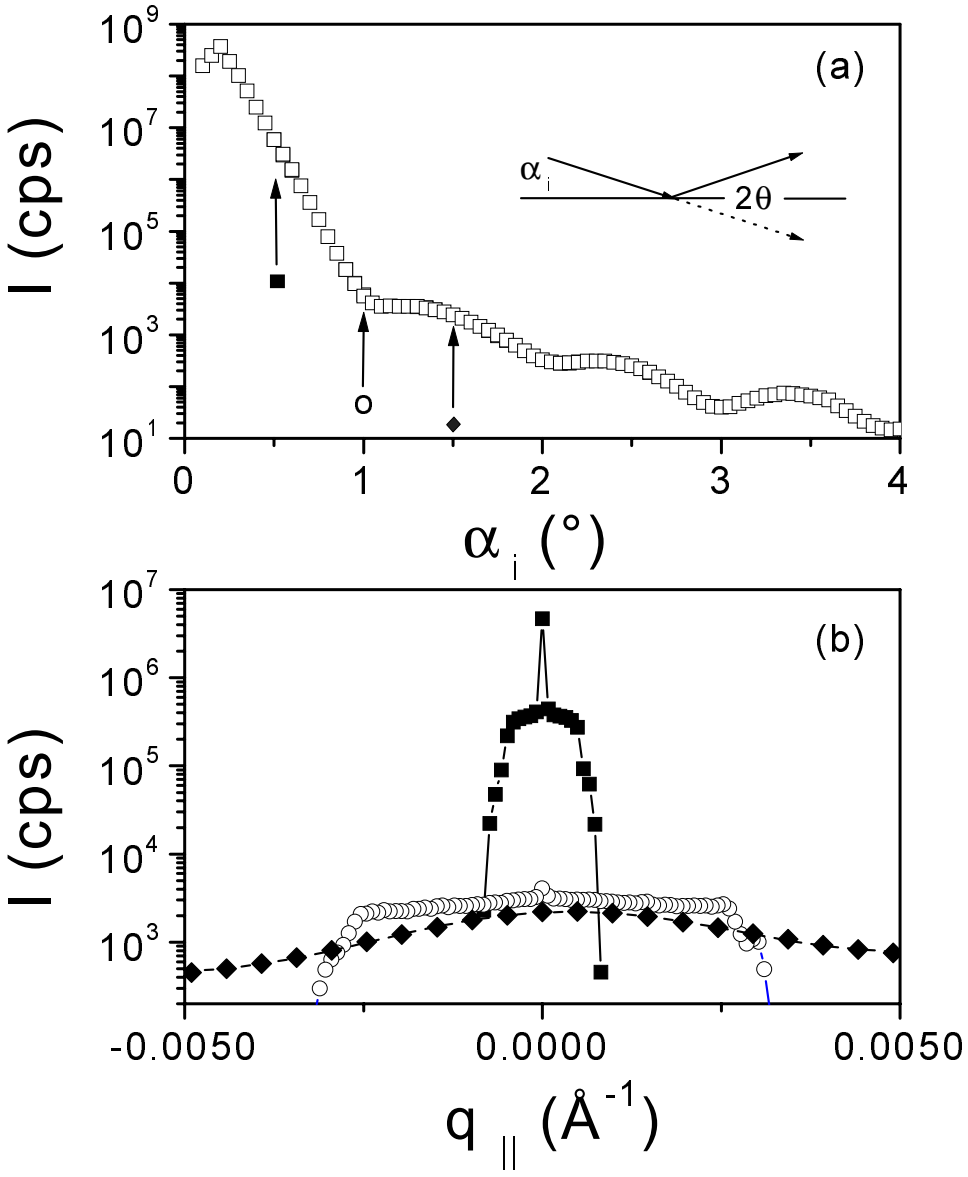

Figure 6.11: (a) X-ray reflectivity as superposition of specular and diffuse intensity. The arrows indicate the different angles where rocking scans have been performed. (b) Rocking scans. Solid squares: $2\theta = 1°$, open circles: $2\theta = 2°$, the solid line are a guide to the eye. Diamonds: $2\theta = 3°$. The dashed line is a fit with a Gaussian line shape.

Fig. 6.12 shows the same scenario for a 140 Å film, but with the fundamental FeCo(002) peak measured before and after the annealing. Before annealing the film is continuous, which can be easily seen from the 143 Å thickness oscillations. After the annealing a narrow peak emerges whose width suggests single crystalline islands with an average thickness of 600 Å. This is equivalent to an increase by a factor of 4.2 with respect to the initial thickness of 143 Å. The intensity in the central part increased by a factor of 68. Assuming that the scattered intensity is proportional to N^2 (i.e., that the islands are single-crystal) this indicates that the island size increased in all tree dimensions by a factor of 4.

The above observations which include island formation and bare substrate in between suggest that the phase separation can be classified as a dewetting process. An additional MgO capping layer may suppress the dewetting, since in this case the interface energy balance of the two interfaces cancel. This is reported below.

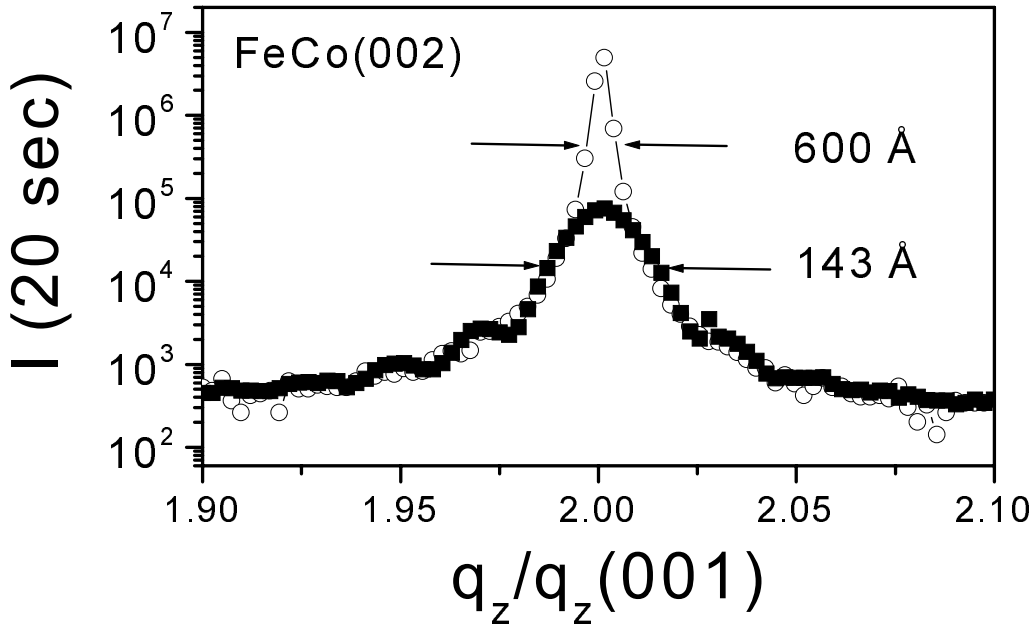

Figure 6.12: A q_z-scan trough the FeCo(002) reflection. Before the annealing Laue-oscillations of an 143 ÅFeCo-film are observed (solid squares). After annealing, a narrow peak emerges (the solid line is a guide to the eye).

6.4.2 Morphology stabilization by MgO capping

An additional capping layer of MgO was deposited on the thinner FeCo films, using an electron beam evaporator as reported in [113]. This capping layer suppressed all tendencies of FeCo-dewetting. No changes of the film morphology are observed at all after exposing a capped 100 Å film to about 720 °C for two weeks, as shown in Fig. 6.6.

This is possible for the following reason. The surface energy of FeCo ($\gamma_{\mathrm{FeCo}} \sim 3$ J/m^2) [114] is higher than the surface energy of MgO(001) ($\gamma_{\mathrm{MgO}} =$

0.9 J/m^2) [115]. Young's equations read [116] p.108

$$\begin{aligned} \gamma_{\mathrm{MgO}} \cdot \cos\ \theta_{\mathrm{MgO}} &= \gamma_{\mathrm{FeCo}} - \gamma_{\mathrm{FeCo/MgO}} \\ \gamma_{\mathrm{FeCo}} \cdot \cos\ \theta_{\mathrm{FeCo}} &= \gamma_{\mathrm{MgO}} - \gamma_{\mathrm{FeCo/MgO}} \end{aligned} \tag{6.1}$$

where θ_{MgO} and θ_{FeCo} are the contact angles for the equilibrium line shapes of MgO on FeCo and FeCo on MgO, respectively. $\theta = 0^o$ is equivalent to complete wetting; $\theta = 180^o$ is equivalent to dewetting. For the prediction of the wetting behavior one needs to know the interface energy $\gamma_{\mathrm{FeCo/MgO}}$, such as from ab-initio calculations or from experimental measurements. In general this requires a detailed knowledge of the atomic arrangement at the interface; this is a current field of experimental and theoretical research (see Refs. [117, 118] and references therein). Further complications arise due to microscopic defects which enhance the adhesion of metals on oxides significantly [119]. However, Li *et al.* calculated the interface properties of Fe on MgO(001). They found little direct chemical interaction [104], i.e. the electron transfer is less than 0.05 e/atom. Assuming therefore $\gamma_{\mathrm{FeCo/MgO}} \ll \gamma_{\mathrm{MgO}}$, the energy balance in Young's equation reads

$$\begin{aligned} \gamma_{\mathrm{MgO}} \cdot \cos\ \theta_{\mathrm{MgO}} &\approx \gamma_{\mathrm{FeCo}} \\ \gamma_{\mathrm{FeCo}} \cdot \cos\ \theta_{\mathrm{FeCo}} &\approx \gamma_{\mathrm{MgO}}, \end{aligned} \tag{6.2}$$

yielding

$$\begin{aligned} \theta_{\mathrm{MgO}} &\lesssim 0^o \\ \theta_{\mathrm{FeCo}} &\approx 70^o, \end{aligned} \tag{6.3}$$

which is in good agreement with the observation that MgO wets FeCo completely but that FeCo wets MgO incompletely (Fig. 6.10). Of course these estimates are rather qualitative, however, it may be interesting in the future to study the dewetting mode in more detail [120]. The stabilization of

ferromagnetic nanostructures during annealing and oxidation by means of MgO-capping may be an important technological application of these observations.

Chapter 7

X-ray study of the ordering phenomena in FeCo films

7.1 Introduction

After the growth and characterization of the FeCo samples at the laboratory, they were transferred into mobile UHV-chambers without exposing the samples to the atmosphere. This preserves the cleanliness of the surface. The UHV-chambers are equipped with battery-powered ion pumps, which allows transporting the samples *in vacuo* to the different synchrotron radiation laboratories in Grenoble and Hamburg. Synchrotron x-ray radiation is needed to record the weak x-ray scattering signals from these thin films while maintaining the resolution needed to reconstruct the temperature- and depth-dependent order parameter profiles from the diffraction pattern.

7.1.1 Temperature control

The heating station is depicted in Fig. 7.1. A Ta-filament heats the sample via radiation. The sample (10 mm $\cdot$ 10 mm) is mounted onto a transferable

Mo or Ta holder. To reach a sample temperature of 800°C, it is important that the sample has full view of the heater, therefore a rectangular opening (9 mm · 9 mm) was cut in the sample holder. Since MgO is transparent for visible and infrared light, a niobium film of ≈ 7000 Å was deposited onto the backside of the substrate prior to growth in order to increase the heat absorption. The typical heating power was 80 W, generated from a DC power supply. The Nb film also enabled the use of an optical pyrometer to monitor the sample temperature for temperatures above 500°C. The optics of the pyrometer focus an area of about (2 mm · 2 mm). Based on our previous experience [41] a pyrometer is the most reliable temperature measurement method since it excludes the long term drifts and contact changes which are usually observed with a thermocouple at high temperatures for several days. However, the heating station is also equipped with a spring-loaded W/Rh thermocouple. A feedthrough and cables of the same material as the thermocouple are used to read out the thermovoltage with a temperature controller. The temperature of the Cu clamps of the temperature controller is measured and corrected. The thermocouple was used in the temperature region up to 500 °C. The temperature controller was remotely operated by a PC via an RS232 interface.

7.1.2 Chamber configurations

Mobile UHV chambers were taken to each synchrotron experiment. The different possible configurations are depicted in Fig. 7.2.

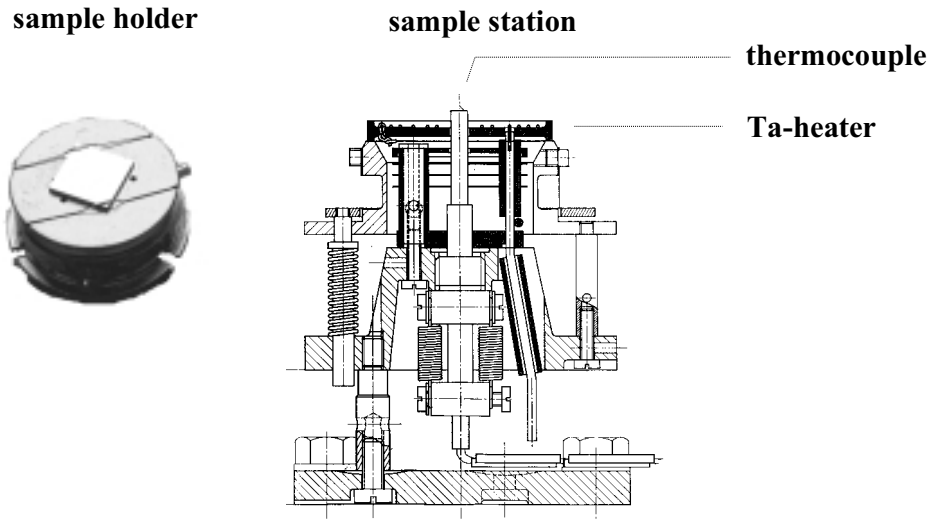

Figure 7.1: The Mo/Ta sample holder and the heating station. The diameter of the sample holder is 2.54 cm. A rectangular substrate (10 mm · 10 mm) is fixed with Ta-wires.

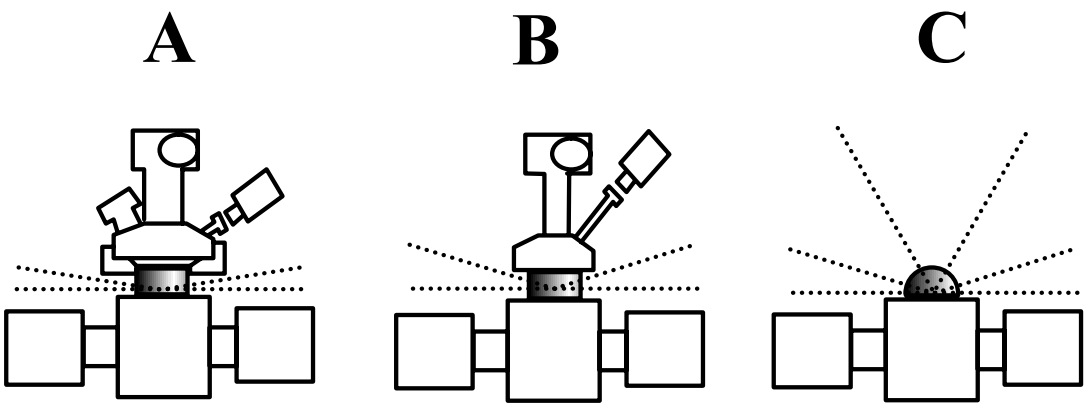

Figure 7.2: The different configurations of the UHV chambers as described in the text.

All chambers are equipped with beryllium windows. Since the adsorption for the typical x-ray wavelength used in the experiments (1 Å $<\lambda<$2 Å) is small for Be, this material is a common choice for UHV-chambers that have to give access to an external x-ray beam. Two shapes are available; a cylindrical shape and a dome-like shape. Configuration A (see Fig. 7.2) is a "classical" in-plane chamber for grazing angle diffraction: the cylindrical beryllium window allows a 360° in-plane access so that all Bragg reflections in the sample surface ($q_z = 0$) can be measured. The chamber has an option for sputtering, as well as several free ports which can be used to dose the sample with N_2 or oxygen. A disadvantage of this chamber is that only a few Bragg reflections along the surface normal can be accessed, since the maximal angle between the sample surface and the x-ray beam is restricted to 10° ($2\theta = 20^o$). Using a wavelength of $\lambda = 1$ Å, only the FeCo(001) reflection is accessible [41] in this configuration. This chamber was usually used for test samples; for example, the data shown in Fig. 6.8 have been taken using this chamber.

Configuration B (see Fig. 7.3) is similar to A, but the maximal angle between the sample surface and the x-ray beam is enlarged to 20° ($2\theta = 40^o$). With $\lambda = 1$ Å the fundamental FeCo(002) and the superstructure FeCo(001) reflection are both accessible. Since the temperature-dependent measurement took usually one week per sample, the FeCo(002) reflection was used as a critical test of whether the structural properties of the film remain unchanged during this time. The experiment on the bare 350 Å FeCo(001) film has been performed using configuration B and $\lambda = 1$ Å.

As explained in section 6.4.2, some FeCo films have been capped with a MgO overlaver to enhance thermal stability. Another important advantage of this capping is that the MgO overlayer acts also as a protection against oxidation and contamination of the FeCo surface. For these samples, configuration C with a dome-shaped berillium window was used. To mount the

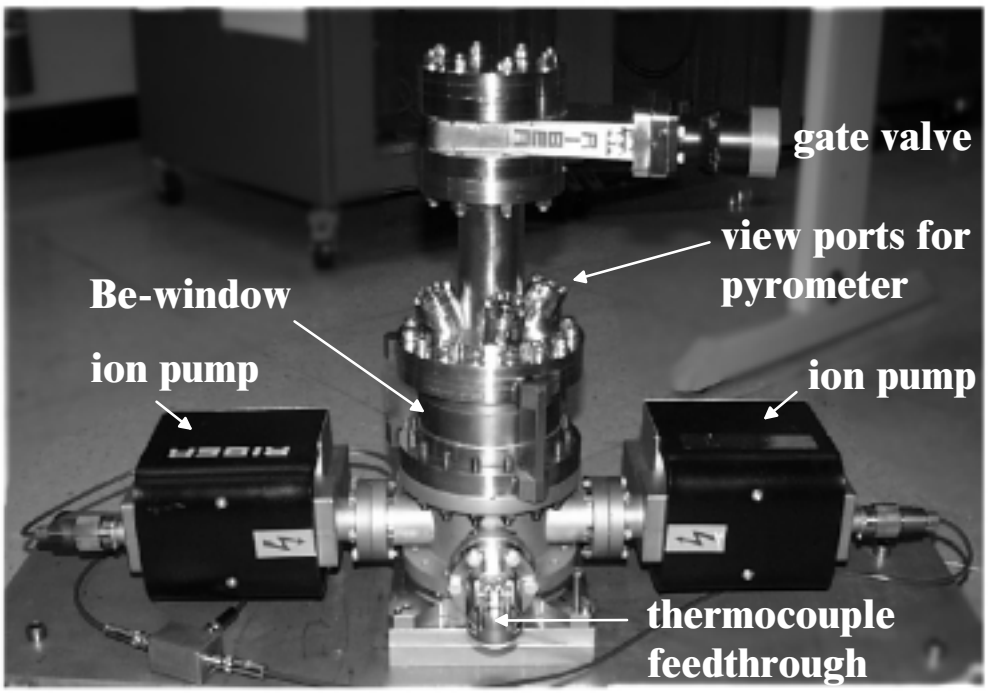

Figure 7.3: Photograph of the mobile UHV chamber B. The main UHV components are labeled.

sample the chamber had to be vented and a turbo molecular pump was used to generate the vacuum. The advantage of the dome chamber is that the entire half space above the sample horizon is accessible for the x-ray beam and therefore it was possible to enhance the scattering contrast between iron and cobalt by measuring close to the resonance edge at considerable longer wavelength ($\lambda \simeq 1.67$ Å, see Fig. 7.7). However, a pyrometer could not be used in this configuration.

7.2 Synchrotron beamlines

Most of the measurements have been done at the European Synchrotron Radiation Facility (ESRF) in Grenoble, France. The ESRF is a state-of-the art 3rd generation synchrotron. The electron storage ring is operated at 6 GeV; after injection the typical electron current is 200 mA with a lifetime of about 55 h. The experiments have been carried out at the general-purpose Troïka beamline, which is described below. Two experiments have been done at Hamburger synchrotron laboratory (HASYLAB) in Hamburg, Germany. This is a 2nd generation 4.4 GeV electron storage ring which operates with a typical electron current of 100 mA. The respective beamlines CEMO and W1 at HASYLAB are described briefly. Extensive information about the ESRF and HASYLAB can be found on their webpages [1].

7.2.1 Troika I

The Troïka I beamline at the ESRF is a multipurpose beamline that can easily be adapted to different kinds of experiments, e.g. surface diffraction, magnetic resonance or coherent diffraction. The FeCo-experiments have been done in the surface diffraction mode, which is described below.

Instrumentation

The Troïka I station is equipped with a horizontal diffractometer. Two horizontal turntables define the scattering angles and a third turntable carries the detector assembly. A vertical translation stage allows measurements in which the sample has to be kept in the horizontal plane. The sample stage is equipped with an x-y translation assembly and a double tilt stage with a range of $\pm 20^o$. The possibility to mount heavy equipment was the main cri-

[1] http://www.esrf.fr and http://www-hasylab.desy.de

teria for choosing the Troïka I beamline for these experiments, (see Fig. 7.4). The diffractometer is equipped with a vertical arm which provides a vertical scattering geometry with six-circle capability. This option has been used to carry out in-plane and out-of plane measurements with the same chamber configuration. The diffractometer is mounted on a platform that can be moved on air cushions in order to operate at different energies (7.5 keV <E <20 keV). Energy tuning includes movements of the diffractometer due to the single bounce monochromator, see Fig. 7.5. Adjustment of the scattering angles is fully computer controlled by the commercial software system SPEC [2]. Alignment of the x-ray optics was usually performed by Troïka scientist Dr. C. Detlefs.

The Undulator Source

At the Troïka beamline, the x-ray beam is generated by two undulators in series with a 38 periods. This results in a peak brilliance of $10^{19} \frac{\text{photons}}{\text{s} \cdot \text{mrad}^2 \cdot \text{mm}^2}$ at 0.1% bandwidth, for an electron current of 100 mA and a photon energy of 8 keV.

Monochromator

Troïka I is equipped with a UHV multi-crystal single bounce monochromator operating with four different monochromator crystals: diamond(111), diamond(220), beryllium(002) and silicon(111). The crystals are vertically stacked on a water cooled multi-crystal mount such that the momentum transfer vectors for all four crystals are parallel. The diamond crystals have a thickness of less than 500 μm. One crystal allows accessing the diamond(111) Bragg reflection in asymmetric Laue geometry and the second crystal uses reflection from (220) in symmetric Laue geometry. The diamonds have near-

[2] http://www.certif.com

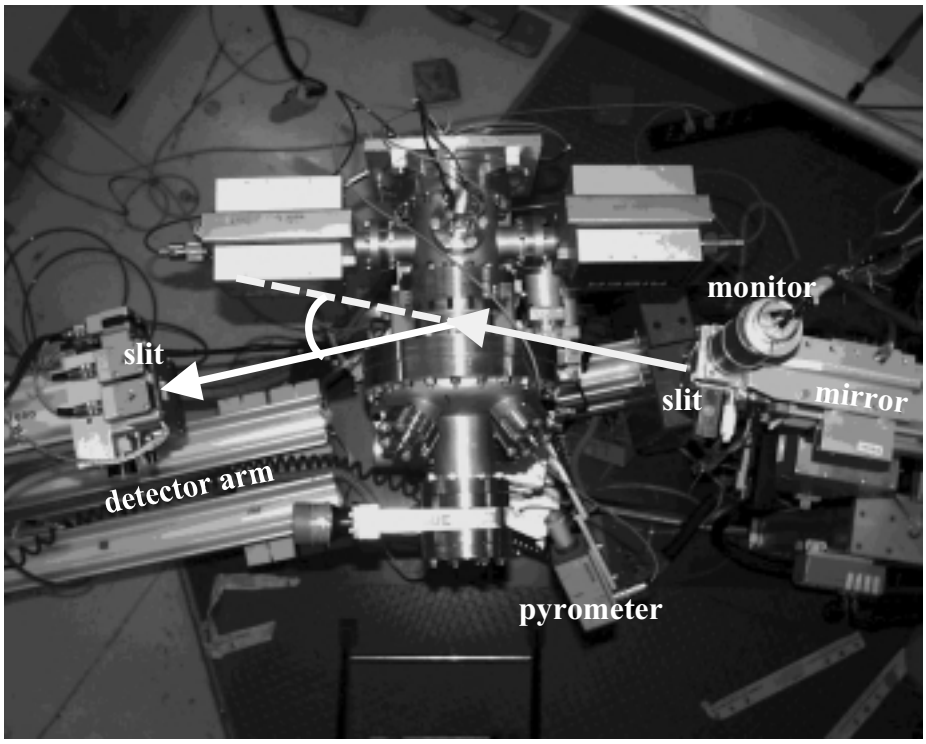

Figure 7.4: Top view on chamber A mounted with a vertical sample position on the Troïka I diffractometer. The indicated angle is 2θ, compare also to Fig. A.2.

perfect structural perfection with a rocking width of typically 0.002^o. At 9 keV, the angular and energy acceptances of the (111) diamond in the 35.5^o asymmetric Laue geometry are 12.7 μrad and $\Delta\lambda/\ \lambda = 3.6 \cdot 10^{-5}$. The angular emittance is 21.2 μrad. Further, a Si(111) crystal in symmetric Bragg geometry is available. Downwards, up to two flat Rh-coated Si mirrors are used to cut off higher harmonics.

Due to the complicated interplay between the undulator characteristics

and the limited scattering angles at the Troïka beamline, the best configuration for each experiment depends on the needed wavelength. Good results have been obtained with the dia(111) reflection in combination with a single reflecting mirror. The resulting beam size at the sample position is typically $2 \cdot 0.4$ mm^2 (HxV), and the total flux for this configuration is 10^{11} photons/s, as confirmed by a calibration measurement. The setup is shown in Fig. 7.5.

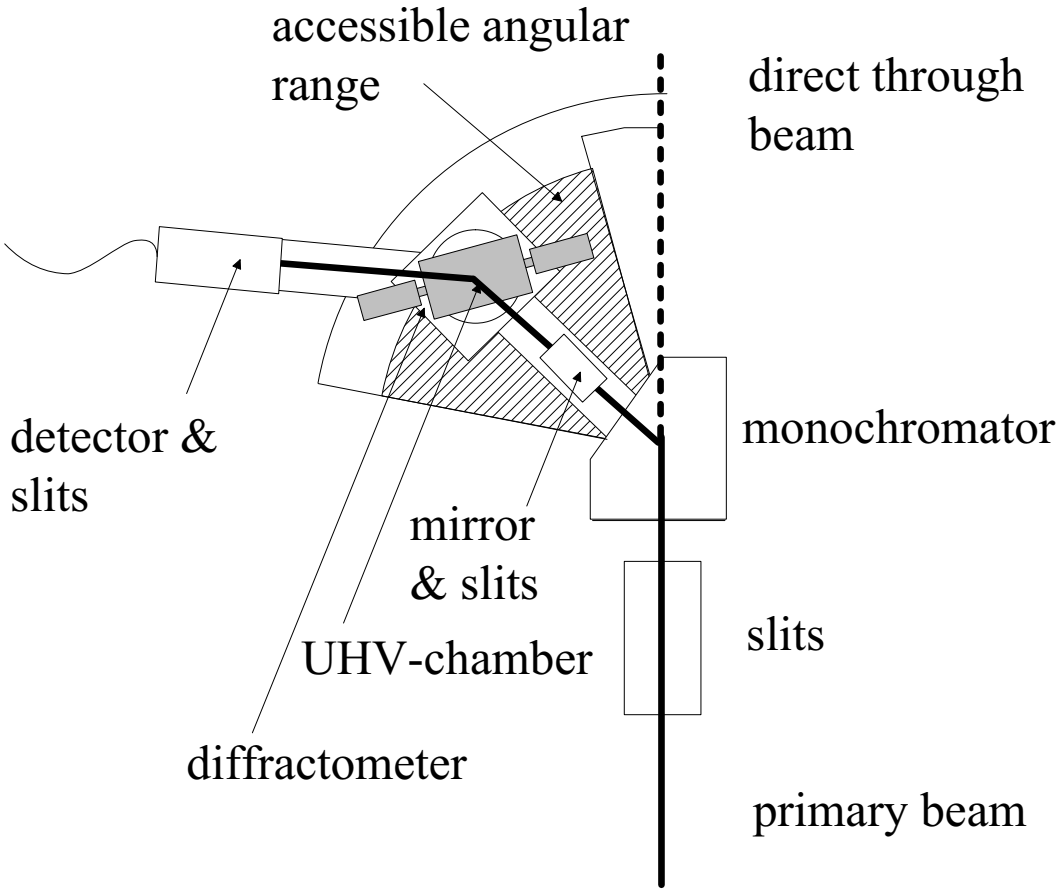

Figure 7.5: Troïka I setup for surface diffraction, as described in the text.

7.2.2 CEMO and W1

The CEMO beamline at HASYLAB is a multipurpose beamline which is used for x-ray diffraction, standing waves experiments, EXAFS, anomalous dispersion and magnetic x-ray scattering. A bending magnet is followed by a Pd-coated focusing mirror and a constant exit double bounce silicon monochromator, which makes energy tuning fast and easy. The resulting beam size at the sample position is typically (3 mm $\cdot$ 1 mm) (HxV) and banana-shaped. The intensity at the sample position is aproximately $3 \cdot 10^9$ photons/s when the electron current is 100 mA.

The diffractometer setup is similar to the Troïka I setup, but rotated by 90° to simplify vertical detector movements in order to avoid polarization losses. The W1 beamline is identical to the CEMO beamline, except that the bending magnet is replaced by a wiggler insertion device. The good counting statistics of the CEMO beamline result from the large divergence of the beam. Due to the large mosaic distribution of the thin FeCo films ($\approx$1°), the entire monochromatic beam coming from the focusing mirror contributes to the scattering signal and therfore no slits are needed to define the beam size. The excellent signal to background ratio at the CEMO beamline results from an energy dispersive detector[3] that was used to discriminate against fluorescence and other background radiation.

7.3 Contrast variation

Fe and Co are neighboring elements in the periodic table and the x-ray scattering contrast between them results only from one electron. Therefore, one might think of choosing a wavelength close to an absorption edge of Fe or Co to enhance the scattering contrast by fine tuning of the imaginary part

[3]The energy dispersive detector is a Röntec clone provided by Dr. B. Adams.

of the atomic scattering factor (f') (see Fig. 7.6).

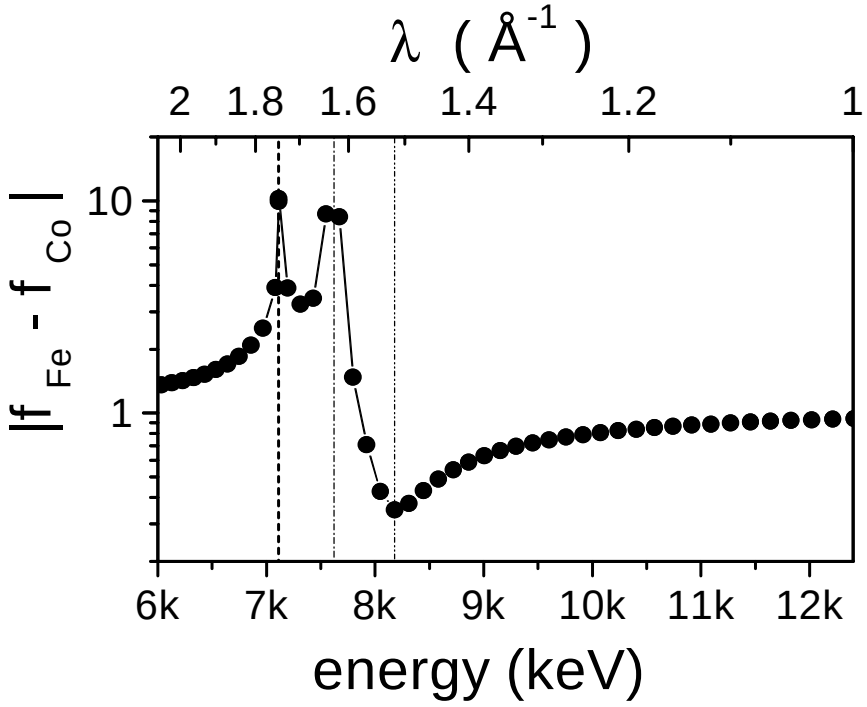

Figure 7.6: Scattering contrast between Fe and Co [92]. The vertical lines indicate the energies used for the measurement depicted in Fig. 7.7.

Fig. 7.7 shows a measurement at ambient conditions on a capped 100 Å FeCo film. Various interesting features are observed. First, the diffraction pattern exhibits Laue oscillations and a detailed fit will allow extracting the order parameter profile $\Psi(z)$, as will be shown later. The dash-dotted line reveals that a satellite peak minimum obtained during the 7.111 keV measurement equals a satellite peak maximum obtained during the 7.620 keV measurement. This is a clear hint that the observed intensity is influenced by the interference term given in Eq. 5.31. Further, a measurement using an energy of 8.178 keV has been carried out to minimize the contrast between Fe and Co (see Fig. 7.6). Indeed, no central maximum is observed since

the quadratic Laue term in Eq. 5.31 contributes negligibly to the scattering signal in this case. The contrast variation does not only influence intensities but it also affects the qualitative shape of the intensity distribution. This indicates that a detailed simulation of the measured intensities is mandatory for interpreting the data.

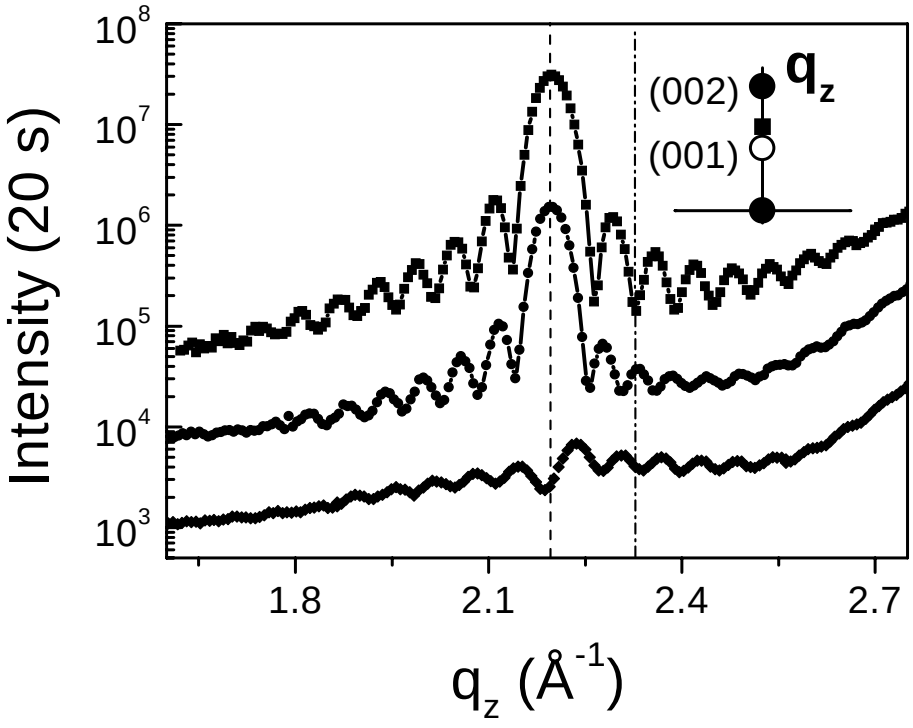

Figure 7.7: Intensity distribution for the MgO-capped 100 Å FeCo film around the FeCo(001) reflection at room temperature, using three different x-ray energies (squares = 7.111 keV, circles = 7.620 keV, diamonds = 8.178 keV). Strong interference effects are observed, as explained in the text. The lines are a guide to the eye, and the curves have been shifted along the y-axis, for clarity.

Due to the restrictions of the UHV transport chambers (see Fig. 7.2) and

the UHV transfer system, only MgO-capped samples can be measured under resonant conditions.

7.4 Overview of the experiments

Four of the samples listed in Table 6.1 have been measured at different temperatures in detail (mbe73, mbe139, mbe140 and mbe155). The FeCo-film thickness, the capping layer material, the synchrotron beamlines and the used wavelength and sample geometry are summarized in Table 7.1. The measurements cover the FeCo-film thickness range from 50 Å to 350 Å, or $21 < N < 110$, where N is the number of unit cells. They allow for a comparison of uncapped and MgO-capped samples. To obtain a qualitative overview of the measurements, five temperatures have been selected for each sample. The respective x-ray intensity distributions around the FeCo(001) superstructure reflection and an extended scan covering the fundamental FeCo(002) reflection are depicted in Fig. 7.8, Fig. 7.17, Fig. 7.21 and Fig. 7.26.

sample name	D(FeCo)	cap layer	instrument	λ	geometry
mbe73	350 Å		Troïka I 2/98	0.980 Å	sample vertical, chamber B
mbe139	100 Å	MgO	Troïka I 6/99	0.930 Å	sample vertical, chamber A (Fig. 7.4)
			CEMO 8/99	1.630 Å	sample horizontal, chamber C
mbe140	50 Å	MgO	Troïka I 12/99	1.743 Å	sample vertical, chamber C (Fig. B.2)
mbe155	320 Å	MgO	Troïka I 9/99	1.037 Å	sample vertical, chamber C

Table 7.1: The FeCo(001) samples that were studied at different temperatures in detail.

7.5 The uncapped 350 Å FeCo film

7.5.1 Raw data

Selected x-ray intensity distributions for a uncapped 350 Å FeCo film at different temperatures are shown in Fig. 7.8. For each temperature a scan along the surface normal through the FeCo(001) and FeCo(002) reflections is recorded. Both reflections (001 + 002) show Laue oscillations. Whereas the FeCo(002) oscillations are symmetric, the FeCo(001) reflections are highly asymmetric. This interference phenomenon results from the coherent growth of the FeCo film on the MgO substrate and this is discussed in more detail in Sec. 7.6.1. Increasing the temperature, the intensity in the center of the FeCo(001) reflection decreases and the oscillations disappear. This agrees with the expected disordering of the FeCo film (see Fig. 4.3). The observation that the oscillations do not broaden with increasing temperature indicates that the disordering is homogeneous over the whole thickness. At higher temperatures, a broad asymmetric peak with decreasing intensity and increasing width remains. This scattering resembles critical diffuse scattering, as reported in the experimental results [14]. However, this broad intensity is only extended in the q_z-direction, but it is delta shaped along the sample surface (see Fig. 7.9abc). The observed angular peak width of 0.34^o results from both the mosaic distribution of the film and the near-surface region of the substrate. This establishes that the broad intensity distribution at high temperatures is not critical diffuse scattering. In Fig. 5.8 it is demonstrated that this broad intensity is in fact the fingerprint of an exponentially-decaying order parameter profile $\Psi(z)$ localized at the MgO substrate. This is discussed in more detail in Sec. 7.6.2.

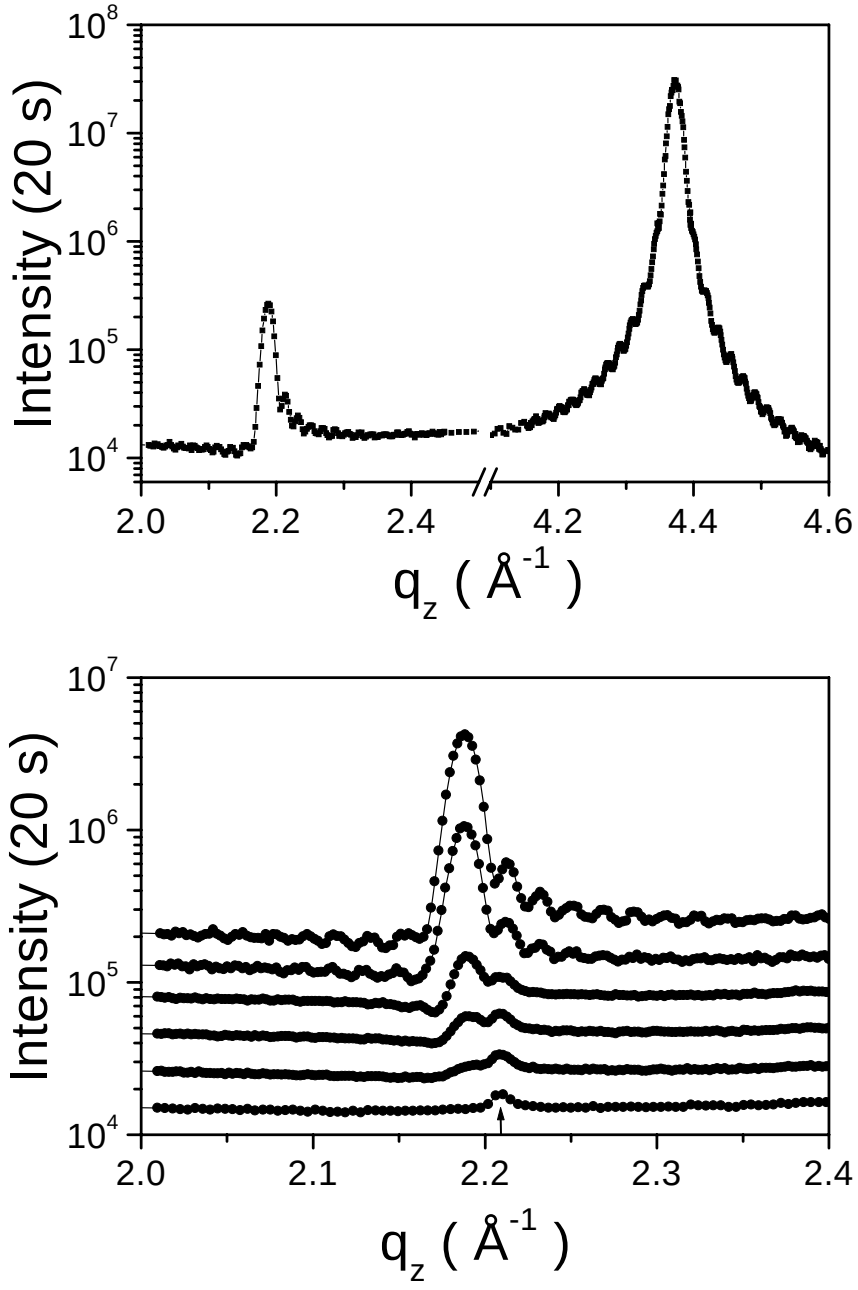

Figure 7.8: X-ray scattering from a bare 350 Å FeCo film. (Top) q_z scan including the FeCo(001) reflection and the FeCo(002) reflection. The lines are a guide to the eye. (Bottom) Temperature dependence of the FeCo(001) reflection. The curves have been shifted for clarity. Pyrometer temperatures: from top, 620.0 °C, 680.0 °C, 697.8 °C, 699.0 °, 701.0 °C, 711.0 °C.

The background radiation for this measurement is about 500 cps. This background can be divided into two main contributions: background contributions from the optical components of the beamline, and thermal diffuse scattering from the sample. To lower the background of the first type, the monochromator of the Troïka beamline was redesigned and indeed the background in Fig. 7.17, measured after the redesign, is one order of magnitude lower. The thermal diffuse scattering originates from the sample and has to be determined and subtracted to obtain the pure Bragg signal. This procedure will be described next. A common problem during synchrotron experiments is a contamination of the incident x-ray beam by high-energy harmonic wavelengths due to the different undulator maxima. Reflecting mirrors are used in the primary beam to suppress these energies, but nevertheless the elimination of this kind of scattering requires some experience with the optical components of the beamline. The arrow in Fig. 7.8 shows an example of high energy contamination. A temperature-independent high-energy wavelength is not unexpected since this measurement was done without a reflecting mirror for technical reasons. The higher energy signal may be discriminated by means of the detector electronics using the pulse height of the counting signal. However, when the harmonic fulfills the Bragg condition of the substrate, about $1/3$ of its intensity is reflected from the sample. Then the NaJ detector saturates and the high energy signal can no longer be discriminated properly. For the analysis of these data this peak is not a serious problem: it is temperature-independent, very sharp, and it can be easily subtracted from the raw data. To clarify the origin of this peak, the high energy character was confirmed by placing an 1 mm aluminum attenuator in front of the detector; whereas the Bragg signal was strongly suppressed by a factor of about 10, the high energy peak was only slightly attenuated, indicating an energy of at least $\lambda/2$. In Fig. 7.21, a similar problem occurs and this time the contaminated region was left out to protect the energy dispersive

detector.

7.5.2 Background subtraction

The first step in analyzing the experimental data is the separation of the Bragg signal from the background. The separation is straightforward. Each scan along q_z was performed with a set of perpendicular scans, so called χ- or θ-scans (rocking scans). The Bragg signal may be identified by its angular width which is given by the mosaic distribution, in this case 0.34°. Fig. 7.9 shows by the way of example χ-scans at T=696°C (a-c). The Bragg signal is given by a Gaussian lineshape. Then the background is interpolated along q_z with a physically-motivated model function $A + B(q_z - q_{\mathrm{MgO}})^{-2}$ which takes into account the peaking of the thermal diffuse scattering at the MgO-Bragg reflection (see Fig.7.9d). Next, the high-energy, temperature-independent peak at $q_z = 2.21\text{Å}^{-1}$ is added to the background and the total background (dashed area in Fig. 7.9d) is subtracted to obtain the pure Bragg signal. Finally, the resulting data are corrected for the Lorentz-polarization factor $L \cdot P$ (see Eq. 5.13 and Eq. 5.10). The corrected intensities are depicted in Fig. 7.12a.

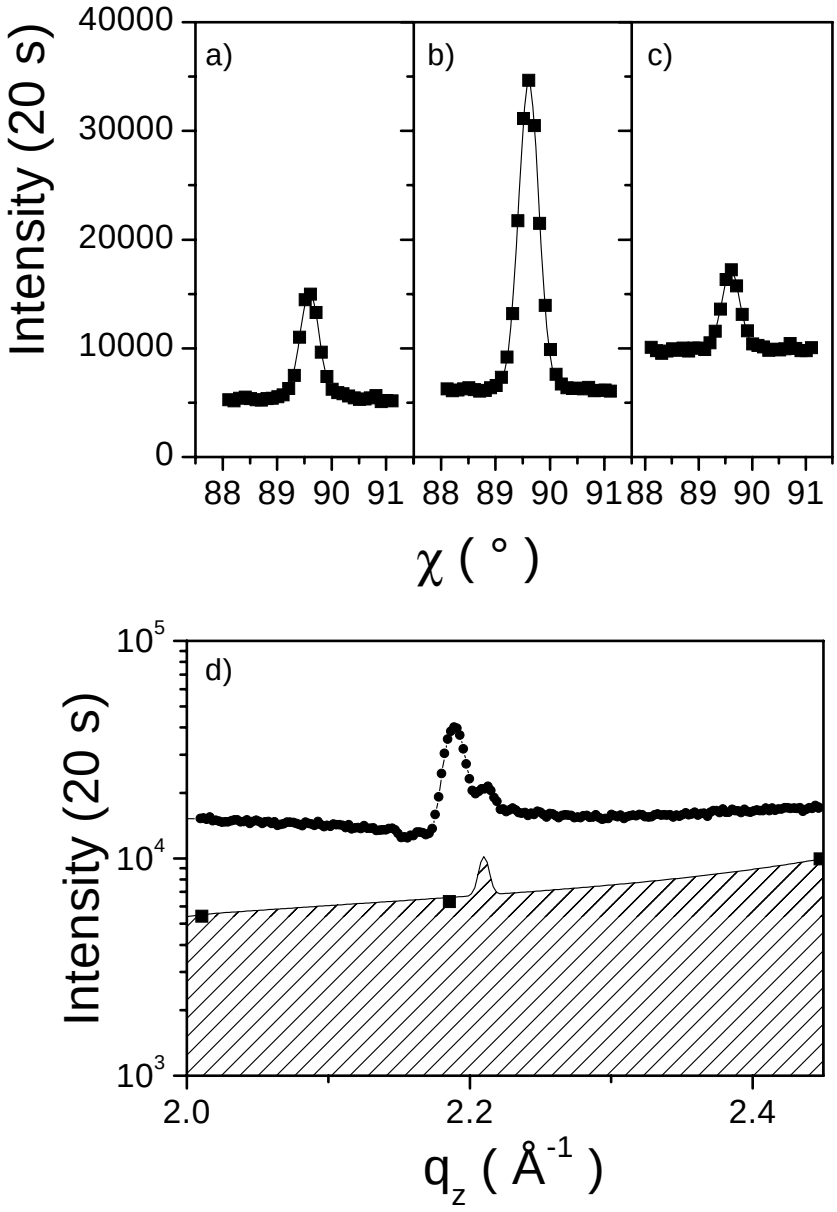

Figure 7.9: X-ray scattering from the bare 350 Å FeCo film. Background determination at T=696°C. (a), (b) and (c) are selected χ-scans. (d) The connected circles are the raw data and the dashed area is the total background.

7.6 Data analysis for the uncapped 350 Å FeCo film

7.6.1 Constant order far below T_c

First a measurement at T=690°C is considered. The simplest assumption about the ordered state of the film is $\Psi(z) = \Psi_{\mathrm{hom}}$, i.e. a homogeneous, depth-independent order throughout the whole thickness. Based on the observation from Fig. 7.7 that the intensity is strongly influenced by interference effects, the scattering amplitude of the film and the substrate must add up coherently (Eq. 5.31) in order to model the recorded diffraction pattern. This implies the structural model that is schematically shown in Fig. 5.5. The two adjustable parameters for the modeling are the FeCo-MgO distance d (see Fig. 5.5) and the homogeneous order parameter Ψ_{hom} (see Fig. 7.10). All other parameters needed to calculate the scattering intensity (i.e. the lattice constants and the film thickness) are already known from the modeling of the measured FeCo(002) reflection, namely the FeCo lattice constant ($a_{\mathrm{FeCo}} = 2.873$ Å) and the FeCo film thickness ($N = 121$ unit cells). Excellent agreement of a least squares fit to the data is found for a MgO/FeCo distance $d = 2.30$ Å and a homogeneously ordered sample $\Psi_{\mathrm{hom}} = 0.47$, as shown in Fig. 7.10. In Ref. [104], values of d for a similar epitaxial system Fe(001) on MgO(001) are reviewed, they range from between 2.0 Å and 2.3 Å which is in good agreement with the determined value.

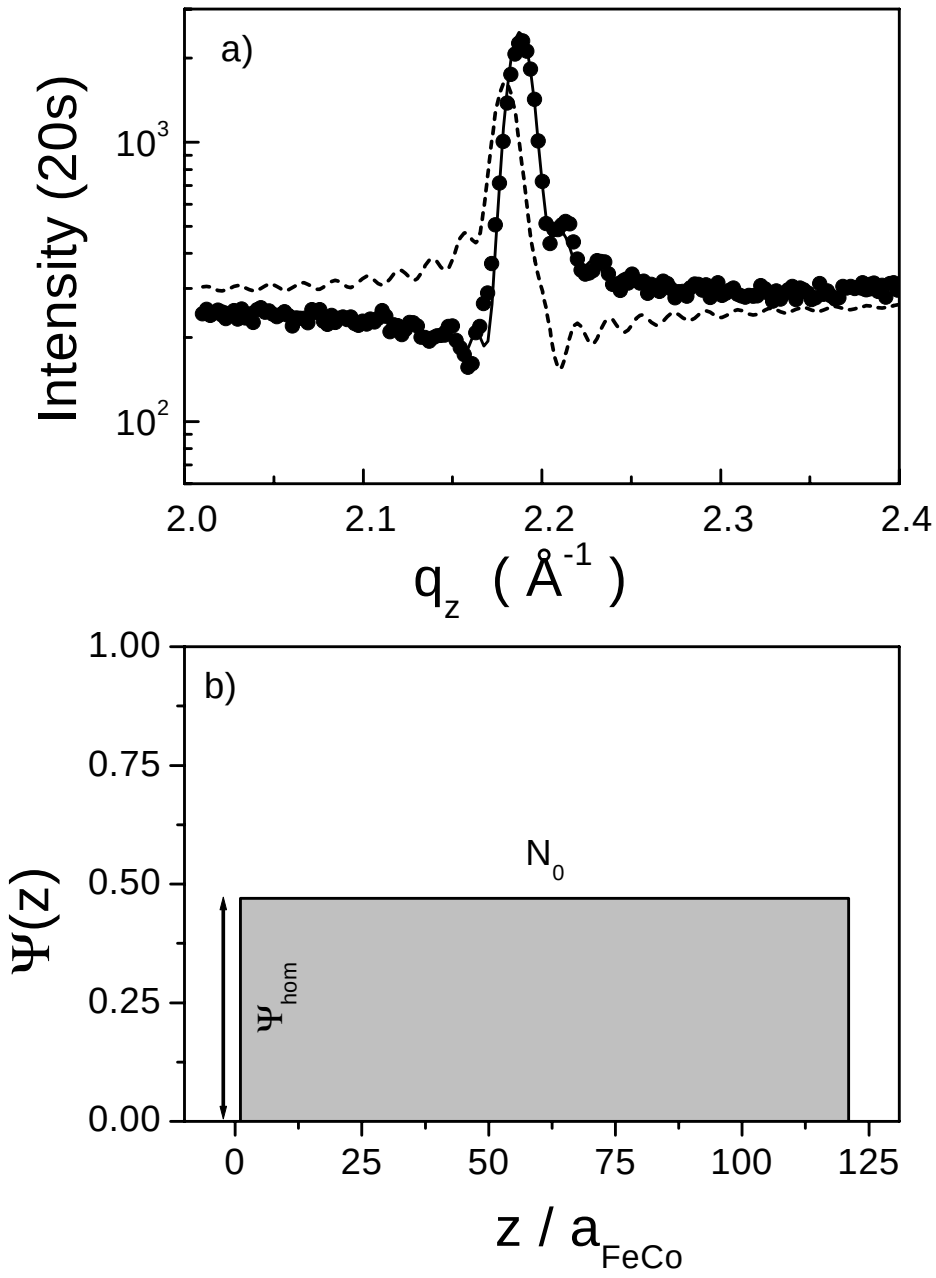

Figure 7.10: X-ray scattering from an uncapped 350 Å FeCo film at T=690°C. (a) solid (dashed) line: fit to the data, assuming a homogeneous order profile ($\Psi(z) = \Psi_{\rm hom}$). The first layer at the interface is occupied mainly by Co (Fe). (b) The order parameter profile $\Psi(z)$.

Due to the coherent scattering between the film and the substrate, it is possible to convert Ψ_{hom} into the occupation probability of the two sublattices (A and B) with Fe or Co atoms. If the sublattice that contains the first atomic layer towards the MgO interface (called sublattice A in the following) is preferentially filled by Co atoms, one obtains the solid line in Fig. 7.10, which is in good agreement with the data points[4]. If sublattice A is filled with Fe atoms instead, one obtains the dashed line in Fig. 7.10 which is definitely not observed experimentally. Therefore, the interference of the film with the substrate allows fixing the component dominating at the interface. For bulk samples, this information is usually lost, since diffraction experiments have only access to the modulus square of the scattering amplitude. The present case is an example of how a phase reference (here, the substrate) can partially mitigate the phase problem.

7.6.2 Adsorption profiles above T_c

Now a measurement at T=701°C is considered, see Fig. 7.11a. At this temperature, the diffraction pattern exhibits a smooth, broad feature without thickness oscillations. These data cannot be modeled with a homogeneous order parameter profile $\Psi(z)$, since no Laue oscillations are observed. Since theory predicts adsorption profiles with exponential tails (see Eq. 3.40), an exponentially decaying order parameter profile $\Psi(z) = \Delta\Psi_0 \cdot \exp\ (-\frac{z}{\xi \cdot a_{\mathrm{FeCo}}})$ is considered, localized to either the surface or the interface, see Fig. 7.11. These two situations can be discriminated quite well from a least squares fit (solid line in Fig. 7.11a). An order parameter profile that describes adsorption at the FeCo-MgO interface is in good agreement with the experimental data, while a profile that describes absorption at the free surface can be

[4]The order parameter is actually negative in this case. The negative sign has been omitted in the following for convenience.

excluded (dashed line in Fig. 7.11a).

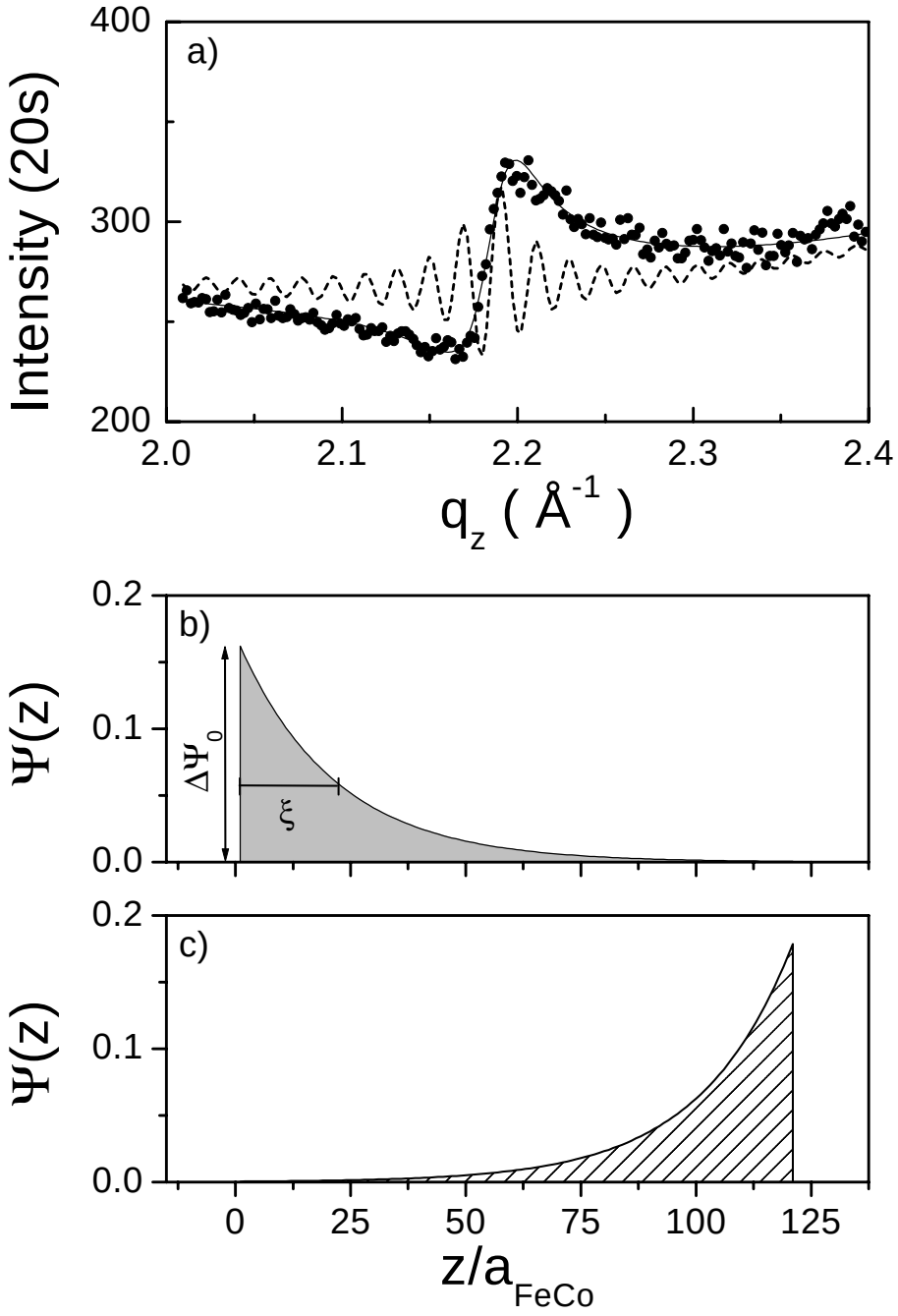

Figure 7.11: X-ray scattering from the bare 350 Å FeCo film at T=701°C. (a) The solid line is a least squares fit, assuming an exponentially-decaying profile $\Psi(z)$ localized at the MgO interface, as shown in (b). The dashed line is a simulation which assumes that the profile is localized at the free surface, as shown in (c).

The least square fit is achieved with two adjustable parameters, the interface order enhancement $\Delta\Psi_0$ and the decay length ξ. Due to the simultaneous modeling of the temperature-independent FeCo(002) reflection (see Fig. 6.7) $\Delta\Psi_0$ is known on an absolute scale, i.e. $\Delta\Psi_0 = 0.17$ and therefore $\Delta\Psi_0 \lhd 1$. This indicates that the h_1 surface field is weak (see Fig. 3.12). The numerical value obtained for ξ at this temperature is $\xi = 21.02$ unit cells, or $\xi \simeq N/\,6$. This is a reasonable order of magnitude, however, to decide whether this decay length may be identified with the correlation length, one needs to know the variation with temperature and especially the location of T_c.

7.6.3 Determination of T_c

To analyze the complete temperature range, the temperature-dependent diffraction pattern is modeled by an order parameter profile $\Psi(z) = \Psi_{\mathrm{hom}} + \Delta\Psi(z)$ that is divided into a constant term Ψ_{hom} and an exponentially-decaying term, $\Delta\Psi(z) = \Delta\Psi_0 \cdot \exp\,(-\frac{z}{\xi \cdot a_{\mathrm{FeCo}}})$. This separation is motivated by the observation that the order parameter profiles at lowest temperatures are dominated by a constant contribution, whereas the order parameter profiles at highest temperatures show only an exponentially decaying contribution. Further, the hypothesis expressed in Eq. 3.50, which is justified for weak h_1 surface fields (Eq. 3.29), corroborates this separation from the theoretical point of view. Fig. 7.12a shows the resulting least square fits for the same temperatures as in Fig. 7.8. A good description of the data for all temperatures is possible. The corresponding order parameter profiles are depicted in Fig. 7.12b).

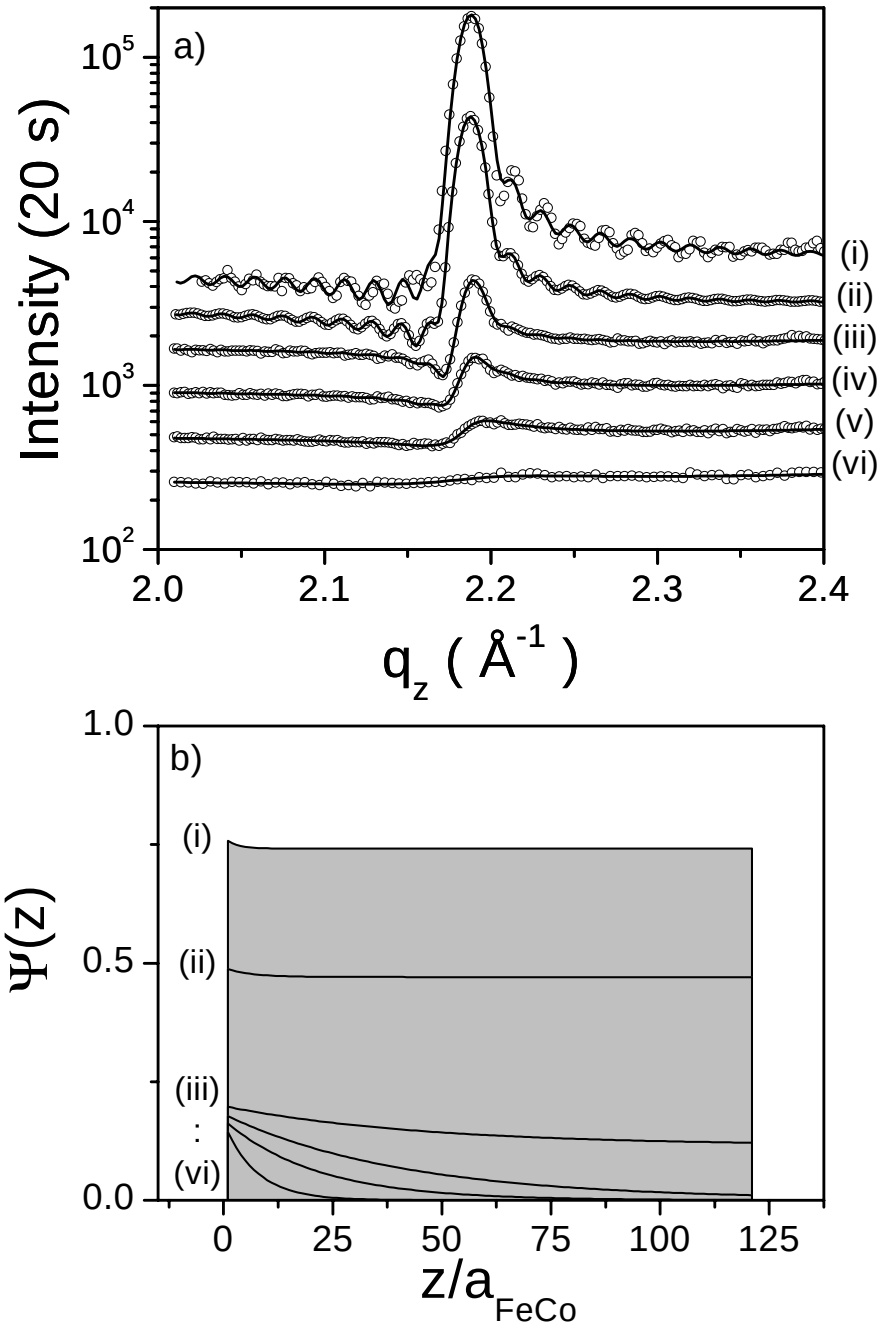

Figure 7.12: X-ray scattering results from the bare 350 Å FeCo film. a) Same temperatures as in Fig. 7.8 with least squares fits as explained in the text. The curves are shifted for clarity. b) Corresponding order parameter profiles $\Psi(z)$ (not shifted).

Following the arguments that established Eq. 3.50, $\Psi_{\rm hom}(T)$ represents the field-free order parameter of a bulk system with a temperature dependence as shown in Fig. 4.3. A profile without a $\Psi_{\rm hom}$-contribution is therefore above T_c. This suggests $T_c = 698.0 \pm 0.1$°C.

7.7 Results and discussion

7.7.1 Dimensional crossover

Due to the strong domination of the ordering behavior by $\Psi_{\rm hom}$ at low temperatures, it is difficult to determine ξ unambiguously below T_c. Therefore, after determining T_c from the vanishing of $\Psi_{\rm hom}$, $\xi(T_c - \Delta T) = \xi(T_c + \Delta T)$ is superimposed. Then, $\xi(T_c + \Delta T)$ is the free fit result interpolated from the data above T_c [5]. The resulting temperature dependence of $\Psi_{\rm hom}$ and ξ is depicted in Fig. 7.13.

Approaching T_c from above, ξ increases. A logarithmic presentation of the data (Fig. 7.14a) reveals a power-law like divergence. To check whether ξ may be identified with the bulk correlation length, the observed power law behavior (solid lines in Fig. 7.13a and Fig. 7.14a) is compared to the expected bulk power law behavior of the correlation length. A least square fit gives $\xi(t) = \xi_0 \, |t|^{-\nu}$ with $\xi_0 = 0.43 \pm 0.15$ (u.c.) and $\nu = 0.65 \pm 0.02$. This result is in good agreement with the expected 3d-Ising values (see Table 3.3) $\nu = 0.643$ and $\xi_0 = 0.448$, and therefore it suggests that the identification of the profile decay length with the bulk correlation length is reasonable. Consequently the observed order parameter profile can be classified as a critical adsorption phenomenon. A close inspection of Fig. 7.14a reveals a deviation of the data point close to T_c ($t = 4\ 10^{-4}$) from the $3d$-power-law behavior. Most remarkable, this is just the temperature window where a saturation of the

[5] An alternative choice would have been $\xi(T_c - \Delta T) = 1/2 \cdot \xi(T_c + \Delta T)$, see Eq. 3.19.

divergence of ξ is expected. Theoretical estimates suggest that this saturation value should be $N/\,2.89 = 42$ ([77], compare to Eq. 3.51), whereas Fig. 7.14a suggests a saturation at $\xi = 45$ unit cellt, i.e. at $\xi = N/\,2.69$, in agreement with the theoretical prediction.

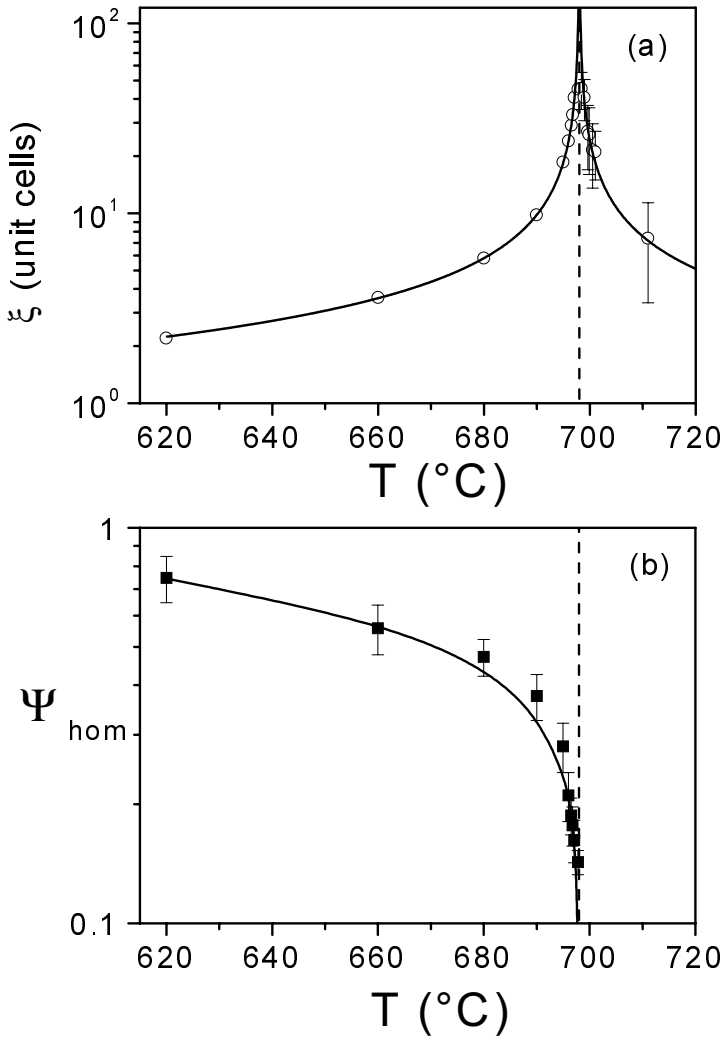

Figure 7.13: a) Temperature dependence of ξ (open circles). b) Temperature dependence of $\Psi_{\rm hom}$ (squares). The solid lines represent power law behavior, the dashed line indicates T_c.

Approaching T_c from below, Ψ_{hom} vanishes (see Fig. 7.13b). A logarithmic presentation of the data (Fig. 7.14b) reveals a power law dependence, as indicated by the solid line. The obtained power-law is $\Psi_{\text{hom}} = \Psi_0 \, |t|^{\beta}$ with $\beta = 0.347 \pm 0.016$ and $\Psi_0 = 1.79 \pm 0.1$. β is in good agreement with the theoretical $3d$-value $\beta = 0.314 \pm 0.004$ ([18], see Table 3.3). The agreement with the theoretical estimates $\Psi_0 = 1.49$ is moderate; however this disagreement should not be overemphasized. It may reflect the limited accuracy of the normalization by simultaneous modeling of the FeCo(002) intensity distribution. Further, a moderate agreement for the amplitudes is quite common and this may result from the range of interactions considered in the theory, which influences Ψ_{hom} but not β. The good agreement of Ψ_{hom} with bulk $3d$-behavior over a broad temperature range confirms the separation of the order parameter profile $\Psi(z)$ into a constant part Ψ_{hom}, which represents the field-free behavior, and a critical adsorption profile. This indicates that the h_1-field giving rise to the adsorption profile is weak.

Close to T_c a deviation from the $3d$-power-law behavior is observed. As shown by the dashed line, the slope may change from $\beta = 0.347$ to $\dot{\beta} = 0.125$ in the vicinity of T_c. This is consistent with the expected $3d - 2d$ crossover, which should occur within the same reduced temperature range as the observed saturation of ξ. For a thinner film, this temperature range will be more extended (see Fig. 7.25).

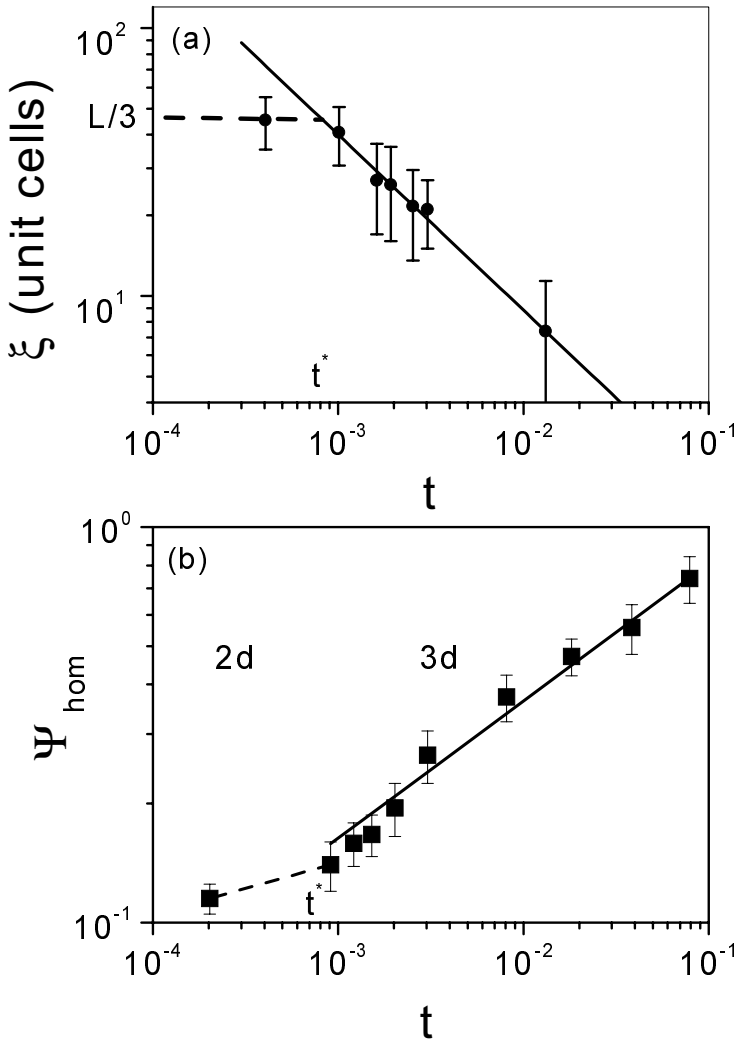

Figure 7.14: A logarithmic plot of the data in Fig. 7.13. Solid lines: obtained $3d$-behavior for $t > t^* \sim 10^{-3}$. Dashed lines: Expected $2d$-behavior in the vicinity of the phase transition, $t < t^*$. a) Temperature dependence of ξ. b) Temperature dependence of $\Psi_{\rm hom}$.

7.7.2 Weak field adsorption ($h_1 \ll 1$)

The amplitude $\Delta\Psi_0$ of the order parameter profile is only weakly temperature-dependent (see Fig. 7.15). As discussed in Sec. 3.4.1, the amplitude of the exponential tail scales with $\Delta\Psi_0 = \Psi_0 \cdot P_\infty^+ \cdot t^\beta$ in the limit of a strong surface-field ($h_1 \to \infty$). This behavior is represented by the dashed line in Fig. 7.15. Only the data points for $t < \hat{t} \approx 10^{-3}$ follow this behavior. Above this temperature, the amplitude $\Delta\Psi_0$ decreases. This behavior is qualitatively different and it suggests that the scaling variable $y = \xi / l_1$ crosses over from strong ($y \gg 1$) to weak ($y \ll 1$) absorption (see Eq. 3.42) at $\hat{t}$. Consequently, the behavior above this temperature may be described by the weak field expression $\Delta\Psi_0 = h_1 \cdot \xi^{1-\eta_\perp} = h_1 \cdot \xi_0^{1-\eta_\perp} \cdot t^{-\nu(1-\eta_\perp)}$ (see Eq. 3.40), with h_1 as an adjustable parameter. The dotted line in Fig. 7.15 reflects this behavior with $h_1 = 0.10$ or $l_1 = 0.10^{-\nu/\Delta_1} = 25$ u.c. (see Eq. 3.38). A good description of the experimental data is possible. The solid line in Fig. 7.15 suggests a weak-to-strong crossover function.

The observed crossover from strong to weak adsorption sets in at $\hat{t} = 1.5 \cdot 10^{-3}$. From scaling arguments, one expects the crossover to set in at $y = \xi / l_1 = 1$, or at $t = 1.8 \cdot 10^{-3}$, in reasonable agreement with the data. This agreement is surprisingly good, since the value A_{l_1} in Eq. 3.38 has been set to 1 in our analysis due to the lack of numerical estimates for $3d$-systems, indicating that this is close to the exact value ($A_{l_1} = 0.909$ for a $2d$-Ising system [34]). In addition, the dimensional crossover at $t^* < \hat{t}$ should also merge into this adsorption scenario. However, the limited number of data points in this temperature region makes a more quantitative analysis difficult.

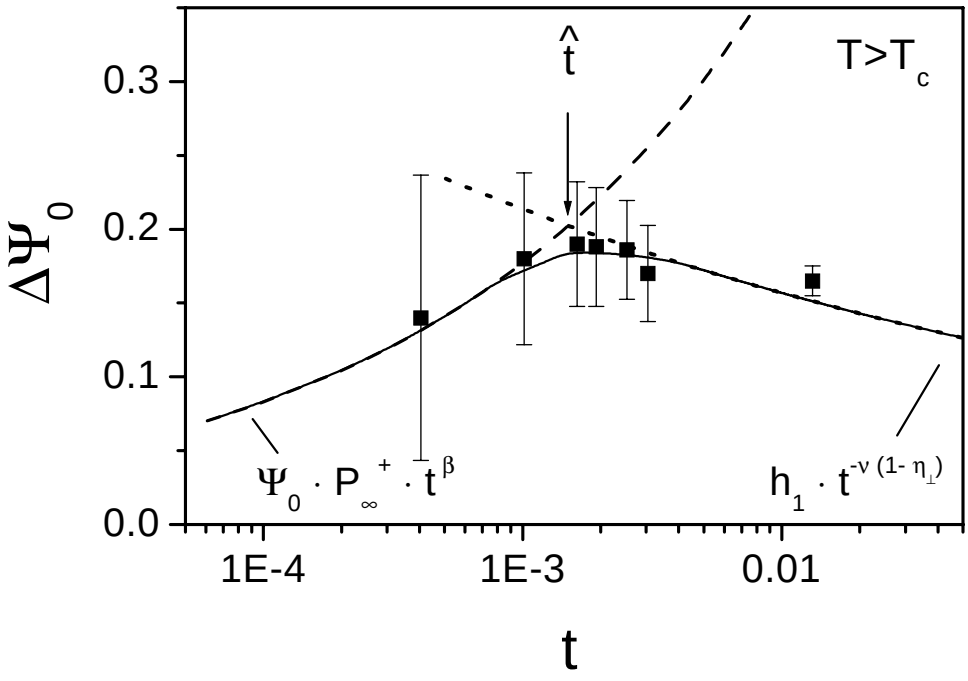

Figure 7.15: Weak (dotted line) to strong (dashed line) adsorption crossover, observed in a 350 Å FeCo film. The data points $\Delta\Psi_0$ (squares) are plotted versus the reduced temperature. The solid line shows schematically a weak-to-strong crossover function.

Since $\Psi(z)$ is known on an absolute scale, the order parameter profile can be converted to the Fe and Co concentration of the atomic layers of the film, using Eq. 4.3. Since the average concentration per unit cell (atomic bilayer) is fixed to $Fe_{44}Co_{56}$ in the analysis, each enhancement in one atomic layer is followed by a depletion of the same species in the next atomic layer by the same amount. In this sense, the adsorption profile $\Delta\Psi(z)$ can be interpreted as an oscillating segregation profile, a phenomenon which occurs at many binary alloy surfaces [121, 122]. In Fig. 7.16, the order parameter profile (see Fig. 7.11b) has been converted to an oscillating Co-segregation profile. For

clarity, only the first 50 atomic layers (25 unit cells) are shown. Compare also to Fig. 5.5.

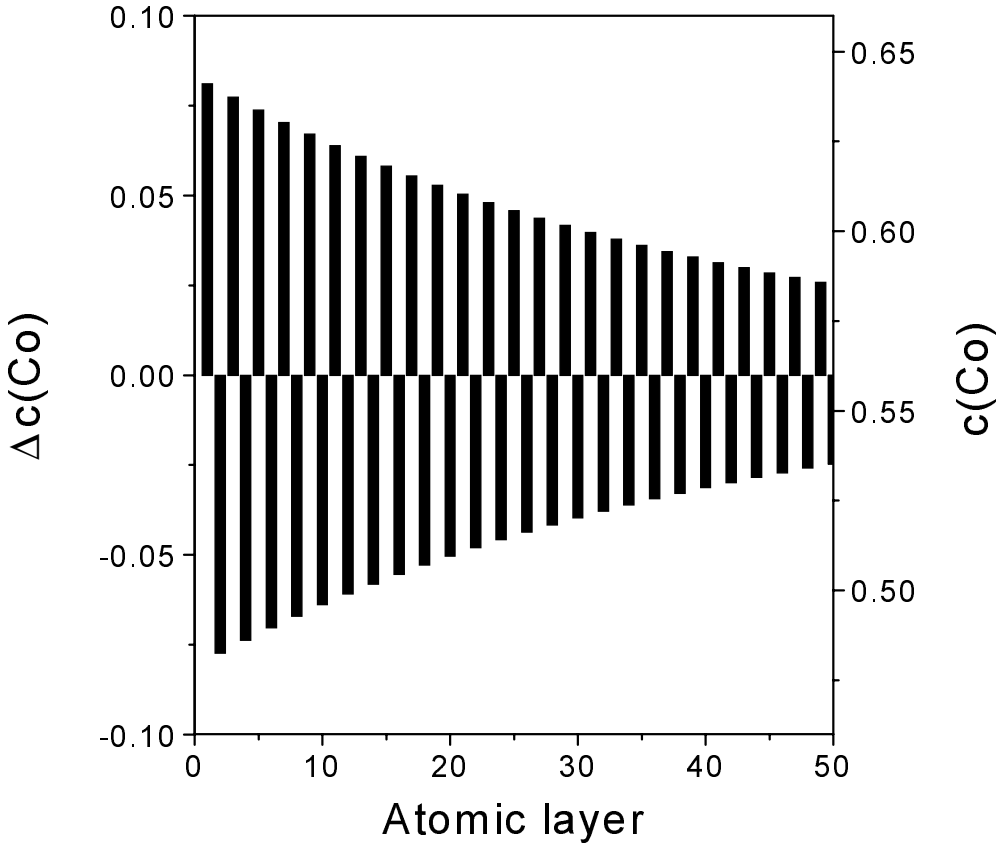

Figure 7.16: Subset of an order parameter profile $\Psi(z)$, represented as an oscillating Cobalt-segregation profile. Same temperature as in Fig. 7.11b. Left y-axis: deviation of the Co-concentration from the average value. Right y-axis: total Co-concentration c_{Co}.

The microscopic origin of the h_1-field, which promotes the Co-enrichment of about 8% at the interface is now subject to further investigation. A renor-

malization group analysis suggests that a deviation from ideal stoichiometry ($Fe_{50}Co_{50}$) may act like an effective h_1-field [44] and indeed, all samples have been grown by purpose as $Fe_{44}Co_{56}$. However, this does not explain why the profile is localized only at the MgO-interface. To clarify this question experimentally, another sample has been prepared with a similar FeCo-film thickness but capped with an MgO overlayer.

7.8 The MgO-capped 320 Å FeCo film

A MgO-capped 320 Å FeCo-sample was grown with the intention to directly compare with the bare 350 Å sample. To simplify the comparison, measurements were performed at virtually the same wavelength (see Table 7.1) and at a comparable film thickness. Selected q_z-scans at temperatures given in the figure caption are depicted in Fig. 7.17. All features of the measurements performed on the uncapped 350 Å FeCo film are reproduced qualitatively (see Fig. 7.8). From the similar shape of the intensity distribution around the FeCo(001) reflection at higher temperatures, it can be concluded that the MgO-capping layer does not induce a second ordering profile at the interface with the capping layer. Otherwise, intensity oscillation should be observed, as explained in the context of Fig. 7.11. This corresponds with LEED measurements performed on the MgO capping layer which indicate that the structural quality of the overlayer is low. Similar observations are made for the thinner films (see below).

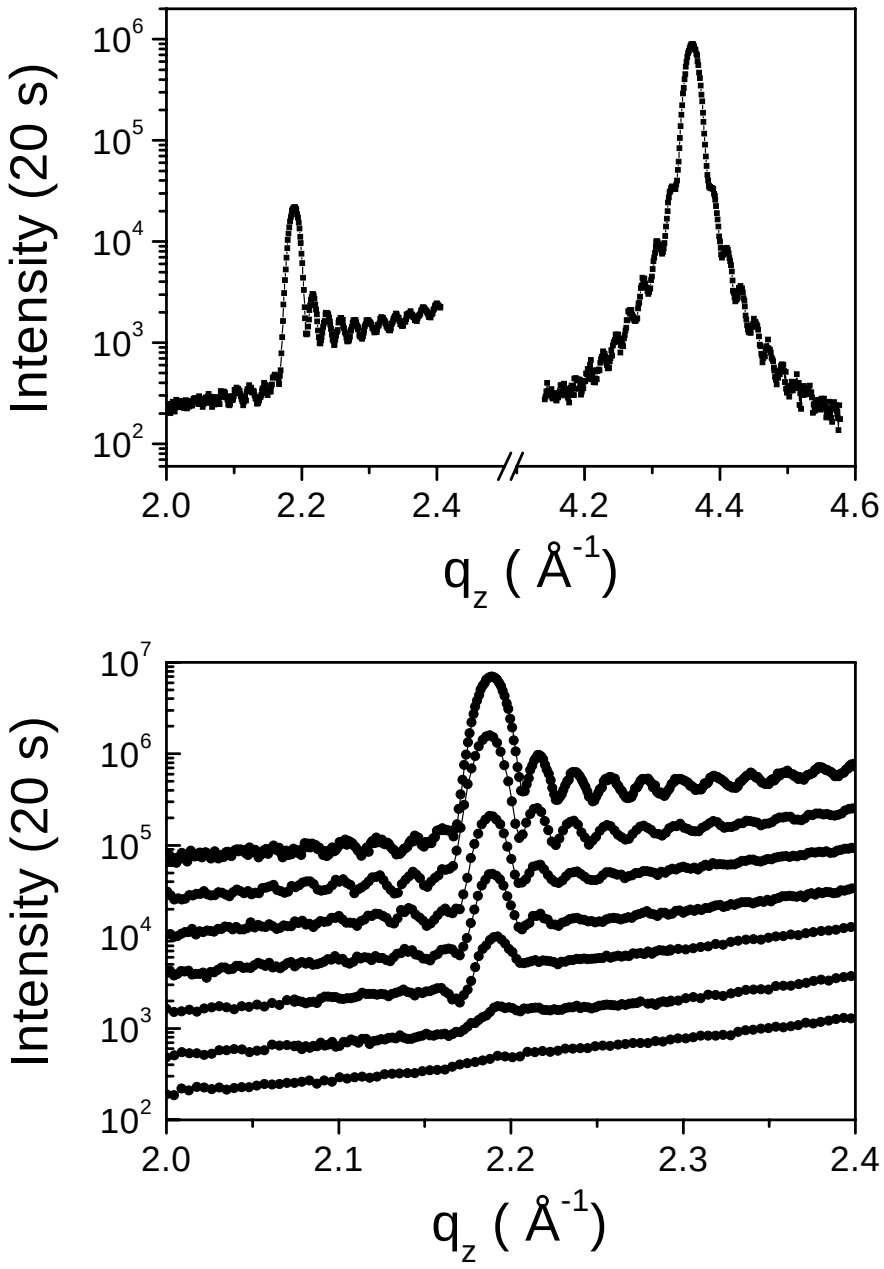

Figure 7.17: X-ray scattering from the MgO-capped 320 Å FeCo film. (Top) The FeCo(001) reflection and the FeCo(002) reflection. The lines are a guide to the eye. (Bottom) Temperature-dependence of the FeCo(001) reflection. The curves have been shifted for clarity. Sample temperatures from top: 501.0 °C, 590.1 °C, 642.0 °C, 649.0 °C, 652.0 °, 656.1 °C, 660.1 °C.

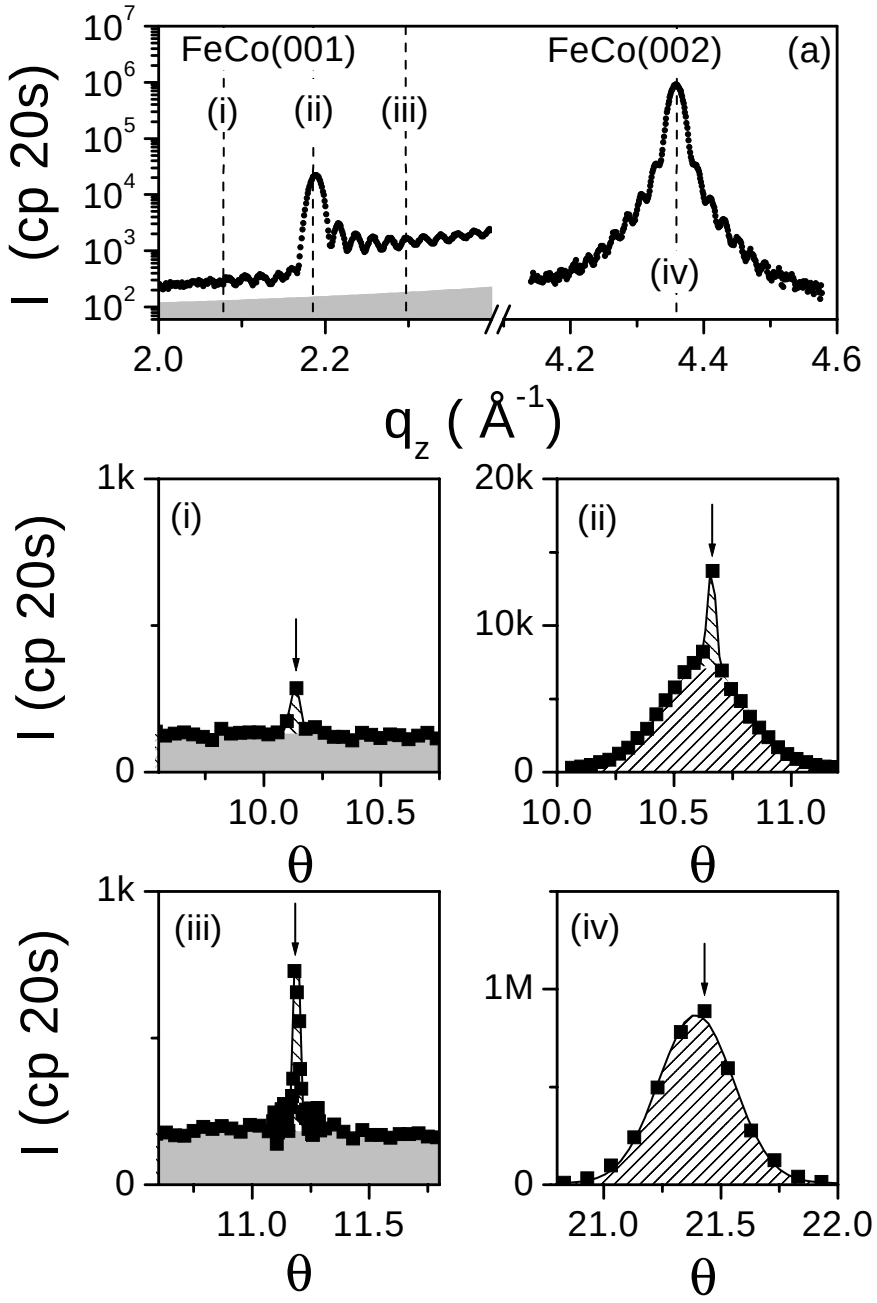

Figure 7.18: a) Extended q_z-scan at $T = 501^oC$. i+ii+iii+iv) Rocking scans at the q_z-positions indicated in (a). The arrows indicate the θ-values used for the q_z-scan.

Fig. 7.18a indicates the q_z-positions (dashed lines, labeled "i"-"iv") where rocking (θ) scans have been performed to analyze the intensity distribution perpendicular to the q_z direction. A broad Gaussian peak with a FWHM of ($\mu = 0.32^o$) is observed in the center of the FeCo(002) reflection (Fig. 7.18iv). The value of μ is close to the value of the uncapped film ($\mu = 0.34^o$). μ represents the mosaic distribution of the FeCo-film. However, the rocking scan performed at the center of the FeCo(001) reflection (Fig. 7.18ii) reveals the occurrence of two line shapes, a broad one (FWHM = 0.37^o), and a sharp one (FWHM = 0.017^o). The sharp component represents the mosaic distribution of the MgO substrate surface[6]. Additionally, Fig. 7.18ii reveals that the broad and the sharp components do not peak at exactly the same θ-value ($\Delta\theta = 0.03^o$).

To explain this difference, one has to understand the microscopic picture of a crystalline surface. A real crystal may exhibit a slight misorientation between the average physical surface (characterized by the surface normal $\overrightarrow{n}$) and the lattice planes (characterized by the miller index [00L]), see Fig. 7.19. This misorientation is called the miscut angle of the surface. As a result, real surfaces are composed of terraces which are aligned along the lattice planes and (monatomic) steps. Due to the good collimation ($\Delta\theta \sim 0.002^o$) and the good energy resolution ($\Delta\lambda/\ \lambda \sim 10^{-5}$) the x-ray beam averages coherently over an in-plane length $\Lambda_{||}$ along the sample surface which is of the order of $\Lambda_{||} = R \cdot \Delta\theta/\ \sin(\theta) \sim O(100\ \mu\text{m})$. Since $\Lambda_{||}$ is much larger than the typical length of a single terrace (see Fig. 7.19) the crystal truncation rod scattering signal is extended along the normal of the average surface as indicated in Fig. 7.19 by the dashed lines. Consequently, the MgO and the FeCo scattering signal are not centered at the same θ-value, but rather they differ by an amount which is of the order of the miscut angle.

[6]The MgO substrates of superior quality have been obtained from HTC, 4 rue Louis Blérlot, F-78130 Les Mureaux.

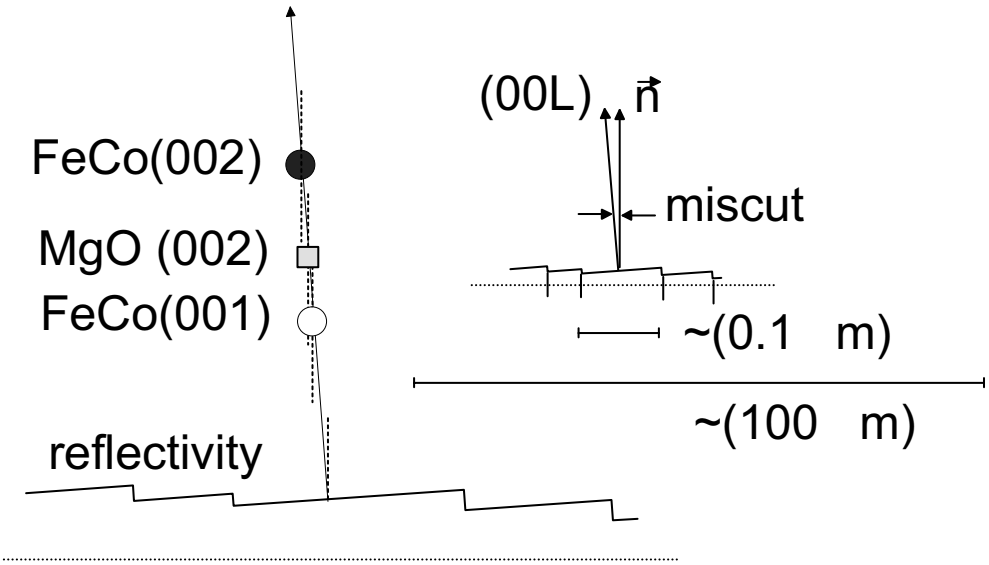

Figure 7.19: A well-defined crystalline surface that exhibits a small miscut angle between the optical surface and the lowest-indexed plane parallel to the surface is built up of terraces. If the coherence of the x-ray beam along the sample surface ($\Lambda_{||}$) is much larger, the x-ray signal (dashed lines) is extended along the direction of the average surface normal. This gives rise to a peak-shift in Fig. 7.18ii.

Due to the different line shape of the film and substrate contribution (see Fig. 7.18) it is also possible to estimate the film (A_{film}) and substrate (A_{sub}) contribution to the total scattering amplitude (A, see Eq. 5.30). At higher temperatures ($T = 656.1^{o}$C, see Fig. 7.20) only the sharp component is observed around the FeCo(001) reflection. This implies that the scattering intensity (see Eq. 5.31) is governed by the substrate term ($|A_{\mathrm{sub}}|^2$) and the interference term ($2 \cdot \mathrm{Real}\left(\overline{A_{\mathrm{film}}} \cdot A_{\mathrm{sub}}\right)$) only. This indicates that at this temperature the whole scattering signal from the film is contained in the interference term. Consequently, without the substrate contribution (A_{sub}), the whole scattering contribution of the film (A_{film}) would be lost.

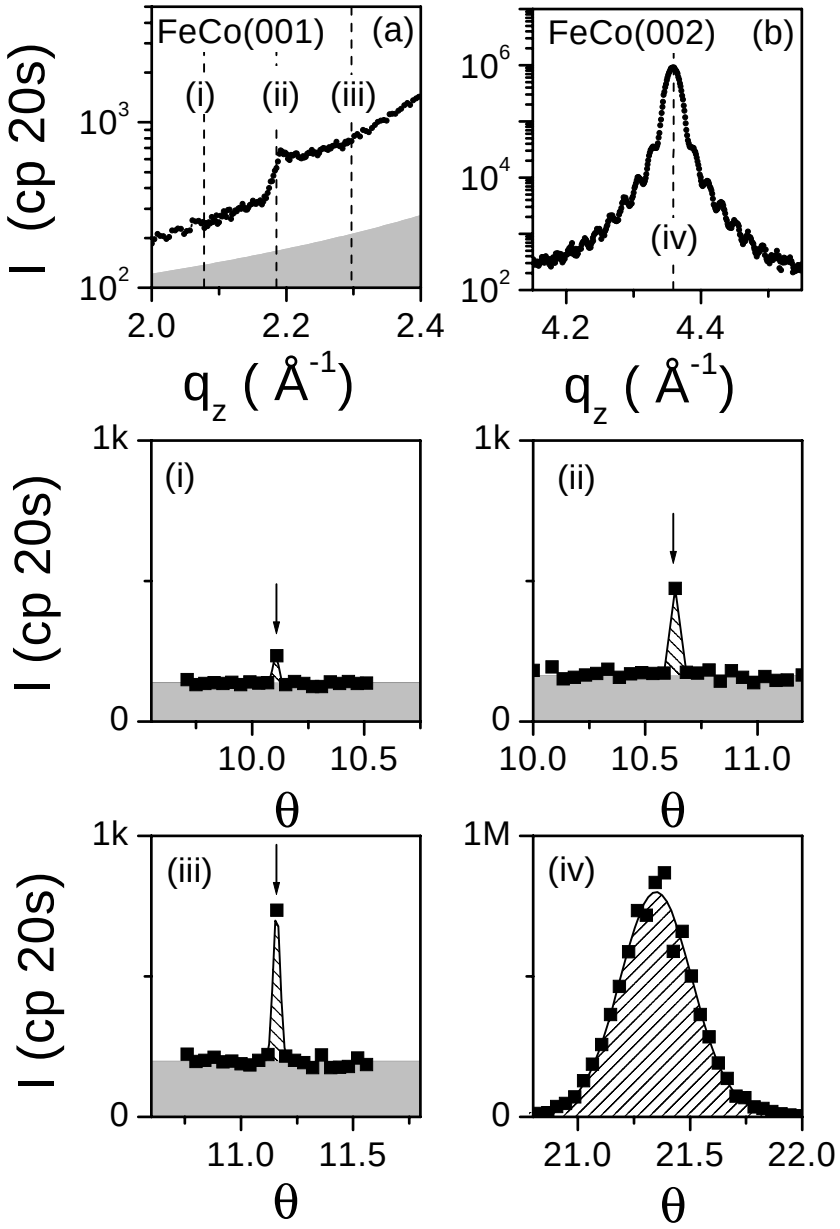

Figure 7.20: X-ray scattering from a MgO-capped 320 Å FeCo film. (a) q_z-scan around the FeCo(001) reflection at $T = 656.1^o$C. (b) q_z-scan around the FeCo(002) reflection at $T = 501^o$C. i+ii+iii+iv) Rocking scans at the q_z-positions indicated in (a+b). The arrows indicate the θ-values used for the q_z-scan.

7.9 The MgO-capped 100 Å FeCo film

7.9.1 Raw data

The MgO-capped 100 Å FeCo film was measured resonantly ($\lambda = 1.63$ Å) to enhance the scattering contrast between Fe and Co (compare Fig. 7.6). Fig. 7.21 depicts the experimental results obtained at the CEMO beamline at HASYLAB in Hamburg, Germany. The intensity oscillations are much wider with respect to the 320 Å-film, as expected. Furthermore, the intensity oscillations are enhanced towards lower q_z-values. However, apart from the different asymmetry in the intensity distribution, the qualitative behavior is similar to Fig. 7.12. Above a certain temperature the intensity oscillations vanish and smooth broad peak remains. This indicates that the MgO-cap induces no second adsorption profile, otherwise intensity oscillations should occur for all temperatures as explained in Sec. 5.6.2.

A lineshape analysis of the diffraction signal at selected q_z-positions is depicted in Fig. 7.22. These rocking (θ) scans reveal two contributions, a broad one (FWHM$\approx 0.75^o$) and a sharper one (FWHM$\approx 0.12^o$). These two scattering signals are indicated in Fig. 7.22 by the shaded areas. As explained in Sec. 7.8, the broad component indicates the mosaic distribution of the 100 Å FeCo film ($\mu = 0.75(5)^o$), which has increased in comparison to the 350 ÅFeCo film. This results presumably from the annealing of the thicker film at 600 ^{o}C after growth.

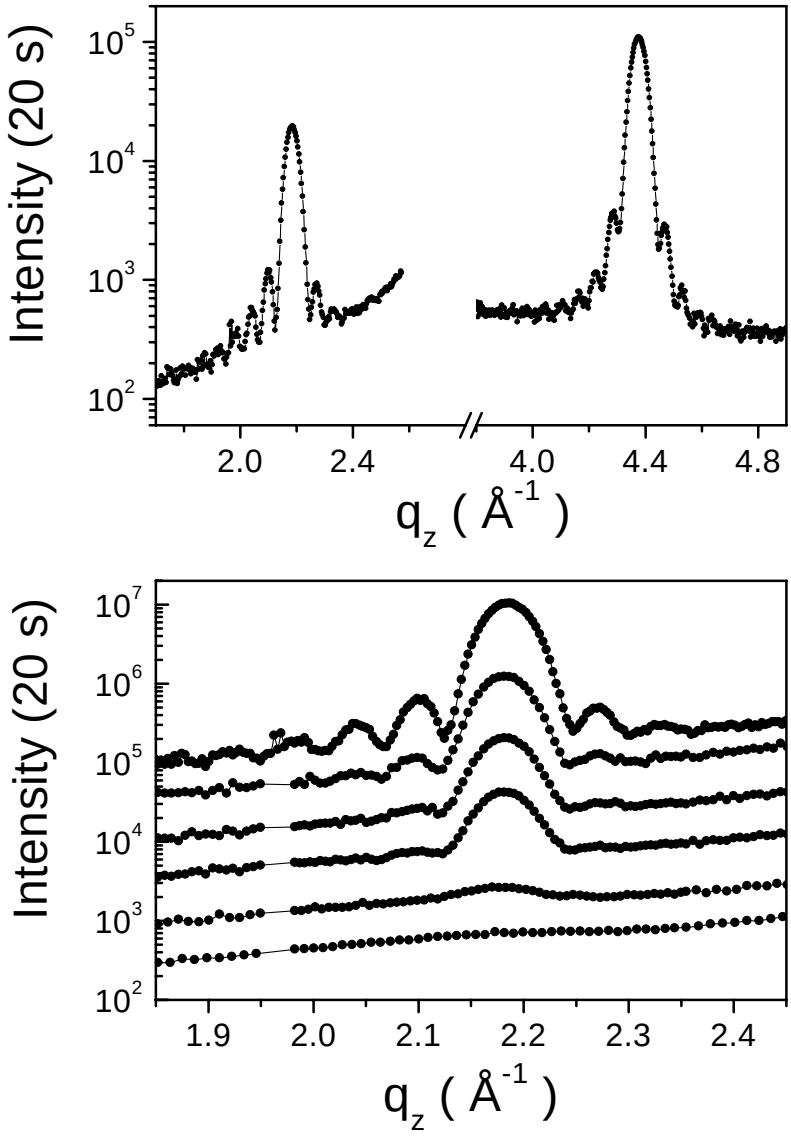

Figure 7.21: X-ray scattering results from the MgO-capped 100 Å FeCo film. (Top) q_z scan including the FeCo(001) and the FeCo(002) reflection. The solid lines are a guide to the eye. (Bottom) Temperature dependence of the FeCo(001) reflection; the curves have been shifted. Sample temperatures from top: 500 °C, 730 °C, 742 °C, 748 °, 760 °C, 785.5 °C.

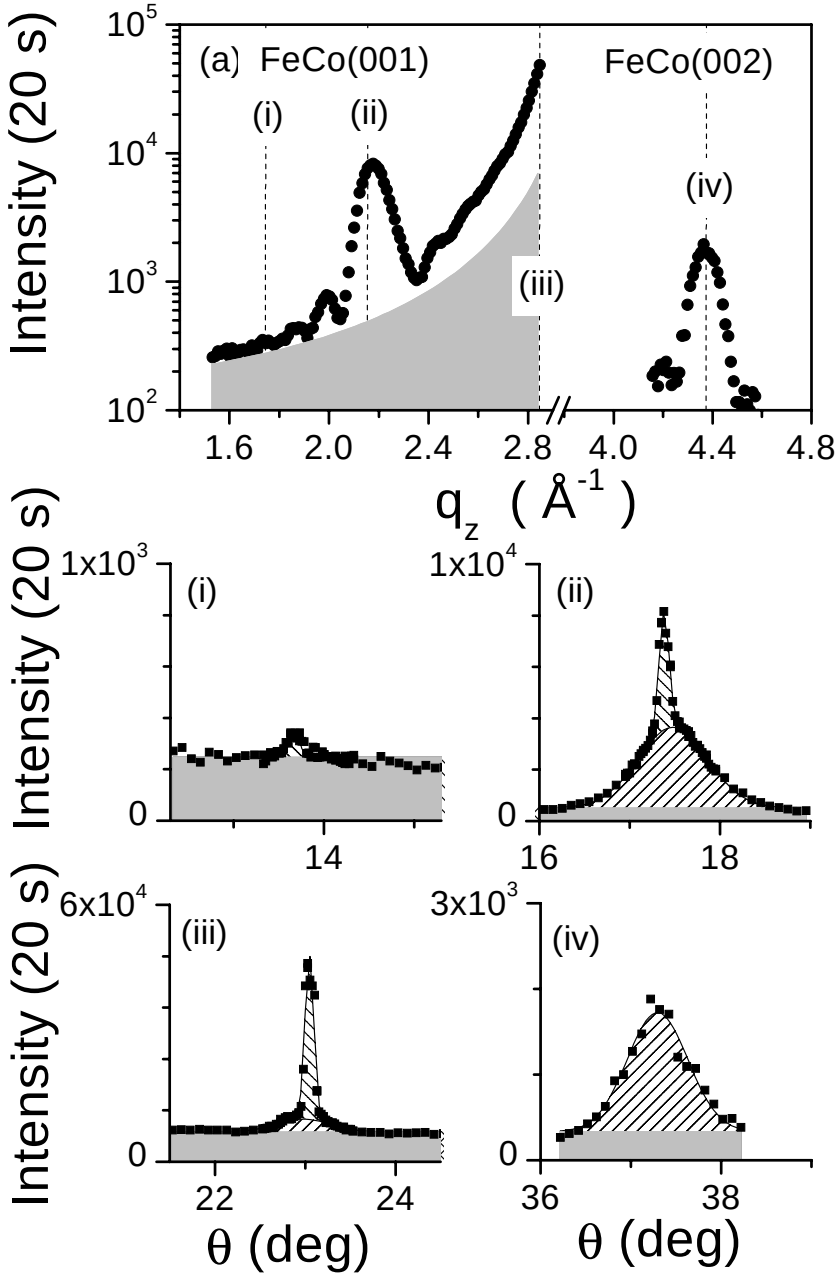

Figure 7.22: X-ray diffraction pattern obtained from a capped FeCo 100 Å film at 571 ^{o}C. a) An extended q_z-scan. i)-vi) Lineshape analysis (rocking scans) at the q_z-positions indicated by the dashed lines in (a).

7.9.2 Far below T_c

The diffraction pattern at $T = 500$ °C including the FeCo(002) reflection is depicted in Fig. 7.23a (squares). The solid lines indicate the intensity distributions associated with the order parameter profiles $\Psi(z)$ as depicted in Fig. 7.23b. A good description of the data at $T = 500$ °C is possible with a sample thickness of $N = 36$ unit cells ($D = 103$ Å). The deduced roughness parameters are $\sigma = 0.9$ Å for the substrate/film interface and $\sigma = 4.4$ Å for the film/MgO-cap interface. The component enriched at the interface with the substrate is Co in agreement with the two other samples (Secs. 7.6.1 and 7.8) discussed above. The dotted line indicates the constant contribution ($\Psi_{\mathrm{hom}} = 0.44$) to the order parameter profile. In addition, a weak order parameter profile located at the interface with the substrate is present.

7.9.3 Below T_c

The diffraction pattern of the FeCo(001) reflection at $T = 742$ °C (circles in Fig. 7.23a) exhibits two satellite peaks. An order parameter profile $\Delta\Psi(z)$ that is located at the interface with the substrate and in addition a constant contribution Ψ_{hom} with $N = 32$ is deduced in order to model the intensity distribution. This decrease in thickness (N) can be attributed to a disordering of the FeCo/MgO-cap interface. A disordering behavior is indeed expected for a field free interface ($h_1 = 0$, ordinary behavior, see Figs. 3.4 and 3.5). Therefore, the order at the interface with the MgO-cap ($\Psi(z = D)$) is now introduced as an adjustable parameter, see Fig. 7.24. Furthermore, it is assumed that the lowered order relaxed relaxes within the same length ξ which describes the decay of the adsorption profile $\Delta\Psi(z)$. N is fixed to the value deduced from the FeCo(002) reflection ($N = 36$).

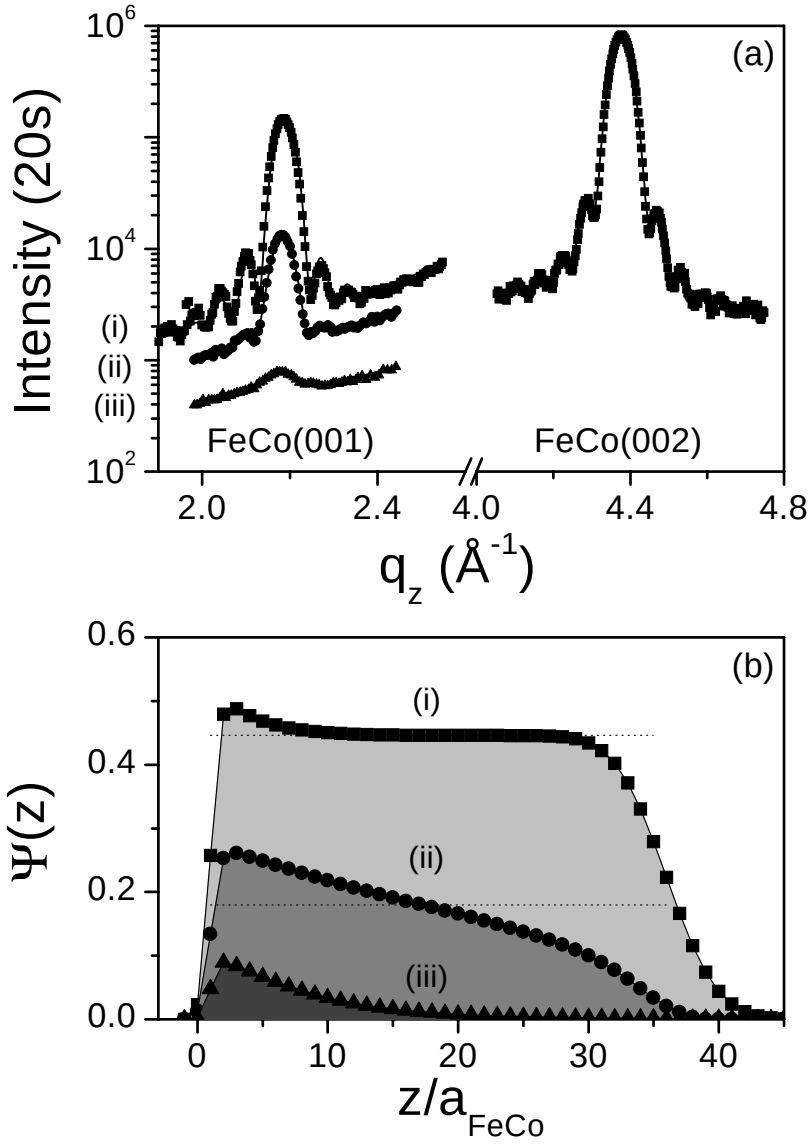

Figure 7.23: X-ray diffraction pattern of a MgO-capped 100 Å FeCo film (a), and the associated order parameter profiles (b). The temperatures are $T = 500\ ^o$C (squares), 742 ^{o}C (circles), and 760 ^{o}C (triangles). The solid lines in (a) represent the simulated intensities which are based on the order parameter profiles depicted in (b).

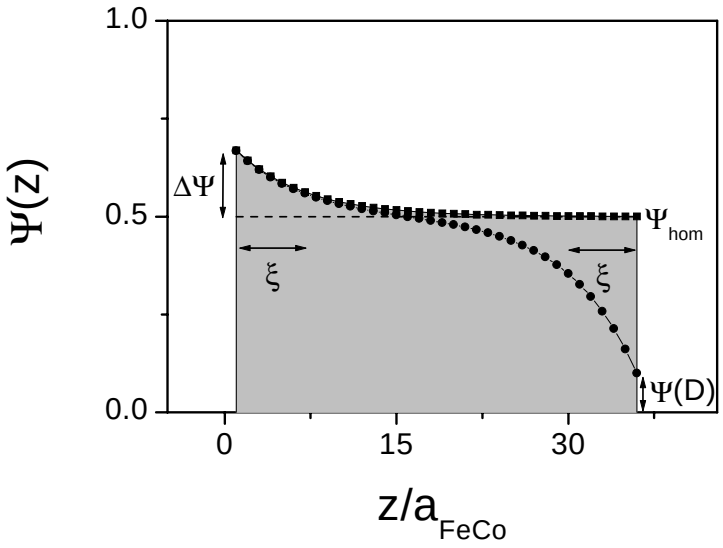

Figure 7.24: Schematic of the order parameter profile. Squares: Initially assumed order parameter profile without disordering interface. Circles: Deduced order parameter profile with disordering interface.

In Fig. 7.24, a schematic including the adjustable parameters ($\Psi_{\rm hom}$, $\Delta\Psi$, $\Psi(D)$, and ξ) is depicted. The intensity distribution based on the order parameter profile shown in Fig. 7.23b (circles) is indicated by the solid line in Fig. 7.23a (circles). Also indicated in Fig. 7.23b is the value of $\Psi_{\rm hom} = 0.18$. The interface with the MgO-cap is considerably disordered ($\Psi(D) = 0.04$), with $\xi = 12$ unit cells. The lowered order at the film/cap interface could also result from a negative surface field ($h_1 < 0$). This case (positive surface field at one interface, negative surface field at the other interface) is denoted in the literature as a (+-)-boundary condition. For the (+-) case, the sign of $\Psi_{\rm hom}$ results from spontaneous symmetry breaking. In this case, an asymmetric order parameter profile is expected above the phase transition temperature ($T = T_c$, $\Psi_{\rm hom} = 0$).

7.9.4 Above T_c

A measurement at $T = 760$ ^{o}C is shown in Fig. 7.23a (triangles); the deduced order parameter profile is depicted in Fig. 7.23b. An order parameter profile localized at the interface with the substrate is observed. However, no (negative) order parameter profile is observed at the interface with the MgO-capping layer. This indicates that the decrease of the order parameter at this interface below T_c reflects indeed the ordinary field-free case. A disordering behavior has not been observed at the free surface, i.e. for the uncapped 350 Å sample. However, in the latter case the effective change of the thickness of the ordered region would be only 3.3 % and therefore the quality of the experimental data does not allow to exclude that also in this case the order at the surface was lowered.

7.9.5 Dimensional crossover

To extract the average ordering behavior at the phase transition without applying a certain model, the difference of the central FeCo(001) intensity and the assumed MgO CTR-intensity is analyzed. Fig. 7.25 shows a logarithmic plot. Two temperature regimes that can be identified with *2d*- and *3d*-behavior are observed. For the 100 Å FeCo film, the temperature region that shows $2d$-behavior is more extended with respect to the 350 Å film, as expected from scaling arguments. A detailed analysis of the diffraction pattern by modeling of the observed intensity distributions may allow for reconstructing the order parameter profiles. However, Fig. 7.23 indicates that the clear cut separation of the order parameter profile in a homogeneous part and a profile localized at the interface with the substrate is difficult. Presumably, a rigorous theoretical interpretation will require the detailed knowledge of the profiles that are expected for the (+O)-boundary conditions, if the surface field-induced length l_1, the correlation length ξ and the film thick-

ness D are of the same order of magnitude. However, these profiles have been calculated yet only within certain limits, i.e. strong adsorption at one interface, that do not apply for the given case.

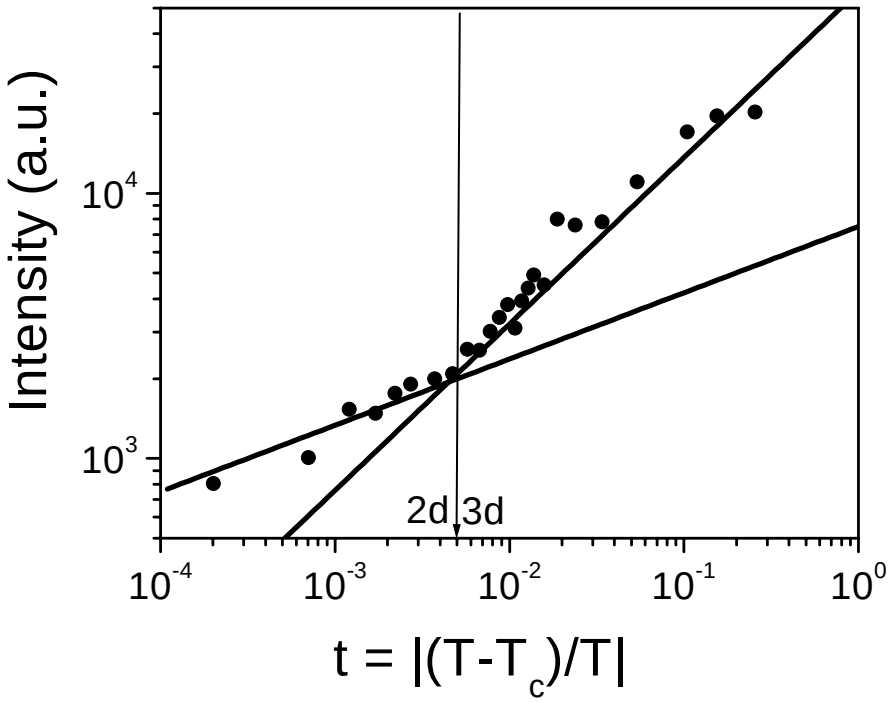

Figure 7.25: Preliminary data analysis for the 100 Å FeCo film. The slope of the solid lines indicates the prediction of the theory for 2d and 3d behavior, assuming $I \sim t^{2\beta}$, with $\beta_{2d} = 0.125$ and $\beta_{3d} = 0.314$. The arrow indicates the crossover reduced temperature t^*, as expected from scaling arguments: $t^* = (D/\ (3 \cdot a \cdot \xi_0))^{-1/\nu} = 0.006$, with $D = 103.7$ Å, $\xi_0 = 0.448$, $\nu\ = 0.643$, $a = 2.86$ Å.

7.10 The MgO-capped 50 Å FeCo film

The MgO-capped FeCo film with a nominal thickness of 50 Å is the thinnest sample that has been studied for various temperatures. The FeCo(002) reflection (Fig. 7.26) is strongly suppressed since it was measured resonantly and with a horizontal detector geometry, with the detector close to 90° at the (002) position. This results in a factor $P = 0.12$ (see Eq. 5.10). The qualitative behavior of the intensity distribution is reproduced. The oscillations vanish and a broad, smooth peak is observed when T_c is crossed, indicating that an order parameter profile localized at the interface with the substrate is present. The angular scans (Fig. 7.27) reveal a mosaic distribution of the FeCo film of $0.67(9)^o$. The detailed analysis of the intensity distribution of the thinner films (50 Å and 100 Å) relies partially on appropriate theoretical estimates of the expected order parameter profiles and will be subject to further studies.

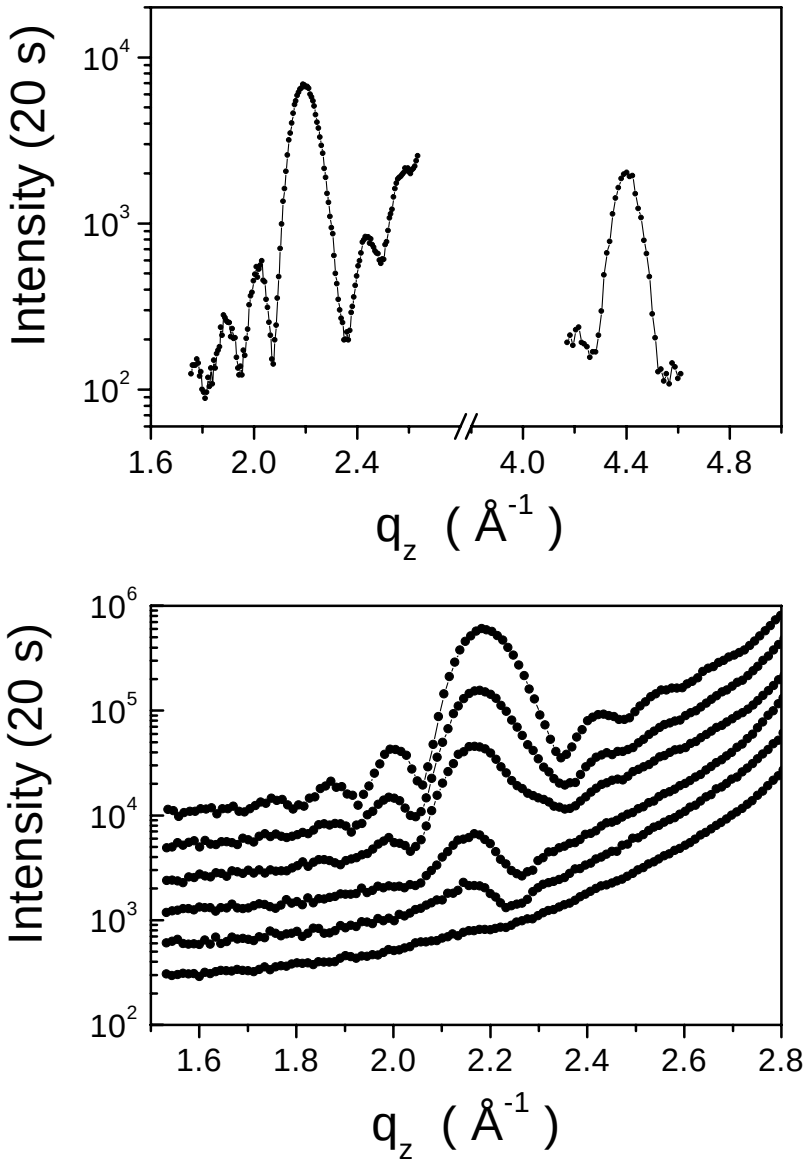

Figure 7.26: X-ray scattering from the capped FeCo 50 Å film. Top) q_z scan including the superstructure FeCo(001) reflection and the fundamental FeCo(002) reflection. Bottom) Temperature-dependence of the FeCo(001) reflection. The curves have been offset for clarity. Sample temperatures (from top): 501 °C, 571 °C, 600 °C, 623 °, 629 °C, 656 °C.

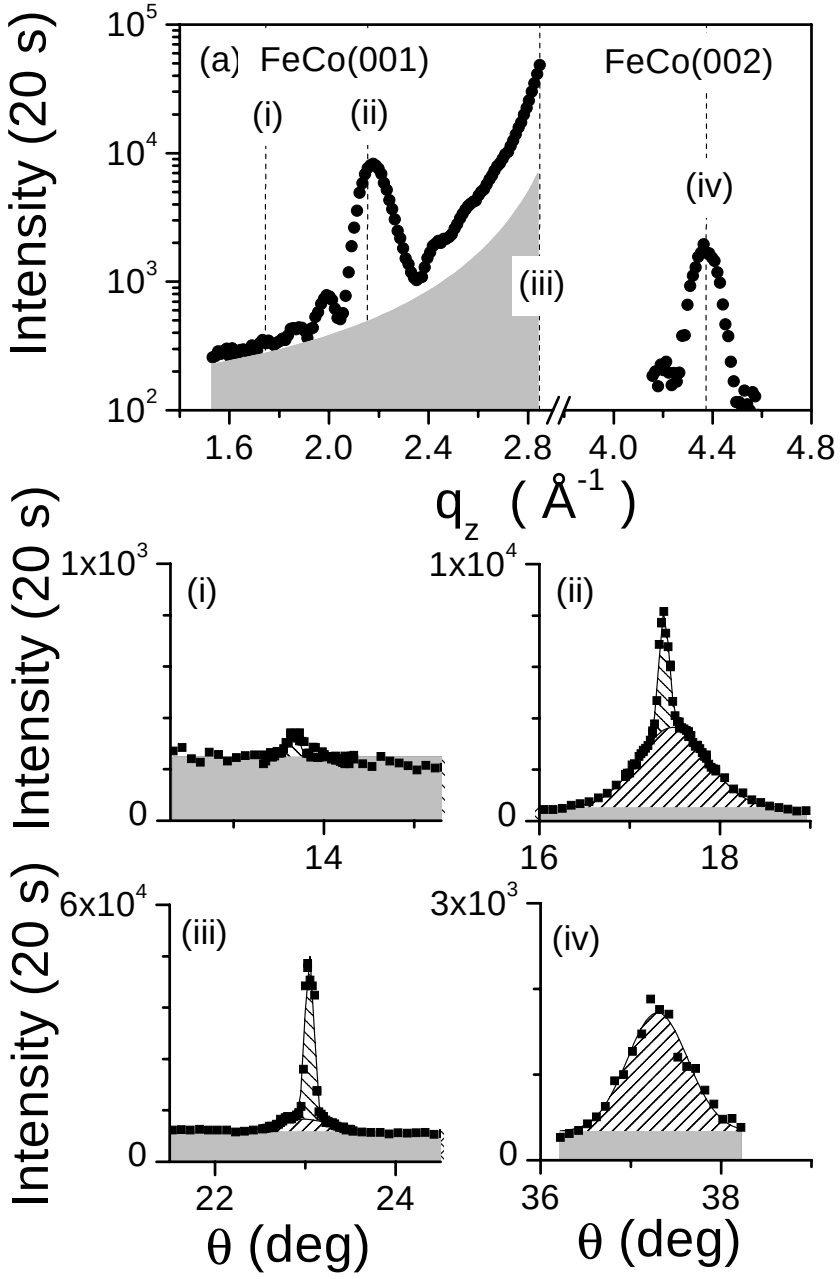

Figure 7.27: X-ray diffraction pattern obtained from a capped FeCo 50 Å film at 571 ^{o}C. a) Extended q_z-scan around the FeCo(001) and FeCo(002) reflections. i)-iv) Lineshape analysis (rocking scans) at the q_z-positions indicated by the dashed lines in a.

Chapter 8

Antiferromagnetic coupling in Fe/Cr multilayers

8.1 Introduction

The antiferromagnetic coupling of Fe layers, separated by a Cr spacer of several atomic monolayers was discovered in 1986 by means of light scattering techniques [9]. Two years later, it was discovered [7] that the resistance of such a multilayer depends strongly on the applied external field. This phenomenon is called the giantmagneto resistance effect (GMR). It is observed for a variety of different systems and it is a textbook example of how fast industry can employ new scientific results in applications. For example, modern hard disks have read/write heads which use the GMR effect and suppliers of cars intend to use it as a sensor for the mechanical control systems. As will be discussed in the Sec. 8.2, interlayer magnetic coupling and the GMR effect depend crucially on the real structure of the Fe/Cr interfaces. Therefore the question arises as to which extent information about the magnetic and chemical structure of deeply buried interfaces in multilayer samples can be obtained. The experimental approach that has been chosen in this

work is spin-resolved neutron scattering. This measurement technique has the potential to extract the laterally-averaged magnetic and chemical depth profiles. Furthermore, it gives access to the local correlations of the magnetic and chemical arrangements, i.e. the local deviations from the mean structure which then might be associated with real structural effects such as for example terraces or a hill-and-valley structure. This is discussed in Sec. 8.3. For a clear-cut discrimination between the magnetic and non-magnetic contributions to the scattering signal it is mandatory to polarize the incident neutron beam and to analyze the spin-states of the scattered neutrons. If large sections in reciprocal space are to be explored, multi-detection techniques (wire detectors) should be used in order to obtain feasible measurement times. This requires the development of new neutron-spin analyzers and this is an active field of research. In this work, polarized ^{3}He has been used for the first time as an analyzer in a neutron reflectivity experiment and an appropriate instrumental setup was developed for the EVA reflectometer. This is reported in Sec. 9.1.2. The experimental results obtained with this setup from an Fe/Cr multilayer are presented in Sec. 9.3.

8.2 Antiferromagnetic coupling and the GMR effect

By systematically varying the Cr-buffer thickness in Fe/Cr multilayer samples, a maximum in the antiferromagnetic coupling strength for a spacer thickness of about 16 Å was revealed [123]. In 1991, two groups discovered that in thin films with sharp interfaces, the thickness dependence of the magnetic coupling is more complex [10, 124]. A period with two monolayers of Cr and a longer period of 11 monolayers (15.5 Å) switch the coupling from ferromagnetic to antiferromagnetic. In samples with less well-defined inter-

faces, only the 11 monolayer oscillation is observed[10]. The experimental results are given in Fig. 8.1.

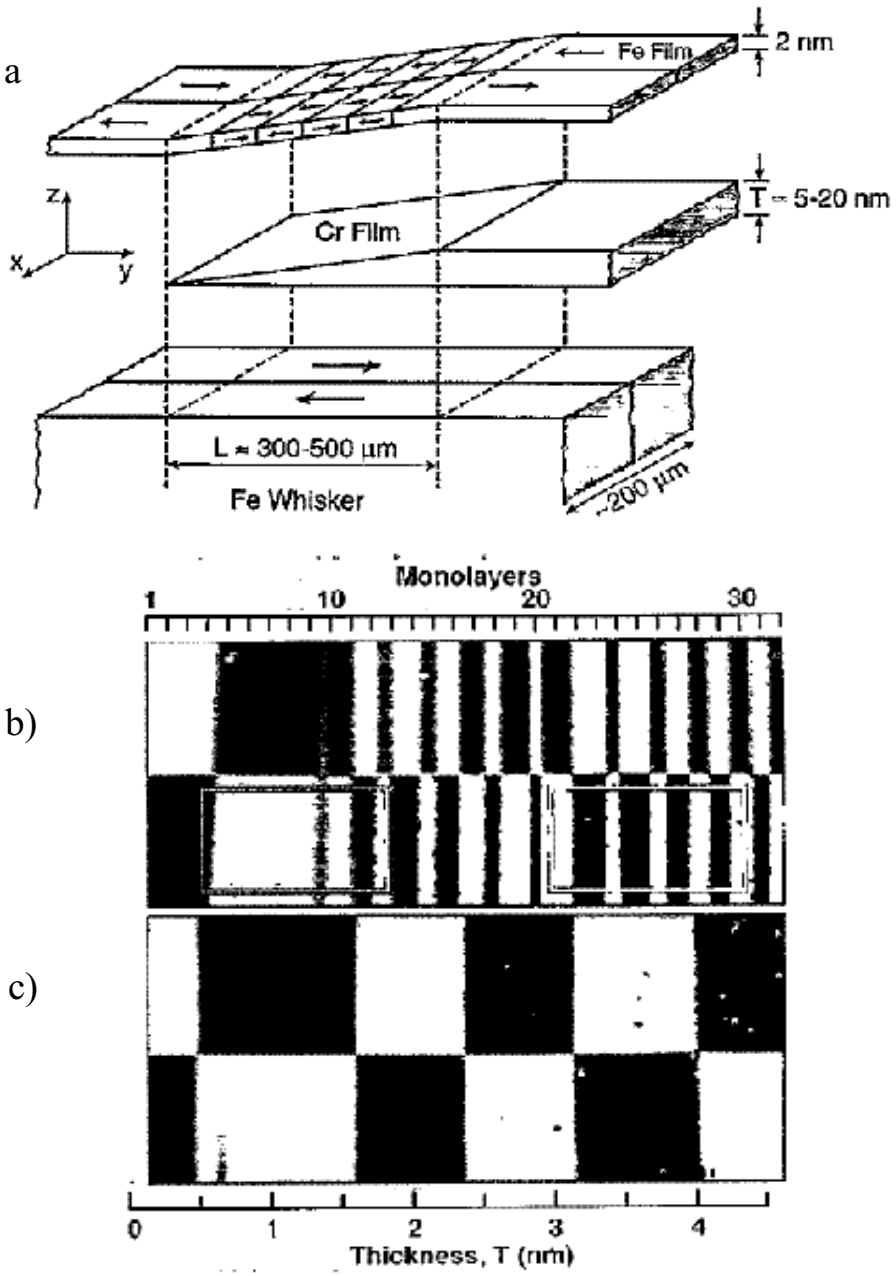

Figure 8.1: a) Figure of a wedge-like Fe/Cr/Fe(001) sandwich. b+c) SEMPA pictures. b) Sharp interfaces; within one additional monolayer Cr, the coupling changes, resulting in a change from black to white in the microscope. c) Rough interfaces. Figures from [10].

The quality of the interfaces may even affect the direction of the coupling. For non ideal interfaces, a pronounced biquadratic coupling, which favors a 90° orientation of adjacent iron layers is observed [125]. Theoretical calculations using exchange energies of ideal systems allowed to connect biquadratic coupling to the presence of terraces [11]. More generally, biquadratic coupling is expected, if the two monolayer oscillations in the coupling of the respective ideal system are pronounced, since terraces easily generate magnetic frustrations in this case. A figure of a magnetically frustrated system is given in Fig. 8.2. Other possible origins of biquadratic coupling are loose spins in the spacer material [126] and pinholes through the spacer material [127]. By correlating specular x-ray measurements on more than one hundred Fe/Cr multilayer samples with the respective magneto transport measurements it has also been shown that roughness increases the GMR effect[128]. Recent experiments revealed that for Cr-spacers thicker than 42 Å cooling below the Neél temperature may suppress biquadratic coupling [129].

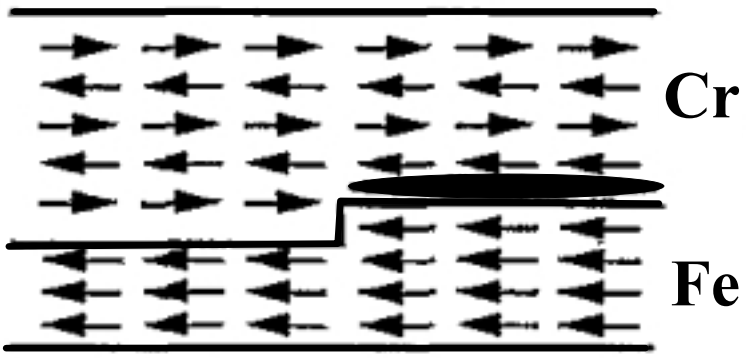

Figure 8.2: Figure of a magnetically frustrated system (shaded area). Figure from [129].

The theory that connects the coupling and the electronic band structure in this system is the RKKY-theory (Ruderman, Kittel, Kasuja, Yosida) [126]. This picture is further complicated by the magnetic state of the chromium,

i.e. the existence of spin density waves and their coupling to the iron layers [130, 131, 132]. The ultimate information that one would like to have at hand is the spatially-resolved distribution of the atoms and their magnetic moments, especially at the interfaces. One experimental approach in this direction is the use of neutron scattering methods, which allow determining the local correlations of the magnetic moments.

8.3 Off-specular neutron scattering and real structure

The diffraction pattern from imperfect magnetic multilayers, see Fig. 8.3a, can be divided into two contributions. The sharp, specularly reflected intensity which is characterized by in-plane momentum transfer $q_{\parallel} = 0$ in Fig. 8.3b originates from the laterally-averaged density profile. The off-specular diffuse scattering is caused by local deviations from the average profile. This off-specular scattering appears as a broad diffuse background around the specular reflected beam and it exhibits a characteristic angular dependence which originates from the correlations of the local imperfections.

In order to reconstruct the microscopic details of magnetic roughness and of magnetic domains, it is mandatory to measure the weak diffuse background in the entire reciprocal space within the first Brillouin zone. Fig. 8.3b shows schematically the diffuse scattering associated with the real structure of Fig. 8.3a as a function of the in-plane momentum transfer $q_{\parallel}$. The broad, featureless component results from the local steps and kinks at the interfaces. Its inverse half width is given by the in-plane correlation length ξ_{R} which is assumed here to be microscopically small. The other diffuse component is due to small angle scattering from magnetic domains of submicrometer size ξ_{D}. Roughness or domain correlations between adjacent layers can be seen

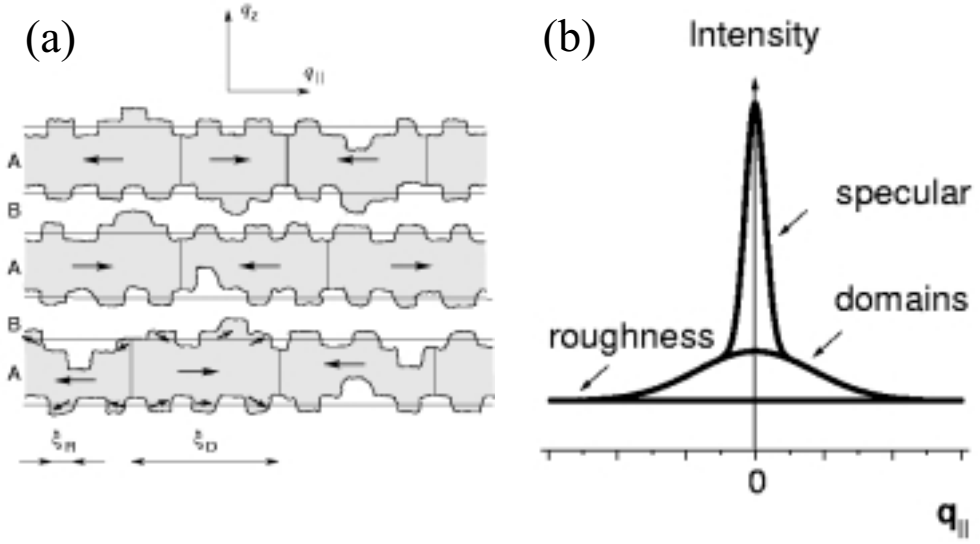

Figure 8.3: a) Sketch of a rough multilayer and possible magnetic configurations. b) Resulting diffraction pattern, composed out of different contributions.

in a characteristic modulation of this diffuse scattering as a function of the momentum transfer perpendicular to the surface q_z (see [133]).

Due to the small number of local scatterers present in high-quality multilayer systems, the magnetic off-specular diffuse scattering intensity caused by magnetically rough interfaces and magnetic domains is rather small and this may be buried under the off-specular scattering contribution from the chemical roughness of the interfaces. X-ray scattering techniques appear at first sight more favorable for the study of magnetic roughness correlations than neutron scattering, mainly because of the availability of highly brilliant synchrotron sources providing high x-ray flux at the sample surface. Indeed, in recent experiments the potential of magnetic off-specular x-ray scattering has been successfully explored [134]. Despite the success of these experiments, however, magnetic off-specular x-ray scattering is hampered by

a very low magnetic x-ray scattering cross-section and a rather complicated magnetic x-ray interaction potential, which prevents direct and quantitative access to local correlations of the magnetic moments.

Off-specular diffuse neutron scattering allows to avoid all the aforementioned problems, since it is governed by a rather simple scattering cross-section with a direct access to the spin–spin correlation function, as demonstrated recently for a selected scan in reciprocal space [135]. However, it generally suffers from the low brilliance of available neutron sources. Recording the very low scattering intensity with sufficient resolution but still within reasonable measuring times requires multidetection techniques. On the other hand, the magnetic diffuse scattering must be separated from the nuclear diffuse neutron scattering arising from chemical roughness of the interfaces by using polarized neutrons and applying a spin-analysis of the scattered neutrons. In order to combine these two prerequisites, i.e. the spin-analysis of the scattered neutrons and the application of multidetector systems, a polarized ^{3}He gas spin-filter was used to analyze the polarization of each scattered neutron recorded in the multidetector system.

8.4 The supermatrix approach

Modeling and analyzing off-specular neutron scattering intensities requires an appropriate tool to analyze and model the expected off-specular intensities. Fortunately, the analysis of off-specular scattering is today understood in great detail due to many x-ray experiments and related theoretical work. However, neutrons require a different treatment since they are spin 1/ 2 particles. A proper description of neutron scattering has to account for the neutron spin and possible spin-flip processes. Recently, it has been demonstrated by Rühm *et al.* that the supermatrix formalism [136] is well-suited to calculate the cross-sections observed in reflectivity experiments from arbi-

trary layered magnetic configurations. Combining this formalism with well-established concepts from x-ray off-specular diffraction makes it feasible to model the off-specular neutron scattering cross sections. The total neutron scattering cross section of a magnetic multilayer can be written in the form [111]

$$\sigma_{\,tot} = \bar{A}\mathcal{R}(\mathbf{k}_\mathrm{i}) + \int_{\Delta\Omega_\mathrm{f}} \frac{\mathrm{d}\sigma}{\mathrm{d}\Omega}\,(\mathbf{k}_\mathrm{i}, \mathbf{k}_\mathrm{f})\;\mathrm{d}\Omega_\mathrm{f}\;, \tag{8.1}$$

where $\mathcal{R}(\mathbf{k}_\mathrm{i})$ is the polarized neutron reflectivity, $\bar{A}$ is the cross-section of the detected portion of the reflected beam, $\mathrm{d}\sigma$ / $\mathrm{d}\Omega$ is the differential cross-section for diffuse scattering of polarized neutrons, and $\Delta\Omega_\mathrm{f}$ is the solid angle covered by the detector. $\mathrm{d}\sigma$ / $\mathrm{d}\Omega$ can be represented in the form [137]

$$\frac{\mathrm{d}\sigma}{\mathrm{d}\Omega} = \frac{Ak_0^4}{16\pi^2} \sum_{n,n'=1}^{N} K_{nn'} C_n C_{n'}^*, \tag{8.2}$$

where A is the illuminated surface area, $k_0 = 2\pi/\,\lambda$ is the wave-number of the incident neutrons, and C_n are the complex scattering amplitudes associated with the N rough interfaces $n = 1, ..., N$. To simplify the treatment here it is assumed that all interfaces have the same lateral morphology, which is described by a lateral structure factor

$$S(\mathbf{q}_{||}) = (2\pi)^{3/2} \cdot \xi_{||} \cdot \exp\left(-\frac{1}{2}\;\mathbf{q}_{||}^2 \cdot \xi_{||}^2\right). \tag{8.3}$$

The coefficients $K_{nn'}$ are determined from roughness correlations among the interfaces of different layers. For perfect vertical correlations (compare Fig. 9.6) $K_{nn'}$ reads [137, 138]

$$K_{nn'} = S(\mathbf{q}_{||}). \tag{8.4}$$

Since the diffuse Bragg sheets that are discussed in Sec. 9.3 indicate a highly correlated roughness morphology the model is restricted to this case. Then one obtains

$$\frac{\mathrm{d}\sigma}{\mathrm{d}\Omega} = \frac{Ak_0^4}{16\pi^2} \cdot S(\mathbf{q}_{||}) \cdot \left|\sum_{n=1}^{N} C_n\right|^2. \tag{8.5}$$

The scattering amplitudes C_n are given, within the distorted wave Born approximation (DWBA), by [138]

$$C_n = \int_{z_n}^{\infty} \langle \psi^{\mathrm{f}}(z)|\hat{V}_n(z)|\psi^{\mathrm{i}}(z)\rangle \mathrm{d}z \quad + \int_{-\infty}^{z_n} \langle \psi^{\mathrm{f}}(z)|-\hat{V}_n(z)|\psi^{\mathrm{i}}(z)\rangle \mathrm{d}z \quad ,$$

where $|\psi^{\mathrm{i,f}}\rangle$ denote the neutron wave-functions within the idealized magnetic media without roughness. $\pm\hat{V}_n(z)$ is the scattering potential arising from the roughness σ_n of interface n, located at a distance z_n from the surface. The scattering potential can be modeled by an error function:

$$\hat{V}_n(z) = \frac{1}{2}\left(1 + \mathrm{Erf}\left(-\frac{|z-z_n|}{\sqrt{2}\sigma_n}\right)\right) \cdot \Delta\hat{V}_n \tag{8.6}$$

where $\Delta\hat{V}_n = (4\pi/k_0^2)\cdot(\hat{N}_{n-1} - \hat{N}_n)$. Following Ref. [136], the operator $\hat{N}$ is defined in terms of its eigenvalues and the vector $\hat{\boldsymbol{\sigma}}$ of Pauli matrices,

$$\hat{N}_n = N_n^{\mathrm{nuc}} \; + \; N_n^{\mathrm{mag}} \cdot \mathbf{b}_n \hat{\boldsymbol{\sigma}} \tag{8.7}$$

with N_n^{nuc} denoting the nuclear and N_n^{mag} denoting the magnetic scattering length densities in layer n, and $\mathbf{b}_n$ the unit vector along the respective magnetic field. For small angles of incidence ($q\prime_z \ll 2\pi/\sigma_n$, with $q\prime_z$ as the momentum transfer within the layers) it can be shown that

$$C_n \approx (2/\pi)^{\frac{1}{2}} \cdot \sigma_n \cdot \langle \psi_n^{\mathrm{f}}|\Delta\hat{V}_n|\psi_n^{\mathrm{i}}\rangle. \tag{8.8}$$

The neutron wave-functions $|\psi^{\mathrm{i,f}}\rangle$ can be calculated using the supermatrix formalism developed in Ref. [136] by Adrian Rühm and coworkers. Motivated by the spin-resolved diffuse neutron scattering maps presented in Sec. 9.3.3, he developed a C^{++} program that has been used to analyze the scattering maps rigorously. His contributions are gratefully acknowledged.

Chapter 9

Neutron experiments on Fe/Cr multilayers

9.1 The evanescent neutron wave diffractometer EVA

The off-specular neutron scattering experiments have been performed at the evanescent neutron wave diffractometer EVA at the research reactor of the Institute Laue-Langevin in Grenoble. The high-flux neutron reactor operates at a thermal power of 58 MW using a single fuel-element. A horizontal cold source of liquid deuterium (D) at 25 K enhances the neutron flux at wavelengths above 3 Å. The wavelength used at EVA ($\lambda = 5.5$ Å) is close to the flux maximum. The neutrons are guided to the instrument by ^{58}Ni-coated mirrors. EVA is designed as a test instrument to explore the potential of neutron surface- and interface-scattering using tunneling (evanescent) neutron waves [139][140].

Three techniques can be employed:

1. Reflectometry, to examine the depth dependence of the refractive index

from solids and liquids.

2. Off-specular (diffuse) scattering, which is sensitive to magnetic and nonmagnetic roughness correlations.

3. Grazing incidence diffractometry, which reveals the depth dependence of lateral order. This technique is used to study surface and interface effects in antiferromagnetic and ferromagnetic crystals and thin epitaxial films [141, 142].

9.1.1 Experimental setup: monochromator, detector and polarization

A sketch of the experimental setup is shown in Fig. 9.1. The instrument is supplied with neutrons of wavelength $\lambda = 5.5$ Å by a horizontally focusing monochromator, which is assembled of five highly oriented pyrolytic graphite (HOPG) crystals with an individual mosaic spread of 0.3° FWHM (full width at half maximum). The focal length is conveniently tunable by stepping-motor-controlled goniometer heads. For reflectivity experiments the focal spot is tuned to the sample position to maximize the flux at the sample surface. Furthermore, the reflected beam from the monochromator can be tilted vertically for experiments on liquid surfaces, as sketched in Fig. 9.2. For example, the free surface of a ferrofluid has been studied at EVA using this setup [143] and spin-resolved measurements are planned for the future.

The monochromatic beam can be polarized in the y-direction by means of a polarizing transmission mirror (PM) with a polarizing efficiency of $p_1 = 97$ %. By a downstream Mezei flipper SF_1 (with a flipping efficiency of $f_1 = 97.5$ %) the polarization of the beam can be reversed into the $-$y-direction. At the sample position a magnetic field B of between 50 and 400 mT can be applied parallel to the sample surface (y-direction). The

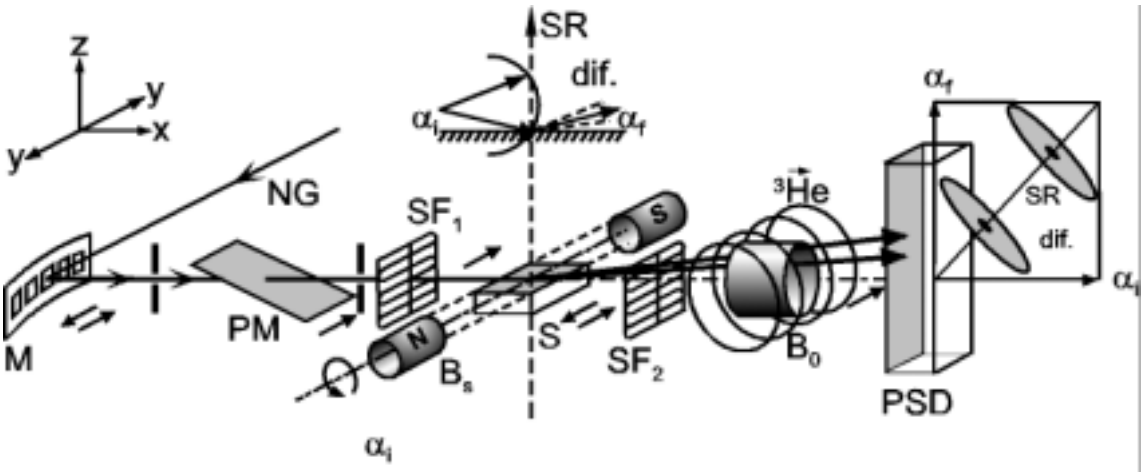

Figure 9.1: Outline of the experimental setup, including the ^{3}He analyzer. The neutrons are supplied by a neutron guide NG and diffracted by a monochromator M. After passing a slit they are polarized by a transmission mirror PM and may be flipped by a Mezei flipper SF_1. The sample S is placed in an external field B and can be inclined by an angle α_i. The reflected or scattered neutrons pass a second flipper SF_2 before entering the ^{3}He vessel placed in a homogeneous field B_0. A position sensitive detector PSD acquires the exit angle profiles containing the specular rod SR ($\alpha_i = \alpha_f$) together with the off-specular scattering.

specularly reflected and off-specular scattered neutrons are simultaneously recorded by a linear position-sensitive wire counter providing exit-angle scans ('α_f-scans'), as shown in Fig. 9.1.

Two analyzer systems are available. The first one is a polarizing transmission mirror, similar to the polarizer. Due to the simple transmission geometry the alignment is fast and easy. This analyzer setup is used for reflectivity experiments. A flipping ratio of 24 is obtained routinely[1]. For some appli-

[1]The flipping ratio is defined as the ratio of the polarized beam intensities for different flipper settings and is a measure of the degree of polarization. The flipping ratio of an unpolarized beam is 1.

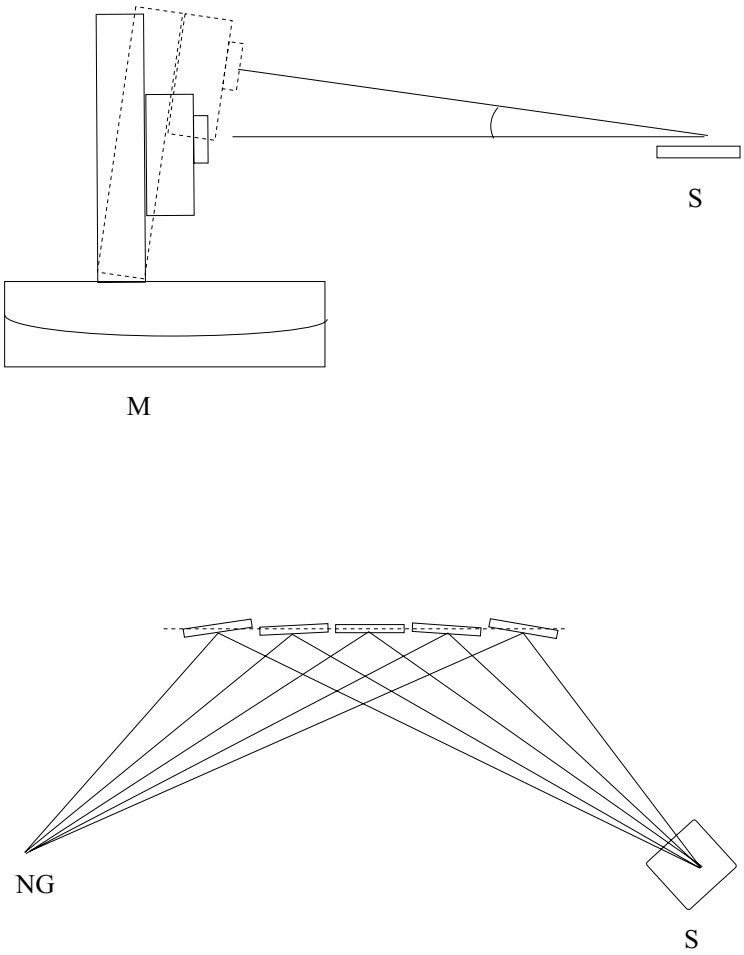

Figure 9.2: Top: Side view of the monochromator setup (M) for reflectivity measurements on liquid surfaces (S). Bottom: The neutrons are provided by a neutron guide (NG) and the monochromatic neutron beam may is focused horizontally on the sample position (S).

cations, however, the low acceptance rate of the transmission mirror (about 0.06°) is not satisfying. In these cases a ^{3}He analyzer is used, which will be

described now.

9.1.2 The ^{3}He analyzer.

For the analysis of the spin state of neutrons recorded in the detector a polarized ^{3}He gas neutron spin filter can be installed between the sample and the detector (details of the ^{3}He filter will be given below). This setup allows recording an α_f-scan for all four cross-sections $|++\rangle$, $|--\rangle$, $|+-\rangle$ and $|-+\rangle$ (here $+$ refers to the spin up and $-$ to the spin down state of the neutron) for each set of incidence angles (α_i) with respect to the sample surface. An α_f-profile measurement is typically completed within 1000 s.

The neutron spin filtering technique is based on the strongly spin-dependent neutron absorption cross-section of ^{3}He. Is is $\sigma_{\uparrow\downarrow}$=3000 bn for antiparallel and $\sigma_{\uparrow\uparrow}$=5 bn for parallel neutron states with respect to the ^{3}He polarization. For a given ^{3}He polarization P_{He} the neutron transmission $T_\pm$ of the ^{3}He filter can be written as [144]

$$T_\pm = 0.5 \cdot \exp\Big(-\varrho \cdot (1 \mp P_{\mathrm{He}}) \Big) \tag{9.1}$$

where ϱ is the dimensionless opacity ($\varrho = 0.073 \cdot \frac{p}{\mathrm{bar}^{-1}} \cdot \frac{l}{\mathrm{cm}^{-1}} \cdot \frac{\lambda}{\mathrm{\AA}^{-1}}$). l is the length of the ^{3}He cell, p is the ^{3}He gas pressure and λ is the neutron wavelength. The associated polarization of the neutrons after passing the ^{3}He cell is then given by

$$p_2 = \frac{T_+ - T_-}{T_+ + T_-}. \tag{9.2}$$

The ^{3}He spin filter used in this test experiment is a cylindrical cell with 100 mm length and 50 mm outside diameter (wall thickness is 5 mm) fabricated of duran glass with monocrystalline silicon caps of 4 mm thickness (used for beam entry and exit) filled with polarized ^{3}He gas to a pressure of 1.45 bar, resulting in $\varrho = 5.82$. The figures of merit for this setup are listed in Table 9.1.

	0 h	24 h	48 h
P_{He}	55 %	37 %	25 %
T_+	3.6%	1.3%	0.6 %
T_-	0.0062%	0.017 %	0.0035%
p_2	99.7%	97.3%	89.3%

Table 9.1: Calculated parameters of the used neutron spin filter, using $p = 1.45\ bar$ and $\tau = 60\ h$.

After filling the ^{3}He polarization cell with typically 55 % polarized gas, the polarization decays with a relaxation time of $T_1 = 60$ h. This means that the ^{3}He polarization has decayed from 55 % to 37 % after a typically 24 h measuring time. The initial polarization efficiency of this spin-filter arrangement is $p_2 = 99.7\%$, which is excellent compared with other filter schemes. After 24 h, the polarization efficiency is still 97.3%. In order to archive this long relaxation time, the ^{3}He vessel has to be installed in a homogeneous magnetic environment assuring a small magnetic field gradient $(1/\ B)\mathrm{d}B/\ \mathrm{d}x$ of less than $3 \cdot 10^{-4}$ cm^{-1} [144]. For the EVA setup this homogeneity is achieved using a so-called Braunbek coil arrangement [145] around the ^{3}He vessel (see Fig. 9.1). Fig. 9.3 shows the measured magnetic field distribution inside the Braunbek coils in the presence of a sample magnetization field of $B = 4$ kG. Due to the heavy shielding of the sample magnet, the field gradient is within the allowed limit. A photograph of the experimental arrangement is presented in Fig. 9.4.

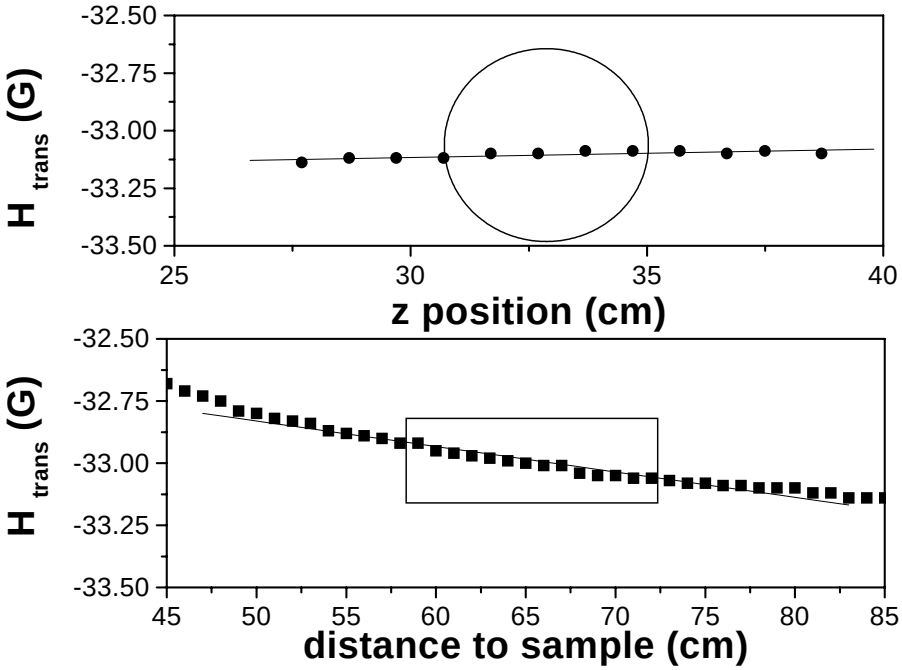

Figure 9.3: The homogeneity of the transverse field at the spin filter position. The field at the sample position is 56 mT. The field distribution was measured using a Hall probe.

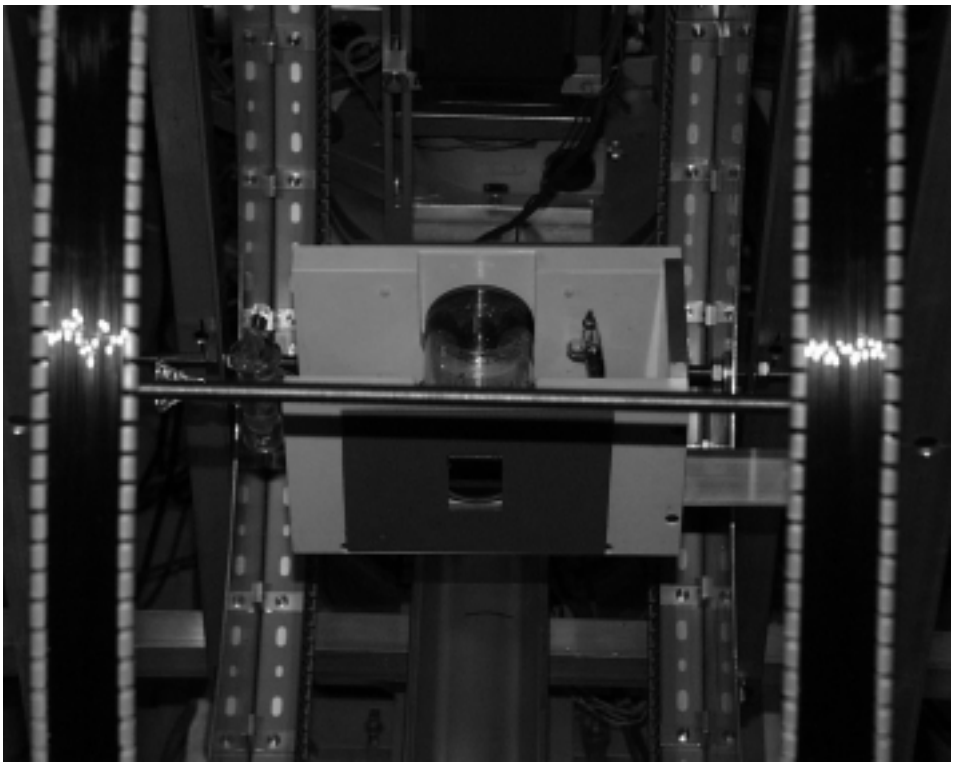

Figure 9.4: Photograph of the ^{3}He spin filter cell, placed inside the Braunbeck coils and masked with B_4C.

9.1.3 The efficiency of the ^{3}He filter

Prior to the actual spin-resolved off-specular scattering experiments the performance of the arrangement has been tested carefully (without sample) to determine the efficiency of all components acting on the neutron spin. This was done in accordance with the procedure described in Refs. [146, 147] which allows to determine the transmission coefficients T_+, T_- of the ^{3}He-analyzer setup as well as the polarizer (p_1) and analyzer (p_2) efficiencies and the flipper (f_1, and f_2) efficiencies. In this procedure, each optical component is described by a (2×2) matrix that acts on the initial polarization of the neu-

tron beam. The parameters of the ^{3}He filter setup, reconstructed from the measurement of the direct beam intensities ($I_{\text{on on}}, I_{\text{on off}}, I_{\text{off on}}, I_{\text{off off}}$)[2] are summarized in Table 9.2. The analyzer efficiency p_2 is close to the estimated values listed in Table 9.1. However, the efficiency of the second flipper ($f_2 = 94(2)\%$) is relatively low with respect to the expected efficiency of $f_2 = 99\%$. Therefore, in future experiments, the second flipper will be magnetically shielded from the guide field of the Braunbek coils.

	1h	24 h	1 h	24 h
$I_{\text{on on}}$	30.0	11.4	26.5	16.5
$I_{\text{on off}}$	2.0	1.9	1.6	2.5
$I_{\text{off on}}$	3.4	3.2	1.8	3.9
$I_{\text{off off}}$	31.2	11.9	28.2	16.5
$f_2(\%)$	93.0	93.0	97.0	93.5
$T_+(\%)$	4.2	1.55	3.55	2.25
$T_-(\%)$	0.08	0.25	0.065	0.25
$p_2(\%)$	96.3	72.0	96.4	80

Table 9.2: The parameters of the analyzer optics (spin flipper and ^{3}He neutron spin filter) for two different filling cycles of the neutron spin filter. All count rates are monitor normalized and equivalent to counts/sec.

9.2 Fe/Cr sample preparation

In order to explore the potential of the experimental setup described in Sec. 9.1.2 for detecting spin-resolved off-specular neutron scattering, Fe/Cr

[2]The index indicates whether flipper one and flipper two (see Fig. 9.1) are active ("on") or not ("off").

was chosen as a model system of a magnetic multilayer. A multilayer sample with 200 periods of 19 Å Fe and 42 Å Cr has been grown [131][3] on a Nb buffer on a large (5×5 cm^2) substrate Al_2O_3 $(1\bar{1}02)$ substrate. Nb(001) grows epitaxially on an $Al_2O_3(1\bar{1}02)$ surface with a tilt angle of about 3° with respect to the sapphire surface[148, 149, 150]. The tilt axis is the Nb$[1\bar{1}0]$ axis, which is parallel to the $Al_2O_3[11\bar{2}0]$ axis. As a result the niobium film surface has terraces with step edges running parallel to Nb$[1\bar{1}0]$. A typical terrace length l can be estimated from simple geometrical arguments to be

$$l = 1.65 \text{ Å}/ \sin(3^\circ) = 31.5 \text{ Å} \tag{9.3}$$

The actual value of l is also influenced by the physical miscut of the sapphire surface, which can also influence the direction of the tilt axis [150]. Fig. 9.5 shows an STM measurement performed on similar sample. While a 250 Å Cr-layer was grown on top of the niobium buffer, the crystallinity of the Cr surface improves [150] with increasing Cr-thickness as verified by RHEED measurements. At the same time, a pronounced terrace structure develops.

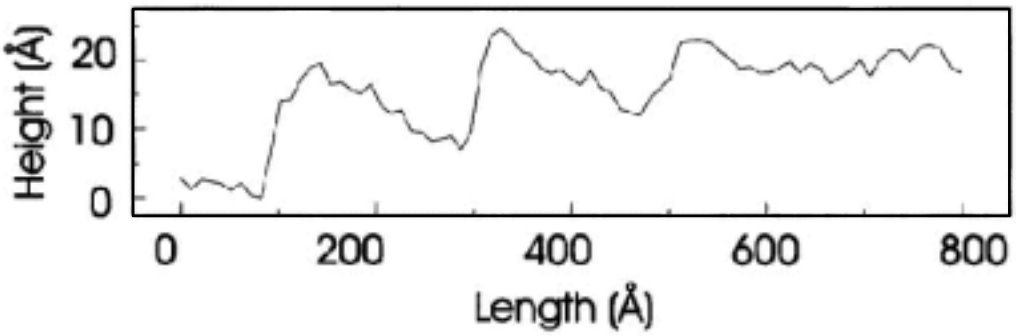

Figure 9.5: STM measurement showing the stepped surface of a 250 Å Cr(001) film on 250 *Å* $Nb/\,Al_2O_3(1\bar{1}02)$. Figure from [150].

For the sample used in this work, Fe and Cr were deposited at 300°C in

[3]in the MBE (molecular beam epitaxy) system of the Ruhr-Universität Bochum

ultrahigh vacuum (better than 10^{-10} mbar) using growth rates of 0.16 Å/s for Cr and 0.2 Å/s for Fe. In situ RHEED measurements performed during growth indicated a smooth growth front with steps. For protection against oxidation, the sample was covered with a 20 Å Cr layer [151]. High angle x-ray data with sharp superlattice peaks up to third order are proof of a coherent superlattice structure. Energy dispersive x-ray (EDX) analysis gave the relative Fe and Cr concentration which, combined with the measured superlattice period, provided the layer thicknesses. X-ray scattering and EDX spectra taken from the center and near the edges of the samples confirmed the lateral homogeneity, due to the continuous rotation of the sample during growth. A combined small angle reflectivity and high angle neutron scattering study yielded a commensurate antiferromagnetic frustrated spiral structure of the Cr which causes the non-collinear coupling between the Fe layers in this sample. The expected growth induced terraced multilayer structure of the sample is depicted in Fig. 9.6.

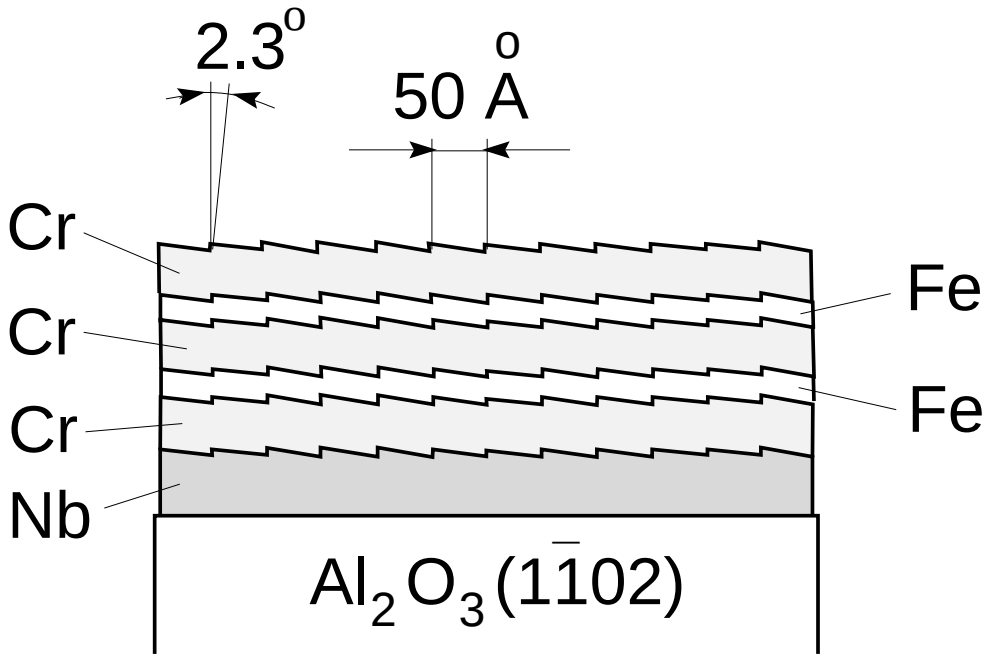

Figure 9.6: The expected structure of the Fe/Cr multilayer according to the epitaxial boundary conditions.

9.3 Results and discussion

9.3.1 Unpolarized diffuse maps

The measured $\alpha_i - \alpha_f$-map is shown in Fig. 9.7, disclosing a specular intensity along q_z ($\alpha_i = \alpha_f$-line) superimposed with a strong diffuse scattering; this is essentially bunched into two diffuse sheets perpendicular to the specular rod. The specular intensity (labeled a in Fig. 9.7) is depicted in Fig. 9.8 and it consists of three features which may be understood in a rather simple way: the total reflection regime is seen for small angles of incidence, and a full-order Bragg reflection from the Fe/Cr double-layer unit cell occurs at α_i=2.6° associated with a perpendicular momentum transfer $q_z = 0.011\text{Å}^{-1}$. This

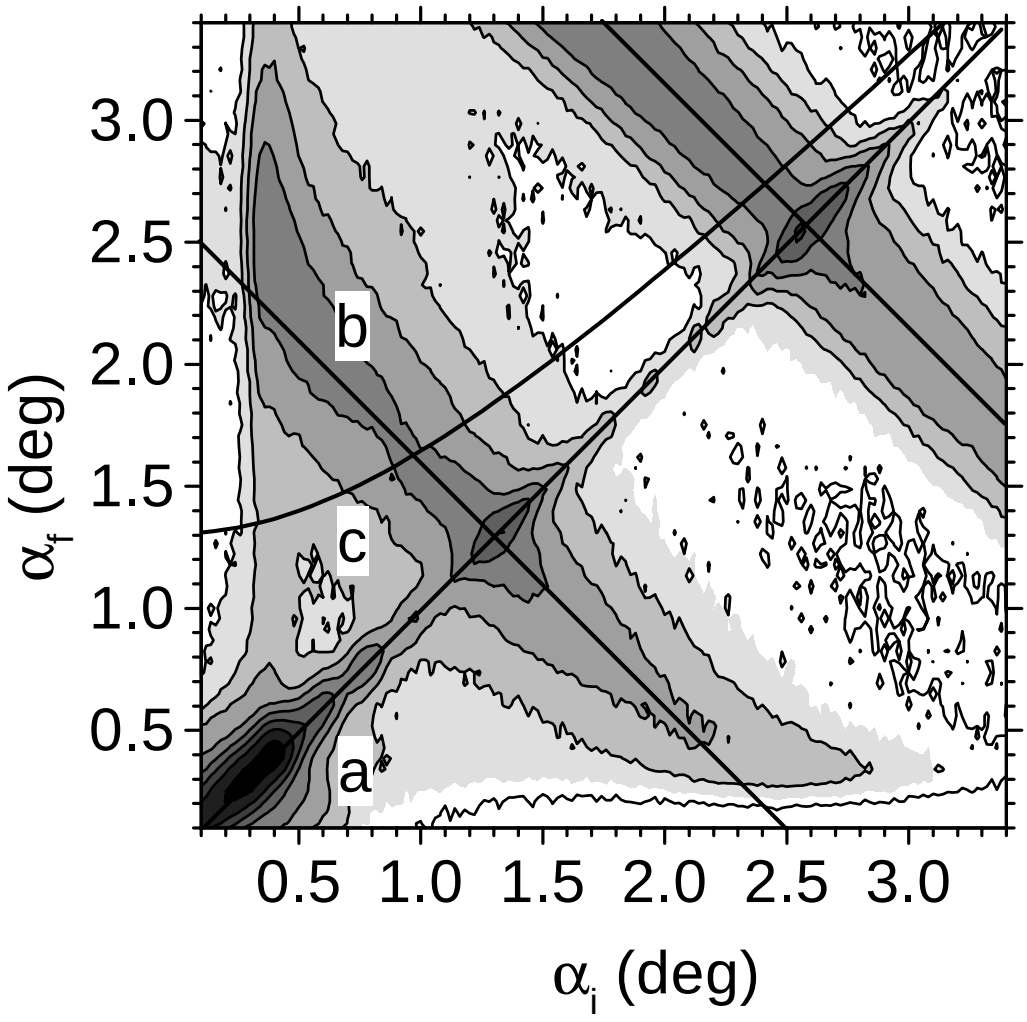

Figure 9.7: The α_i - α_f map generated from 170 α_i measurements. The total acquisition time is 650 sec. Each point in the intensity map is averaged over 1 mm of the PSD (10 channels) ($\delta\ \alpha_f = 0.044°$). The intensity ranges from 20 to 20000 counts, and the scale is logarithmic. The contour lines are separated by a factor of 2.78. The lines and labels refer to linescans which will be extracted from the two dimensional data sets.

periodicity ($L = 1$) is mediated by the chemical unit cell and ferromagnetic contributions in the magnetic structure of the Fe layers. The additional Bragg reflection observed at the half-order ($L = 0.5$) position is due to the doubling of the unit cell caused by an antiferromagnetic arrangement of magnetic moments in adjacent Fe layers; this is therefore of purely magnetic origin.

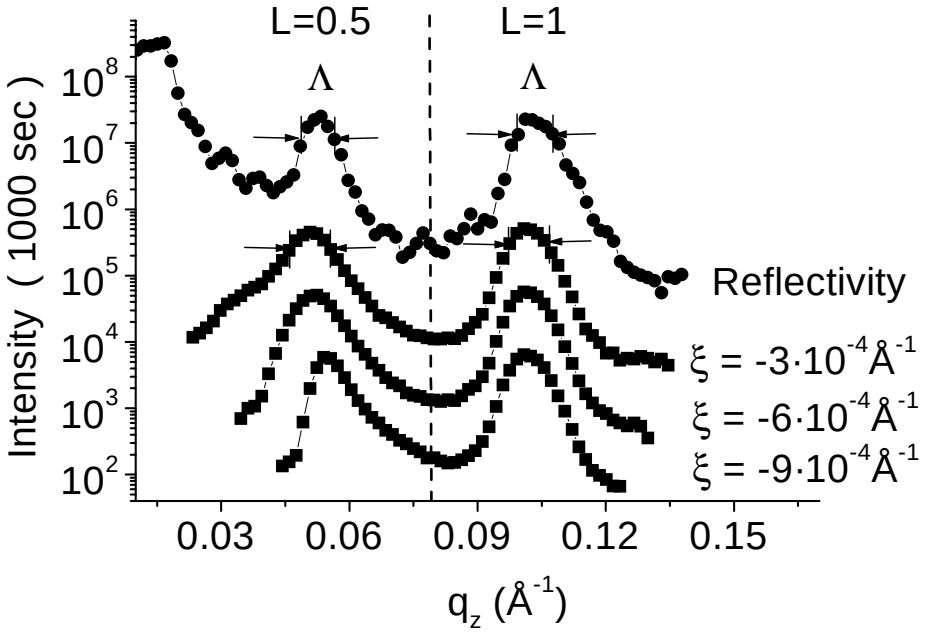

Figure 9.8: Reflectivity and offset linescans along q_z extracted from the two dimensional scattering map (see Fig. 9.7, labels "a" and "c").

The strongly bunched diffuse sheets which emanate at the full-order and at the half-order Bragg positions are caused by the miscut-induced roughness of the Fe/Cr interfaces, which is apparently strongly correlated in growth direction. The diffuse scattering (Fig. 9.9) is almost constant in the in-plane direction (the distortions of the intensity contours visible at the half-order diffuse sheet are due to Yoneda scattering). This observation can be understood in a straightforward way by the short in-plane length scale of approximately

50 Å; this gives rise to a smooth intensity distribution in the α_i-scan. The slope of the $q_\parallel$-scan in Fig. 9.9 is mainly caused by the unidirectional step structure of the sample, giving rise to an asymmetry in the diffuse intensities in the $q_\parallel$-direction [137]. This effect is superimposed on an asymmetric resolution function [152]. A closer inspection of the in-plane scans in Fig. 9.9 reveals a larger length scale in the diffuse scattering at the half-order reflection. This additional scattering is caused by magnetic domains with a typical lateral length scale of 1 μ which are antiferromagnetically ordered in growth direction of the multilayer [135]. In the following the smooth component arising from the interfacial roughness will be analyzed. Fig. 9.8 shows some typical scans parallel to the specular rod in the q_z-direction (offset scans). The FWHM of the full-order diffuse peak is consistent with the correlation length deduced from the widths of the specular peaks. This observation implies that the vertical roughness correlations are limited by the coherence of the average multilayer structure.

9.3.2 Polarized diffuse maps

The contour maps obtained with a polarized incident neutron beam are shown in Fig. 9.10a. In Fig. 9.10b the associated specular intensities are shown. On the specular rod, a slight shift of the critical angle between the $|+\rangle$ and the $|-\rangle$-state is observed; this is indicative of a net magnetization in the sample. In addition, the intensities at the integer-order reflection differ by a factor of four. These observations give unambiguous evidence for a ferromagnetic contribution in the integer-order scattering. The simultaneous observation of a bunched intensity at the half-order position implies the presence of an antiferromagnetic component in the stacking of Fe layers. This points to a non-collinear coupling of the Fe layers across the Cr-spacers. The simplest arrangement of magnetic moments that can explain both ob-

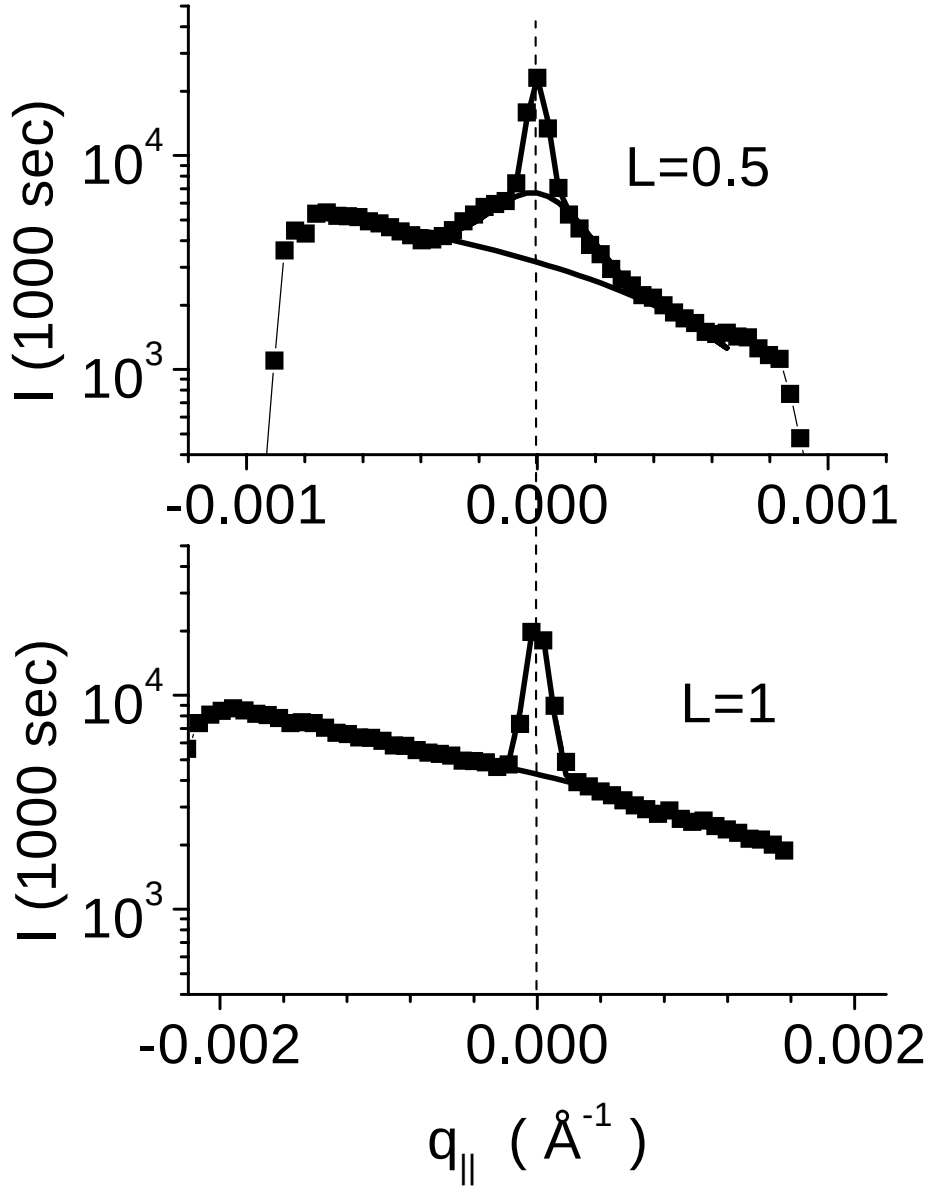

Figure 9.9: A q_p linescan along the two diffuse sheets at the half-order position $L = 0.5$ (top) and the full-order position $L = 1$ (bottom). See the text for a discussion of the lineshape.

servations is drawn in Fig. 9.11. The scattering geometry can be seen in Fig. 9.11a, while Fig. 9.11b shows the average layer magnetization of adjacent iron layers and Fig. 9.11c shows the projections of the layer magnetizations. $M_{\parallel}$ points along the external field H_{ext} and ($M_{\perp}$) perpendicular to it. The suggested arrangement of the magnetic moments implies that the intensity at $L = 1/\,2$ is purely of spin-flip nature [131]. This can be verified by means of complete spin analysis.

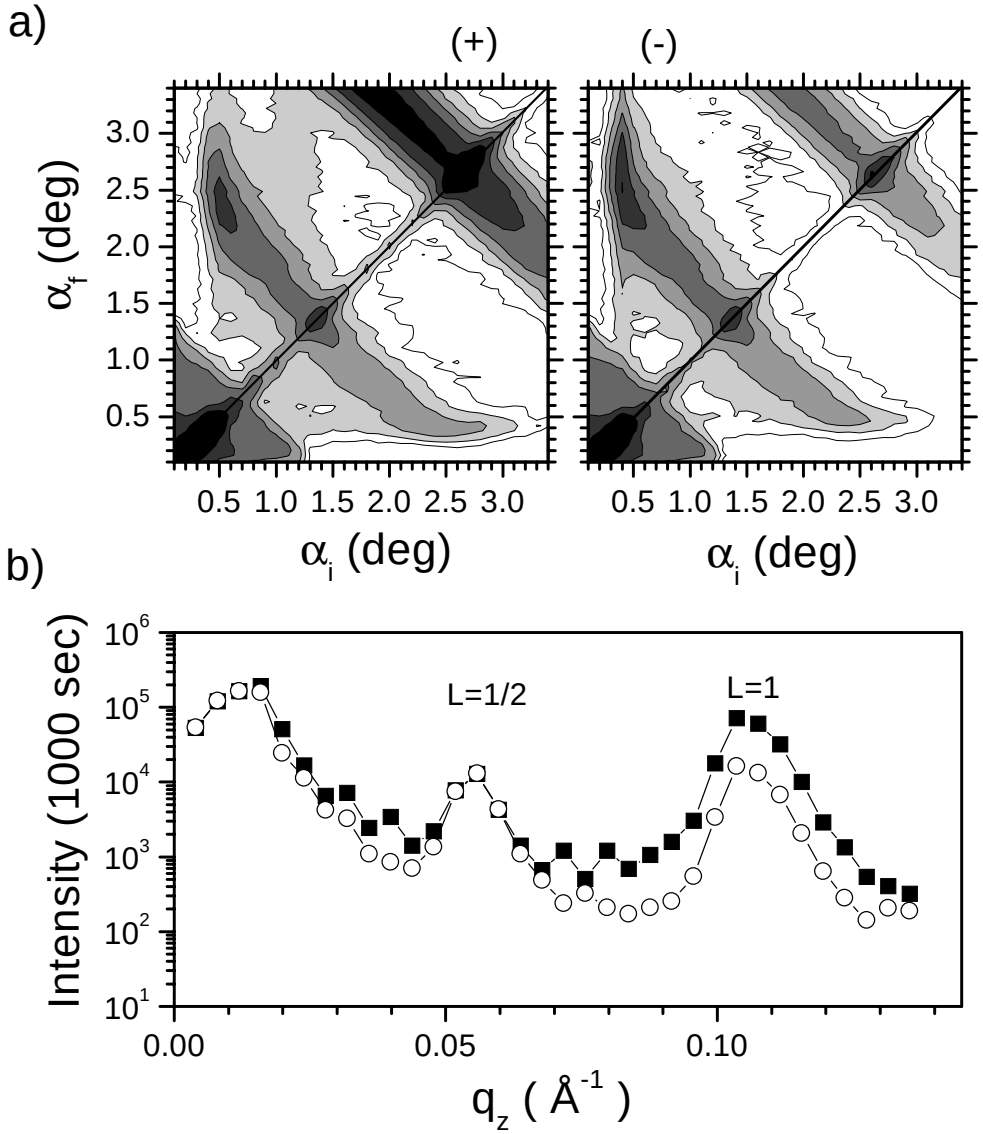

Figure 9.10: a) The same representation as in 9.7, but using polarized neutrons. Left (right) part: neutron spin parallel, $|+\rangle$ (antiparallel, $|-\rangle$) to the external field. The counting time is 2300 s, and the intensity ranges from 60 to 60000 counts on a logarithmic scale. The contour lines are separated by a factor of 2.36. b) Polarized reflectivity. Solid squares: neutron spin along the external field, $|+\rangle$, open circles: neutron spin antiparallel to the external field, $|-\rangle$.

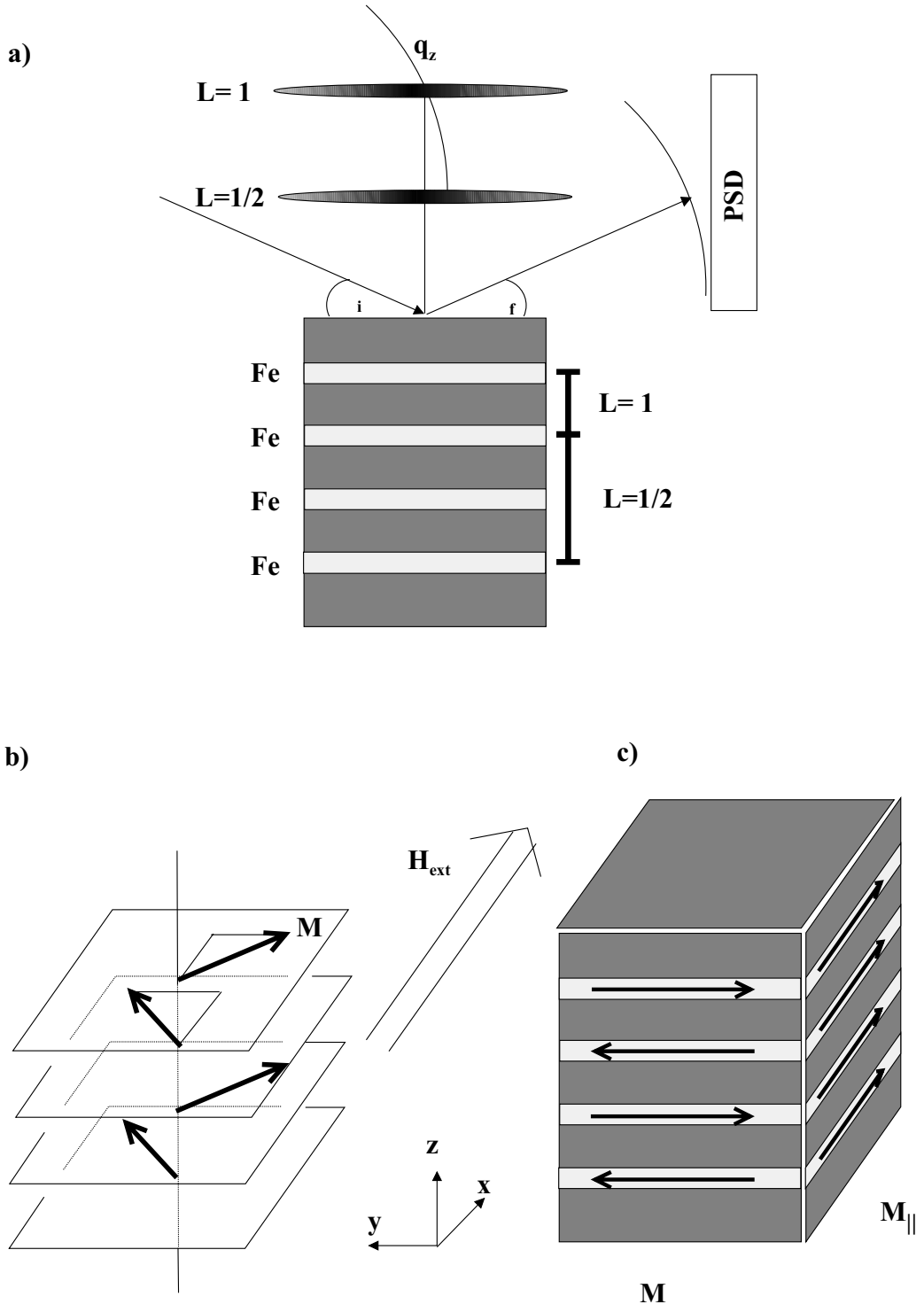

Figure 9.11: Qualitative picture of the mean magnetic configuration inferred from the polarized neutron maps (Fig. 9.10).

9.3.3 Spin-resolved diffuse maps

The four spin-resolved off-specular neutron scattering maps obtained using a ^{3}He filter in combination with a multidetection system are the primary results of this study. They are summarized in Fig. 9.12. Most interestingly, the spin analysis subdivides the maps into two regimes. The off-specular scattering around the integer-order position is essentially of non-spin-flip character ($|++\rangle$, $|--\rangle$). In contrast, the off-specular intensity around the half-order position is dominated by spin-flip ($|+-\rangle$, $|-+\rangle$) scattering. This confirms the magnetic arrangement depicted in Fig. 9.11b, as far as the specular reflectivity is concerned. The spin-dependence of the diffuse scattering is qualitatively identical to that of the specular signal. This suggests that the magnetic roughness correlations are closely related to structural effects decorating the layer-averaged magnetic structure, rather than being affected by qualitatively different other effects.

While basic features of the real magnetic structures can be inferred directly from a simple eye inspection of the maps, a rigorous theoretical treatment is necessary in order to obtain a quantitative measure of the magnetic roughness correlation. This will be addressed in the next section.

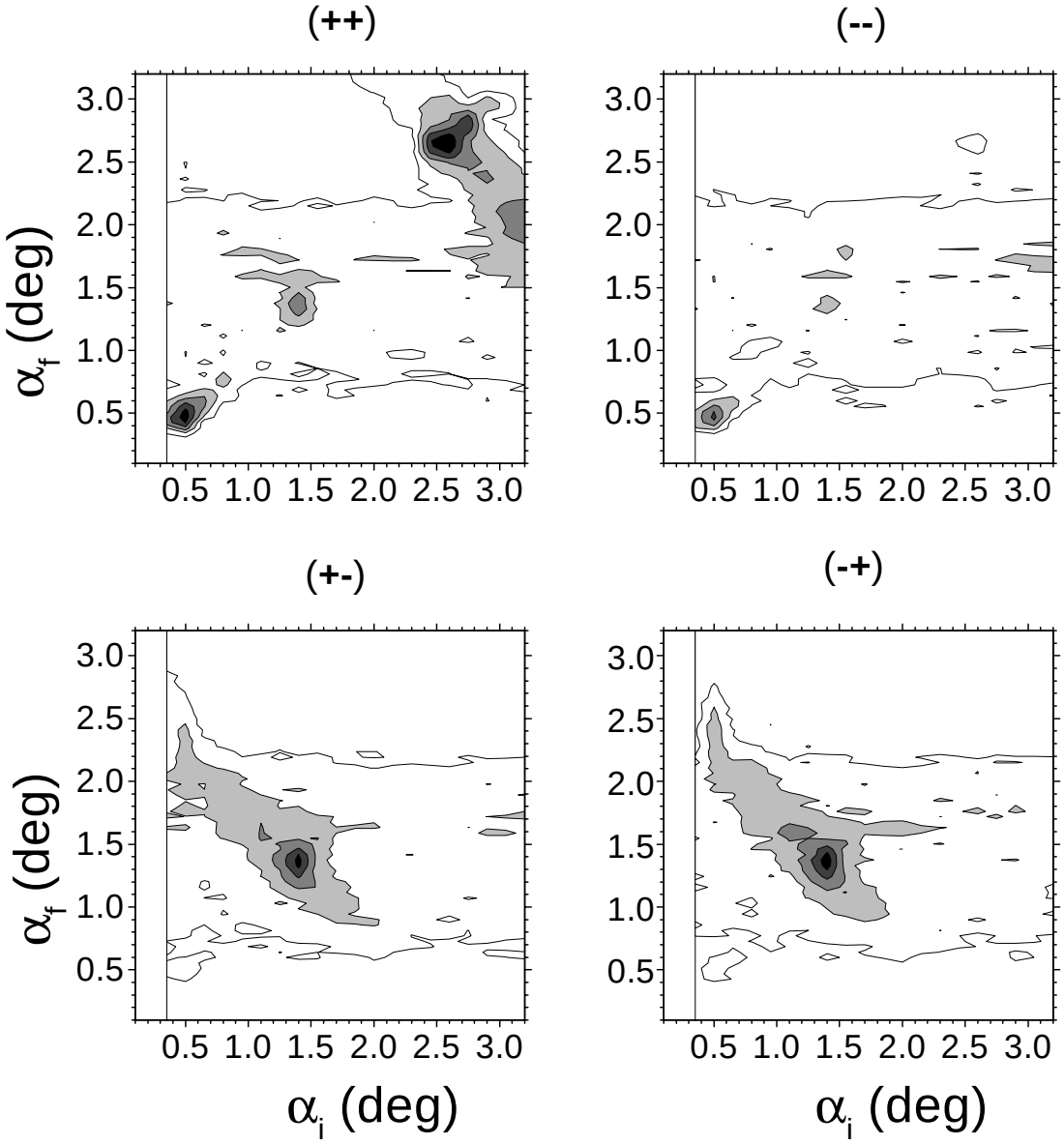

Figure 9.12: The four cross-sections as a function of the incident and exit angles. The scattering maps are generated from α_{f}-profiles recorded at 20 α_{i}-positions. The intensity ranges from 100 to 3000 counts (2200 sec) on a logarithmic scale. The contour lines are separated by a factor of 1.53.

9.3.4 Simulation using the supermatrix formalism

As a starting point for a calculation a simplified model of the magnetic configuration is needed. This model will be based on the following set of parameters:

- The thickness of the Fe and Cr layers is $d_{\mathrm{Fe}} = 19$ Å and $d_{\mathrm{Cr}} = 42$ Å, respectively. The coupling angle between the magnetic moments in sequential Fe layers is 50°.

- The lateral correlation length of about 50 Å is assumed to be microscopic whereas the sample is fully correlated along the growth direction. This implies that the initial terrace structure is transferred throughout the whole sample as suggested by Fig. 9.6. Here, the lateral correlation length represents a typical terrace length [141, 142].

- The roughness σ_n is the basic adjustable parameter in Eq. 8.6. It is assumed that σ_n has no layer dependence ($\sigma_n = \sigma$) and that both the chemical and the magnetic roughness are about 4 Å.

The result of the model calculation based on these parameters is shown in Fig. 9.13. All basic features of the experimental data in Fig. 9.12 are reproduced if the scattering potential is modeled according to Eq. 8.6. This suggests, as the main result of this study, that chemical and magnetic roughness correlations are closely related. In particular, the data are not consistent with a scenario of purely chemical roughness correlations and an arbitrary spin-decoration of the Fe/Cr interfaces which may be introduced via an (effective) $N_n^{\mathrm{mag}} = 0$ in the definition of the scattering potential in Eq. 8.6.

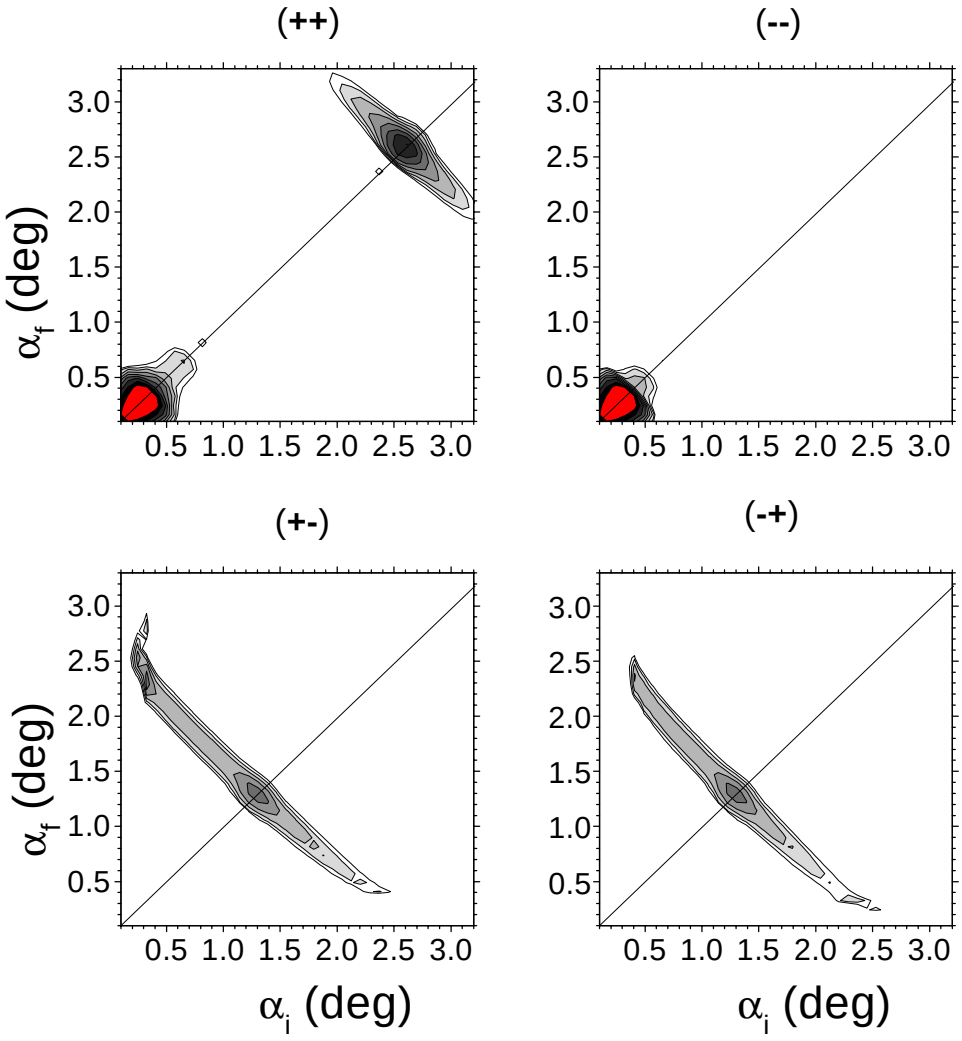

Figure 9.13: The four calculated spin-resolved distributions of intensities as a function of incident and exit angle. See the text for details of the model calculations.

The agreement between measured and calculated data should not be considered to be fully quantitative, though. Technically, the scattering maps were calculated for a system of only 16 rather than 200 bilayers, in order to keep the computing time within a reasonable range. To compensate for the discrepancy in the number of layers, appropriate scaling factors were introduced. Additional scaling factors were applied during analysis of the specular and diffuse intensities in order to improve the agreement with the experimental data. This is to be considered as legitimate, since roughness effects were not taken into account in the calculation of the neutron wave-functions which would complicate the calculations considerably. Furthermore, the q-range probed is not large enough to unambiguously determine the roughness σ , and most likely a roughness gradient is present in the sample, but not taken into account in the calculation.

Chapter 10

Summary and future prospects

10.1 X-ray scattering on thin films of FeCo

This work has produced important, new information about critical phase transitions in thin film of binary alloys. The chief results can be summarized as follows:

- Epitaxial films with thickness between 50 and 500 Å of FeCo(001) have been grown on MgO(001) by means of molecular beam epitaxy. The films are crystalline throughout their entire thickness. Whereas the thicker films ($D \geq 200$ Å) are stable at elevated temperature ($T_{\max} = 800\ ^{\circ}C$), the thinner films had to be capped with MgO to suppress dewetting from the substrate.

- Due to the high structural coherence, x-ray interference effects occur between the x-ray scattering amplitude from the film and the scattering amplitude from the substrate. This allows the extraction of the depth-dependence of the B2 order parameter profiles $\Psi(z)$ on an absolute scale.

- In all films an exponentially-decaying order parameter profile $\Delta\Psi(z) = \Delta\Psi \cdot \exp(-z/\,\xi)$, localized at the interface with the MgO substrate is observed. The decay length of these profiles is identified with the correlation length ξ.

- Below T_c a homogeneous order parameter contribution Ψ_{hom} is observed in addition to the adsorption profile. The total order parameter profile $\Psi(z)$ is given by $\Psi(z) = \Psi_{\mathrm{hom}} + \Delta\Psi(z)$. One sample has been analyzed in great detail (N=121 u.c., D=345 Å). For this sample the temperature dependencies of ξ and Ψ_{hom} are in accordance with the power laws expected from a 3d-Ising model until close to T_c i.e. $\xi = \xi_0 \cdot t^{-\nu}$, with $\xi_0 = 0.43 \pm 0.15, \nu = 0.65 \pm 0.02$ and $t = |(T - T_c)/\,T_c|$. Ψ_{hom} shows also a power law behavior until close to T_c, namely $\Psi_{\mathrm{hom}} = \Psi_0 \cdot t^{\beta}$, with $\beta = 0.347 \pm 0.016$ and $\Psi_0 = 1.79 \pm 0.1$.

- In a narrow temperature window close to T_c ($t^* \simeq 10^{-3}$), we observe a finite size effect. The divergence of ξ stops at $\xi \cong D/\,3$. Furthermore, the temperature dependence of Ψ_{hom} is no longer in agreement with $\beta = 0.347$, but suggests $\dot{\beta} = 0.125$, which indicates that the system behaves like a 2d-Ising system in the vicinity of the phase transition. A detailed analysis of the thinner samples is in progress. A preliminary analysis indicates that the crossover range t^* is much wider for the thinner films ($D \leq 100$ Å), as expected from scaling arguments.

- The temperature dependence of the adsorption profile amplitude $\Delta\Psi$ exhibits a weak to strong absorption crossover. This crossover sets in at a temperature $\hat{t} = 1.5 \cdot 10^{-3}$ since at this temperature, the correlation length ξ becomes comparable to $l_1 = 25$ FeCo unit cells. l_1 is the extend of the region at the FeCo-MgO interface that responds linearly to the weak surface field $h_1 = 0.10$.

10.2 Neutron scattering on Fe/Cr

Exploration and development of new neutron scattering techniques is often struggling since neutron experiments suffer from a notorious lack of some orders of magnitude in flux when compared to modern x-ray sources. Since the criterion of sufficient intensity in the detector dictates which experiments can be performed it was of therefore of high priority to improve the flux of the instrument. The first step towards an intensity optimization of the EVA instrument was the construction and implementation [1] of a focusing monochromator combined with a tilt stage. This setup increased the flux by 40%.

The second modification was the implementation of transmission mirrors [2] which made experiments with polarized neutrons very easy to set up. Later, an analyzer based on transmission mirrors was developed. For the first time, reflectivity experiments with full neutron-spin analysis were possible at EVA. Since ILL is currently the world-leading institute for the development of ^{3}He neutron instrumentation, this research promoted attempts to invent new experimental methods to study magnetic behavior at interfaces. The experimental goal has been to explore to what extent the real structure of a multilayer (structural and magnetic domains, terraces, magnetic roughness, loose spins, thickness fluctuations, coupling angles) can be measured and understood by means of polarized neutron diffraction experiments. To produce a magnetic multilayer with a strongly anisotropic interface structure, a Nb(001) buffer has been deposited on a $Al_2O_3(1\bar{1}02)$ substrate. Since Nb is known to exhibit an epitaxial misorientation of about 3° when grown on sapphire of the this orientation, a pronounced terrace structure is present in the niobium buffer. On this buffer system, a $[Cr_{42\ \mathring{A}}/\ Fe_{19\ \mathring{A}}]_{200}$ multilayer

[1] The monochromator was built by Dipl. Ing. A.Steinhäuser and the machine shop of Max-Planck-Institute in Stuttgart.

[2] This was provided by Dr. T.Krist from Hahn-Meitner Institut, Berlin.

has been deposited in collaboration with the Ruhruniversität in Bochum, Germany.

In summary, the study of this system has encompassed the following experimental results:

- Both the neutron reflectivity from the Fe/Cr multilayer, and its off-specular diffuse scattering have been examined at the surface neutron diffractometer EVA.

- Two neutron intensity maxima along the specular path are observed, one at $L = 1/\ 2$, confirming antiferromagnetic coupling of the iron layers, and a second maximum at $L = 1$. The width of these maxima indicated that the vertical coherence length is about 8 unit cells only. At both maxima, diffuse sheets perpendicular to the specular path are observed, indicating a strong magnetic and structural roughness on an in-plane length scale smaller than 100 Å; this can be related to the terrace structure. Pronounced changes in the off-specular scattering distribution are observed if the angle between the neutron beam and the terraces is varied. The asymmetry of the Bragg-sheets is related to the orientation of the miscut terraces.

- To separate out magnetic contributions, a fully spin-analyzed experiment has been performed. In this experiment polarized ^{3}He was used for the first time as analyzer for a neutron reflectivity experiment. A major advantage of such a setup is the large angular acceptance of the ^{3}He spin filter, which enabled the use of multi-detectors, i.e. a 10 cm extended wire detector. This results in a dramatic improvement in data collection speed.

- In order to obtain a quantitative measurement of the magnetic roughness correlations, a rigorous theoretical analysis of the data is neces-

sary. The experimental results have been modeled with an extension of the supermatrix formalism to the case of off-specular scattering. The analysis is based on a simple real structure model. In this model, it is assumed, that neighboring Fe layers couple with 50^o. Further, the Fe/Cr interfaces exhibit a roughness of $\sigma = 4\mathring{A}$. In particular, the chemical and the magnetic roughness are described by the *same* numerical value. Furthermore, the analysis indicates the in plane correlation length of about 50 Å for the chemical and magnetic roughness is in agreement with the terrace structure of the multilayer. The good agreement between the measured data and the simulation indicates the high potential of the method to obtain a quantitative description as well as a qualitative description of these measurements. data.

Further experiments have been scheduled in order to record different orientations of the terraces with respect to the incident beam[3]. These experiments will provide a basis for a deeper theoretical description of the measured intensity distribution.

[3]The experiment is performed by J.Major and A.Vorobiev, Max-Planck Institut für Metallforschung, Stuttgart, Germany.

Appendix A

Details of the scattering theory

A.1 The ideally imperfect crystal

In Eq. 5.9 the number density n was introduced. At this point, assumptions were made about the defect structure and morphology of our FeCo-samples, namely, that they are ideally-imperfect crystals. The meaning of this well established-concept is depicted in Fig. A.1, as discussed by [90].

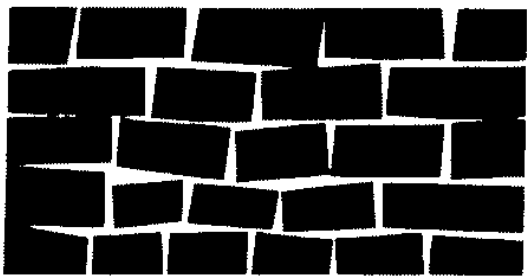

Figure A.1: Sketch of an ideal imperfect crystal [90].

For an ideal sample, the intensity is proportional to the square of the

number of scatterers. For many reasons, this is commonly not observed in a real experiment. For the FeCo-samples studied in this work, a mosaic distribution up to 1°) has been observed. These films therefore consist of many single crystalline islands whose lattice planes are slightly tilted with respect to each other and for this reason they do not interfere but rather add up incoherently [90]. The total intensity is proportional to the number of islands, whereas the intensity of each island still scales with the square of the number of scatterers. The average diameter of the islands can be inferred from the width of the Bragg reflections along $q_{\parallel}$.

A.2 Resolution

The resolution element in reciprocal space is given by the divergence of the incoming and the scattered beam and by the energy resolution of the experimental setup. All experiments have been done with a very good energy resolution. For instance, the energy resolution of the Troïka beamline is

$$\frac{d\lambda}{\lambda} = 10^{-5}, \tag{A.1}$$

achieved using a diamond crystal with (110) surface in transmission and the (111) reflection. Therefore, the incident x-ray wave can be assumed to be ideally monochromatic and the resolution is dominated by the collimating system. The beam divergence in real space corresponds to a resolution element in reciprocal space, as indicated by the parallelogram depicted in Fig. A.2. From geometric considerations the resolution volume dV_q is

$$dV_q = (\ q_i \cdot d\alpha_{i,(x,z)} \cdot q_f \cdot d\alpha_{f,(x,z)}\ ) \cdot (\ q_i \cdot d\alpha_{i,(y)} + q_f \cdot d\alpha_{f,(y)}\ ) \sin(2\theta) \tag{A.2}$$

The index (x, z) denotes the divergence of α in the scattering plane and (y) the divergence perpendicular to this. For the x-ray experiment under consideration, it was essential to keep σ_z, the resolution in the q_z direction

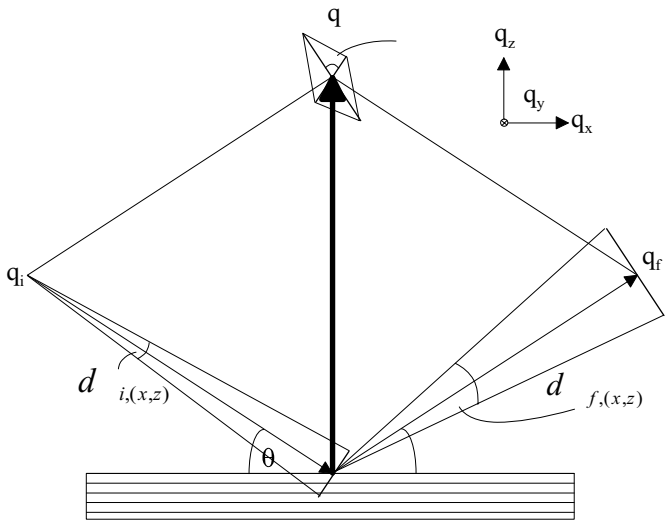

Figure A.2: The resolution volume in reciprocal space is defined by the beam slit collimation system. See the text for an explanation.

small, since the signal shows oscillations in this direction which are not to be smeared by resolution effects. σ_z is given by

$$\sigma_z = q_f \cdot \alpha_{f,\,(x,z)} \cdot \cos\,(\theta) \tag{A.3}$$

if the resolution is dominated by the collimating slits of the detector, as shown in Fig. A.2.

A.3 Mosaicity

Due to the relatively large mosaic distribution μ of the thin films ($\mu \geq 0.3°$) the density of intensity in reciprocal space is proportional to $1/\,\pi q_z^2 \sin^2\,(\mu/\,2)$), as can be seen from Fig. A.3. Assuming that the angular resolution α is much smaller than the mosaic distribution μ, the measured intensity becomes

$$I_{exp}(q_z) = \frac{I_{ideal}(q_z) \cdot dV_q}{\pi \cdot q_z^2 \cdot \sin^2\,(\mu/\,2)}. \tag{A.4}$$

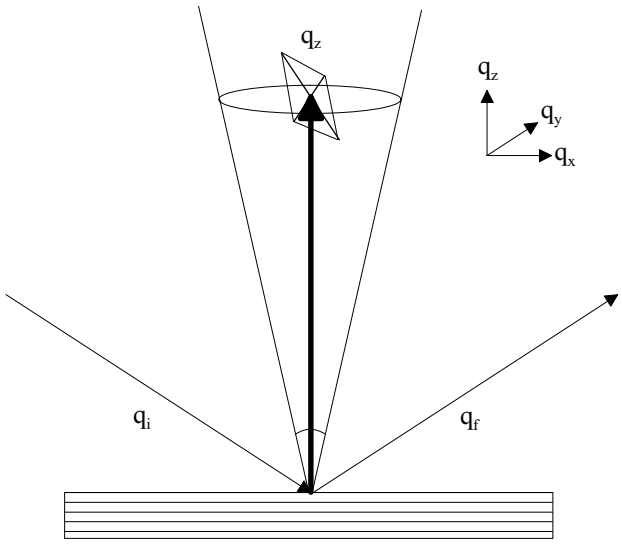

Figure A.3: The x-ray scattering intensity of a film with a large mosaic distribution (μ) is cone-shaped in reciprocal space.

A.4 Lorentz factor

In a real experiment normalized intensities are measured. The angular dependent correction factors are collected in the Lorentz factor, which is

$$\begin{aligned} L(\theta) &= \frac{dV}{\pi \cdot q_z^2 \cdot \sin^2\ (\mu/\ 2)} \propto \frac{\sin\ (2\theta)}{\sin^2\ (\theta)} \propto \frac{2 \cdot \cos\ (\theta) \cdot \sin(\theta)}{\sin^2\ (\theta)} \\ &\propto \frac{\cos\ (\theta)}{\sin\ (\theta)}. \end{aligned} \tag{A.5}$$

This has been used in Eq. 5.13.

Appendix B

Photos

The following photographs depict the different experimental setups.

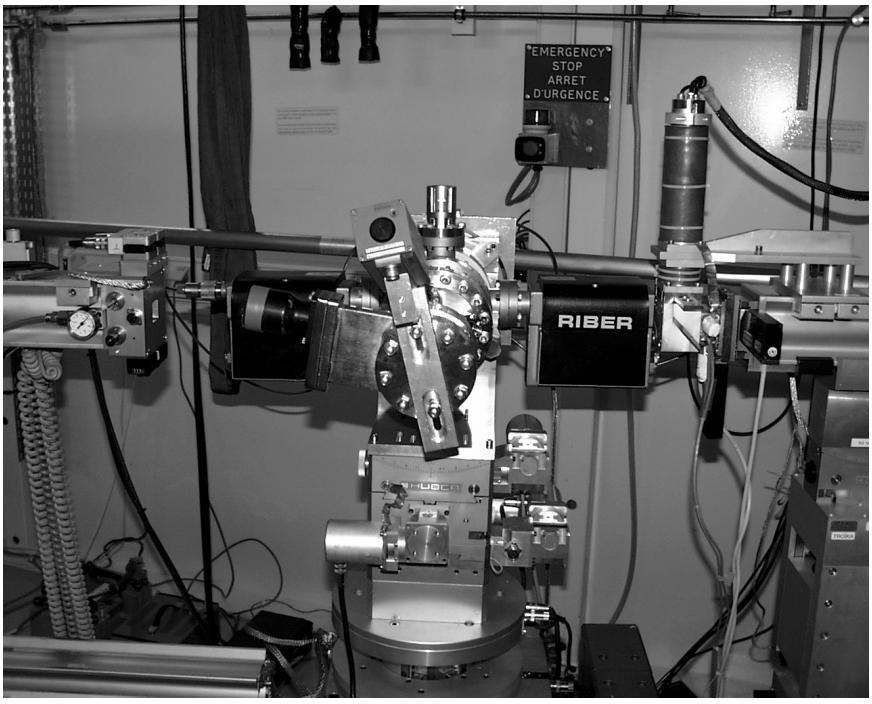

Figure B.1: Chamber B mounted on Troïka I (ESRF) in June 1999.

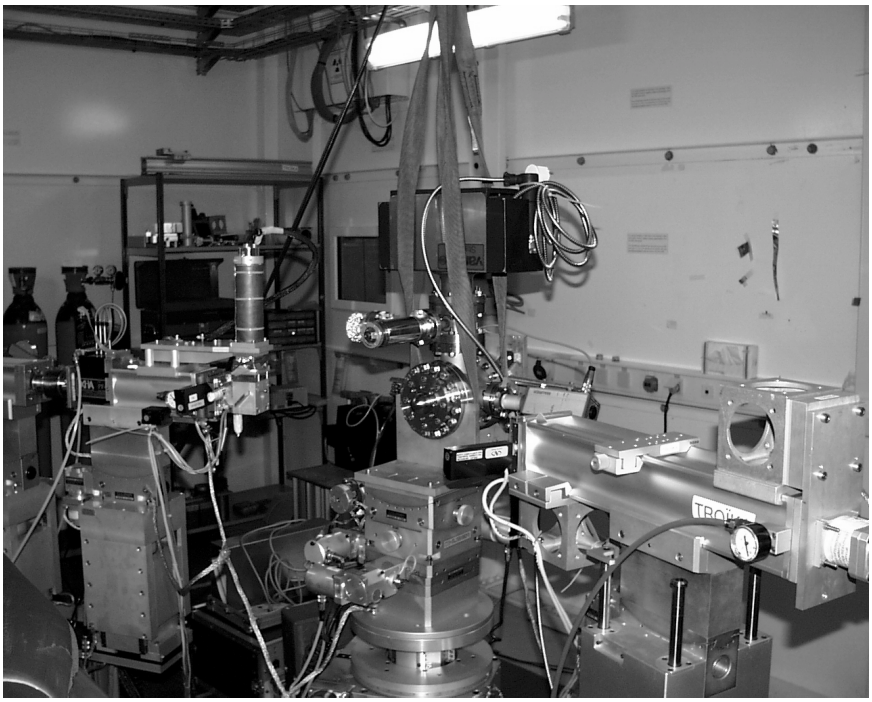

Figure B.2: The dome chamber C mounted on Troïka I (ESRF) in December 1999.

Bibliography

[1] W. Friederich, P. Knipping, and M. Laue, *Interferenz-Erscheinungen bei Röntgentrahlen*, Sitzungsberichte der Kgl. Bayrischen Akademie der Wissenschaften (1912).

[2] J. M. Bijvoet, W. G. Burgers, and G. Haegg, *Early Papers on Diffraction of X-rays by Crystals*, A. Oosthoek's Uitgeversmaatschappij N. V., Utrecht (1969).

[3] C. G. Shull and S. Siegel, *Neutron Diffraction Studies of Order-Disorder in Alloys*, Phys. Rev. **75**, 1 (1949).

[4] C. G. Shull, *Early development of neutron scattering*, Rev. Mod. Phys. **67**, 753 (1995).

[5] J. A. Oyedele and M. F. Collins, *Composition dependence of the order-disorder transition in iron-cobalt alloys*, Phys. Rev. B **16**, 3208 (1977).

[6] M. E. Fisher, *The theory of critical point singularities*, Proceedings of the international school of physics Enrico Fermi edited by M. S. Green (1971).

[7] M. N. Baibich, J. M. Broto, A. Fert, F. Nguyen Van Dau, F. Petroff, P. Etienne, G. Creuzet, A. Friederich, and J. Chazelas, *Giant Magnetoresistance of Fe(001)/ Cr(001) Magnetic Superlattices*, Phys. Rev. Lett. **61**, 2472 (1988).

[8] M. Freitag, P. Schmollngruber, and G. Haas, *Entwicklung von GMR-Schichtsystemen für Sensoren im KFZ*, DPG Frühjahrstagung, Hauptvortrag AM 5.3 (2000).

[9] P. Grünberg, R. Schreiber, Y. Pang, M. B. Brodsky, and H. Sowers, *Layered Magnetic Structures: Evidences for Antiferromagnetic Coupling of Fe Layers across Cr Interlayers*, Phys. Rev. Lett. **57**, 2442 (1986).

[10] J. Unguris, R. J. Celotta, and D. T. Pierce, *Observation of Two Different Oscillation Periods in the Exchange Coupling of Fe/Cr/Fe(001)*, Phys. Rev. Lett. **67**, 140 (1991).

[11] J. C. Slonczewski, *Fluctuation Mechanism for Biquadratic Exchange Coupling in Magnetic Multilayers*, Phys. Rev. Lett. **67**, 3172 (1991).

[12] F. L. Lederman and M. B. Salamon, *Experimental verification of scaling and test of the universality hypothesis from specific heat data*, Phys. Rev. B **9**, 2981 (1972).

[13] P. C. Hohenberg and B. I. Halperin, *Theory of dynamical critical phenomena*, Rev. Mod. Phys. **49**, 435 (1977).

[14] J. Als-Nielson, *Neutron scattering and spatial correlation near the critical point* in Phase transitions and critical phenomena, ed. by C. Domb and M. Green, volume 5a, Academic Press (1976).

[15] M. E. Fisher, *The theory of equilibrium critical phenomena*, Rep. Prog. Phys. **30**, 615 (1967).

[16] L. S. Ornstein and F. Zernike, *Die linearen Dimensionen der Dichteschwankungen*, Physik. Zeitschr. **19**, 134 (1918).

[17] J. J. Binney, N. J. Dowrick, A. J. Fisher, and M. E. J. Newman, *The theory of critical phenomena*, Claredon Press - Oxford (1992).

[18] M. E. Fisher and R. J. Burford, *Theory of critical-point scattering and correlations, I. The Ising Model*, Phys. Rev. **156**, 583 (1966).

[19] B. Park, G. B. Stephenson, S. M. Allen, and K. F. Ludwig, *Development of fluctuations into domains during ordering in Fe_3Al*, Phys. Rev. Lett. **68**, 1742 (1992).

[20] W. Koch, V. Dohm, and D. Stauffer, *Order-parameter relaxiation time of finite three-dimensional Ising-like systems*, Phys. Rev. Lett. **77**, 1789 (1996).

[21] H. B. Callen, *Thermodynamics*, John Wiley and Sons (1960).

[22] K. G. Wilson, *The renormalization group theory - introduction* in Phase transitions and critical phenomena, ed. by C. Domb and M. Green, volume 6, Academic Press (1976).

[23] Z. Q. Qiu, J. Pearson, and S. D. Bader, *Two-dimensional Ising transition of epitaxial Fe films grown on Ag(100)*, Phys. Rev. B **49**, 8797 (1994).

[24] M. Henkel, S. Andrieu, P. Bauer, and M. Piecuch, *Finite-size scaling in thin Fe/Ir(100) layers*, Phys. Rev. Lett. **21**, 4783 (1998).

[25] J. H. Barry and M. W. Meisel, *Exact solutions in a S = 1/2 quantum spin ladder model with pair and quartic interactions*, Phys. Rev. B **58**, 3129 (1998).

[26] H. J. Schulz, *Phase diagrams and correlation exponents for quantum spin chains of arbitrary spin quantum number*, Phys. Rev. B **34**, 6372 (1986).

[27] M. E. Fisher, *Renormalization group theory: its basis and formulation in statistical physics*, Rev. Mod. Phys. **70**, 653 (1998).

[28] L. Guttman, *Variation of long range order in Fe_3Al near its transition temperature*, Phys. Rev. Lett. **22**, 517 (1969).

[29] L. Guttman, *Critical scattering of X-rays from Fe_3Al*, Phys. Rev. Lett. **22**, 520 (1969).

[30] J. C. Le Guillou and J. Zinn-Justin, *Critical exponents from field theory*, Phys. Rev. B **21**, 3976 (1980).

[31] R. Suter and C. Hohenemser, *Review of measurements of critical exponent β in simple magnetic systems*, J. Appl. Phys. **50**, 1814 (1979).

[32] M. E. Fisher and P. E. Scesney, *Visibility of critical-exponent renormalization*, Phys. Rev. A **2**, 825 (1970).

[33] H. W. Diehl, *Field-theoretical approach to critical behavior at surfaces* in Phase transitions and critical phenomena, ed. by C. Domb and J. L. Lebowitz, volume 10, (1986).

[34] K. Binder, *Critical behavior at surfaces* in Phase transitions and critical phenomena, ed. by C. Domb and J. L. Lebowitz, volume 8, (1983).

[35] T. C. Lubensky and M. H. Rubin, *Critical phenomena in semi-infinite systems. II. Mean field theory*, Phys. Rev. B **12**, 3885 (1975).

[36] T. C. Lubensky and M. H. Rubin, *ϵ -Expansion in semi-infinite systems*, Phys. Rev. Lett. **31**, 1469 (1973).

[37] T. C. Lubensky and M. H. Rubin, *Critical phenomena in semi-infinite systems. I. ϵ $-$Expansion for positive extrapolation length*, Phys. Rev. B **11**, 4533 (1974).

[38] L. Mailänder, H. Dosch, J. Peisel, and R. L. Jonson, *Near surface critical X-ray scattering from Fe_3Al*, Phys. Rev. Lett. **64**, 2527 (1990).

[39] H. W. Diehl, *Surface critical behavior in fixed dimensions d <4: Nonanalyticity of critical surface enhancement and massive field theory approach.*, Phys. Rev. Lett. **73**, 3431 (1994).

[40] L. Mailänder, *Experimentelle Untersuchung kritischen Verhaltens in Oberflächennähe am Legierungssystem Eisen-Aluminium.*, PhD thesis Ludwig-Maximilians-Universität München (1990).

[41] S. Krimmel, W. Donner, B. Nickel, and H. Dosch, *Surface segregation-induced critical phenomena at FeCo(001) surfaces*, Phys. Rev. Lett. **78**, 3880 (1997).

[42] S. Krimmel, *Röntgenstreuexperimente zum Ordnungsverhalten von Eisenlegierungen in Oberflächennähe*, PhD thesis Bergische Universität Gesamthochschule Wuppertal (1997).

[43] private communication H. Dosch.

[44] F. Schmid, *Surface order in body-centered cubic alloys*, Z. Phys. B **91**, 77 (1993).

[45] M. A. Vasiliev, *Surface effects of ordering in binary alloys*, J. Phys. D: Appl. Phys. **30**, 3037 (1997).

[46] Uwe Ritschel and Peter Czerner, *Near-Surface Long-Range Order at the Ordinary Transition*, Surf. Sci. Rep. **77**, 3645 (1996).

[47] M. E. Fisher and P.-G. de Gennes, *Physique des colloides - Phenomenes aux parois dans un melange binaire critique.*, Acad. Sci. Paris Ser. B **287**, 207 (1987).

[48] L. Peliti and S. Leibler, *Strong adsorption in critical binary mixtures*, J. Phys. C **16**, 2635 (1983).

[49] H. W. Diehl and M. Smock, *Critical behavior at the extraordinary transition: Temperature singularity of surface magnetisation ant order parameter profile to one loop order*, Phys. Rev. B **47**, 5841 (1993).

[50] H. W. Diehl and M. Smock, *Erratum: Critical behavior at the extraordinary transition: Temperature singularity of surface magnetisation and order parameter profile to one loop order*, Phys. Rev. B **48**, 6740 (1993).

[51] G. Flöter and S. Dietrich, *Universal amplitudes and profiles for critical adsorption*, Z. Phys. B **97**, 213 (1995).

[52] J. R. Howse, J. Bowers, E. Manzanares-Papayanopoulous, A. McLure, and R. Steitz, *Neutron reflectivity studies of critical adsorption: The correspondence between a critical adsorption profile and specular neutron reflectivity.*, Phys. Rev. E **59**, 5577 (1999).

[53] S. Dietrich and R. Schack, *One to one correspondence between slowly decaying interfacial profiles and reflectivity*, Phys. Rev. Lett. **58**, 140 (1987).

[54] H. Zhao, A. Penninckx-Sans, L.-T. Lee, D. Beysens, and G. Jannink, *Probing the universal critical adsorption profile by neutron reflectivity*, Phys. Rev. Lett. **75**, 1977 (1995).

[55] A. J. Liu and M. E. Fisher, *Universal critical adsorption profile from optical experiments*, Phys. Rev. A **40**, 7202 (1989).

[56] P. S. Pershan A. Braslau, A. H. Weiss, and J. Als-Nielsen, *Smectic layering at the free surface of liquid crystals in the nematic phase: X-ray reflectivity*, Phys. Rev. B **35**, 4800 (1987).

[57] J. Als-Nielsen, F. Christensen, and P. S. Pershan, *Smectic-A order at the surface of a nematic liquid crystal: synchrotron X-ray diffraction*, Phys. Rev. Lett. **48**, 1107 (1982).

[58] P. S. Pershan and J. Als-Nielsen, *X-ray reflectivity from the surface of a liquid crystal: surface structure and absolute value of critical fluctuations*, Phys. Rev. Lett. **52**, 759 (1984).

[59] M. Schlossman, Xiao-Lun Wu, and C. Franck, *Order-parameter profiles at long distances in an adsorbed binary liquid mixture near criticallity*, Phys. Rev. B **31**, 1478 (1985).

[60] Ch. Bahr, C. J. Booth, D. Fliegner, and J. W. Goodby, *Critical adsorption at the free surface of a smectic liquid crystal possessing a second order phase transition*, Phys. Rev. Lett. **77**, 1083 (1996).

[61] D. S. P. Schmith and B. M. Law, *Ellipsometric measurement of surface amplitude ratio near a critical end point*, J. Chem. Phys. **99**, 9836 (1993).

[62] J. W. Schmidt, *Universal adsorption at the vapor-liquid interface near the consolute point*, Phys. Rev. A **89**, 885 (1990).

[63] R. Süssmann and G. Findenegg, *Critical adsorption at the surface of a polymer solution. Analysis of ellipsometric data on the depletion layer near the critical solution point*, Physica A **156**, 114 (1989).

[64] J. S. Rowlinson and B. Widom, *Mollecular theory of capillarity*, Oxford University, London (1982).

[65] F. Ramos-Gomez and B. Widom, *Noncritical interface near a critical end point II*, Physica **104A**, 595 (1980).

[66] I. L. Pegg, M. C. Groh, R. L. Scott, and C. M. Knobler, *Tricritical and Critical-End-Point Behavior of interfacial tensions in fluid mixtures*, Phys. Rev. Lett. **55**, 2320 (1985).

[67] A. Ciach and U. Ritschel, *Critical adsorption in systems with weak surface field: The renormalization-group approach*, Nuclear Physics B **489**, 653 (1997).

[68] A. Ciach, A. Maciolek, and J. Stecki, *Critical adsorption in the undersaturated regime: Scaling and exact results in Ising strips*, J. Chem. Phys. **108**, 5913 (1998).

[69] A. Maciolek, A. Ciach, and A. Drzewiński, *Crossover between ordinary and normal transition in two dimensional critical Ising films*, Phys. Rev. E **60**, 2887 (1999).

[70] E. Brezin and S. Leibler, *Critical adsorption: The renormalization-group approach*, Phys. Rev. B **27**, 594 (1983).

[71] N. S. Desai, S. Peach, and C. Franck, *Critical adsorption in the undersaturated regime*, Phys. Rev. E **52**, 4129 (1995).

[72] M. E. Fisher and P. J. Upton, *Fluid interface tensions near critical end points*, Phys. Rev. Lett. **65**, 3405 (1990).

[73] Z. Borjan and P. J. Upton, *Order-parameter profiles and Casimir amplitudes in critical slabs*, Phys. Rev. Lett. **81**, 4911 (1998).

[74] K. Binder, D. P. Landau, and A. M. Ferrenberg, *Character of the phase transition in thin Ising films with competing walls*, Phys. Rev. Lett. **74**, 298 (1995).

[75] M. Krech, *Casimir forces in binary liquid mixtures*, Phys. Rev. E **56**, 1642 (1997).

[76] M. N. Barber, *Finite size scaling* in Phase transitions and critical phenomena, ed. by C. Domb and J. L. Lebowitz, volume 8, Academic Press (1983).

[77] H. Nakanishi and M. E. Fisher, *Critical point shifts in films*, J. Chem. Phys. **78**, 3279 (1983).

[78] M. R. Meadows, B. A. Scheibner, R. C. Mockler, and W. J. O'Sullivan, *Critical phenomena in fluid films: Critical temperature shift, crossover temperature, and coexistence curve amplitude exponents, and a fluid boundary interaction*, Phys. Rev. Lett. **43**, 592 (1979).

[79] B. A. Scheibner, M. R. Meadows, R. C. Mockler, and W. J. O'Sullivan, *Critical phenomena in fluid films: Scaling crossover and law of corresponding states*, Phys. Rev. Lett. **43**, 590 (1979).

[80] B. A. Scheibner, M. R. Meadows, R. C. Mockler, and W. J. O'Sullivan, *Erratum: Critical phenomena in fluid films: Scaling crossover and law of corresponding states*, Phys. Rev. Lett. **43**, 1200 (1979).

[81] Y. Li and K. Baberschke, *Dimensional Crossover in Ultrathin Ni(111) Films on W(110)*, Phys. Rev. Lett. **68**, 7202 (1992).

[82] A. O. Parry, E. D. Macdonald, and C. Rascón, *Local functional models of critical correlations in thin films*, Phys. Rev. Lett. **85**, 4108 (2000).

[83] R. Klimpel and S. Dietrich, *Structure factor of thin films near continuous phase transitions*, Phys. Rev. B **60**, 16977 (1999).

[84] R. H. Yu, S. Basu, Y. Zhang, and J. Q. Xiao, *Magnetic domains and coercivity in FeCo soft magnetic alloys*, J. Appl. Phys. **85**, 6034 (1999).

[85] R. H. Yu, S. Basu, Y. Zhang, A. Parvizi-Majidi, and J. Q. Xiao, *Pinning effect of the grain boundaries on magnetic domain wall in FeCo-based magnetic alloys*, J. Appl. Phys. **85**, 6655 (1999).

[86] T. B. Massalski, *Binary alloy phase diagrams* volume 2, ASM International Metals Park, Ohio 2. edition (1996).

[87] B. G. Lyashenko, *Neutron diffraction study of Iron-Cobalt Alloy I*, Sov. Phys. Cryst. **6**, 443 (1962).

[88] F. J. Martínez Herrade, F. Mejía Lira, F. Aguilera Granja, and J. L. Morán López, *Theory of phase equilibrium in Co-Fe alloys*, Phys. Rev. B. **31**, 1686 (1985).

[89] J. Kudrnowsky, *Magnetism-induced ordering in two and three dimensions*, Phys. Rev. B **50**, 1 (1994).

[90] B. E. Warren, *X-Ray Diffraction*, Dover Books on Physics and Chemistry, Dover Publications (1969).

[91] J. S. Kasper and K. Lonsdale, *Physical and chemical tables* volume 3 of *International tables for x-ray crystallography.*, D. Reidel for I.U.CR, Publication (1985).

[92] B. L. Henke, E. M. Gullikson, and J. C. Davis, *Atomic Data and Nuclear Data Tables 54* volume 3, Kluwer Academic Publishers (1993), The www-adress is http://www-cxro.lbl.gov/optical_constants.

[93] I. K. Robinson, *Crystal truncation rods and surface roughness*, Phys. Rev. B. **33**, 3830 (1986).

[94] I. K. Robinson and D. J. Tweet, *Surface X-ray Diffraction*, Rep. Prog. Phys. **55**, 599 (1992).

[95] M. Born and E. Wolf, *Principles of optics: electromagnetic theory of propagation, interference and diffraction of light*, Cambridge 2. edition (1997).

[96] A. Caticha, *Diffraction of x-rays at the far tails of Bragg peaks*, Phys. Rev. B **47**, 76 (1993).

[97] B. W. Batterman and H. Cole, *Dynamical diffraction of x-rays by perfect crystals*, Rev. Mod. Phys. **36**, 681 (1964).

[98] C. Schamper, H. L. Meyerheim, and W. Moritz, *Resolution Correction Surface X-ray diffraction at high beam exit angles*, J. Appl. Cryst. **26**, 687 (1993).

[99] M. Toney and D. G. Wiesler, *Instrumental effects on measurements of surface X-ray diffraction rods: resolution function and active sample*, Acta. Cryst. **A49**, 624 (1993).

[100] H. Landolt et al., *Numerical data and functional relationships in science and technology* volume 26 of *New Series III*, Springer (1990).

[101] R. A. Cowley and C. A. Lucas, *X-ray scattering from surfaces and interfaces*, Faraday Dis. Chem. Soc. **89**, 181 (1990).

[102] C. A. Lucas, P. D. Hatton, S. Bates, T. W. Ryan, S. Miles, and B. K. Tanner, *Characterization of nanometer-scale epitaxial structures by grazing-incidence X-ray diffraction and specular reflectivity.*, J. Appl. Phys. **63**, 1936 (1988).

[103] I. K. Robinson, R. T. Tung, and R. Feidenhans'l, *X-ray interference method for studying interface structures.*, Phys. Rev. B. **38**, 3632 (1988).

[104] Chun Li and A. J. Freeman, *Giant monolayer magnetization of Fe on MgO; A nearly ideal two-dimensional magnetic system*, Phys. Rev. B **43**, 780 (1991).

[105] private communication F. Schlesener.

[106] S.M. Jordan, J.F. Lawler, R. Schad, and H. van Kempen, *Growth temperature dependence of the magnetic and structural properties of epitaxial Fe layers on MgO(001)*, J. Appl. Phys. **84**, 1499 (1998).

[107] S. M. Jordan, R. Schad, A. M. Keen, M. Bischoff, D. S. Schmool, and H. van Kempen, *Nanoscale Fe islands on MgO(001) produced by molecular-beam epitaxy*, Phys. Rev. B **59**, 7350 (1999).

[108] S. Yadavalli, M. H. Yang, and C. P. Flynn, *Low-temperature growth of MgO by molecular-beam epitaxy*, Phys. Rev. B **41**, 7961 (1990).

[109] H. Kiessig, *Interferenz von Röntgenstrahlen an dünnen Schichten*, Ann. Physik **5**, 769 (1931).

[110] L. G. Parrat, *Surface studies of solids by total reflection of X-rays*, Phys. Rev. **95**, 359 (1954).

[111] S. K. Sinha, E. B. Sirota, S. Garoff, and H. B. Stanley, *X-ray and neutron scattering from rough surfaces*, Phys. Rev. B **38**, 2297 (1988).

[112] D. K. G. de Boer, *X-ray reflection and transmission by rough surfaces*, Phys. Rev. B **51**, 5297 (1995).

[113] D. J. Keavney, E. E. Fullerton, and S. D. Bader, *Perpendicular conductance and magnetic coupling in epitaxial Fe/MgO/Fe(100) trilayers*, J. Appl. Phys. **81**, 795 (1997).

[114] K. F. Wojciechowski, *Surface energy of metals: theory and experiment*, Surf. Sci. **437**, 285 (1999).

[115] Jacek Goniakowski, *Characteristics of Pd deposition on the MgO(111) surface*, Phys. Rev. B **V60**, 16120 (1999).

[116] H. Lüht, *Surfaces and interfaces of solid materials*, Springer Study Edition, Springer Verlag 3rd edition (1996).

[117] G. Renaud, *Oxide surfaces and metal/oxide interfaces studied by grazing incidence x-ray scattering*, Surf. Sci. Rep. **32**, 5 (1998).

[118] V. E. Henrich and P. A. Cox, *The surface science of metal oxides*, Cambridge University Press (1994).

[119] Y. F. Zhukovskii, E. A. Kotomin, P. W. M. Jacobs, and A. M. Stoneham, *Ab initio modeling of metal adhesion on oxide surfaces with defects*, Phys. Rev. Lett. **84**, 1256 (2000).

[120] J. Bischof, D. Scherer, S. Herminghaus, and P. Leiderer, *Dewetting modes of thin metallic films : Nucleation of holes and spinodal dewetting*, Phys. Rev. Lett. **77**, 1536 (1996).

[121] S. Deckers, F. H. P. M. Habraken, W. F. van der Weg, A. W. Denier van der Gon, B. Pluis, J. F. van der Veen, and R. Baudoing, *Segregation at the $Pt_{0.5}Ni_{0.5}$(111) surface studied by medium-energy ion scattering*, Phys. Rev. B **42**, 3253 (1990).

[122] H. Reichert, P. J. Eng, H. Dosch, and I. K. Robinson, *Thermodynamics of surface segregation profiles at Cu_3Au(001) resolved by x-ray scattering*, Phys. Rev. Lett. **74**, 2006 (1995).

[123] J. J. Krebs, P. Lubitz, A. Chaiken, and G. A. Prinz, *Magnetic Resonance Determination of the Antiferromagnetic Coupling of Fe Layers through Cr*, Phys. Rev. Lett. **63**, 1645 (1998).

[124] S. T. Purcell, W. Folkerts, M. T. Johnson, N. W. E. McGee, K. Jager, J. aan de Stegge, W. B. Zeper, W. Hoving, and P. Grnberg, *Oscillations with a Period of Two Cr Monolayers in the Antiferromagnetic Exchange Coupling in a (001) Fe/Cr/Fe Sandwich Structure*, Phys. Rev. Lett. **57**, 903 (1991).

[125] M. Rührig, R. Schäfer, A. Hubert, R. Mosler, J. A. Wolf, S. Demokritov, and P. Grünberg, *Domain Observations on Fe-Cr Layered Structures (Evidence for a Biquadratic Coupling Effect)*, Phys. Status Solidi (a) **125**, 635 (1991).

[126] J. C. Slonczewski, *Origin of biquadratic exchange in magnetic multilayers (invited)*, J. Appl. Phys. **73**, 5957 (1993).

[127] J.-F. Bobo, M. Piecuch, and E. Snoek, *Complex AF couplings for Cu-Co multilayers with low copper thickness*, J. Magn. Magn. Mater **126**, 440 (1993).

[128] E. E. Fullerton, David M. Kelly, J. Guimpel, Ivan K. Schuller, and Y. Bruynseraede, *Roughness and Giant Magnetoresistance in Fe/Cr Superlattices*, Phys. Rev. Lett. **68**, 859 (1992).

[129] E. E. Fullerton, K. T. Riggs, C. H. Sowers, S. D. Bader, and A. Berger, *Suppression of Biquadratic Coupling in Fe/Cr Superlattices below the Neel Transition of Cr*, Phys. Rev. Lett. **75**, 330 (1995).

[130] E. E. Fullerton, S. D. Bader, and J. L. Robertson, *Spin-Density-Wave Antiferromagnetism of Cr in Fe/Cr(001) Superlattices*, Phys. Rev. Lett. **77**, 1382 (1996).

[131] A. Schreyer, C. F. Majkrzak, Th. Zeidler, T. Schmitte, P. Bödeker, K. Theis-Bröhl, A. Abromeit, J. A. Dura, and T. Watanabe, *Magnetic Structure of Cr in Exchange Coupled Fe/Cr(001) Superlattices*, Phys. Rev. Lett. **79**, 4914 (1997).

[132] R. S. Fishman and Zhu-Pei Shi, *Collinear spin-density waves ordering in Fe/Cr multilayers and wedges*, Phys. Rev. B **59**, 13849 (1999).

[133] V. Holy and T. Baumbach, *Layered Magnetic Structures: Evidences for Antiferromagnetic Coupling of Fe Layers across Cr Interlayers*, Phys. Rev. B **49**, 10668 (1994).

[134] C. S. Nelson, *Charge-magnetic roughness correlations in an Fe/Gd multilayer*, Phys. Rev. Lett. **60**, 12234 (1999).

[135] J. A. Borchers, J. A. Dura, J. Unguris, D. Tulchinsky, M. H. Kelley, C. F. Majkrzak, S. Y. Hsu, R. Loloee, W. P. Pratt Jr., and J. Bass, *Observation of Antiparallel Magnetic Order in Weakly Coupled Co/Cu Multilayers*, Phys. Rev. Lett. **82**, 2796 (1999).

[136] A. Rühm, B. P. Toperverg, and H. Dosch, *Supermatrix approach to polarized neutron reflectivity from arbitrary spin structures*, Phys. Rev. B. **60**, 16073 (1999).

[137] E. A. Kondrashkina, S.A. Stepanov, R. Opitz, M. Schmidbauer, R. Kohler, R. Hey, M. Wassermeier, and D. V. Novikov, *Grazing-incidence X-ray scattering from stepped interfaces in AlAs/GaAs superlattices*, Phys. Rev. B **56**, 10469 (1997).

[138] S. Dietrich and A. Haase, *Scattering of X-rays and neutrons at interfaces*, Phys. Rep. **260**, 1 (1995).

[139] H. Dosch, K. Al Usta, A. Lied, W. Drexel, and J. Peisl, *The evanescent wave diffractometer: On the way to surface sensitive neutron scattering.*, Rev. Sci. Inst. **63**, 5533 (1992).

[140] R. Günther, *Doppelbrechung und Streuung evaneszenter Neutronen an ferromagnetischen Oberflächen*, PhD thesis Bergische Universität GH Wuppertal (1997).

[141] R. Günther, W. Donner, B. P. Toperverg, and H. Dosch, *Birefringent Bragg Diffraction of Evanescent Neutron States in Magnetic Films*, Phys. Rev. Lett. **81**, 116 (1998).

[142] R. Günther, S. Odenbach, O. Schaerpf, and H. Dosch, *Reflectivity and evanescent diffraction of polarized neutrons from Ni(110)*, Physica B **234**, 508 (1997).

[143] B. P. Toperverg, A. Vorobyev, G. Gordeyev, B. Nickel, W. Donner, H. Dosch H, and T. Rekveldt, *Reflectivity and off-specular scattering from ferrofluid*, Physica B **283**, 203 (2000).

[144] W. Heil, K. Andersen, D. Hofmann, H. Humblot, J. Kulda, E. Lelievre-Berna, O. Scharpf, and F. Tasset, *^{3}He neutron spin filters at ILL*, Physica B **241–243**, 56 (1998).

[145] W. Braunbek, Z. Phys. **88**, 399 (1934).

[146] W. G. Williams, *Polarized Neutrons*, Clarendon Oxford (1988).

[147] A. R. Wildes, *The polarizer-analyzer correction problem in neutron polarization analysis experiments*, Rev. Sci. Inst. **70**, 4241 (1999).

[148] G. Gutenkunst, J. Mayer, and M. Rühle, *Atomic structure of epitaxial Nb-Al_2O_3 interfaces (I. Coherent regions)*, Phil. Mag. **75**, 1329 (97).

[149] G. Gutenkunst, J. Mayer, and M. Rühle, *Atomic structure of epitaxial Nb-Al_2O_3 interfaces (II. Misfit dislocation)*, Phil. Mag. **75**, 1357 (97).

[150] K. Theis-Bröhl, I. Zoller, P. Bödeker, T. Schmitte, H. Zabel, L. Brendel, M. Belzer, and D. E. Wolf, *Temperature- and rate-dependent RHEED oscillation studies of epitaxial Fe(001) on Cr(001)*, Phys. Rev. B **57**, 4747 (1998).

[151] A. Stierle and H. Zabel, *Cr Oxidation*, Europhys. Lett. **37**, 365 (1997).

[152] A. Gibaud, G. Vignaud, and S. K. Sinha, *The correction of geometrical factors in the analysis of x-ray reflectivity*, Acta Cryst. **A49**, 642 (1993).

List of Figures

List of Tables

Dank

Prof. Dr. H. Dosch danke ich für die interessante Themenstellung und die Möglichkeit, diese Arbeit unter hervorragenden Bedingungen in einem internationalen Umfeld durchführen zu können. Bei Prof. Dr. M. Mehring bedanke ich mich für die Übernahme des Nebenberichts. Dr. Wolfgang Donner danke ich für seine fachkundige Einführung in die Welt des Ultrahochvakuums. Seine Anregungen und die Teilnahme an den zahlreichen Meßreisen nach Hamburg und Grenoble haben wesentlich zum Erfolg dieser Arbeit beigetragen. Dr. Adrian Rühm danke ich für die Mitarbeit bei der quantitativen Auswertung der Neutronendaten und für ein kritisches Lesen großer Teile der vorliegenden Arbeit. Bei Arndt Steinhäuser und Veit Schönherr bedanke ich mich für die angenehme Zusammenarbeit bei der Weiterentwicklung des EVA-Diffraktometers. Dr. Janos Major danke ich für seine Beiträge bei dem Design eines Probenmagneten und eines Führungsfeldes für das ^{3}He-Experiment. Meinem Mitstreiter Christian Ern danke ich für die Gastfreundschaft bei meinen Stuttgart-Aufenthalten und für seine Unterstützung auf Meßreisen. Auch Andreas Schöpps hat zum Gelingen einiger Synchrotron-Experimente beigetragen. Dank ihrer beider Einsatz fand ich die MBE-Anlage stets in einem gutem Zustand vor. Herrn Frank Schlesener aus der Gruppe von Prof. Dr. Siegfried Dietrich danke ich für klärende Gespräche zum FeCo-Projekt. Prof. Dr. Hartmut Zabel und Dr. Andreas Schreyer, beide Ruhruniversität Bochum, danke ich für die Überlassung der Fe/Cr-Probe. Dr. Boris Toperverg und Dr. Andreas Stierle danke ich für Ratschläge bei streutheoretischen Aspekten des FeCo-Projektes. Annette Weißhardt danke ich für die Mikroskopie-Aufnahmen.